



Λ Baryon Production in $\bar{\nu}_\mu$ Interactions in the MicroBooNE Detector

Christopher James Thorpe, MPhys (Hons)
Department of Physics
Lancaster University

A thesis submitted for the degree of
Doctor of Philosophy

August, 2023

Declaration

I declare that the work presented in this thesis is, to the best of my knowledge and belief, original and my own work. The material has not been submitted, either in whole or in part, for a degree at this, or any other university. This thesis does not exceed the maximum permitted word length of 80,000 words including appendices and footnotes, but excluding the bibliography. A rough estimate of the word count is: 40984 .

Much of the work presented in this thesis builds upon that of the rest of the MicroBooNE collaboration. References to published works have been provided where possible. The components of this work by the author are listed in the following paragraphs.

The development of the entire event selection was performed by the author, from scratch, starting with the preselection cuts described in Section 4.3. The only significant component of the event selection not created by the author was the log-likelihood particle identification score. The simulation samples studied were manufactured by the MicroBooNE collaboration, save for the specialist hyperon production, neutron scattering, and NuWro alternative generator events, which were made with tools built by the author.

Most of the calculations of the systematic uncertainties due to neutrino the flux, background cross sections, and detector response, were performed with tools created by the MicroBooNE collaboration. The author made contributions to the Geant4Reweight software employed to propagate systematic uncertainties related to secondary interactions, primarily in the fitting procedure used to perform global fits to data. The visual scanning and sideband constraint studies were conducted by the author. The procedure for extracting the cross section measurement through pseudo-experiments and Bayesian statistics was created by the author.

Christopher James Thorpe

Λ Baryon Production in $\bar{\nu}_\mu$ Interactions in the MicroBooNE Detector

Christopher James Thorpe, MPhys (Hons).

Department of Physics, Lancaster University

A thesis submitted for the degree of *Doctor of Philosophy*. August, 2023

Abstract

The Cabibbo suppressed production of Λ baryons in anti-neutrino interactions with nuclei is a rare process that is yet to be measured with a modern neutrino detector with automated reconstruction. The cross section for this process is sensitive to a number of unique nuclear effects, most notably the secondary interactions of the produced hyperon while attempting to escape from the nucleus. Other interactions within the nuclear remnant can impact the estimation of neutrino energy in oscillation measurements, and thus an accurate description of the nuclear environment is required. The strangeness violating hyperon production process is only available to anti-neutrinos.

The model of this interaction is implemented into the NuWro neutrino interaction Monte Carlo simulation, and some predictions are presented, focusing on the role of nuclear effects. This model introduces a hyperon-nucleus potential, which calculations from hypernuclear theory permit to be strongly repulsive in the case of Σ baryons. The presence of this potential is found to sculpt the shape of the differential cross section in some variables.

The MicroBooNE detector will be described, followed by a description of a measurement of the flux averaged, restricted phase space cross section of Cabibbo suppressed Λ baryon production. A sophisticated event selection is employed, as a very large quantity of background neutrino interactions must be removed to perform the measurement with any sensitivity. This selection introduces some novel techniques such as the island finding method, and achieves a background reduction of $\sim 10^6$, with an efficiency of around 7%. The calculation of the systematic uncertainties will be explained, including two procedures explored to handle sources of background with extremely poor simulation statistics: an in-situ constraint using data from sidebands, and a visual inspection of the data and simulation to remove the troublesome background events.

The sensitivity to the Λ baryon production cross section is calculated in the form of Bayesian posterior probability distributions, combining the systematic uncertainties with data and simulation statistical uncertainties. As a rare process, the statistical uncertainties are highly non-Gaussian, and the Bayesian approach is applied to include the full shapes of these uncertainties. Data corresponding to 2.2×10^{20} protons on target of neutrino mode running and 4.9×10^{20} protons on target of anti-neutrino running is analysed. When the data was unblinded, five Λ production candidates were selected from the data, consistent with the MC simulation prediction of 5.3 ± 1.1 events. The final estimated cross section is $1.8_{-1.6}^{+2.0} \times 10^{-40} \text{cm}^2/\text{Ar}$ when employing the sideband constraint procedure. A similar result of $2.0_{-1.8}^{+2.2} \times 10^{-40} \text{cm}^2/\text{Ar}$ is obtained when performing the visual scan instead. The methods

used in this analysis are intended to be easily exported to other LArTPC detectors such as the Short Baseline Near Detector.

Publications

The following publications have been generated while developing this thesis, and to an extent have guided this thesis into what it has become:

Much of the discussion in Chapter 2 was previously published in C. Thorpe *et al.* “Second class currents, axial mass, and nuclear effects in hyperon production”. *Phys. Rev. C* 104.3 (2021), p. 035502.

The author of this thesis contributed material describing the fitting procedure applied in Section 5.6 to: J. Calcutt *et al.* “Geant4Reweight: a framework for evaluating and propagating hadronic interaction uncertainties in Geant4”. *JINST* 16.08 (2021), P08042.

The main measurement described in Chapters 4- 6 has been published as: P. Abratenko *et al.* “First Measurement of Quasielastic Λ Baryon Production in Muon Antineutrino Interactions in the MicroBooNE Detector”. *Phys. Rev. Lett.* 130.23 (2023), p. 231802.

Acknowledgements

Firstly, I would like to thank my wonderful supervisor, Professor Jarosław Nowak, for his guidance, enthusiasm, and ability to find me so many opportunities to share my work with others (or “throwing me under the bus”, as you once put it).

I could never have completed this thesis without the support of my collaborators on MicroBooNE. The list of people I’m indebted to is far too long to write here, so instead I give special mentions to Kirsty Duffy, Elena Gramellini, Lauren Yates, Steven Gardiner, Afroditi Papadopoulou, Krishan Mistry, Matt Toups, David Caratelli, Sophie Berkman, Andy Furmanski, Tim Bolton, Vassili Papavassiliou, and Justin Evans. To my hand scanners, David Marsden, Niam Patel, Ishanee Pophale, and Natsumi Taniuchi, I think I still owe each one of you a drink!

Much of what I present in this thesis was motivated by the work I began as an MPhys student working on NuWro, which I was able to continue with the help of Jan Sobczyk, Cezary Juszczak, and Kajetan Niewczas (the latter also becoming an excellent tour guide when I came to visit Wrocław).

I wish to thank Andy Blake for a fantastic internship (also about hyperons) all those years ago and for showing me how to write my first Root macro, and Dom Brailsford for knowing how to ask challenging questions, but always helping me to figure out the answers.

My time in Lancaster has been made far more enjoyable by the other PhD students and postdocs (and taxidermied animals) I was lucky enough to share an office with: Ishanee, Katherine, Niam, Will, Henry, Lingxin, Elliot, Ruby, Ryan, and Neza. I’m especially thankful to Tristan Doyle for providing some calming advice and encouragement concerning applying to PhDs, and later research positions, when I really needed it.

Last, but certainly not least, I will always be grateful to Mum, Dad, Emily, Becky, and the rest of my family, for their love and support.

In loving memory of Grandma Lily

Contents

1	The Neutrino	1
1.1	Proposal and Discovery	1
1.1.1	Trouble with β Decay	1
1.1.2	The Electron Neutrino	1
1.1.3	The Muon Neutrino	2
1.1.4	The Tau Neutrino	3
1.1.5	How Many Flavours?	4
1.2	The Standard Model Neutrino	5
1.2.1	Symmetries of the Standard Model	5
1.2.2	Neutrino Interactions	6
1.2.3	Neutrino Mass	7
1.3	Neutrino Oscillation	8
1.3.1	Experimental Hints	8
1.3.2	Mathematical Description	8
1.4	Short Baseline Oscillations	11
1.4.1	Gallium	11
1.4.2	LSND	12
1.4.3	The MiniBooNE Low Energy Excess	13
1.4.4	Neutrino-4	14
1.4.5	The Sterile Neutrino: A Solution?	15
1.5	Neutrino Interaction Processes	17
1.5.1	Elastic and Quasi-Elastic	18
1.5.2	Resonance Production (RES)	19
1.5.3	Deep Inelastic Scattering (DIS)	21
1.5.4	Meson Exchange Current (MEC)	22
1.5.5	Coherent Neutrino-Nucleus Scattering (COH)	22
1.5.6	Nuclear Effects	23
1.5.7	Measuring Oscillation	24
1.6	Summary of Chapter 1	25
1.7	Thesis Outline	26

2	Direct Hyperon Production	27
2.1	Hyperons	27
2.2	Free Nucleon Cross Sections	28
2.2.1	Matrix Element	28
2.2.2	Form Factors	31
2.2.3	Predictions	34
2.3	Nuclear Effects	36
2.3.1	Struck Nucleon Kinematics	36
2.3.2	Final State Interactions	37
2.3.3	The Hyperon-Nucleus Potential	39
2.4	Comparisons Between NuWro and GENIE	42
2.5	Summary	42
3	MicroBooNE	46
3.1	The Liquid Argon Time Projection Chamber	46
3.2	The MicroBooNE LArTPC	49
3.2.1	Cryostat and Charge Readout	50
3.2.2	Light Collection System	50
3.2.3	Triggers	52
3.2.4	Detector Effects	54
3.2.5	Particle Identification Methods	56
3.3	The BNB and NuMI Beams	63
3.4	Event Simulation	67
3.4.1	Neutrino Fluxes	67
3.4.2	Neutrino Interactions	68
3.4.3	Particle Propagation	69
3.4.4	Detector Response	70
3.4.5	Cosmic Rays	70
3.4.6	NuWro An Alternative Event Generator	71
3.5	Reconstruction	73
3.5.1	Hit Finding	73
3.5.2	Tracks, Showers, and Vertices	74
3.5.3	Truth Matching	75
4	Event Selections	77
4.1	Signal Definition	77
4.1.1	Which Decay Mode?	77
4.1.2	Detection Thresholds and Phase Space	79
4.1.3	BNB or NuMI?	80
4.1.4	Flux-Averaging	80

4.1.5	Signal Criteria	82
4.2	Monte Carlo Simulation and Data Samples	83
4.2.1	Hyperon Only Samples	84
4.2.2	Neutron Only Samples	84
4.2.3	Background Neutrino Interactions	85
4.2.4	Out-of-cryostat (Dirt) Samples	85
4.2.5	EXT Samples	85
4.3	Preselection	86
4.3.1	Reconstructed Vertex Location and the Fiducial Volume	86
4.3.2	Three Track Requirement	86
4.3.3	Zero Shower Requirement	89
4.4	Muon Identification	89
4.4.1	Reasoning	90
4.4.2	The Log-likelihood Ratio PID	90
4.4.3	Quality Cuts	91
4.4.4	Optimisation	93
4.5	Selection of the Proton and Pion Tracks	94
4.5.1	Useful Variables	94
4.5.2	The Three Plane Mean dE/dx	95
4.5.3	Boosted Decision Trees	99
4.5.4	Performance	103
4.6	Kinematic Variables	103
4.6.1	Proton and Pion Momentum Estimation	106
4.6.2	Reconstructed Invariant Mass	107
4.6.3	Angular Deviation	108
4.7	Island Finding	110
4.7.1	Reconstructed Decay Length	110
4.7.2	Island Finding Algorithm	112
4.7.3	Selection Criteria	114
4.8	Summary	117
4.8.1	Performance	117
4.8.2	Response to Other Sources of Hyperons	121
4.8.3	The Mis-reconstruction Background	123
4.8.4	The Neutron Background	124
4.8.5	Phase Space Dependence	127
5	Uncertainties	131
5.1	Introduction	131
5.2	Treatments	132
5.3	Low Simulation Statistics Background	134

5.3.1	Sideband Constraint	135
5.3.2	Visual Scanning	137
5.4	Neutrino Flux	140
5.4.1	Hadron Production	142
5.4.2	Beamline Geometry	145
5.4.3	POT Counting	145
5.4.4	Summary of Flux Uncertainties	146
5.5	Background Cross Sections	147
5.5.1	The MicroBooNE Cross Section Tune and Uncertainties	147
5.5.2	Alternative Models and CCQE RPA	149
5.5.3	CCQE Hyperon Cross Sections	150
5.5.4	Summary of Background Cross Section Uncertainties	151
5.6	Secondary Interactions	152
5.6.1	Protons	153
5.6.2	Λ Baryons	154
5.6.3	Charged Pions	155
5.6.4	Neutrons	159
5.6.5	Summary of Secondary Interaction Uncertainties	160
5.7	Detector Response	161
5.7.1	Detector Variations	161
5.7.2	Light Yield	164
5.7.3	Wire Response	164
5.7.4	Recombination Model	165
5.7.5	Space Charge	166
5.7.6	Detector Uncertainties Summary	167
5.8	Miscellaneous	168
5.8.1	Visual Scanning	168
5.8.2	Sideband Fit Uncertainty	169
5.8.3	Signal Selection Efficiency	170
5.8.4	Out-of Cryostat Contribution	170
5.9	Summary of Systematic Uncertainties	172
5.10	Cross Section Extraction	173
5.10.1	Data Statistical Uncertainties	174
5.10.2	Monte Carlo Statistical Uncertainties	175
5.10.3	Sensitivity	177
6	Result and Summary	178
6.1	Selected Data	178
6.2	Visual Scan of Data	180
6.3	Cross Section Measurement	182

6.4	Distributions	182
6.5	Outlook	183
References		185
Appendix A Partial Phase Space Definition		196
Appendix B Selection Performance Tables		199
Appendix C Vertex Finding		201
Appendix D Systematics Calculations		204
D.1	Beamline Geometry	205
D.2	Background Cross Section Uncertainties	207
D.3	Light Yield Simulation	209
Appendix E When Applying the Visual Scan		210
E.1	Neutrino Flux	210
E.2	Background Cross Sections	213
E.3	Secondary Interactions	216
E.4	Detector Response	218
Appendix F Data MC Comparisons		220
F.1	Normalisation	221
F.2	Vertex x position.	222
F.3	Vertex y position.	223
F.4	Vertex z position.	224
F.5	Leading Track Length	225
F.6	Second Track Length	225
F.7	Leading Track Polar Angle	226
F.8	Leading Track Azimuthal Angle	226
F.9	BDT Input Variables	227
F.10	BDT Response Score	228
F.11	Kinematic Variables	229
F.12	Sidebands	230
Appendix G Flux		231

List of Figures

1.1	Spark Chamber ν_μ Candidate	3
1.2	Four ν_τ Events Observed by the DONUT Experiment	4
1.3	Number of Neutrino Flavours from the Z Boson Decay Width	5
1.4	Neutrino Feynman Vertices	7
1.5	Results of Gallium Experiments	12
1.6	Electron Neutrino Excess Observed By LSND	13
1.7	Particle Identification in MiniBooNE	14
1.8	The MiniBooNE Low Energy Excess	15
1.9	Values of Δm^2 and $\sin^2(\theta)$ Required by MiniBooNE	16
1.10	Signal Observed by Neutrino-4	17
1.11	Separate Fits to Short Baseline Appearance and Disappearance Data	18
1.12	Feynman Diagrams of Elastic and Quasi-elastic Neutrino Interactions	19
1.13	Feynman Diagram of a Resonant Neutrino Interaction	20
1.14	Event Rate at Different W for the Neutrino Event Generators	21
1.15	Feynman Diagram of Meson Exchange Current	22
1.16	Feynman Diagram of Charged Current Coherent Pion Production	23
1.17	Illustration of Nuclear Effects in Scattering	24
2.1	Annotated Feynman Diagram of Hyperon Production	29
2.2	$\bar{\nu}_\mu + p \rightarrow \Lambda + \mu^+$ Measurements vs NuWro Predictions	35
2.3	$\bar{\nu}_\mu + p \rightarrow \Sigma^0 + \mu^+$ Measurements vs NuWro Predictions	36
2.4	Hyperon Production Cross Sections for $\bar{\nu}_\mu + C$ Before and After FSI	39
2.5	Predicted limits on neutron/hyperon star masses	40
2.6	Σ^0 Kinetic Energy Distributions Using Different Hypernuclear Potentials	43
2.7	Comparisons of Differential Cross Sections Between NuWro and GENIE for Λ Production	44
2.8	Comparisons of Differential Cross Sections Between NuWro and GENIE for Σ^0 Production	45
3.1	Operational Principle of the LArTPC	48
3.2	Example MicroBooNE Event Display	49

3.3	Diagram of MicroBooNE Cryostat and Field Cage	51
3.4	Diagram of the MicroBooNE TPC	52
3.5	Diagram of a MicroBooNE Photomultiplier Tube	53
3.6	The Space Charge Effect in MicroBooNE	55
3.7	Effect of Dead Channels	56
3.8	The Bethe-Bloch Curve	58
3.9	Predicted Energy Loss Rates for Protons, Kaons, Charged Pions, and Muons	58
3.10	Event Display of Simulated Muon	59
3.11	Event Display of Simulated Proton	59
3.12	Event Display of Simulated π^+	60
3.13	Event Display of Simulated K^+	61
3.14	Event Display of Simulated e^-	61
3.15	Diagram of Electromagnetic Shower Development	62
3.16	Shower dE/dx of Photons and Electrons	62
3.17	Event Display of Simulated π^0	63
3.18	Position of MicroBooNE in the NuMI Beamline	65
3.19	The Booster Neutrino Beam Flux	66
3.20	The NuMI Beam Flux	66
3.21	Example of Overlay Event	71
3.22	CCQE Cross Section of GENIE and NuWro	72
3.23	Validation of the NuWro Flux/Geometry Simulation	73
3.24	Creating Hits from Wire Signals	74
3.25	Pandora Reconstruction	75
4.1	Event Display of Simulated Λ Production Interaction in MicroBooNE	78
4.2	Phase Space Acceptance	80
4.3	Anti-neutrino fluxes For Available Data	81
4.4	Predicted Numbers of Tracks	87
4.5	Examples of Failed Reconstruction of the Λ Baryon Decay Vertex	88
4.6	Predicted Numbers of Showers	89
4.7	Particles Creating the Longest Track	90
4.8	The Log-likelihood PID Score for Different Particles	92
4.9	Muon ID Performance Metrics	94
4.10	BDT Input Variables	97
4.11	Lengths of Λ Decay Product Tracks	98
4.12	Log-likelihood PID Score and Three Plane Mean dE/dx Calculated for Tracks of Different Lengths	100
4.13	Example of a Decision Tree	101
4.14	BDT Response Score Distributions	102
4.15	Decay Selection MVA ROC Curves	104

4.16	Muon/Proton/Pion Confusion Matrix	105
4.17	Proton and Pion Momentum Estimator Performances	107
4.18	Reconstructed Invariant Mass Distributions for Signal and Background	108
4.19	Diagram of Angular Deviation Calculation	109
4.20	Angular Deviation Values Calculated for Signal and Background	110
4.21	Event Display with Displaced Vertex	111
4.22	Reconstructed Decay Length Calculated for Signal and Background	112
4.23	Background Event with Unexpectedly Large Decay Length	113
4.24	Example of Island Finding Algorithm Applied to a Signal Event	115
4.25	Example of Island Finding Algorithm Applied to a Background Event	116
4.26	Example of Bad Reconstruction Background	124
4.27	Example of Bad Reconstruction Background	125
4.28	Event Display of the Neutron Background	126
4.29	Comparison of the Signal and Neutron Background with the Kinematic Variables Employed by the Event Selection	126
4.30	Efficiency as a Function of Anti-neutrino Energy	128
4.31	Efficiency as a Function of Λ Baryon Momentum	128
4.32	Efficiency as a Function of the Λ Baryon Range	129
4.33	Efficiency as a Function of the Opening Angle Between the Proton and π^-	129
4.34	Efficiency as a Function of the Opening Angle Between the Proton and π^-	130
5.1	Breakdown of Signal and Background Passing Automated Event Selection	132
5.2	Regions Defining the Near and Far Sideband Regions	136
5.3	Data Used in Sideband Constraint	137
5.4	Breakdown of Predicted backgrounds Before and After Application of the Sideband Constraint	138
5.5	Visual Output of Island Finding Given to Hand Scanners (Signal)	139
5.6	Visual Output of Island Finding Algorithm Given to Hand Scanners (Back- ground)	139
5.7	Breakdown of Predicted backgrounds Before and After Application of the Hand Scanning Weights	141
5.8	Fractional Uncertainties in Flux At Different Neutrino Energies/Directions	143
5.9	Flux Simulation's Hadron Production Variations	144
5.10	Predicted Neutrino Energies and Directions of the Selected Signal Events	144
5.11	Fractional Uncertainties from Flux	146
5.12	Selected Signal and Background with Background Cross Section Variations with Fractional Covariance Matrix	149
5.13	Background CCQE-like Hyperon Production Variations	150
5.14	Breakdown of fractional uncertainties.	152
5.15	Summary of Background Cross Section Uncertainties	152

5.16	Selected Signal and Background with the GEANT 4 p -Ar Cross Section Variations	154
5.17	Selected Signal and Background with the GEANT 4 Λ -Ar Cross Section Variations	155
5.18	Charged Pion Exclusive Channel Rates	157
5.19	Sample of Data Fitted with Geant4Reweight	157
5.20	Selected Signal and Background with the GEANT 4 π^\pm -Ar Cross Section Variations	159
5.21	CAPTAIN n -Ar Cross Section Data Compared with GEANT 4 Predictions .	160
5.22	Selected Signal and Background with the GEANT 4 n -Ar Cross Section Variations	160
5.23	Fractional Uncertainties in Signal and Background from Secondary Interactions	162
5.24	Predicted Signal and Background with the Wire Response Variations	165
5.25	Predicted Signal and Background with the Alternative Recombination Model and Fractional Covariance Matrix	166
5.26	Predicted Signal and Background with the Alternative Space Charge Map and Fractional Covariance Matrix	166
5.27	Summary of Detector Response Uncertainties	167
5.28	Hand Scan Uncertainty Variations	169
5.29	Sideband Fit Error Variations	169
5.30	Cross Section Shape Variations	171
5.31	Breakdown of Uncertainties in the Predicted Signal and Background in Different Categories	172
5.32	Bayesian Posterior Probability Density Distributions Describing Data Statistical Uncertainties	175
5.33	Bayesian Posterior Probability Density Distributions Describing MC Simulation Statistical Uncertainties	176
5.34	Final Sensitivity Curves	177
6.1	The Five Selected Data Events	179
6.2	Hand Scanning Results for Both Sets of Simulation Events	181
6.3	Unblinded Cross Section Probability Distributions	182
6.4	Distributions of data events after complete selection.	184
C.1	Diagram of the Vertex Finding Procedure	203
D.1	Predicted Signal and Background for the Beamline Geometry Variations . .	206
D.2	Selected Signal and Background with Alternative Background Cross Section Models and CCQE RPA Variations	208
D.3	Predicted Signal and Background for the Light Yield Variations	209

E.1	Selected signal/background.	210
E.2	Production Variations from the Flux Simulation	210
E.3	Predicted Signal and Background for the Beamline Geometry Variations	212
E.4	Selected Signal and Background with Background Cross Section Variations with Fractional Covariance Matrix	213
E.5	Background CCQE-like Hyperon Production Variations	213
E.6	Selected Signal and Background with Alternative Background Cross Section Models and CCQE RPA Variations	215
E.7	Secondary Interaction Cross Section Variations	216
E.8	Neutron Cross Section Variations	217
E.9	Detector Variations	219
F.1	Data/Monte Carlo Simulation Comparisons: Normalisation	221
F.2	Data/Monte Carlo Simulation Comparisons: x Vertex Position	222
F.3	Data/Monte Carlo Simulation Comparisons: y Vertex Position	223
F.4	Data/Monte Carlo Simulation Comparisons: z Vertex Position	224
F.5	Data/Monte Carlo Simulation Comparisons: Leading Track Length	225
F.6	Data/Monte Carlo Simulation Comparisons: Second Longest Track Length	225
F.7	Data/Monte Carlo Simulation Comparisons: Leading Track θ Angle	226
F.8	Data/Monte Carlo Simulation Comparisons: Leading Track ϕ Angle	226
F.9	Data/Monte Carlo Simulation Comparisons: BDT Input Variables	228
F.10	Data/Monte Carlo Simulation Comparisons: BDT Response Score	228
F.11	Data/MC Simulation Comparisons: Kinematic Variables	229
F.12	Data/MC Simulation Comparisons: Sidebands	230

List of Tables

1.1	Global Fit of Oscillation Parameters	11
2.1	Hyperon Properties	28
2.2	Hyperon Production Form Factors	33
2.3	Symmetry breaking corrections from Ref.[84].	34
3.1	Details of the Three Wire Planes in the MircoBooNE TPC	51
3.2	MicroBooNE's Data Taking Periods	67
3.3	Neutrino Interaction models employed by MicroBooNE	69
4.1	Number of Signal Events Expected from Each Data Taking Period	83
4.2	Integrated ROC Curve Values for MVA Algorithms	104
4.3	Performance of the Island Finding	117
4.4	Selection Summary	119
4.5	Selection Performance Metrics	120
4.6	Reduction of the Direct Σ^0 Background from the Event Selection	121
4.7	Reduction of the RESHyperon Background from the Event Selection	122
4.8	Reduction of the DIS Hyperon Background from the Event Selection	123
5.1	Results of the Visual Scanning Study	140
5.2	Beamline Geometry Parameters Varied	145
5.3	Fractional Covariance in ϵ , Φ , and B from Neutrino Flux Systematics	146
5.4	Background Cross Section Parameters Varied in Parallel	148
5.5	Alternative Background Cross Section Model Variations	150
5.6	Fractional Covariance in ϵ , Φ , and B from Cross Section Systematics	151
5.7	List of Pion Reinteraction Channels	156
5.8	π^+ Fit Covariance Matrix	158
5.9	π^+ Fit Covariance Matrix	158
5.10	Fractional Covariance in ϵ , Φ , and B from Secondary Interaction Systematics	161
5.11	List of Detector Model Variations	163
5.12	Fractional Covariance in ϵ , Φ , and B from Detector Response Systematics	167

5.13 Fractional Covariance in ϵ , Φ , and B	173
6.1 Data Events Selected by Visual Scanners	180
B.1 Event Selection Performance	200
G.1 Muon Anti-neutrino Flux Corresponding to Data Analysed	232

Chapter 1

The Neutrino

1.1 Proposal and Discovery

1.1.1 Trouble with β Decay

Measurements of the radioactive β decay of nuclei in the early 20th century exhibited a puzzling feature: a single electron was emitted, with a continuous spectrum of kinetic energies. This observation conflicts with several well established conservation laws, namely those applying to energy, momentum, and angular momentum.

In what he described as a “desperate remedy”, Wolfgang Pauli postulated the presence of a third particle that could carry the missing energy, momentum, and angular momentum [4]. So described, as this third particle would carry no electric charge, and only make its presence known through the disappearance of the aforementioned quantities, interacting with matter only very weakly rendering direct detection virtually impossible. Pauli named this particle the “Neutron”, though this name was also given to the neutrally charged nuclear particle discovered by James Chadwick. Enrico Fermi suggested the light neutral particle produced in β decay instead be named the “Neutrino”, meaning “little neutral one”, which has been in use ever since. In the same paper, Fermi constructed a quantitative description of β decay involving the new particle [5].

1.1.2 The Electron Neutrino

Two decades after Pauli’s proposal, in an experiment first proposed in Ref. [6], Fredrick Reins and Clyde Cowan attempted to directly detect electron anti-neutrinos produced by nuclear reactor at the Hanford site in the state of Washington, USA (and repeated at the Savannah River Plant, South Carolina), through the process of inverse β decay:

$$\bar{\nu}_e + p \rightarrow n + e^+, \tag{1.1}$$

the cross section of which could be estimated from Fermi's theory of β decay.

Their detector comprised several layers of dissolved cadmium-chloride, employed as a target material, separated by tanks of liquid scintillator instrumented with photomultiplier tubes (PMTs) [7, 8]. The interaction of an electron neutrino would be detected by first observing scintillation light produced when the positron underwent annihilation with an electron in the detector, producing a "prompt" light signal, followed by a delayed light signal when the neutron was captured by a cadmium nucleus, resulting in a γ ray photon. The experiment recorded a signal to background ratio of approximately 3. Additional tests performed included comparing changes in the observed event rate to those in the power output of the reactor, and replacing the water in the target volumes with heavy water (D_2O), effectively halving the mass in the detector that could undergo reaction 1.1, and observing a 50% decrease in the event rate.

Frederick Reines was awarded the Nobel Prize in 1995 for the discovery. Clyde Cowan had passed away in 1974 and the Nobel Prize is not awarded posthumously.

1.1.3 The Muon Neutrino

The experiment used to discover the muon neutrino [9] was the first foray into accelerator based neutrino experiments. The experiment employed the proton beam produced by the Alternating Gradient Synchrotron at Brookhaven National Laboratory (BNL), to produce charged pions that would decay to muons and neutrinos ¹:

$$\pi^\pm \rightarrow \mu^\pm + \nu. \quad (1.2)$$

They would then detect the neutrino with a spark chamber: a series of aluminium plates separated by thin layers of gas, with a large voltage applied between the plates, such that when a charged particle ionised the gas a spark would be produced and recorded by instruments. A muon detected by the experiment is shown in Figure 1.1. Under the hypothesis of a single variety of neutrino, the experiment would expect to observe roughly equal numbers of muons and electrons. Instead, the majority of events observed were from muons. The explanation was that there were two distinct varieties (now called flavours) of neutrino, one that would always produce electrons in charged current interactions, and one that produced muons:

$$\nu_e + n \rightarrow e^- + p, \quad (1.3)$$

$$\nu_\mu + n \rightarrow \mu^- + p. \quad (1.4)$$

Leon Lederman, Melvin Schwartz, and Jack Steinberger were jointly awarded the Nobel Prize in 1988 for this discovery.

¹This technique is still used by modern accelerator neutrino beams, and is discussed in more detail in Section 3.3

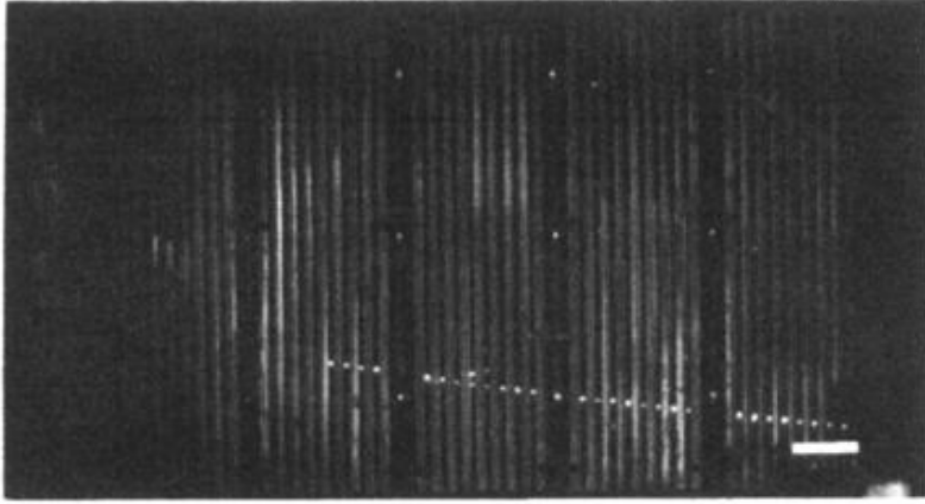


Figure 1.1: A single muon event observed by the spark chamber. The roughly horizontal row of white spots indicates the trajectory of the muon. Figure from Ref. [9].

1.1.4 The Tau Neutrino

The τ particle was discovered in 1975 [10], with properties suggesting it was a new charged lepton. Neutrino partners of the electron and muon had already been discovered, and the existence of the τ neutrino was postulated. The DONUT experiment [11] used 800 GeV protons from the Fermi National Accelerator Laboratory’s Tevatron collider to produce a flux of charmed mesons, some of which were predicted to decay into τ leptons and τ neutrinos:

$$D_S \rightarrow \bar{\nu}_\tau + \tau^- \quad \begin{array}{l} \searrow \\ \hookrightarrow \nu_\tau + \dots \end{array} \quad (1.5)$$

These would then interact via charged current processes in the detectors, producing τ leptons:

$$\nu_\tau + n \rightarrow \tau^- + \dots \quad (1.6)$$

$$\bar{\nu}_\tau + p \rightarrow \tau^+ + \dots \quad (1.7)$$

The experiment identified charged current τ neutrino interactions by looking for tracks with a “kink” very close to the interaction vertex, illustrated in Figure 1.2, signalling the decay of the very short lived τ lepton. Four τ neutrino candidates were detected, indicating the presence of ν_τ , with an expected background contamination of 0.34 ± 0.05 .

Most neutrino experiments are insensitive to the charged current interactions of the τ neutrino due to the large mass of the τ lepton. Aside from the DONUT experiment, two other experiments have directly observed the τ neutrino, OPERA [12], and IceCube [13]. The Super-Kamiokande experiment has studied the appearance of ν_τ in neutrinos resulting

from the interactions of cosmic rays in the upper atmosphere (atmospheric neutrinos) [14, 15], though this detector cannot directly observe the τ lepton.

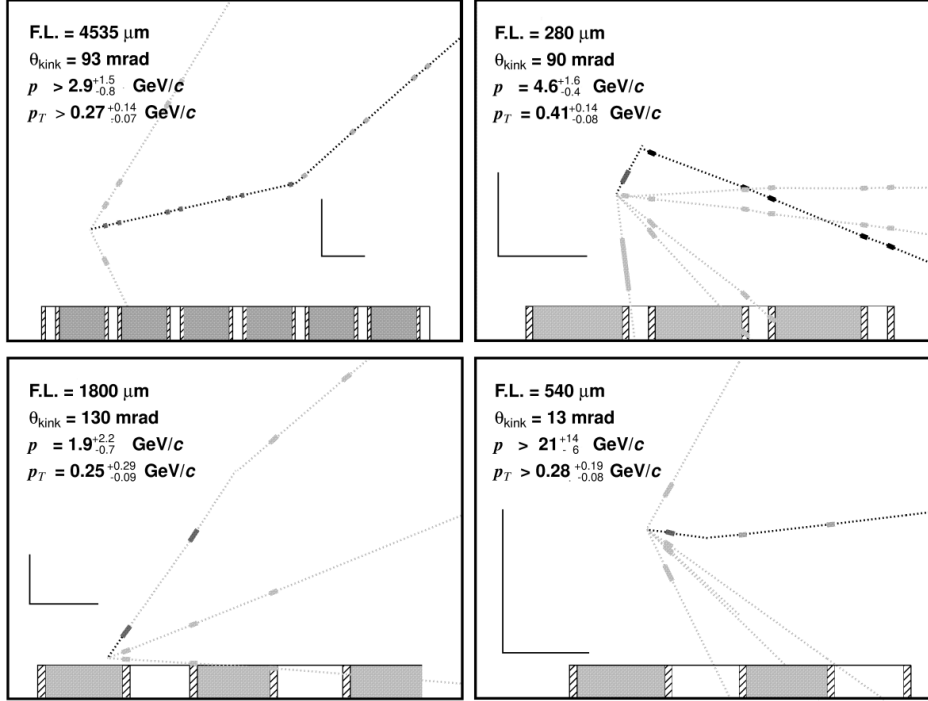


Figure 1.2: The ν_τ events observed by the DONUT experiment, indicating the trajectories of particles through the emulsion based tracker stage of the detector array. Figure from Ref. [11].

1.1.5 How Many Flavours?

The decay width of the Z boson is precisely predicted by the standard model, as are the partial widths of its various decay modes, which satisfy the following equation:

$$\Gamma = \sum_q \Gamma(Z \rightarrow q\bar{q}) + \sum_l \Gamma(Z \rightarrow l^-l^+) + \Gamma(Z \rightarrow W^+W^-) + \sum_l \Gamma(Z \rightarrow \nu_l\bar{\nu}_l). \quad (1.8)$$

Γ is the total decay width of Z , and the terms on the right hand side of Equation. 1.8 the partial widths of its various decay modes. The summations over q and l are over the quark and lepton flavours respectively, excluding the top quark. Equation 1.8 implies the total decay width of the Z boson depends on the number neutrino flavours.

A constraint on the number of neutrino flavours that interact with the Z boson may be established by studying the size and shape of the Z resonance peak observed in the cross

section of e^+e^- collisions, illustrated in Figure 1.3. Fitting this distribution yields an estimate of 2.9963 ± 0.0074 [16] flavours, consistent with the three already discovered.

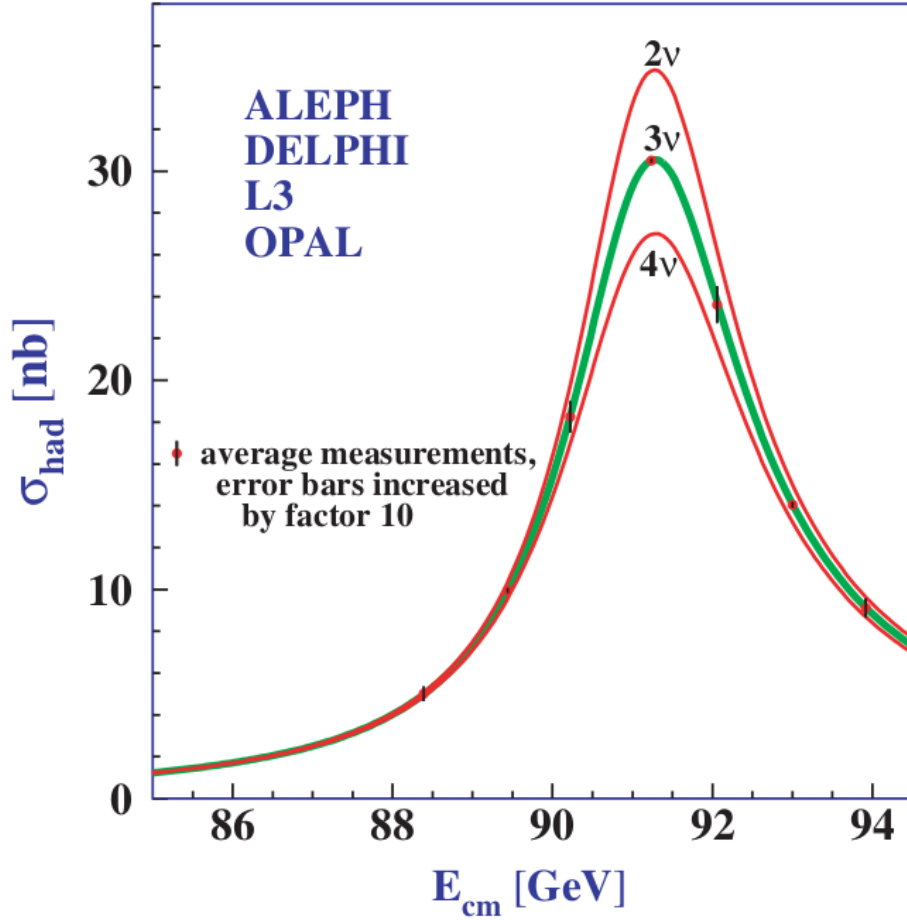


Figure 1.3: Measurements of the hadron production cross section at the Z boson resonance peak from the ALEPH [17], DELPHI [18], L3 [19], and OPAL [20] detectors at the Large Electron-Positron Collider at CERN, overlaid with predictions involving different numbers of light active neutrino flavours. Figure from Ref. [21].

1.2 The Standard Model Neutrino

1.2.1 Symmetries of the Standard Model

The Standard Model (SM) describes the (currently discovered) fundamental particles and the interactions between them, employing the machinery of quantum field theory. This model

includes three of the four fundamental forces: electromagnetism, the strong force, and the weak force. Finding a quantum mechanical description of gravity remains one of physics' greatest challenges. The SM is a gauge theory, with the following gauge group:

$$\text{SU}(3)_C \otimes \text{SU}(2)_L \otimes \text{U}(1)_Y, \quad (1.9)$$

where C denotes the colour charge, L the weak-isospin of fermions with left-handed chirality, and Y the weak hypercharge. The interactions are mediated by vector bosons, the gluon in the case of the strong interactions, the W^\pm and Z bosons in the weak interaction, and the photon for electromagnetism. The weak and electromagnetic forces are unified into the electroweak theory, with the gauge group $\text{SU}(2)_L \otimes \text{U}(1)_Y$.

The electroweak symmetry treats the components of the fermion fields with left-handed chirality and right-handed chirality differently: under the $\text{SU}(2)_L \otimes \text{U}(1)_Y$ symmetry, the left-handed neutrino field and left-handed charged lepton fields are paired into doublets, while there exists only a right-handed charged lepton field, which transforms as a singlet:

$$\psi_l^L = \begin{pmatrix} l^L \\ \nu_l^L \end{pmatrix}, \quad \psi^R = l^R. \quad (1.10)$$

l^L is the left-handed charged lepton field, ν_l^L the corresponding neutrino field, and l^R the right-handed charged lepton field. An important consequence of this formulation is that if a right-handed neutrino (or left handed anti-neutrino) exists, it will not participate in the weak interaction, and since neutrinos carry no electric or colour charges, they cannot interact directly through any other particles in the standard model.

1.2.2 Neutrino Interactions

The weak interactions of neutrinos are described by the following terms in the standard model Lagrangian:

$$\mathcal{L}^{\text{CC}} = \frac{-ig}{\sqrt{2}} \sum_{\alpha} \bar{\nu}_{\alpha}^L \gamma^{\mu} W_{\mu} \alpha^L + \text{H.C.} \quad (1.11)$$

$$\mathcal{L}^{\text{NC}} = \frac{-ig}{2 \cos \theta_W} \sum_{\alpha} \bar{\nu}_{\alpha}^L \gamma^{\mu} Z_{\mu} \nu_{\alpha}^L + \text{H.C.} \quad (1.12)$$

$\bar{\nu}_{\alpha} = \nu_{\alpha}^{\dagger} \gamma^0$, ν_{α} is a Dirac spinor describing the α flavoured, left handed neutrino field, α the corresponding charged lepton field, and \dagger denotes Hermitian conjugation. W_{μ} and Z_{μ} are components of the W boson and Z boson fields. The script μ indicates the four spacetime dimensions, and the Einstein summation convention is used. $\theta_W = 28.7^{\circ}$ is the Weinberg angle [22]. The two corresponding Feynman vertices are illustrated in figure 1.4.

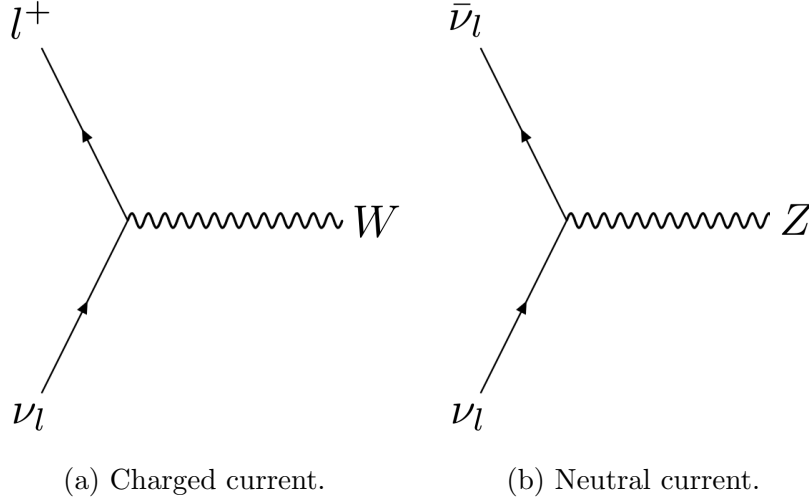


Figure 1.4: Feynman vertices predicted by the terms from standard model Lagrangian listed in equations 1.11 and 1.12.

1.2.3 Neutrino Mass

A generic mass term for a fermion described by the Dirac equation is:

$$-\frac{1}{2}m\bar{\psi}\psi = -\frac{1}{2}m(\bar{\psi}^L\psi^L + \bar{\psi}^R\psi^R) = -\frac{1}{2}m(\psi^{L\dagger}\psi^R + \psi^{R\dagger}\psi^L) \quad (1.13)$$

which evaluates to zero if there is no right handed field. In other words the neutrino, as described by the Standard Model, is massless. An alternative description of fermions found by Ettore Majorana in 1937, considers the possibility of a fermion that is its own anti-particle, otherwise known as a Majorana fermion. In this framework, neutrino mass terms of following form:

$$-\frac{1}{2}m\bar{\psi}_c^L\psi^L, \quad (1.14)$$

$$\psi_c^L = C\gamma^0\psi^{L*}, \quad (1.15)$$

may be constructed entirely from a left handed field. C is the charge conjugation operator. Equation 1.15 is known as the Majorana Condition, and $C\gamma^0\psi^{L*}$ behaves like a right-handed field. The interpretation of this condition is that neutrino/anti-neutrino are no longer distinct particles, but the left and right handed states of the same particle. The neutrino is the only fundamental particle (discovered so far) that can be a Majorana fermion; the quarks and charged leptons have non-zero electric charge and therefore cannot be their own anti-particles.

If the neutrino is a Majorana particle then interactions violating lepton number conservation by ± 2 are allowed, most notably the neutrinoless double β decay of nuclei. A number of experiments are searching for this process to test the Majorana hypothesis [23].

1.3 Neutrino Oscillation

1.3.1 Experimental Hints

The Homestake Mine experiment was constructed by Ray Davis and his collaborators to study the flux of neutrinos produced by the sun and the nuclear fusion processes involved. The experiment consisted of a tank containing 390,000 litres of tetrachloroethylene, and detected electron neutrinos via their capture by the ^{37}Cl nuclei in the tank. The experiment discovered the flux of solar neutrinos was below that of predictions [24], a conflict that later became known as the “Solar Neutrino Problem”. Drawing inspiration from neutral kaon oscillation, Bruno Pontecorvo proposed a solution in which the flavour content of a beam of neutrinos could evolve with distance from its source², an effect now called “Neutrino Oscillation”. The mechanism behind neutrino oscillations will be outlined in Section 1.3.2.

Nearly 50 year later, the Sudbury Neutrino Observatory (SNO) and Super-Kamiokande (Super-K) experiments independently confirmed the existence of neutrino oscillations. Both experiments use water Cherenkov detectors, placed deep underground to minimise cosmic backgrounds. SNO estimated the total solar neutrino flux by observing neutral current interactions (which are flavour insensitive), and compared this to the flux of electron neutrinos measured from their charged current interactions (which were only sensitive to the ν_e component), discovering a deficit in the latter [25]. Super-K studied the fluxes of atmospheric electron and muon neutrinos, the ratio of which, in the absence of oscillations, can be predicted to a high degree of precision. They discovered a deficit in the number of muon neutrinos arriving at the detector, alongside a small enhancement in the electron neutrino flux, strengthening with the distance they had travelled through the earth to arrive at the detector [26]. These experiments were jointly awarded the Nobel Prize for the discovery in 2015.

1.3.2 Mathematical Description

Neutrino oscillations may be explained by describing neutrinos in terms of two sets of eigenstates, which are superpositions of one another:

$$|\nu_\alpha\rangle = \sum_i U_{i\alpha} |\nu_i\rangle, \quad (1.16)$$

$$|\nu_i\rangle = \sum_\alpha U_{i\alpha}^* |\nu_\alpha\rangle. \quad (1.17)$$

The basis states $|\nu_\alpha\rangle$, are the so called “flavour eigenstates”, while the states $|\nu_i\rangle$, are the “mass eigenstates”. $U_{i\alpha}$ are the elements of a matrix that describes the mixing between the

²Pontecorvo initially proposed the existence of $\nu \rightarrow \bar{\nu}$ oscillations, the idea of evolving mixtures of the neutrino flavours came later.

two. This matrix later became known as the Pontecorvo-Maki-Nakagawa-Sakata (PMNS) matrix [27]. Neutrinos are always produced in their flavour eigenstates.

The oscillation effect is a consequence of the different masses of the mass eigenstates and how this affects the way they evolve as the neutrino propagates through spacetime. The propagation of a neutrino mass eigenstate is described by a plane wave:

$$|\nu_i(t)\rangle = e^{-i(E_i t - \mathbf{p}_i \cdot \mathbf{x})} |\nu_i(0)\rangle. \quad (1.18)$$

For a neutrino produced with energy of $E = p$, the energy E_i of the mass eigenstate i with mass m_i , assuming $p_i \gg m_i$:

$$E_i = \sqrt{m_i^2 + p_i^2} \approx p_i + \frac{m_i^2}{2p_i} = E + \frac{m_i^2}{2E}. \quad (1.19)$$

Assuming the neutrino travels at approximately the speed of light, mass eigenstate i after propagating a distance L will be described by:

$$|\nu_i(L)\rangle = e^{-\frac{iLm_i^2}{2E}} |\nu_i(0)\rangle. \quad (1.20)$$

The complete quantum state of a neutrino produced as flavour α after propagating a distance L is described by the superposition:

$$|\nu_\alpha(L)\rangle = \sum_i U_{i\alpha} |\nu_i(L)\rangle = \sum_i U_{i\alpha} e^{-\frac{iLm_i^2}{2E}} |\nu_i(0)\rangle. \quad (1.21)$$

When the neutrino interacts, the superposition of flavour eigenstates collapses and a single flavour state is observed. The probability of observing flavour state β after a neutrino produced in the flavour state α has propagated a distance L is given by the expression:

$$P_{\alpha\beta}(E) = |\langle \nu_\beta(0) | \nu_\alpha(L) \rangle|^2 = \left| \sum_i U_{i\alpha} U_{i\beta}^* e^{-\frac{iLm_i^2}{2E}} \right|^2. \quad (1.22)$$

The existence of neutrino oscillations conflicts with their description in the SM, as they must have nonzero rest masses in order to oscillate. The lack of a right handed neutrino in the SM forbids this.

Two Neutrino Case

If one assumes the existence of two neutrino flavours and two mass eigenstates, the matrix introduced in equation 1.16 may be written in terms of a single mixing angle θ :

$$U = \begin{pmatrix} \cos \theta & \sin \theta \\ -\sin \theta & \cos \theta \end{pmatrix}, \quad (1.23)$$

with which one obtains a compact expression for the transition probability stated in equation 1.22:

$$P_{\alpha \rightarrow \beta}(E) = \sin^2(2\theta) \sin^2\left(\frac{\Delta m^2 L}{4E}\right), \quad (1.24)$$

$$P_{\alpha \rightarrow \beta}(E) = \sin^2(2\theta) \sin^2\left(1.27 \frac{\Delta m^2 [\text{eV}^2] L [\text{km}]}{E [\text{GeV}]}\right), \quad (1.25)$$

substituting in commonly used units in Equation 1.25. $\Delta m^2 = m_1^2 - m_2^2$, is the difference between the squares of the masses of the two mass eigenstates. The oscillation probability is only sensitive to the squared difference between the neutrino masses, and therefore oscillation measurements alone cannot be used to determine the absolute neutrino masses. Other methods such as high precision measurements of the β decay spectrum [28] are required.

Three Neutrino Case

In the case of three flavour eigenstates and three mass eigenstates, the mixing matrix is:

$$U = \begin{pmatrix} U_{e1} & U_{e2} & U_{e3} \\ U_{\mu 1} & U_{\mu 2} & U_{\mu 3} \\ U_{\tau 1} & U_{\tau 2} & U_{\tau 3} \end{pmatrix}, \quad (1.26)$$

which is often written in terms of three mixing angles θ_{12} , θ_{23} , and θ_{13} , δ_{CP} , a parameter enabling the violation of the combined parity and charge conjugation symmetry (CP symmetry), and split into the product of three matrices, representing individual rotations in flavour space:

$$U = \begin{pmatrix} 1 & 0 & 0 \\ 0 & \cos \theta_{23} & \sin \theta_{23} \\ 0 & -\sin \theta_{23} & \cos \theta_{23} \end{pmatrix} \begin{pmatrix} \cos \theta_{13} & 0 & \sin \theta_{13} e^{-i\delta_{CP}} \\ 0 & 1 & 0 \\ -\sin \theta_{13} e^{i\delta_{CP}} & 0 & \cos \theta_{13} \end{pmatrix} \begin{pmatrix} \cos \theta_{12} & \sin \theta_{12} & 0 \\ -\sin \theta_{12} & \cos \theta_{12} & 0 \\ 0 & 0 & 1 \end{pmatrix}. \quad (1.27)$$

The transition probabilities themselves now require two mass splittings, Δm_{21}^2 and Δm_{31}^2 . This permits two possible orderings of masses of the three neutrino mass states: $m_1 < m_2 < m_3$, known as normal ordering (NO), and $m_3 < m_1 < m_2$, known as inverted ordering (IO). Determining the order of the three mass states, called the mass hierarchy, is an ongoing area of study.

The results of a global fit of the neutrino oscillation parameters, under both mass ordering hypotheses, are listed in Table 1.1. The mass splittings are both found to be very small, in the region of 10^{-3} to 10^{-5} eV². Equation 1.25 indicates the first oscillation maxima for these

Parameter	NO Best Fit	IO Best Fit
$\sin^2 \theta_{12}$	$0.303^{+0.012}_{-0.011}$	$0.303^{+0.012}_{-0.011}$
$\sin^2 \theta_{23}$	$0.572^{+0.018}_{-0.023}$	$0.578^{+0.016}_{-0.021}$
$\sin^2 \theta_{13}$	$0.02203^{+0.00056}_{-0.00059}$	$0.02219^{+0.00060}_{-0.00057}$
$\Delta m_{21}^2/\text{eV}^2$	$7.41^{+0.21}_{-0.20} \times 10^{-5}$	$7.41^{+0.21}_{-0.20} \times 10^{-5}$
$\Delta m_{3l}^2/\text{eV}^2$	$+2.511^{+0.028}_{-0.027} \times 10^{-3}$	$-2.498^{+0.032}_{-0.025} \times 10^{-3}$
$\delta_{CP}/^\circ$	197^{+42}_{-25}	286^{+27}_{-32}

Table 1.1: Results from global fits by the NuFIT Collaboration [31]. In the case of NO, $\Delta m_{3l}^2 = \Delta m_{31}^2$ and $\Delta m_{3l}^2 = \Delta m_{32}^2$ for IO.

values of Δm^2 are located at $L/E \sim 10^3$ to 10^5 km/GeV. These oscillation phenomena can be placed under the umbrella of “Long Baseline Oscillations”. Several anomalies that could be attributed to neutrino oscillation at much smaller values of L/E have been found, and are the subject of Section 1.4.

Perhaps the most significant property of neutrino oscillations is the ability to violate charge-parity (CP) symmetry. CP violation is required to explain the matter-antimatter asymmetry observed in the universe [29], and while there is some CP violation in the hadronic sector³, this alone is insufficient. A recent measurement by the Tokai to Kamioka (T2K) experiment suggests non-zero (and possibly even maximal) CP violation in the neutrino oscillations [30].

1.4 Short Baseline Oscillations

1.4.1 Gallium

The experiments GALLEX and SAGE were designed to study solar electron neutrinos, through their capture on Gallium nuclei. They performed calibration studies utilising radioactive sources of known activity, and observed a deficit of electron neutrino interactions [32–37], illustrated in Figure 1.5. This result was later confirmed by the BEST experiment [38, 39].

³A review of this topic can be found on pages 271-284 of Ref. [22].

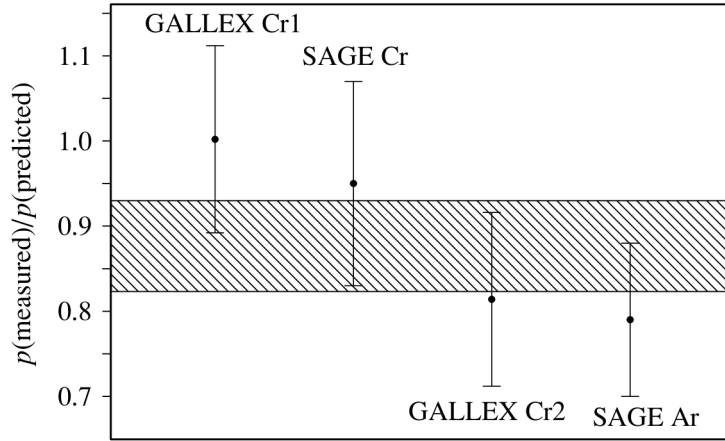


Figure 1.5: Ratios of the event rates observed by Gallium experiments to predictions made assuming no oscillation. The shaded region indicates a weighted average of the four measurements. Figure from Ref. [36].

1.4.2 LSND

The Liquid Scintillator Neutrino Detector (LSND) was operated between 1993 and 1998 and designed to study the oscillation of $\bar{\nu}_\mu$. The experiment primarily used $\bar{\nu}_\mu$ from muon decay at rest (μ DAR), generated with the proton beam at the Los Alamos Meson Physics Facility, with a well predicted $\bar{\nu}_\mu$ energy spectrum. This experiment observed an excess of $\bar{\nu}_e$ interactions [40], at a significance of 3.8σ [40–42], illustrated in figure 1.6. Assuming an oscillation hypothesis, the values $\sin^2(2\theta)$ and Δm^2 favoured by the LSND measurements are displayed in Figure 1.9, which conflict with the results in Table 1.1.

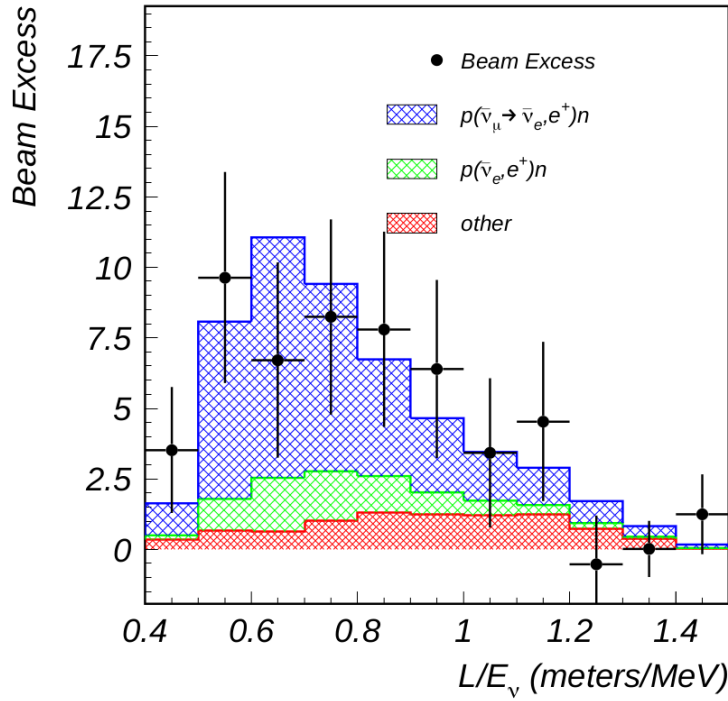


Figure 1.6: The excess of events observed by the LSND Experiment. Figure from Ref. [40].

1.4.3 The MiniBooNE Low Energy Excess

To further investigate the anomalous result reported by LSND, the MiniBooNE experiment [43] was constructed in the Booster Neutrino Beam at the Fermilab, positioned at a baseline to be sensitive to a similar value of L/E to LSND. The apparatus consisted of a spherical vessel 12.2 m in diameter, filled with 818 tons of mineral oil and instrumented with 1520 photomultiplier tubes. A charged particle exceeding the speed of light in the mineral oil would produce a ring of Cherenkov light which would be detected by the photomultiplier tubes. The detector could distinguish the interactions electron neutrinos from muon neutrinos through the shape of their Cherenkov rings: the electron produced in a charged current ν_e interaction would repeatedly scatter, blurring the resulting ring, while muons do not scatter as frequently and produce crisp rings. This identification principle is illustrated in Figure 1.7.

MiniBooNE recorded an excess of low energy electron-like interactions [44], shown in Figure 1.8, with a significance of 4.8σ . Under the hypothesis of short baseline neutrino oscillations, the allowed regions of $[\sin^2(2\theta), \Delta m^2]$ space from the MiniBooNE result, alongside those from LSND, are shown in Figure 1.9. MiniBooNE largely reaffirms the LSND result. This low energy signal is often referred to as the “MiniBooNE Low Energy Excess”, or LEE. Further investigation of the MiniBooNE LEE is one of the physics goals of the MicroBooNE experiment.

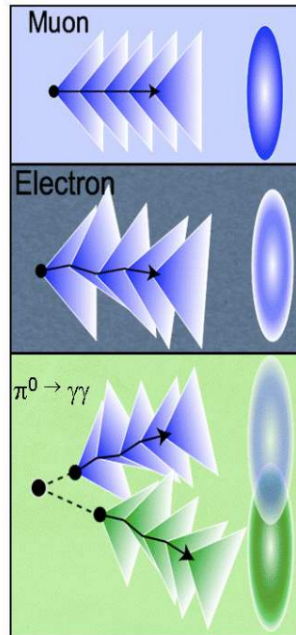


Figure 1.7: The three particle signatures identified by MiniBooNE. Figure from Ref. [46].

Explanations that do not involve oscillations have also been proposed: MiniBooNE could not distinguish between photons and electrons, leading to a number of possible solutions involving photon signals. Perhaps the most notable of these is the radiative decay of Δ baryons, $\Delta \rightarrow N\gamma$, though a measurement of this channel by the MicroBooNE experiment, described in Chapter 3, disfavours this explanation [45].

1.4.4 Neutrino-4

The Neutrino-4 experiment [50] was constructed to study the oscillations of electron anti-neutrinos produced by the SM-3 research reactor in Dimitrovgrad, Russia. The detector consists of a series of gadolinium doped liquid scintillator filled volumes, with the entire assembly placed on rails, enabling measurements of the flux at many values of L/E , the result of which is presented in Figure 1.10. The experiment obtained a best fit of $\Delta m^2 = 7.30 \pm 1.17 \text{ eV}^2$ (combined statistical and systematic uncertainty) and $\sin^2(2\theta) = 0.36 \pm 0.12$ (statistical uncertainty only) [51]. Reanalysis of the data by Giunti *et al* [52] has suggested the oscillation signal claimed by Neutrino-4 is due to statistical fluctuations.

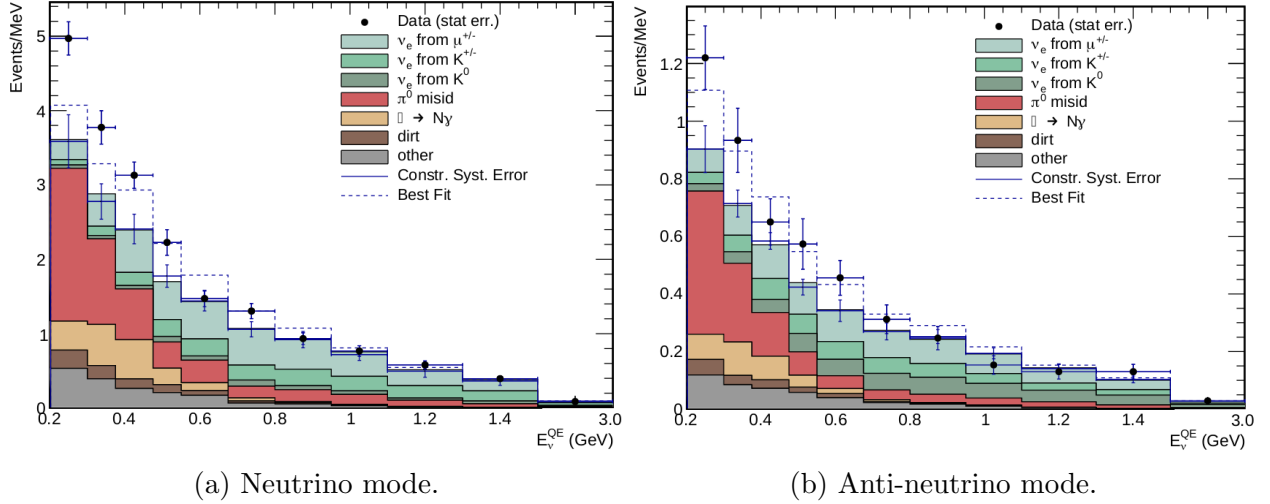


Figure 1.8: The number of electron-like events observed by the MiniBooNE experiment as a function of estimated neutrino energy. The large deviation between the data and prediction at low energy is the MiniBooNE LEE. The best fit is produced using a two neutrino oscillation model and includes data from muon-like events. Figure from Ref. [44].

1.4.5 The Sterile Neutrino: A Solution?

A proposed explanation of these anomalies is to expand the three flavour paradigm and introduce new neutrino mass and flavour states that do not participate in the weak interaction. These new flavour states are sometimes called “sterile” neutrinos. With the addition of a single sterile flavour, the PMNS matrix becomes:

$$U = \begin{pmatrix} U_{e1} & U_{e2} & U_{e3} & U_{e4} \\ U_{\mu1} & U_{\mu2} & U_{\mu3} & U_{\mu4} \\ U_{\tau1} & U_{\tau2} & U_{\tau3} & U_{\tau4} \\ U_{s1} & U_{s2} & U_{s3} & U_{s4} \end{pmatrix}, \quad (1.28)$$

which permits an additional mass splitting Δm_{41}^2 between the 4th mass state and the others, which if sufficiently large, generates short baseline oscillations. The probability of ν_μ oscillating into ν_e , in the short baseline approximation becomes [42]:

$$P(\nu_\mu \rightarrow \nu_e) = 4|U_{e4}|^2|U_{\mu4}|^2 \sin^2 \left(\frac{\Delta m_{41}^2 L}{4E} \right). \quad (1.29)$$

An oscillation model that includes N additional flavours and mass states is called a 3+N model.

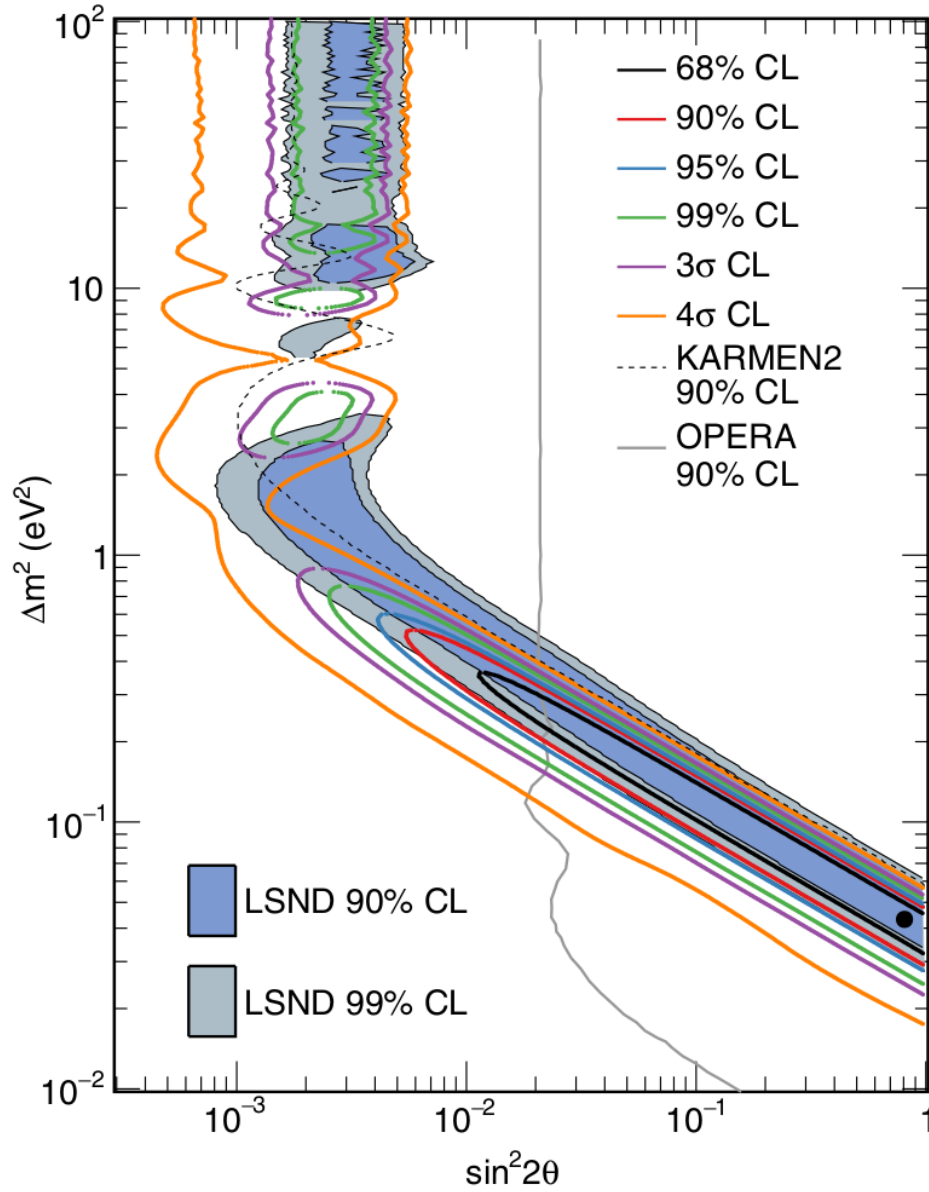


Figure 1.9: Region of Δm^2 and $\sin^2(\theta)$ space permitted by the MiniBooNE measurements, overlaid by the regions excluded by the KARMEN [47] and OPERA [48] experiments. Figure from Ref. [49].

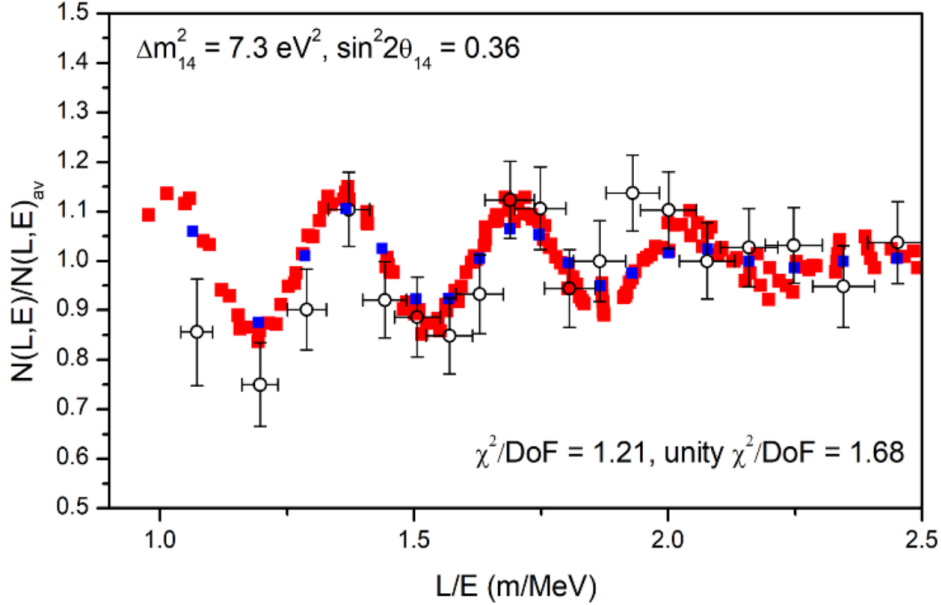


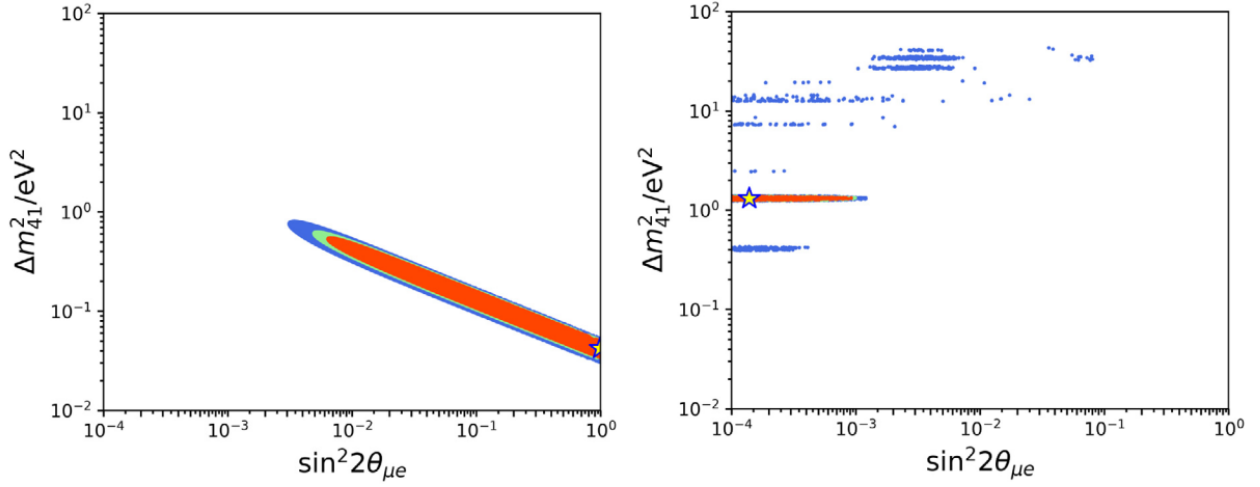
Figure 1.10: The neutrino flux at different values of L/E measured by Neutrino-4. The coloured points correspond to the predicted neutrino fluxes with the extracted values of Δm^2 and $\sin^2(2\theta)$. Figure from Ref. [51].

Some of these anomalies may be resolved *in isolation* with the addition of a new neutrino flavour, but do not always agree on the value of the mixing angle or mass splitting, and the presence of short baseline oscillations is not always backed up by other in-situ measurements such as ν_μ disappearance data. Figure 1.11 shows the results of performing separate fits to appearance and disappearance data, which yield incompatible results. Furthermore, there are numerous, sometimes experiment specific, alternative explanations for these anomalies that do not involve oscillation.

In addition to the discrepancy between the global fits of appearance and disappearance data shown in Figure. 1.11, several other experiments attempting to measure short baseline oscillations have not observed any such signal and excluded portions of the parameter space favoured by LSND and MiniBooNE: KARMEN [47], ICARUS [53], MINOS [54], MINOS and Daya Bay [55], CCFR [56], and Ice Cube [57]. Direct measurements of neutrino masses also place constraints on the maximum values of the Δm^2 parameters of the PMNS matrix [58].

1.5 Neutrino Interaction Processes

The processes described below are different ways to model neutrino interactions with nucleons/nuclei, and are not applicable at all neutrino energy scales. This list is non-exhaustive, and describes the interactions of greatest relevance to the accelerator neutrino



(a) Using only appearance data.

(b) Using only disappearance data.

Figure 1.11: The allowed regions of $[\sin^2(2\theta), \Delta m^2]$ space obtained from performing separate fits to appearance and disappearance measurements. The stars indicate the best fit values. Figure from Ref. [59].

experiments receiving neutrinos of energies from a few MeV to tens of GeV, and to the analysis described in the second half of this thesis. The underlying physics is still the Standard Model, however the non-perturbative nature of QCD at the relevant energy scales renders direct calculations of the cross sections difficult, and the effective interaction Lagrangians are instead constructed from baryon/meson fields, with form factors to account for their composite structure.

1.5.1 Elastic and Quasi-Elastic

The simplest charged current interaction a neutrino/anti-neutrino may undergo with a nucleon is quasielastic (QE) scattering, in which a proton is converted to a neutron or vice versa:

$$\nu_l + n \rightarrow l^- + p, \quad (1.30)$$

$$\bar{\nu}_l + p \rightarrow l^+ + n. \quad (1.31)$$

Feynman diagrams for which are shown in Figures 1.12a and 1.12b respectively. A closely related process, neutral current elastic scattering, is:

$$\nu_l + N \rightarrow \nu_l + N, \quad (1.32)$$

$$\bar{\nu}_l + N \rightarrow \bar{\nu}_l + N, \quad (1.33)$$

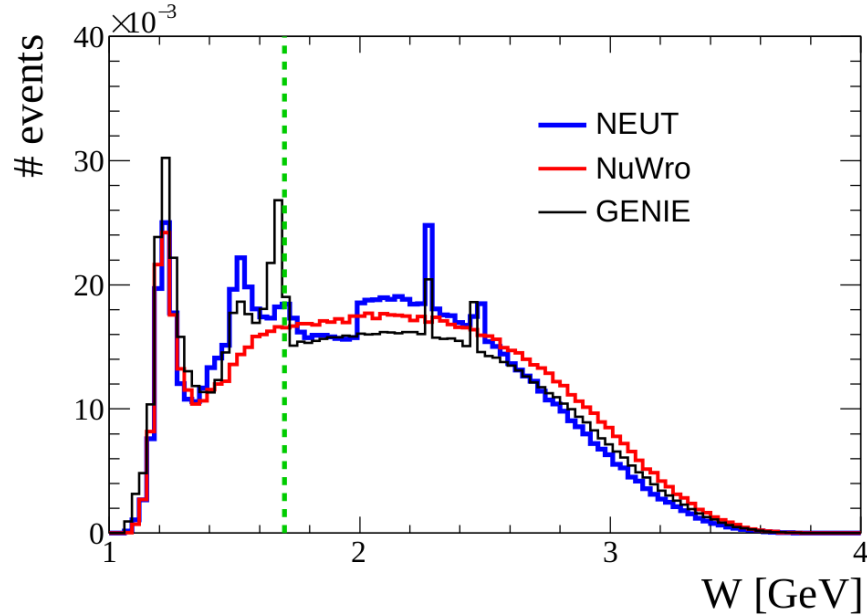


Figure 1.14: Event rates at different hadronic invariant masses predicted by three neutrino event generators, GENIE [63], NEUT [64], and NuWro [65], simulating 6 GeV neutrinos on iron. The first peak corresponds to the excitation of the Δ resonance, with following peaks due to heavier resonances. NuWro does not simulate resonances beyond the Δ and does not predict the existence of these peaks. NEUT switches to DIS model at $W = 2$ GeV, resulting in the discontinuity at this value of W . Figure from Ref. [66].

the amplitude in the cross section computation. These diagrams are collectively known as non-resonant background. The Rein-Sehgal and Berger-Sehgal models do not include non-resonant background.

1.5.3 Deep Inelastic Scattering (DIS)

As the four momentum transferred to the nucleus from the neutrino increases further, the exchanged boson will begin to penetrate into the nucleon, in which case the interaction is better described as the scattering of a neutrino and a quark, followed by hadronisation processes. This kind of interaction is called Deep Inelastic Scattering, and typically produces final states with high hadron multiplicity. Parton structure functions describing the momenta carried by the different flavours of quarks within the nucleon make an appearance in the cross section formulae describing the initial kinematic of the struck quark, which may be tuned to data from collider experiments. Various software packages, most notably PYTHIA [67], are employed to model the hadronisation processes.

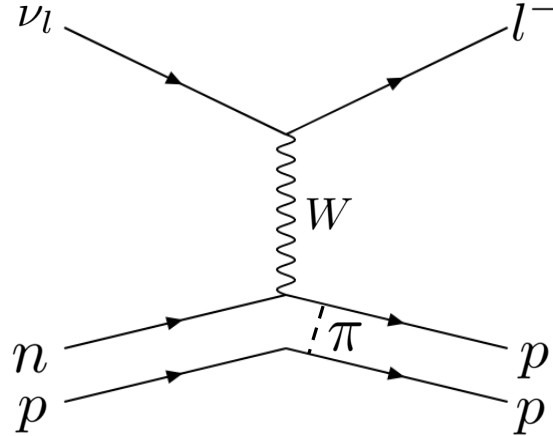


Figure 1.15: A Feynman diagram of a charged current meson exchange interaction, $\nu_l + p + n \rightarrow l^- + p + p$. Many other diagrams of this process exist, and some calculations include three nucleon initial/final states (for example, Ref. [68].)

1.5.4 Meson Exchange Current (MEC)

In the previous sections, the initial state has been an independent nucleon. In most modern neutrino scattering experiments, the target is a nucleus. This introduces the need for new processes with multi-nucleon initial states, also known as n-particle-n-hole (n-pnh) interactions. Meson Exchange Current describes interactions on a correlated pair or trio of nucleons, with the four momentum transfer shared between them. An example Feynman diagram of a meson exchange current process is shown in Figure. 1.15.

1.5.5 Coherent Neutrino-Nucleus Scattering (COH)

If the momentum transfer to the nucleus is sufficiently small, the De-Broglie wavelength of the exchanged particle⁵ approaches the size of the nucleus, with which the neutrino will interact with as a single body:

$$\nu + A \rightarrow \nu + A + X, \quad (1.36)$$

$$\nu + A \rightarrow l^- + A + X, \quad (1.37)$$

where A denotes a nucleus and X possible other particles such as pions. The defining feature of coherent scattering is that the nucleus is left intact, in its ground state. A Feynman diagram of coherent pion production is shown in Figure. 1.16, in which a neutrino emits a W boson that decays into a charged pion, which coherently scatters off a nucleus.

⁵Depending on the reaction, this may be a W/Z boson, but may also include other particles such as the pion in Figure. 1.16.

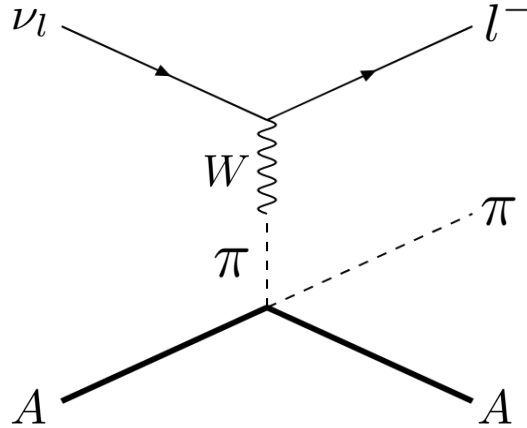


Figure 1.16: Feynman diagram of the charged current coherent pion production process, $\nu + A \rightarrow l^- + \pi^+ + A$.

1.5.6 Nuclear Effects

With the exception of MEC and the coherent interaction, all of the processes described above take place on individual nucleons. MicroBooNE and most other neutrino oscillation experiments employ target materials in which the majority of the target mass is made up of elements such as carbon [43, 69], oxygen [70], argon [71–73], iron [74] and even lead [74]. Most calculations of neutrino nucleus cross sections solve this problem by factorising the neutrino-nucleus interaction into stages, illustrated in Figure. 1.17. One of the previously described interactions is simulated, with the exception of coherent scattering, with a quasi-free nucleon/cluster of nucleons, with the presence of the rest of the nucleus accounted for in the ways outlined below. The implementation of these for the hyperon production model used by NuWro will be described in the next chapter.

Initial State Nucleon Kinematics

The nucleons are not stationary within the nucleus, and will carry some momentum, which modifies the kinematics of the process. Most neutrino event generators and cross section calculations do not attempt to model the nucleus in a fully quantum mechanical way⁶, and instead opt for a statistical description, such as treating the nucleus as a gas of Fermions. Statistical mechanics then predicts their momentum distribution. This approach may be improved by varying the density of the Fermi gas as a function of the distance from the centre of the nucleus, resulting in the Local Fermi Gas model (LFG). There will exist long range interactions between the nucleons, one interpretation of which is the presence of the nuclear binding energy. The nuclear binding energy then modifies the kinematic budget of

⁶A notable exception is the method employed by the GiBUU Monte Carlo simulation [75], which attempts to solve the Boltzmann-Uehling-Uhlenbeck nuclear transport equations.

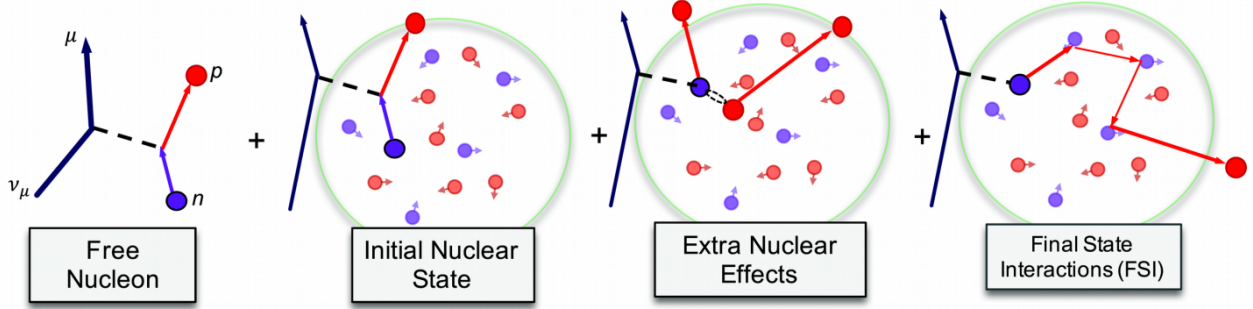


Figure 1.17: The different elements of particle-nucleus scattering. Figure from Ref. [76].

the interaction.

Interaction Dynamics

The fact that the interaction takes place inside the nuclear medium instead of a vacuum is accounted for through a few methods: The propagator of the exchanged boson is modified to account for the polarisation of the nuclear medium through the Random Phase Approximation (RPA). If any nucleons produced in the interaction have energy below that of the Fermi level of the nucleus, they are being produced inside momentum states already occupied by other nucleons, in violation of the Pauli Exclusion Principle. Such interactions are forbidden and cross section calculations must exclude the corresponding region of phase space. This effect is sometimes called “Pauli Blocking”.

Final State Interactions

After the initial neutrino-nucleon interaction has taken place, the resulting particles must escape from the nuclear remnant. This may involve additional collisions with other nucleons, called final state interactions (FSI), resulting in additional particles in the final state. Conversely, these collisions may also dissipate the energy of the particles produced in the initial interaction, preventing them from escaping the nuclear potential. This is illustrated in the fourth panel of Figure. 1.17.

1.5.7 Measuring Oscillation

In order to determine the oscillation parameters, an experiment must observe neutrino interactions in a detector. Assuming a simplified scenario of two neutrino flavours, with a source that exclusively produces neutrinos of flavour α , the rate a detector will observe neutrinos of flavour β , with *reconstructed* energy E_R , can be described schematically as:

$$R(E_R, \beta) \sim \frac{1}{L^2} \int \Phi(E) \sigma_\beta(E) S(E, E_R) P_{\alpha \rightarrow \beta}(E) dE \quad (1.38)$$

$\Phi(E)$ is the flux of neutrinos of flavour α and energy E produced at the source, $\sigma_\beta(E)$ is the cross section for the interaction of neutrinos of flavour β and energy E with the nuclei in the detector. $S(E, E_R)$ describes the detector response, and gives the probability of detecting a neutrino of flavour β with true energy E , and assigning it a reconstructed energy of E_R .

The distinction between reconstructed energy and true energy is important: neutrino experiments cannot produce monoenergetic beams in the way electron scattering/collider experiments can, since the neutrino will not respond to electric/magnetic fields. Flux simulations and in-situ flux measurements such as the use of a second detector at a different baseline or studies of neutral current processes can be used to estimate the shape of $\Phi(E)$, but the event-by-event neutrino energy is unknown. Instead experiments must resort to leveraging other quantities, such as the angle and energy of the outgoing charged lepton. Different sets of oscillation parameters may then be input into Equation 1.38, and the predicted value of R compared with observation to find a best fit, or a deconvolution procedure may be applied to estimate the true neutrino energy spectrum from the observed values of $R(E_R, \beta)$.

Whichever choice is made, the cross section of neutrino interactions is a necessary ingredient, as is the detector response function $S(E, E_R)$. The relationship between E and E_R is often incredibly complex, and is usually estimated from simulations. This function can be very sensitive to how the physics of the neutrino-nucleus interaction is modelled. The effects can be somewhat mitigated by employing a twin detector design, where the first detector is situated near the neutrino source, and used to produce data driven estimates of $\sigma(E)$ and $S(E, E_R)$. However, the resulting uncertainties will not completely cancel out, as the detector response will not be identical for the different neutrino flavours.

1.6 Summary of Chapter 1

Neutrinos were successfully introduced into our collection of fundamental particles to explain the kinematics of the β decay of nuclei. Their existence has since been confirmed by numerous experiments, with measurements indicating there are three flavours that participate in the weak interaction. Several questions have arisen since the discovery of neutrino oscillations: the precise extent of their ability to violate CP symmetry and whether this can explain the matter-anti-matter asymmetry in the universe, where they acquire their masses from and what their absolute masses are, and whether they are Dirac or Majorana particles. Multiple unresolved anomalies exist in short baseline oscillation measurements, and while the existence of sterile neutrinos has been proposed as a solution, this fails to explain all of the results. Indeed, the parameter space preferred by some measurements [40] is excluded by others [47].

A good description of neutrino interactions with nuclei is an essential ingredient in any oscillation analysis in order to connect the neutrino energy spectrum to quantities observable in a detector. No single model is valid at all length/energy scales, and the presence of nuclear effects further complicates the picture.

1.7 Thesis Outline

In chapter 2, the extension of the Llewellyn-Smith model of CCQE to include hyperon production, along with its implementation into the NuWro neutrino Monte Carlo generator will be described. The free nucleon cross sections will be compared with data before moving on to nuclear cross sections, including the effect of FSI and hyperon-nucleus potentials on the predicted cross sections. Chapter 3 gives an overview of the MicroBooNE experiment, including the neutrino fluxes received by the detector, the detection principles of the time projection chamber, and the way the experiment identifies different particles. Chapter 4 describes the event selection used by the Λ baryon production analysis in MicroBooNE, followed by the calculation of the systematic and statistical uncertainties in Chapter 5. Chapter 6 summarises the analysis, lists the main results and lessons, and describes areas that could be improved in future analyses.

Chapter 2

Direct Hyperon Production

Much of the work described in this chapter was previously published in Ref. [1]. The author of this thesis was also the lead author of this publication.

2.1 Hyperons

The term “Hyperon” was first introduced by Louis Leprince-Ringuet in 1953 [77] to describe the V shaped particles observed in Bubble Chambers that we now call Λ baryons. In general, the term hyperon means a baryon with some strangeness and the definition also includes doubly and triply strange particles such as the Ξ and Ω^- baryons. In this thesis, the term hyperon is used to mean the spin $\frac{1}{2}$ Λ^0 and $\Sigma^{0,\pm}$ baryons. The superscript for the Λ baryon will be dropped from this point onward. Hyperons are unstable but, with the exception of the $\Sigma^{0,1}$, possess relatively long lifetimes of a few tenths of a nanosecond, giving proper decay lengths of a few centimetres. Properties of the four hyperons are listed in Table 2.1.

¹The short lifetime of the Σ^0 is the result of the decay mode $\Sigma^0 \rightarrow \Lambda\gamma$, which proceeds via the electromagnetic interaction. The other hyperons all decay via the omission of an off-shell W boson.

Hyperon	Mass (GeV/c ²)	Lifetime (s)	PDL (cm)	Decay Modes (BF)
Λ^0	1.115	2.6×10^{-10}	7.8	$p + \pi^-$ (64%) $n + \pi^0$ (36%)
Σ^+	1.189	8.0×10^{-11}	2.4	$p + \pi^0$ (52%) $n + \pi^+$ (48%)
Σ^0	1.193	7.4×10^{-20}	2.2×10^{-9}	$\Lambda^0 + \gamma$ (100%)
Σ^-	1.197	1.5×10^{-10}	4.5	$n + \pi^-$ (100%)

Table 2.1: Basic properties of hyperons [22]. The list of decay modes is incomplete but those not listed are rare. The proper decay length (PDL) is the lifetime multiplied by the speed of light.

2.2 Free Nucleon Cross Sections

2.2.1 Matrix Element

The anti-neutrino induced CCQE process described in Section 1.5.1, involves the W boson interacting with an up quark, transforming it into a down quark, thereby converting a proton into a neutron. A natural extension to this is to consider the case of W boson instead changing the up quark into a strange quark, producing a hyperon. This defines the CCQE-like or “Direct” hyperon production process. Three channels exist:

$$\bar{\nu}_l + p \rightarrow l^+ + \Lambda, \quad (2.1)$$

$$\bar{\nu}_l + p \rightarrow l^+ + \Sigma^0, \quad (2.2)$$

$$\bar{\nu}_l + n \rightarrow l^+ + \Sigma^-. \quad (2.3)$$

Other mechanisms of hyperon production exist: the excitation of a resonance that decays to a hyperon such as the spin $\frac{3}{2}$ Σ^* particles, which can decay into the spin 1/2 hyperons such as the Λ , and the promotion of an $s\bar{s}$ pair from the quark sea inside a nucleon, which can hadronise into a hyperon and a kaon, or hyperon and anti-hyperon. It should be reiterated that the strangeness violating interaction is *exclusively* available to anti-neutrinos.

Figure 2.1 shows the Feynman diagram for direct hyperon production. The matrix element for the interaction has the form:

$$\mathcal{M} = \frac{G_F \sin \theta_c}{\sqrt{2}} L^\mu H_\mu, \quad (2.4)$$

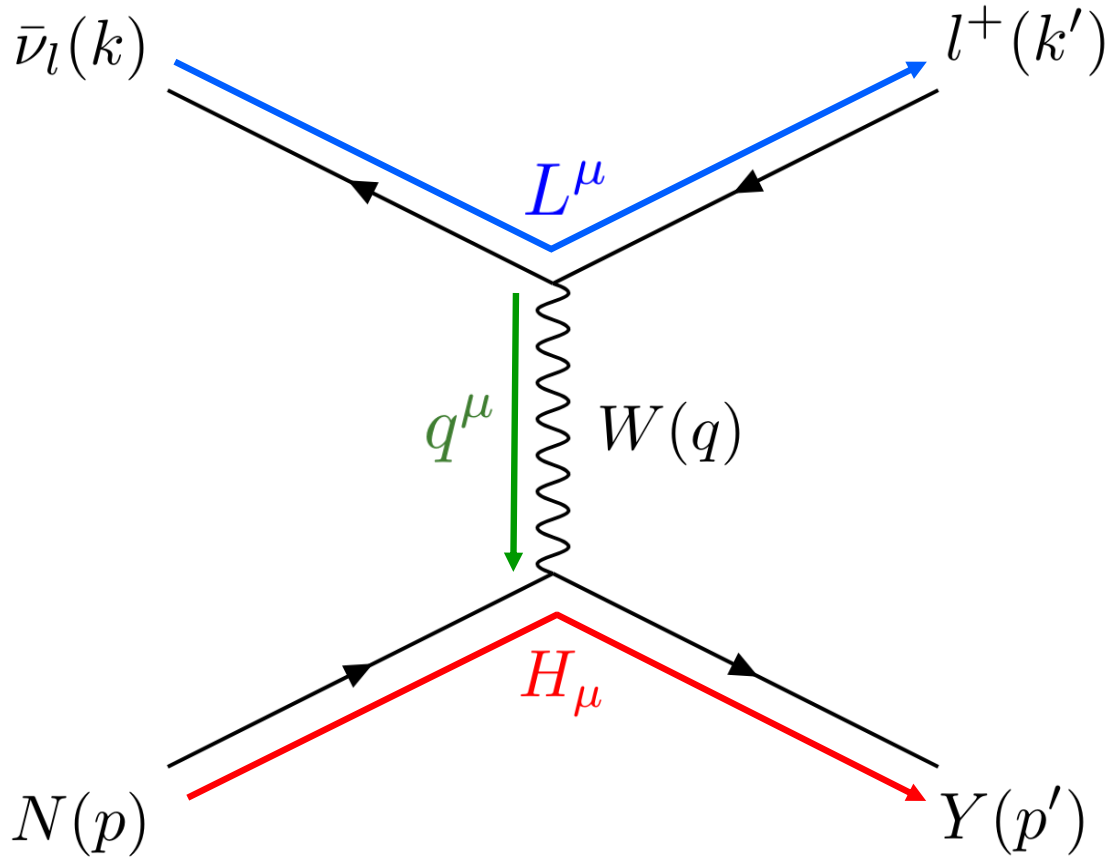


Figure 2.1: Feynman diagram of hyperon production, where N is the nucleon and Y is the hyperon. L^μ is the leptonic current, H_μ is the hadronic current, and q^μ is the four momentum transfer. The quantities in brackets indicate the four momenta of the particles.

where $G_F = 1.66 \times 10^{-5} \text{ GeV}^{-2}$ [22] is the Fermi coupling constant, first introduced in Fermi's model of β decay first mentioned in Section 1.1.1, and $\theta_c = 13.02^\circ$ is the Cabibbo angle. The Einstein summation convention is used. The Fermi coupling constant is used in place of the full W boson propagator, as the squared four momentum transfer, $Q^2 = -q^2$, satisfies $Q^2 \ll M_W^2$, and the following approximation is applied:

$$\frac{1}{M_W^2 - Q^2} \approx \frac{1}{M_W^2}. \quad (2.5)$$

L^μ is the leptonic current, which is derived directly from the V-A theory of the weak interaction [78], resulting in the expression:

$$L^\mu = \bar{v}(k')\gamma^\mu(1 + \gamma_5)v(k) \quad (2.6)$$

where k and k' are the four momenta of the neutrino and charged lepton respectively, and $v(k)$ is the anti-particle solution to the Dirac equation for a particle of four momentum k . γ^μ are the gamma matrices, with $\gamma_5 = i\gamma^0\gamma^1\gamma^2\gamma^3$.

The form of the hadronic current must account for the composite structure of the nucleon and hyperon. H^μ may be expanded in terms of the six Dirac bilinears, with the strength of each controlled by a form factor:

$$H^\mu = \bar{u}(p')\Gamma^\mu u(p), \quad (2.7)$$

$$\Gamma^\mu = V^\mu - A^\mu, \quad (2.8)$$

$$V^\mu = f_1(Q^2)\gamma^\mu + if_2(Q^2)\sigma^{\mu\nu}\frac{q_\nu}{M} + f_3(Q^2)\frac{q^\mu}{M}, \quad (2.9)$$

$$A^\mu = \left[g_1(Q^2)\gamma^\mu - ig_2(Q^2)\sigma^{\mu\nu}\frac{q_\nu}{M} + g_3(Q^2)\frac{q^\mu}{M} \right] \gamma_5. \quad (2.10)$$

The six functions $f_{1,2,3}$ and $g_{1,2,3}$ are the form factors, $M = M_N + M_Y$, $u(p)$ is the particle solution to the Dirac equation for a particle with four momentum p , and $\sigma^{\mu\nu} = \frac{i}{2}[\gamma^\mu, \gamma^\nu]$. The terms paired with the form factors $f_{1,2,3}$ describe vector, tensor, and a scalar currents respectively, while those controlled by $g_{1,2,3}$ describe axial vector, pseudo-tensor, and pseudo-scalar currents. This expression also appears in the QE cross section calculation.

The cross section is proportional to the squared matrix element, averaged/summed over the initial/final state spins. In terms of the hadronic and leptonic currents:

$$|\mathcal{M}|^2 = \frac{G_F^2 \sin^2 \theta_c}{2} \mathcal{H}^{\mu\nu} \mathcal{L}_{\mu\nu}, \quad (2.11)$$

$$\mathcal{H}^{\mu\nu} = \frac{1}{2} \sum_s \sum_{s'} H^\mu H^{\nu\dagger}, \quad (2.12)$$

$$\mathcal{L}^{\mu\nu} = \sum_r \sum_{r'} L^\mu L^{\nu\dagger}. \quad (2.13)$$

$\mathcal{H}^{\mu\nu}$ and $\mathcal{L}^{\mu\nu}$ are the hadronic and leptonic tensors. The summations are over spin states of the nucleon and hyperon (s and s'), and the anti-neutrino and charged lepton (r and r'). The factor of $\frac{1}{2}$ only appears in Equation 2.12 as the anti-neutrino only possesses a single spin state. The hadronic and lepton tensors can be expressed as the following traces:

$$\mathcal{H}^{\mu\nu} = \frac{1}{2} \text{Tr} \left[\Gamma^\mu (\not{p}_N + M_N) \tilde{\Gamma}^\nu (\not{p}_Y + M_Y) \right], \quad (2.14)$$

$$\mathcal{L}^{\mu\nu} = \text{Tr} [\gamma^\mu (1 + \gamma_5) \not{k} \gamma^\nu (1 + \gamma_5) (\not{k}_l - m_l)]. \quad (2.15)$$

$\not{p} = p^\mu \gamma_\mu$, m_l is the mass of the charged lepton, and $\tilde{\Gamma}^\mu = \gamma^0 \Gamma^{\mu\dagger} \gamma^0$. The hadronic tensor contains many terms and the resulting expression will not be given here² the leptonic tensor is:

$$\mathcal{L}^{\mu\nu} = 8k^\mu k'^\nu + 8k'^\mu k^\nu - 8g^{\mu\nu} (kk') - 8i\epsilon^{\mu\nu\sigma\rho} k_\sigma k'_\rho, \quad (2.16)$$

$(kk') = k^\mu k'_\mu$, $\epsilon^{\mu\nu\sigma\rho}$ is the Levi-Civita symbol, and $g^{\mu\nu}$ is the Minkowski metric tensor. The expression for the differential cross section in terms of the leptonic and hadronic tensors is given in Ref. [79] as:

$$\frac{d\sigma}{dQ^2} = \frac{G_F^2 \sin^2 \theta_c}{8\pi E_\nu^2 M_N^2} \mathcal{L}^{\mu\nu} \mathcal{H}_{\mu\nu}, \quad (2.17)$$

where E_ν is the energy of the anti-neutrino in the rest frame of the nucleon.

2.2.2 Form Factors

The form factors cannot be determined from data due to the lack of measurements of hyperon production. Instead, relations with other processes and conditions imposed by the symmetries of the standard model are sought. The form factors in Equations 2.9 and 2.10 have counterparts in CCQE to which relations may be derived [79]. The CCQE interaction is related to electron-nucleon scattering through the electroweak symmetry of the Standard Model, and the expressions for $f_{1,2,3}$ are determined from measurements of this process. The consequences of abandoning some of these assumptions will be explored in the rest of this chapter.

The vector current is conserved in the standard model; imposing this condition on the hadronic current in electron scattering yields $f_3(Q^2) = 0$. All of the form factors must be real for the process to be time reversal invariant. The form factors for protons and neutrons in electron scattering are:

$$f_1^{p,n}(Q^2) = \frac{1}{1 + \tau} \left[G_E^{p,n}(Q^2) - \frac{1}{1 + \tau} G_M^{p,n}(Q^2) \right], \quad (2.18)$$

$$f_2^{p,n}(Q^2) = \frac{1}{1 + \tau} [G_M^{p,n}(Q^2) - G_E^{p,n}(Q^2)], \quad (2.19)$$

²The squared matrix element, expressed in terms of the Mandelstam variables, can be found in the appendices of Ref. [79] by Fatima, Sajjad Athar, and Singh.

where $\tau = Q^2/4M^2$, and $G_E^{p,n}$ and $G_M^{p,n}$ are the Sachs electric and magnetic form factors. The vector form factors for CCQE are given by [79]:

$$f_{1,2}^{pn}(Q^2) = f_{1,2}^p(Q^2) - f_{1,2}^n(Q^2) \quad (2.20)$$

In all subsequent calculations in this thesis, the BBBA05 [80] parameterisation of the vector form factors is used.

The axial form factors do not appear in the electron scattering cross section, and are instead constrained through measurements of the β decay of nucleons and QE scattering. The axial form factor, $g_A = g_1^{pn}$, in the calculations in this chapter, is assumed to be a dipole:

$$g_A(Q^2) = \frac{g_A(0)}{\left(1 + \frac{Q^2}{M_A^2}\right)^2} \quad (2.21)$$

though other parameterisations exist such as the z -expansion [81]. β decay measurements give $g_A(0) = 1.2673$ [82]. The parameter M_A is the ‘‘Axial Mass’’, can only be determined through measurements of neutrino scattering, and is an important systematic parameter in oscillation and cross section measurements. The model inside NuWro supports a separate axial mass parameter for the hyperon production processes.

The form factors f_1 , f_2 and g_1 that appear in the hyperon production cross sections are related to those in electron scattering and QE interaction through the SU(3) quark flavour model, with the expressions given in Table. 2.2. The pseudoscalar form factor, g_3 , is given by the following expression derived by Nambu [83] from the partial conservation of axial current (PCAC) in terms of the axial form factor:

$$g_3^{NY} = \frac{(M_N + M_Y)^2}{2(m_K^2 + Q^2)} g_1^{NY}, \quad (2.22)$$

where $m_K = 0.498$ GeV is the K^0 mass and M_Y is the hyperon mass.

Second Class Currents

G parity reversal is a combination of charge conjugation and a 180° rotation in isospin space: $G = C e^{i\pi I_y}$, where I_y is the generator of rotations around the y axis in isospin space. The strong interaction is invariant under this transformation. The vector and axial vector currents of the SM are G parity even and odd respectively:

$$V^\mu \rightarrow G V^\mu G^{-1} = V^\mu, \quad (2.23)$$

$$A^\mu \rightarrow G A^\mu G^{-1} = -A^\mu. \quad (2.24)$$

Applying the same transformations to bilinears in Equations 2.9 and 2.10 reveals the scalar and pseudo-tensor currents gain an additional minus sign. Currents that transform the wrong

	$f_1(Q^2)$	$f_2(Q^2)$	$g_1(Q^2)$
$p \rightarrow \Lambda$	$-\sqrt{\frac{3}{2}} f_1^p$	$-\sqrt{\frac{3}{2}} f_2^p$	$-\frac{1}{\sqrt{6}} (1 + 2x) g_A$
$p \rightarrow \Sigma^0$	$-\frac{1}{\sqrt{2}} (f_1^p + 2f_1^n)$	$-\frac{1}{\sqrt{2}} (f_2^p + 2f_2^n)$	$\frac{1}{\sqrt{2}} (1 - 2x) g_A$
$n \rightarrow \Sigma^-$	$-(f_1^p + 2f_1^n)$	$-(f_2^p + 2f_2^n)$	$(1 - 2x) g_A$

Table 2.2: List of form factors. The quasielastic axial form factor g_A satisfies $g_A(0) = 1.2673$ described by a dipole of axial mass M_A and $x = 0.365$. Unless otherwise specified we use $M_A = 1$ GeV.

way under G parity are named ‘‘Second Class Currents’’, and are forbidden in the SM. The scalar form factor f_3 must vanish for the vector currents to be conserved. Imposing the requirement that G parity symmetry is respected, $g_2(Q^2) = 0$. With this condition, four form factors remain: f_1 , f_2 , g_1 , and g_3 , all of which have been determined.

The effect of reintroducing the pseudo-tensor current will be discussed later in this chapter. In these discussions, the pseudo-tensor form factor is assumed to be of the same form as the axial form factor:

$$g_2^{pn}(Q^2) = \frac{g_2(0)}{\left(1 + \frac{Q^2}{M_A^2}\right)^2}, \quad (2.25)$$

where M_A is the axial mass introduced in Equation 2.21, and $g_2(0)$ is a new coupling, which will be allowed to take complex values. The form factors g_2^{NY} obey the same relations to g_2^{pn} as g_1 in Table 2.2.

SU(3) Symmetry Breaking

The form factors in Table 2.2 are obtained through relations derived from the SU(3) flavour model of baryons, which is only a true symmetry of the interaction Lagrangian if the baryon masses are identical. Symmetry breaking corrections to the form factors calculated by Schlumpf [84] were implemented into the NuWro hyperon production model, and involve the following adjustments to the form factors:

$$f_1(Q^2) \rightarrow a f_1(Q^2), \quad (2.26)$$

$$g_1(Q^2) \rightarrow b g_1(Q^2). \quad (2.27)$$

The values of the corrections a and b are listed in Table. 2.3.

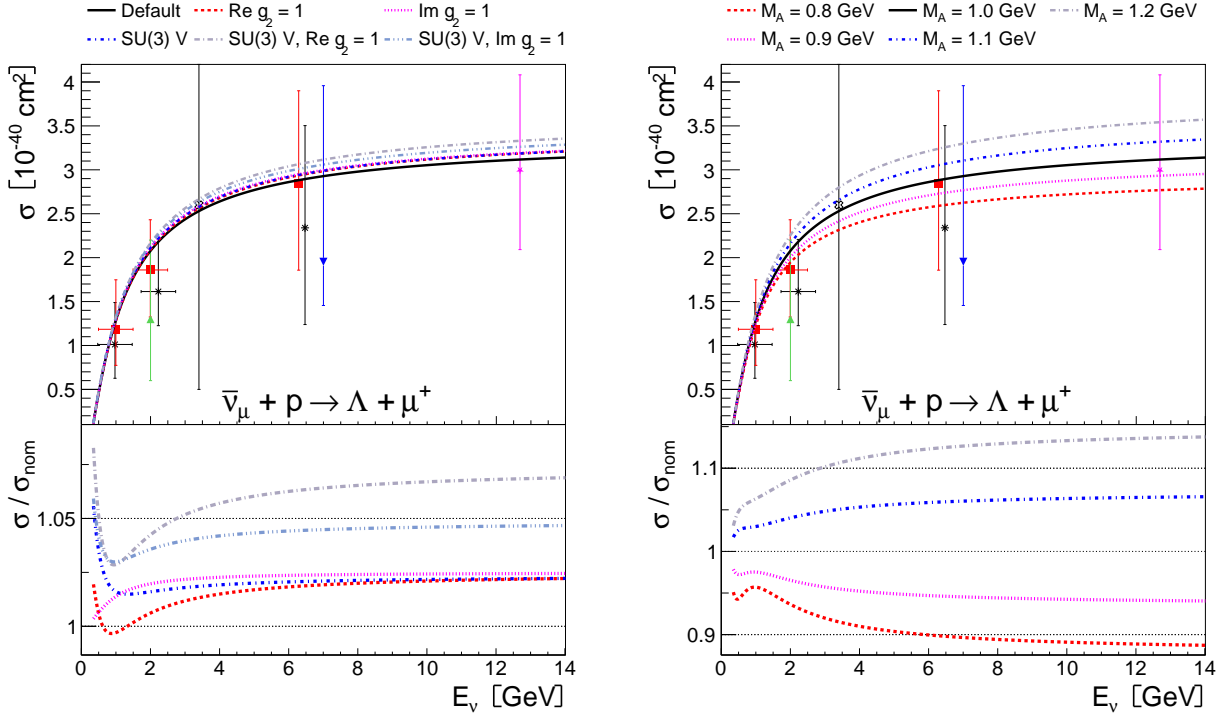
Process	a	b
$p \rightarrow \Lambda$	0.976	1.072
$p \rightarrow \Sigma^0$	0.975	1.051
$n \rightarrow \Sigma^-$	0.975	1.056

Table 2.3: Symmetry breaking corrections from Ref.[84].

2.2.3 Predictions

The free nucleon cross sections predicted by NuWro are compared with existing measurements of Λ and Σ^0 production in Figures 2.2 and 2.3. Two sets of generator configurations are used: separately setting real and imaginary components of the coupling in the pseudo-tensor form factor to 1 and applying the symmetry breaking corrections in Figures 2.2a and 2.3a, and experimenting with varying the axial mass in Figures 2.2b and 2.3b. The data shown form the entire dataset on CCQE-like hyperon production, and are collected from bubble chamber experiments: Gargamelle [85–87], the FNAL BC [88], BNL BC [89], and SKAT [90]. The most recent of these measurements was performed by SKAT in 1990. The only attempt to measure hyperon production in a modern neutrino experiment was performed with data from the Argoneut experiment [91], though the methodology involved is very different from that presented in Chapters 4- 6 of this thesis, relying much more heavily on visual scanning.

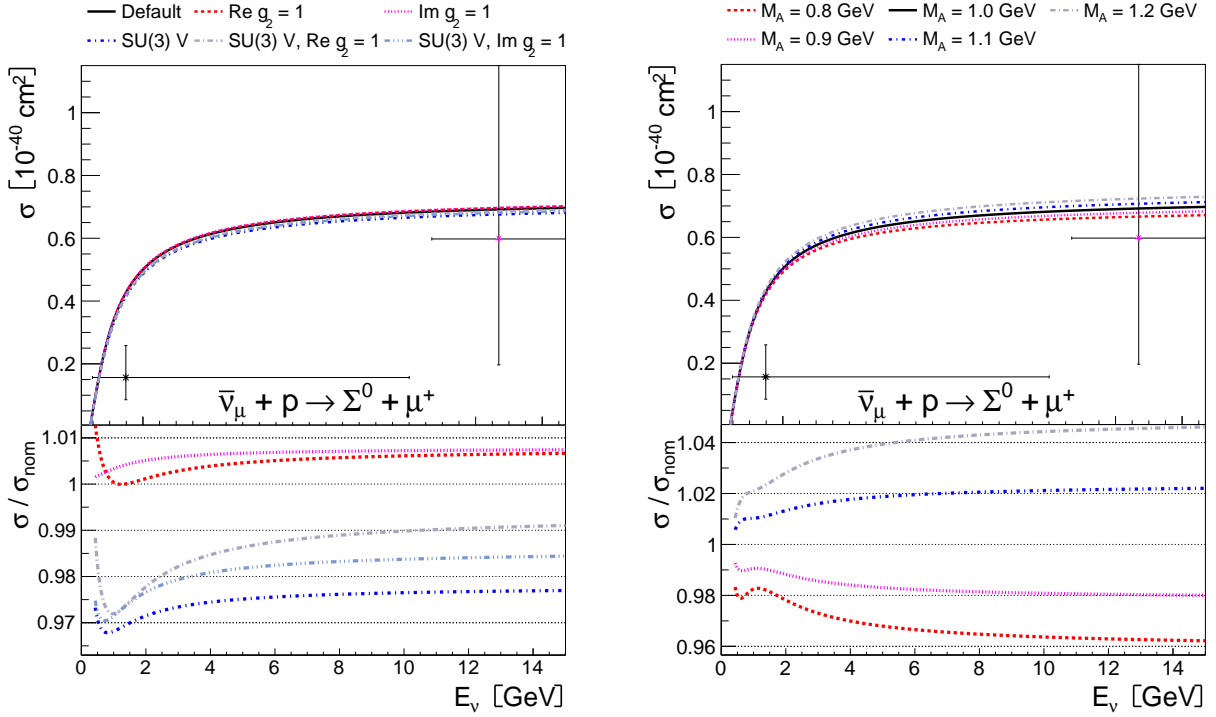
These curves show the cross sections predicted by NuWro are consistent with the available data, though these measurements come with large uncertainties. Predictions with axial mass values between 0.8 and 1.2 GeV are shown, all of which fit comfortably within the uncertainties on the data. In contrast, various fits of the axial mass from CCQE interactions obtain uncertainties of a few tens of MeV [92–94]. The change in the cross section resulting from varying the axial mass is much larger than that of the second class current and symmetry breaking corrections.



(a) Including second class currents and symmetry violations.

(b) Using several values of the nucleon axial mass.

Figure 2.2: Total cross section for the direct production of Λ baryons compared with several predictions from NuWro. Data is from Ammosov [88] (FNAL Bubble Chamber, pink star), Brunner [90] (SKAT, triangle down), Erriquez [85, 86] (Gargamelle, red square and black x respectively), Eichten [87] (Gargamelle, triangle up) and Fanourakis [89] (BNL Bubble Chamber, white cross). Figure originally published in Ref. [1].



(a) Including second class currents and symmetry violations.

(b) Using several values of the nucleon axial mass.

Figure 2.3: Total cross section for the direct production of Σ^0 baryons compared with several predictions from NuWro. Data taken from the same references as in figure 2.2. Figure originally published in Ref. [1].

2.3 Nuclear Effects

2.3.1 Struck Nucleon Kinematics

NuWro contains simulations of several nuclear models, including Global Fermi Gas (GFG), Local Fermi Gas [95], the Bodek-Ritchie correlated Fermi Gas [96], and spectral functions [97]. The effect of nucleon momentum is simulated by randomly sampling a value of nucleon momentum from the selected distribution, and Lorentz transforming into its rest frame before applying Equation 2.17 to obtain the differential cross section for that interaction. Performing this repeatedly allows one to obtain the differential cross section averaged over the nucleon momenta.

The nucleon attraction between the struck nucleon and the other nucleons is handled through a mean field approximation: the nucleon is assigned some binding energy E_b depending on its location within the nucleus and the nuclear model selected. The four

momenta of the struck nucleon is then given by:

$$p_* = (E - E_b, \mathbf{p}), \quad (2.28)$$

where $E = \sqrt{\mathbf{p}^2 + M_N^2}$, and \mathbf{p} is the three momentum of the nucleon in the rest frame of the nucleus. This adjustment is made prior Lorentz transforming to the centre of mass frame for the remainder of the calculation. An option included in the NuWro hyperon production model is to use the effective mass of the nucleon in the expression for the cross section, by making the replacement:

$$M_N \rightarrow M_{N*} = \sqrt{p_*^2}. \quad (2.29)$$

in Equations 2.9, 2.10 and 2.17. No other in-medium effects such as RPA are implemented and Pauli blocking is not applicable to this stage of the interaction, since hyperons occupy a separate set of quantum states to nucleons.

2.3.2 Final State Interactions

As described in section 1.5.6, cross section calculations and neutrino event generators do not attempt to model scattering with the entire nucleus for most interactions. Instead the process is factorised into the scattering of a neutrino with a quasi-free nucleon and FSI. The algorithm for the latter process employed by NuWro uses a semiclassical approximation, in which the particles travel through the nucleus as particles instead of waves, but the location and results of any interaction are determined in a probabilistic manner. The rough algorithm for particle propagation through the NuWro intranuclear cascade is as follows:

1. If the particle is not a nucleon, pion or hyperon, it will exit the nucleus without interacting.
2. Compute the mean free path λ of the particle in the nucleus. The mean free path is given by:

$$\lambda = \frac{1}{\rho_p(r)\sigma_p + \rho_n(r)\sigma_n}, \quad (2.30)$$

where $\rho_{p,n}(r)$ are the densities of protons and neutrons in the nuclear remnant at a distance r from the centre of the nucleus, and $\sigma_{p,n}$ are total scattering cross sections for the projectile with protons and neutrons.

3. Generate a step length L for the particle from this mean free path using $L = -\lambda \ln \xi$ where $\xi \in [0, 1]$ is a uniformly distributed random number.
4. The particle is propagated by a distance $d = \min(L, 0.2 \text{ fm})$. This procedure accounts for the fact that L depends on nuclear density and is calculated locally. If $L > 0.2 \text{ fm}$ the particle is moved by a distance 0.2 fm along its momentum vector and step 2. is repeated.

5. If $d < 0.2$ fm and particle is not outside nucleus an interaction is generated. A reaction is selected by MC method, comparing the cross sections of different reactions. A reaction is only simulated if final states of any nucleons are not Pauli blocked.

This cascade requires in medium hyperon-nucleon cross sections. The fits to free hyperon-nucleon data from [98] are used for total cross sections. The differential cross sections have been assigned the same distributions as NN scattering processes with corresponding electric charges. For example:

$$\frac{d\sigma}{d\Omega}(p\Lambda \rightarrow p\Lambda) \sim \frac{d\sigma}{d\Omega}(pn \rightarrow pn) \quad (2.31)$$

In cases where no similar process in the NN sector exists (e.g. for Σ^- rescatterings), the outgoing particles are scattered isotropically in the CMS frame. The arguments justifying this assumption are that the underlying physics responsible for the interactions, the strong force, is the same and the energy is small enough that any differences in the internal structure of the particles, i.e. the parton distributions, are negligible. The differential cross sections are then obtained from [99] and have the form:

$$\frac{d\sigma}{d\Omega} = K (A \cos^4 \theta + B \cos^3 \theta + 1), \quad (2.32)$$

where K is a normalisation constant, A and B are fitted parameters dependant on the hyperon kinetic energy, and θ is the scattering angle in the CMS frame.

Meson Production and Proton Decay

No meson production channels of the type $N + Y \rightarrow N' + Y' + \pi$ or similar are simulated due to a shortage of data to estimate the cross sections for such processes, though meson production in nucleon-nucleon collisions is simulated. The production of kaons either in associated hyperon production interactions or through a secondary interaction of a hyperon are potential sources of background in proton decay experiments, in which $p \rightarrow K^+ + \bar{\nu}$ is a process allowed by some Grand Unified Theories [100].

Influence on Cross Sections

Comparisons of the differential cross sections predicted by NuWro before and after the inclusion of FSI are shown in figure 2.4. The Λ channel is largely unmodified, a result of the rough cancellation of the reabsorption of the Λ baryons back into the nucleus and the conversion of Σ baryons into Λ baryons, while the Σ^0 and Σ^- channels are suppressed at low Q^2 . The Σ^+ baryon cannot be produced through CCQE-like interactions (at tree level) between neutrinos/anti-neutrinos and nuclei, but may be generated when one of the other particles undergoes a secondary interaction with a nucleon. The resulting cross section for Σ^+ production is predicted to be at least an order of magnitude smaller than that of the other channels.

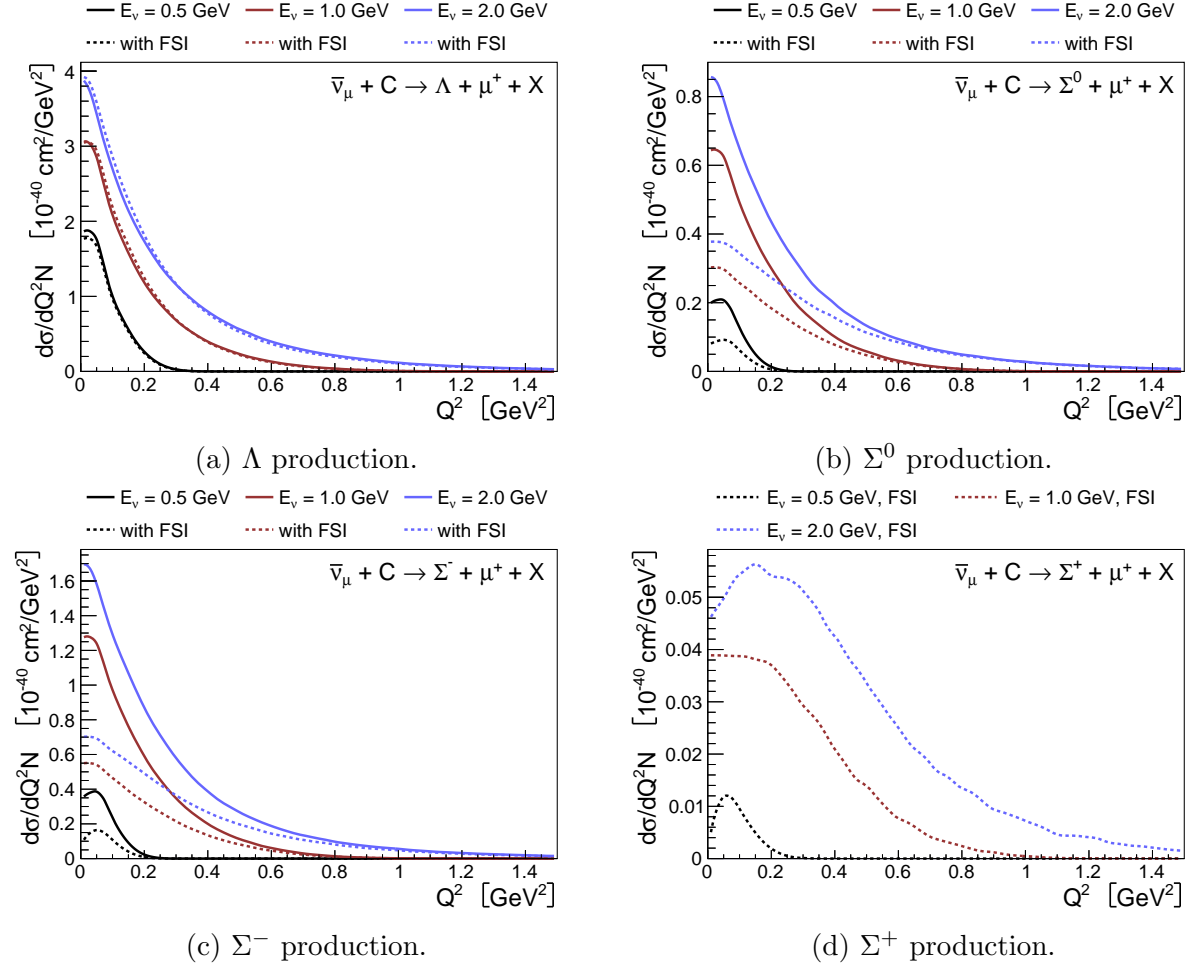


Figure 2.4: Differential cross sections for the production of the different hyperons calculated using NuWro, before and after final state interactions are included in the simulation. Figure published in Ref. [1].

2.3.3 The Hyperon-Nucleus Potential

As with nucleons, hyperons will be affected by the strong nuclear and electromagnetic forces, an effect that remains poorly understood. Some calculations suggest hypernuclear potentials will impact the density at which hyperons begin to be produced within neutron stars. Models attempting to describe the particle content of neutron stars predict the production of hyperons as the density of the neutron star material increases [101]: the nucleons are forced into higher and higher energy states to comply with the Pauli exclusion principle; eventually it becomes energetically favourable for a nucleon to transform into a hyperon. However, models that attempt to incorporate this process obtain a reduced upper limit on the mass

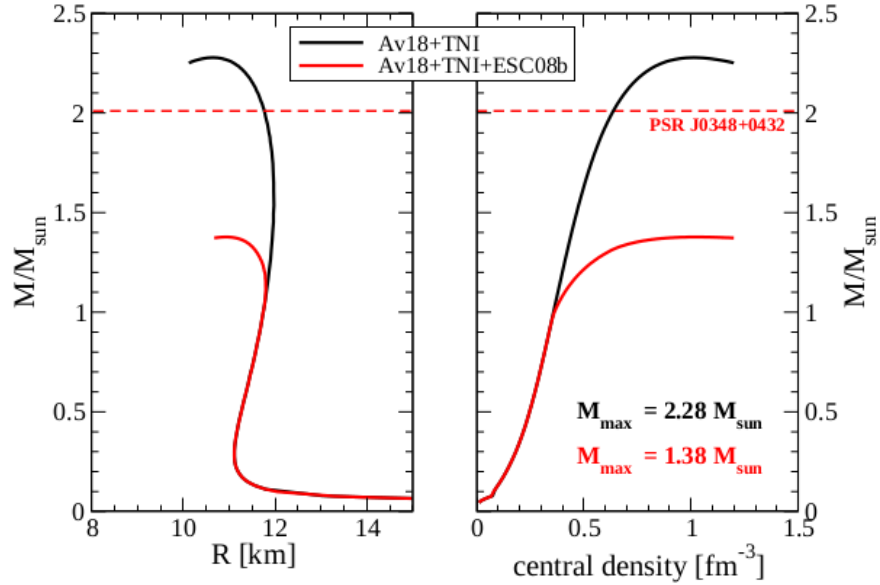


Figure 2.5: Predicted masses of neutron stars as a function of their radii (R) and central density. The model used combines two-nucleon interactions described by the Argonne v18 model (Av18) [103], three nucleon interactions (TNI) from Ref [104] and hyperon nucleon interaction with the ESC08b model [105]. The dashed red line is the measured mass of the pulsar PSR J0348+0432 [106], above the maximum mass predicted when hyperon-nucleon interactions are included. Figure from Ref. [102].

of neutron stars, illustrated in figure 2.5, in tension with astronomical data. This is known as the “Hyperon Puzzle” [102]. NuWro attempts to simulate the hyperon-nucleus potential through the inclusion of a potential proportional to the local density of the nucleus:

$$V(r) = -\alpha \frac{\rho(r)}{\rho(0)}, \quad (2.33)$$

where $\rho(r)$ denotes the density of the nucleus at a distance r from its centre, and α the strength of the potential at $r = 0$. There have been attempts to determine the hyperon nucleus potential using pion-nucleus scattering events in which a kaon is observed in the final state [107–109]. These work suggest separate strengths for the Λ and Σ potentials. When NuWro simulates a primary interaction producing nucleons, the nuclear potential is used to modify their kinematics during FSI:

1. The value of the nuclear potential, V_0 at the point the primary interaction occurred is evaluated.
2. This is added to the energy of the nucleon, and its momentum rescaled accordingly, to

keep the particle on-shell³ The simulation stores the value of V_0 in the particle object as its “binding energy”.

3. The particle propagates with these new kinematics, until an interaction is simulated, or the particle reaches the edge of the nucleus.
4. A pair of nucleons are always produced in the final state of an NN interaction in NuWro (plus up to two pions), the more energetic of which is assigned V_0 as its binding energy, while the value of the nuclear potential at the site of the interaction is retrieved and assigned to the other nucleon (without adjusting its momentum).
5. If after an interaction, or when a particle reaches the edge of the nucleus, the kinetic energy of a particle is found to be less than its binding energy, the particle is reabsorbed into the nucleus and ceases propagation.

The method applied to hyperon production is designed to be as consistent with this algorithm as possible, but the model has to accommodate two additional scenarios: the hyperon being produced inside a repulsive potential, and the hyperon being transformed from a Λ baryon to a Σ baryon or vice versa, thereby switching potentials midway through the cascade.

The former situation is relatively straightforward to handle. The kinetic energy of the hyperon produced in the primary interaction is compared with the value of the potential at the point of the interaction: if the magnitude of the repulsive potential exceeds the kinetic energy of the hyperon, the interaction is interpreted as being blocked, and the corresponding cross section is set to zero. If the hyperon passes this check, it proceeds to the FSI simulation, where the value of the repulsive potential is subtracted rather than added in step 2. The prior check ensures this does not result in a particle with negative kinetic energy. If a secondary interaction occurs in which the hyperon switches families, the hyperon is moved to the new potential: First the kinetic energy of the new hyperon is compared with the difference in the potentials and if $E_k < V_{\text{old}} - V_{\text{new}}$ this secondary interaction is ignored. Then the difference between the two potentials is subtracted from the new hyperon’s energy and its momentum adjusted to continue propagating it on shell. This respects overall energy conservation.

The effects of varying the strengths of these potentials was examined in [1]. The authors of [107] suggest the following range for the Λ nucleus potential for symmetric nuclei:

$$\alpha_\Lambda \in [25 \text{ MeV}, 29 \text{ MeV}]. \quad (2.34)$$

The Σ nucleus potential is less well constrained. [109] compares the range of strengths, in combination with $\alpha_\Lambda = 30 \text{ MeV}$, allowing this potential to be strongly repulsive:

$$\alpha_\Sigma \in [10 \text{ MeV}, -150 \text{ MeV}]. \quad (2.35)$$

³The four momentum (E, \mathbf{p}) of an on-shell particle satisfies the equation $E^2 = m^2 + \mathbf{p}^2$, where m is free rest mass of the particle.

By default, NuWro uses the midpoints of these two ranges: $\alpha_\Lambda = 27$ MeV and $\alpha_\Sigma = -70$ MeV.

Figure 2.6 shows some predictions of the Σ^0 production differential cross section versus kinetic energy. The differential cross section curve exhibits considerable sculpting by the potential, though this shape can be understood when broken down into contributions from different sub-processes which possess different shapes. The components of the overall cross section resulting from $\Sigma^- \rightarrow \Sigma^0$ and $\Lambda \rightarrow \Sigma^0$ conversions tend to contribute the low energy portion of the distribution, however this peak shifts to higher energies as the Σ nucleus potential becomes more repulsive.

2.4 Comparisons Between NuWro and GENIE

The main neutrino event generator employed by the MicroBooNE experiment and used throughout the remainder of this thesis is GENIE⁴ [63]. GENIE does not simulate FSI, nuclear potentials, or effective masses for hyperons. A set of comparisons for the Λ and Σ^0 channels from argon nuclei, using these two neutrino event generators, are shown in Figures 2.7 and 2.8. The default hyperon-nucleus potentials, with the large repulsive Σ -nucleus potential, are used. A large suppression of the Σ^0 baryon channel is predicted by NuWro relative to GENIE, the result of the large repulsive potential raising the kinematic threshold, and conversion of Σ baryons to Λ baryons during FSI. The Λ production channel in contrast is enhanced by FSI.

2.5 Summary

Direct hyperon production is a process with few existing measurements, with none performed in modern neutrino detectors. The cross section model is determined entirely through the exploitation of symmetry relations to other processes. NuWro is the first of the major neutrino event generators to incorporate nuclear effects into the description of this process, and reveals that the cross sections can be strongly influenced by FSI and hyperon-nucleus potentials. The latter is of particular interest as understanding the behaviour of hyperons in the nuclear medium may be a necessary step towards solving the hyperon puzzle. Additional and more subtle effects, such as the breaking of the SU(3) quark flavour symmetry and second class currents also come into play.

The remainder of this thesis describes a measurement of the Λ production cross section with the MicroBooNE detector, and showcases techniques that can be exported to similar detectors employing the same technology expected to obtain larger datasets, such as the Short Baseline Near Detector [73], and the Deep Underground Neutrino Experiment [110, 111], the latter of which is a potential venue for proton decay measurements.

⁴Generates Events for Neutrino Interaction Experiments.

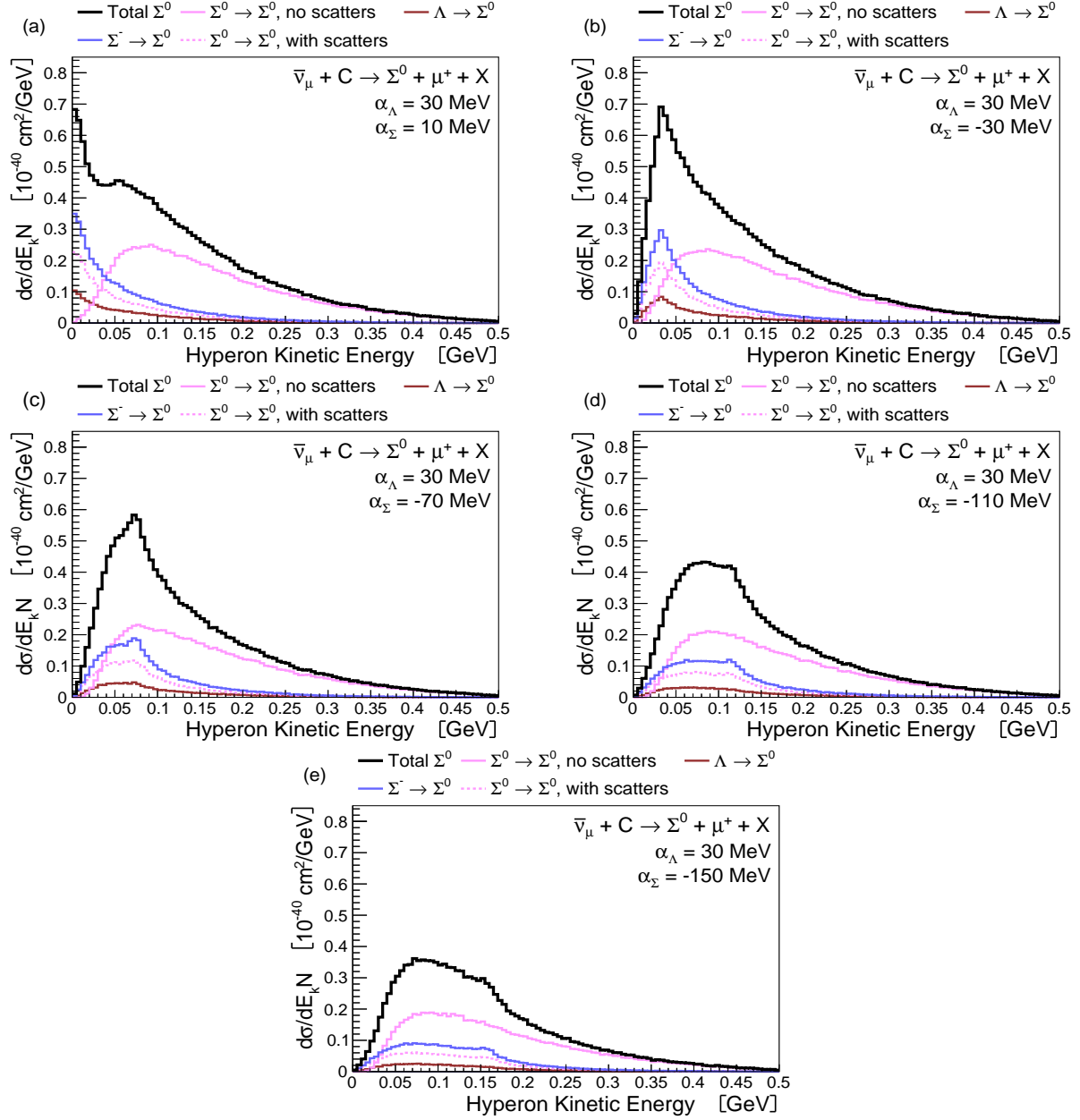


Figure 2.6: Distribution of Σ kinetic energies after final state interactions for several values of the Σ nucleus potential. The total differential cross sections are indicated by the solid black line, equal to the sum of the other distributions. The contribution labelled $\Lambda \rightarrow \Sigma^0$ refers to events in which the primary interaction was $\bar{\nu}_\mu + p \rightarrow \mu^+ + \Lambda$, with the Λ then converting to a Σ^0 through a secondary interaction. Figure published in Ref. [1].

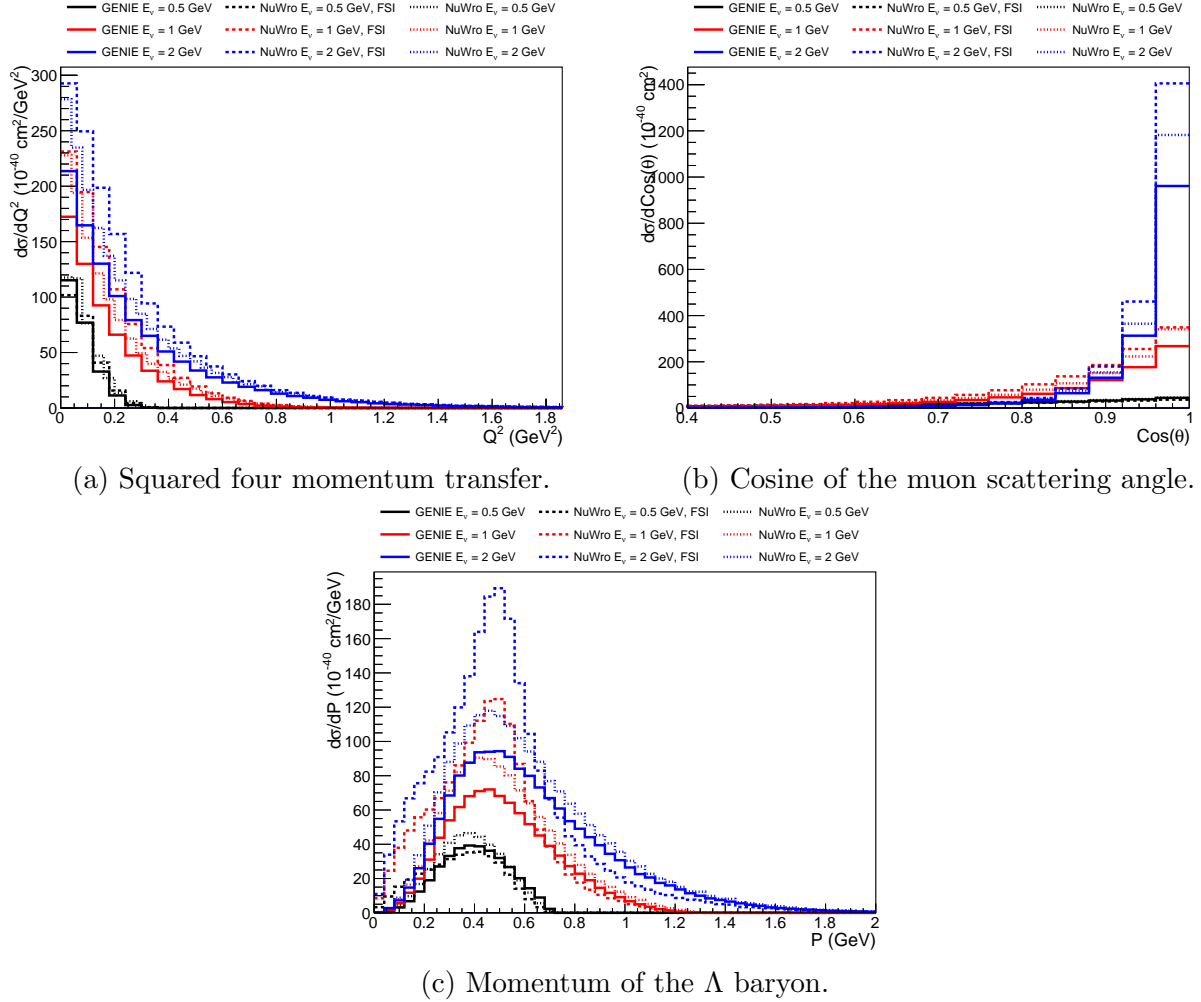


Figure 2.7: Comparisons of the cross sections for the process $\bar{\nu}_\mu + \text{Ar} \rightarrow \mu^+ + \Lambda + X$, with X denoting any additional particles, calculated using NuWro and GENIE. The default parameters from NuWro are used: $M_A = 1.03$ GeV, and $\alpha_\Lambda = 27$ MeV, and $\alpha_\Sigma = -70$. The same axial mass was used to generate the GENIE predictions. The axial mass used for hyperon production in MicroBooNE's GENIE tune is 0.96 GeV.

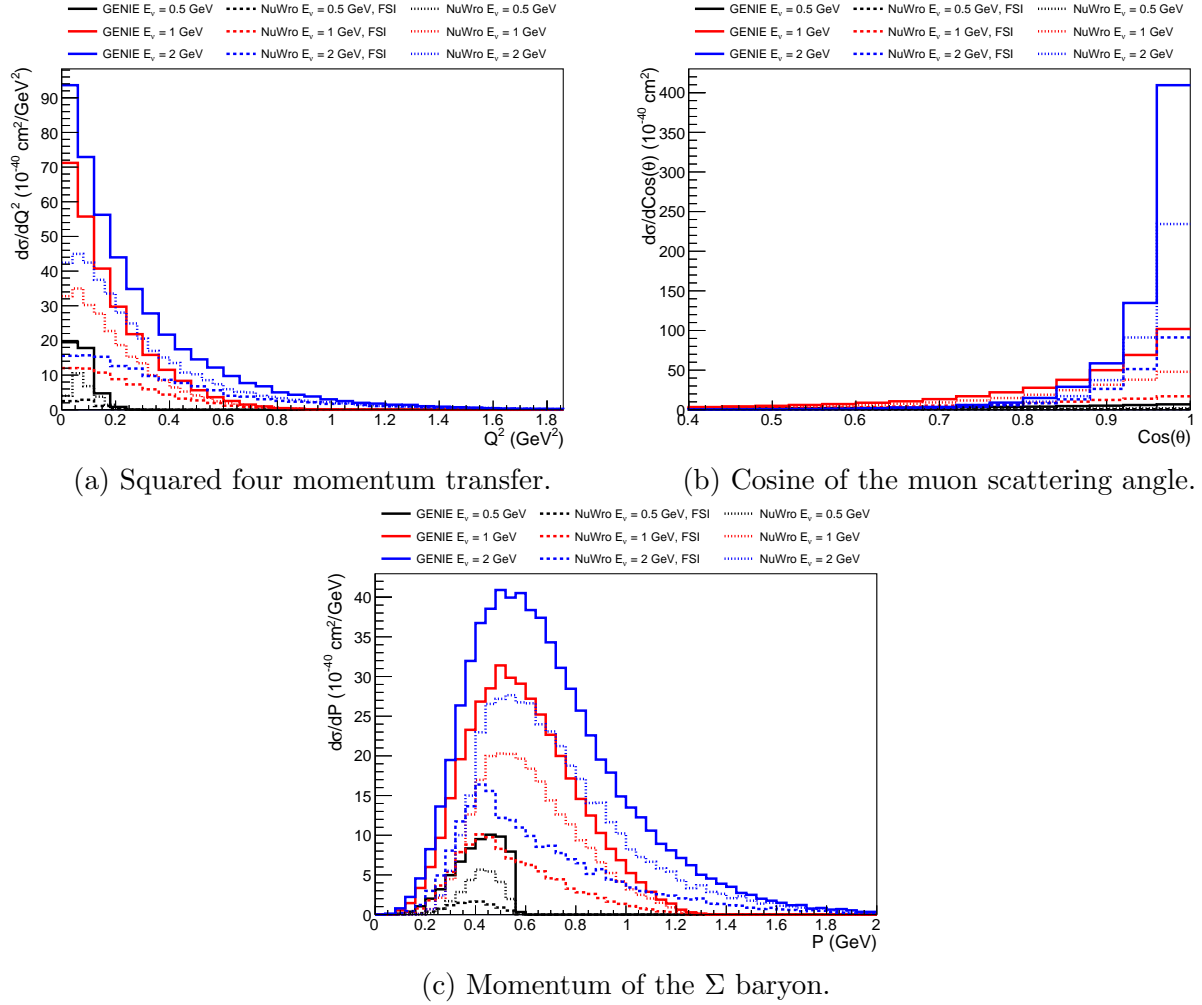


Figure 2.8: Comparisons of the cross sections for the process $\bar{\nu}_\mu + \text{Ar} \rightarrow \mu^+ + \Sigma^0 + X$, with X denoting any additional particles, calculated using NuWro and GENIE.

Chapter 3

The MicroBooNE Experiment

3.1 The Liquid Argon Time Projection Chamber

Whenever an energetic charged particle travels through matter, it will leave behind a trail of ionised atoms and electrons. Ordinarily, these will quickly recombine, and the energy deposited in the ionisation will be released in the form of photons. If a sufficiently strong electric field is applied, the ions/electrons will instead begin to drift along/against the field. Moving charges induce currents in nearby conductors according to the Shockley-Ramo theorem [112, 113]:

$$i = E_w q v \tag{3.1}$$

where i is the induced current, E_w is the “weighting field”, the electric field at the location of the drifting particle if the conductor is placed at a potential of 1 V, and q and v are the charge and velocity of the drifting particle respectively.

The Liquid Argon Time Projection Chamber (LArTPC) is a class of particle detector that exploits this phenomenon. The basic design comprises a volume of liquid argon with a cathode on one side and an anode on the other. Placed in front of the anode are arrays of wires, in planes perpendicular to the field direction, connected to sensors that record current. The ionisation electrons left by a charged particle are pulled by the field towards the wire planes, inducing currents in the wires detected by the sensors, illustrated in Figure 3.1. A two dimensional image, displaying the trajectories of charged particles through the detector, may be produced from the information describing when electrons arrived and at which wires, for example Figure 3.2. Recording signals from multiple planes of wires with different orientations enables reconstruction in three dimensions.

In order to determine the absolute position of any activity in the detector, the time of the ionisation is required. Then the delay between this time and the arrival of the electrons at the wire planes may be used to calculate the distance between the wires and the particle trajectories. In the LArTPC, scintillation light plays this role. Charged particles travelling

through argon produce scintillation light¹, the result of de-exciting argon-argon excimers. This process produces two light signals, one with a peak intensity 6 ns after the passage of the charged particle, and a second that peaks at 1500 ns. These signals arrive much faster than the drifting charges and provide a zero time, to which the arrival times of the electrons can be compared.

The LArTPC detector design furnishes physics analyses with several forms of information that may be used to identify particles: the location of any activity in the detector (tracking) may be used to identify neutrino vertices, the distances travelled by different particles which can serve as a proxy for their kinematics, and the existence of any secondary interactions/decays. The entire target volume can be instrumented, avoiding the need for any extrapolation of particle trajectories to determine the location of the interaction vertex. The strength of the currents recorded is related to the quantity of charge liberated, which in turn indicates how much energy a particle deposited in the argon along its path (calorimetry). This information is often used to distinguish between different kinds of particles, a subject which will be further discussed in Section 3.2.5.

¹A good resource describing the scintillation of liquid argon is Ref. [114].

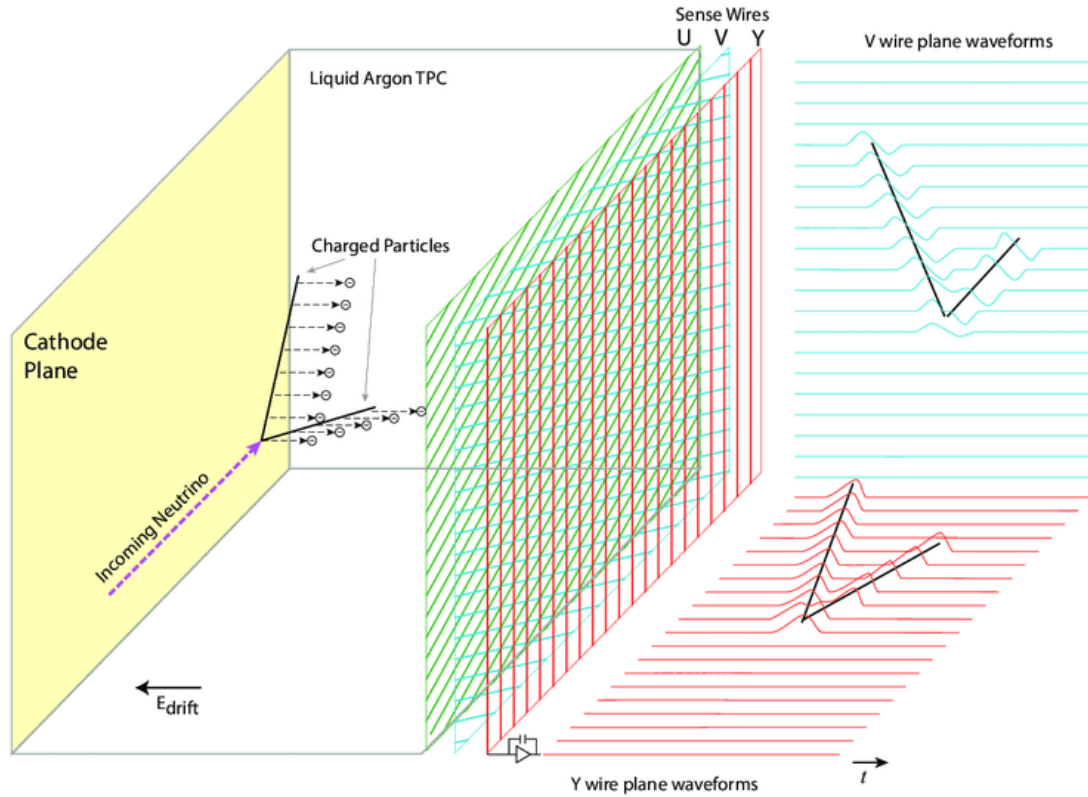


Figure 3.1: Operational principle of the Liquid Argon Time Projection Chamber. Charged particles travelling through the argon create trails of ionisation, the liberated electrons pulled towards an anode, in front of which are several planes of wires. As the electrons drift towards the wires, they induce currents, illustrated on the right hand side of the figure. These currents are deconvolved to reveal two dimensional images of the original charged particles. The wires in the U and V planes form the induction planes, while the wires labelled Y form the collection plane. Figure from Ref. [71].

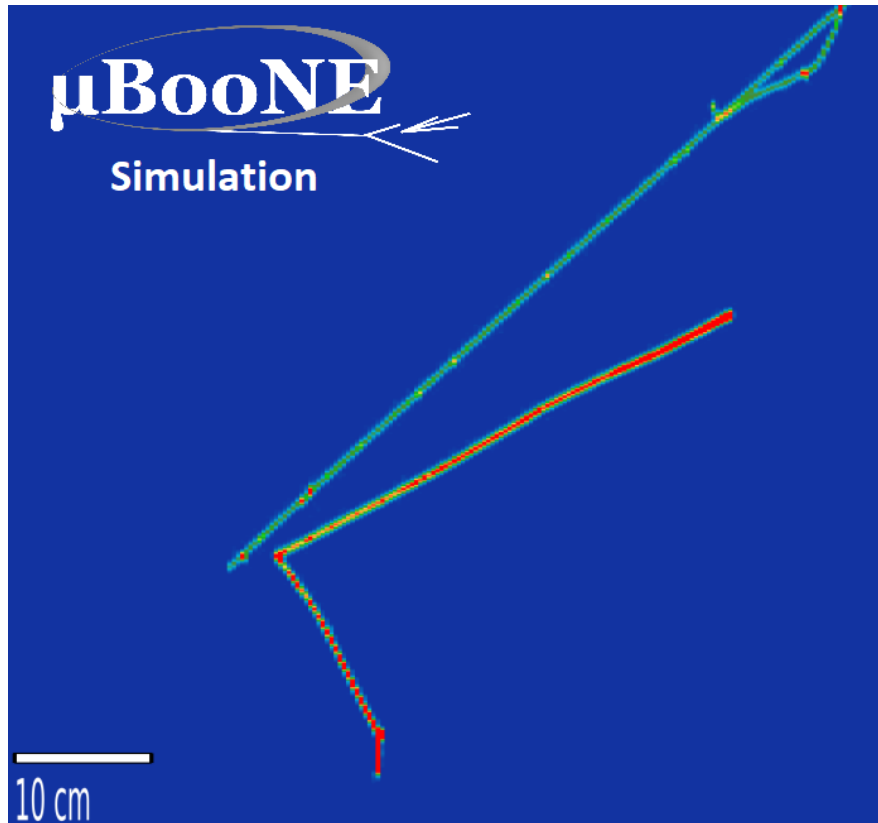


Figure 3.2: Two dimensional event display. The x bins along the x axis indicate the different wire channels, and the y axis indicates time. The coloration indicates the number of electrons arriving at the wires, with green/blue indicating fewer electrons, and red indicating a higher quantity of electrons. This is used to estimate the energy losses per unit distance of particles travelling through the detector.

3.2 The MicroBooNE LArTPC

The Micro Booster Neutrino Experiment (MicroBooNE), is a 170 ton LArTPC located in the Booster Neutrino Beamline at the Fermilab, at a distance of approximately 470 m downstream of the beam source. The primary physics goals of the experiment are to investigate the nature of the anomaly observed by the MiniBooNE experiment, discussed in Section 1.4.3, study the physics of neutrino interactions with argon nuclei, and develop the LArTPC technology. The detector is positioned at a similar distance along the Booster Neutrino beamline at Fermilab to the MiniBooNE experiment, in order to be sensitive to the same oscillation phenomena. Unlike the Cherenkov design employed by MiniBooNE, the LArTPC is able to distinguish between photons and electrons, as described in Section 3.2.5, enabling tests

of both the electron-like and photon-like hypotheses. The detector receives neutrinos (and anti-neutrinos) from two beams, the Booster Neutrino Beam[115, 116] (BNB), and Neutrinos from the Main Injector [117] (NuMI) beam. The operation and characteristics of these beams will be described in Section 3.3.

3.2.1 Cryostat and Charge Readout

The detector [118] consists of a 12.2 m long cylindrical stainless-steel cryostat, filled with high purity liquid argon. Inside the cryostat is a cuboidal 2.6 m \times 2.3 m \times 10.4 m field cage, with the anode placed on side and the cathode on the other. The cryostat and field cage are illustrated in Figure 3.3. In front of the anode are three planes of wires, with one oriented vertically and the other pair at $\pm 60^\circ$ to the vertical. Information about the three plane is listed in Table 3.1. In this thesis, the angled planes will be labelled as Plane 0 and Plane 1, while the vertically oriented wires form Plane 2. The layout of the wire planes in the MicroBooNE TPC is illustrated in Figure 3.4. It should be noted that in Figure 3.4, the beam direction describes the direction of the BNB, and not the NuMI beam used in the analysis described in this thesis. The two neutrino beams detected by MicroBooNE are described in Section 3.3.

The wire responses in the induction and collection plane differ, as illustrated in Figure 3.1. A “peak and dip” shaped signal is generated in the induction planes as the electrons approach and then depart from wires. The wires in the collection plane record a single peak. Noise removal and deconvolution algorithms [119, 120] are applied to these signals, with the end product being a record to the charge arriving at each wire as a function of time.

MicroBooNE is also equipped with a cosmic ray tagger (CRT), installed between the summer of 2016 and early 2017. This system comprises 73 panels of plastic scintillator, located above, below, and alongside the cryostat parallel to the beam direction, described in Ref. [121]. No data from this system is used directly in this analysis: the cosmic ray background is removed by cuts described in the next chapter.

3.2.2 Light Collection System

The scintillation light ² produced by the argon is recorded by a rack of 32 photomultiplier tubes (PMTs), manufactured by Hamamatsu. The wavelength of the scintillation light produced by liquid argon is approximately 128 nm. The photomultiplier tube are only able to detect photons in the 300-650 nm range, and achieve an optimal quantum efficiency at ≈ 400 nm. A plate of tetraphenyl-butadiene (TPB) is placed in front of each PMT to shift the wavelength of the light into a range the PMTs are able to detect, by absorbing the scintillation light emitted by the argon and re-emitting it with a wavelength of 425 ± 20 nm.

²A small quantity of Cherenkov light is also produced.

Alph. Label	Num. Label	Channels	Potential	Signal Type	Orientation
U	0	2400	-110 V	Induction	+60° to vertical
V	1	2400	0 V	Induction	-60° to vertical
Y	2	3256	230 V	Collection	Vertical

Table 3.1: Description of the three wire plane in MicroBooNE. The alphabetical labelling scheme is shown in Figure 3.1. In this thesis, the numerical labelling scheme for the planes will be used. The voltages are chosen to steer the electrons around the induction planes, and onto the collection plane.

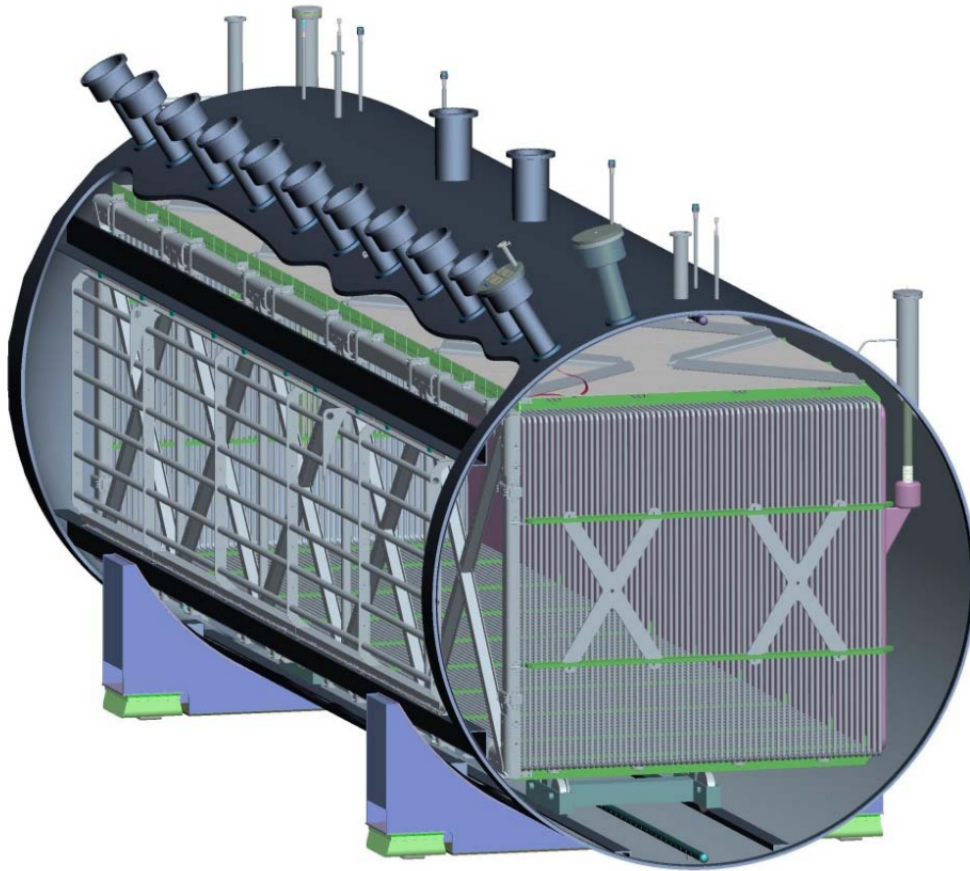


Figure 3.3: Schematic of the MicroBooNE cryostat. The rectangular structure inside the cylinder is the TPC. Figure from Ref. [71].

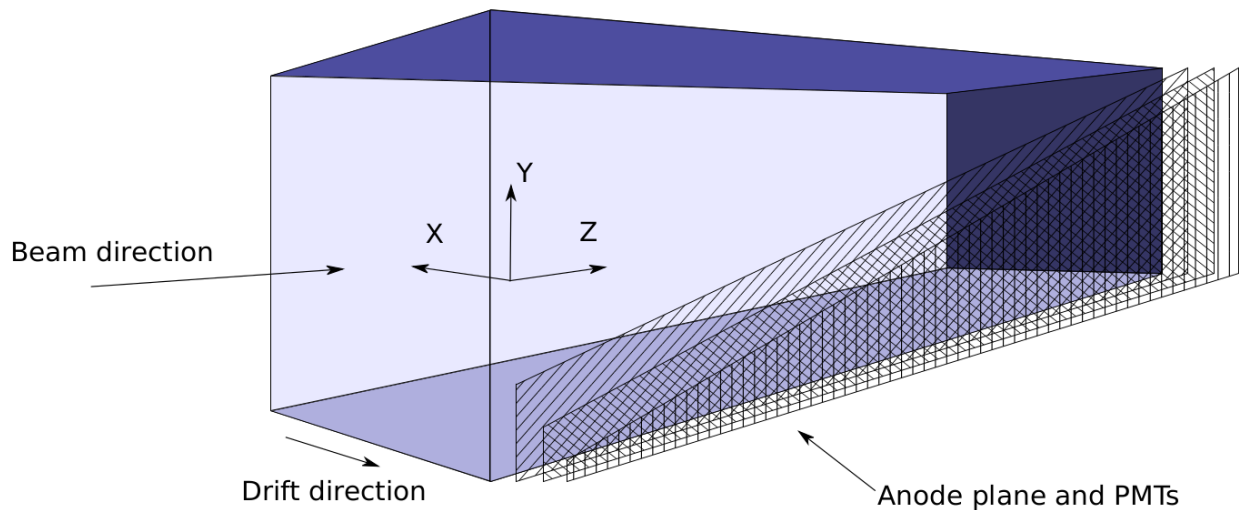


Figure 3.4: Diagram of the MicroBooNE TPC. Figure from Ref. [122]. The direction of the BNB, which points along the z axis, is indicated. In this thesis the NuMI beam is used, which produces its strongest flux at 8° to the z axis in the positive x direction.

Beyond its necessity in calculating the absolute positions of particles as previously described in Section 3.1, the light detection system performs another important function: rejecting cosmic rays. In a surface level time projection chamber such as MicroBooNE, a large number of cosmic ray muons cross the active volume every second, each produces a flash of scintillation light, which gives a very precise indication of when that particle crossed the detector. This time is compared with the time neutrinos from the beam are expected to arrive at the detector, and any activity producing a light flash out of sync with the beam is assumed to be from a cosmic ray.

3.2.3 Triggers

The quantity of information recorded by the detector is far too large to process and store, and triggers are employed to control when the detector records data and manage the flow of information, to maximise the percentage of the recorded data that is useful. An electronic signal is sent by the Fermilab Accelerator Division to the detector whenever a pulse of neutrinos is being produced at the beam source. This is the hardware trigger. In the case of NuMI the hardware trigger initiates a $23 \mu\text{s}$ readout period, called the “beamgate window”. The actual pulse of neutrinos from the NuMI beam is much shorter than this, though its position within the beamgate window varies. Only a few percent of NuMI spills result in a neutrino interaction inside the MicroBooNE detector, and so to avoid wasting large amounts of computational resources, a second, software based trigger is applied. This demands that

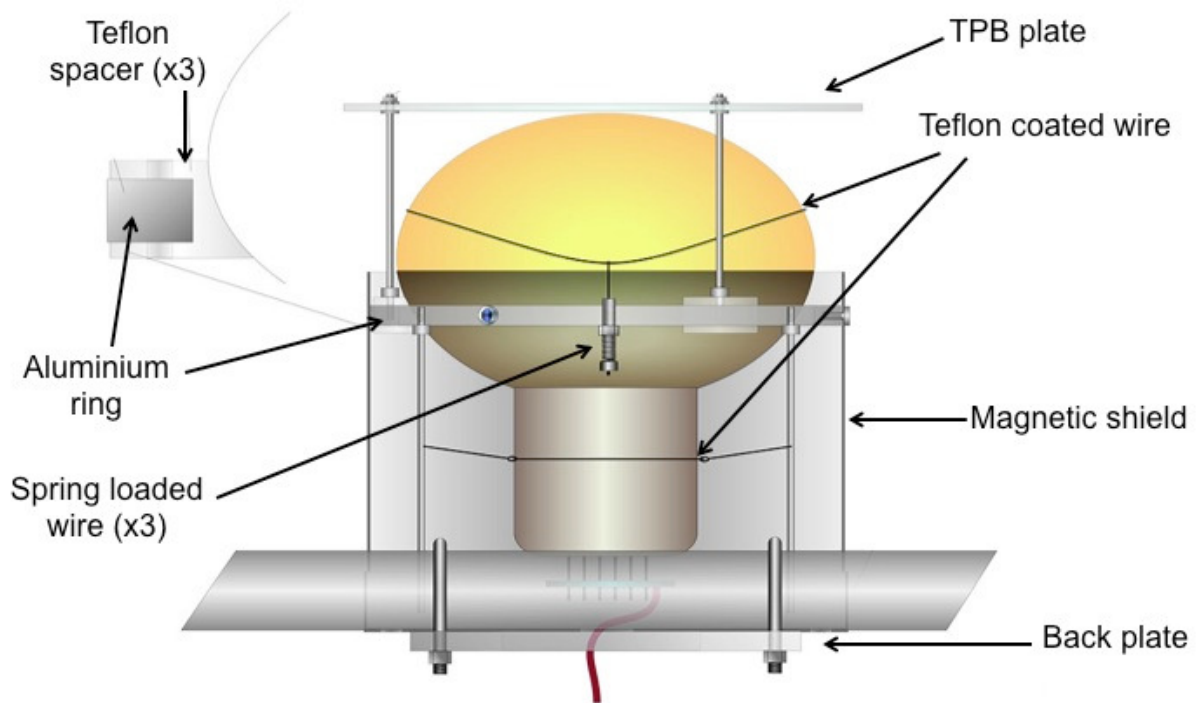


Figure 3.5: The photomultiplier tubes installed inside the MicroBooNE detector. Figure from Ref. [71].

a minimum of 9.5 photoelectrons are recorded by the light collection system within the beamgate window for the event to be recorded.

MicroBooNE receives a significant quantity of cosmic ray muons, and the triggers and reconstruction algorithm can mistake these for neutrino interactions if they arrive within the beamgate window. Any physics analysis must include this as a source of background. This is accomplished by collecting data when the beam is inactive: a configurable pulse generator is used to mimic the signal from the hardware trigger, with the other triggers and data acquisition systems setup as if the detector is expecting neutrinos from the beam. This is called the external trigger, and data collected with this trigger will henceforth be labelled as “EXT”.

3.2.4 Detector Effects

Several physical phenomena occur inside LArTPCs that must be simulated, some of which have associated systematic uncertainties.

The Space Charge Effect

The exposure to cosmic rays results in a buildup of argon ions inside the cryostat, concentrated near the cathode, which modifies the electric field. This is called the space charge effect (SCE), and causes a shift in the locations of reconstructed objects in the detector, as illustrated in Figure 3.6. The space charge effect in MicroBooNE was studied in Ref. [123], and is corrected for in the analysis described in the subsequent chapters of this thesis.

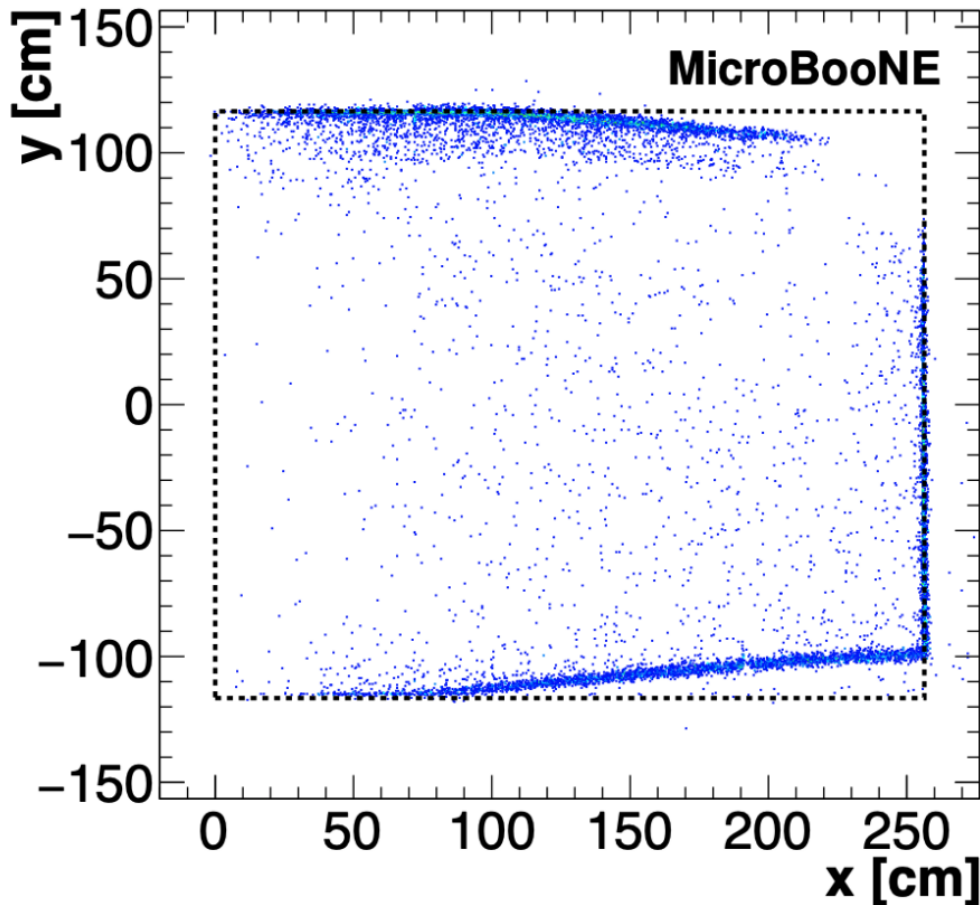


Figure 3.6: The entry/exit points of reconstructed cosmic ray muons in MicroBooNE, with the dashed lines indicating the edges of the TPC. In the absence of the space charge effect, the entry/exit points would be lie on the boundaries of the TPC, indicated by the dashed black line. Figure from Ref. [123].

Diffusion and Recombination

As the electrons are pulled towards to anode, they will begin to spread out, an effect known as diffusion, resulting in blurrier event displays. This effect can be reduced by increasing the strength of the drift field. The electrons can also recombine with nearby argon ions, affecting the number that reach the wire planes. These effects are important, both as noise filtering is applied that may remove very small charge depositions, and because the detected charge is used as a proxy for the energy deposited by a particle in the detector, which some methods of particle identification and estimators of particle kinematics rely on.

Unresponsive Channels

An unresponsive channel can be recognised in an event display as an empty slice extending along the entire vertical axis of the event display, for example the highlighted gap in Figure 3.7. Unresponsive channels are scattered throughout the detector on all three wire planes. These are included in the detector response simulation described in Section 3.4.4, and the reconstruction algorithms employed by MicroBooNE are designed to cope with their existence. There is a section of the TPC between $z \approx 675$ cm and $z \approx 775$ cm containing a high concentration of unresponsive wires, this region will henceforth be referred to as the “dead region”. The event selection described in Chapter 4 will not attempt to identify Λ baryon production events in this portion of the detector, and excludes data with reconstructed neutrino vertices in this region.

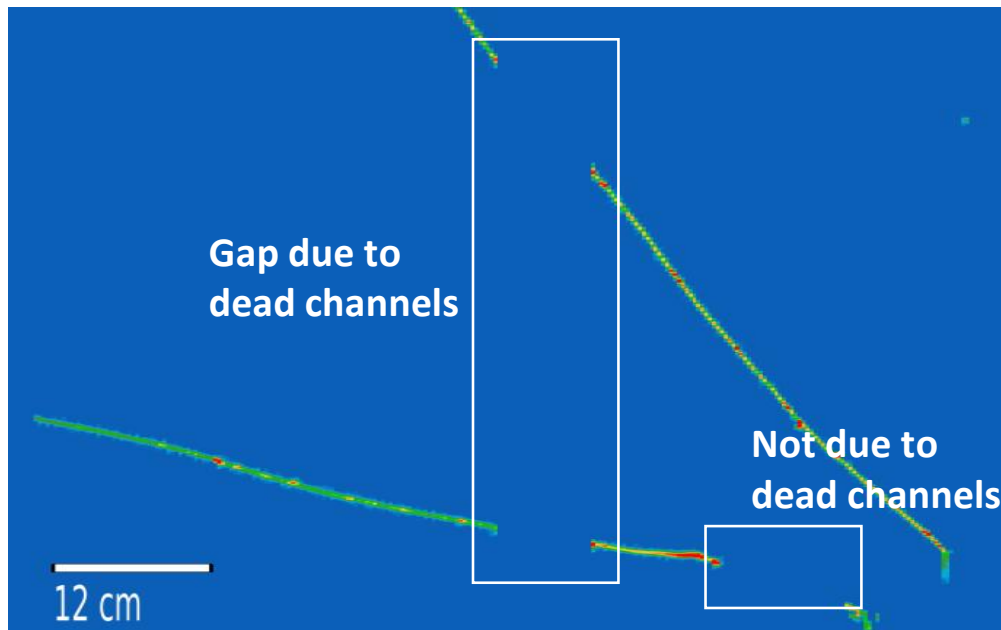


Figure 3.7: Gaps in tracks due to dead channels. A vertical slice cutting through multiple tracks along the same section of the horizontal axis of the event display usually signals the presence of unresponsive wires. It can be deduced the gap in the right hand box is not due to unresponsive wires as there is a track above it without a gap.

3.2.5 Particle Identification Methods

Regarding the signatures they produce, the particles that result from neutrino-nucleus interactions may be roughly sorted into three categories: track-like, shower-like, and invisible. Protons, charged pions, muons, charged kaons, and the charged Σ baryons typically create track like signatures. The shower-like category comprises electrons and photons. Invisible

particles are those that do not ionise the argon, primarily neutrons, and are only detected indirectly if they interact/decay to produce other particles that do ionise the argon. Neutral pions, the Λ baryon, and the Σ^0 baryon are all detected through the presence of their decay products. There is some overlap between these categories, for example, a pion that repeatedly scatters may produce a somewhat shower-like signal, and electrons at low energies often produce track-like signatures.

Particle Energy Loss

Three pieces of information are often used to identify a track-like particle: the intensity of the energy deposition along the track, the presence of any sudden changes in direction, which indicate interactions/decays, and the length of the track. The energy lost per unit distance of a charged particle, in the energy regime applicable to MicroBooNE, is described by the Bethe-Bloch formula:

$$\left\langle \frac{dE}{dx} \right\rangle = Zz^2 \frac{K}{A} \frac{1}{\beta^2} \left(\frac{1}{2} \ln \frac{2m_e \beta^2 \gamma^2 T_{\max}}{I} - \beta^2 - \frac{\delta(\beta\gamma)}{2} \right). \quad (3.2)$$

Z and A are the atomic number and atomic mass of the medium respectively, z the charge of the incident particle (in units of the elementary charge), β the velocity of incident particle, $\gamma = 1/\sqrt{1-\beta^2}$, T_{\max} the maximum kinetic energy that may be transferred to a free electron in a single collision, and I the mean excitation energy of electrons in the medium. $\delta(\beta\gamma)$ is a correction for high momentum particles. The predicted energy losses of a μ^+ in copper at different energies are illustrated in figure 3.8. The predicted values of dE/dx for different particles are shown in Figure 3.9.

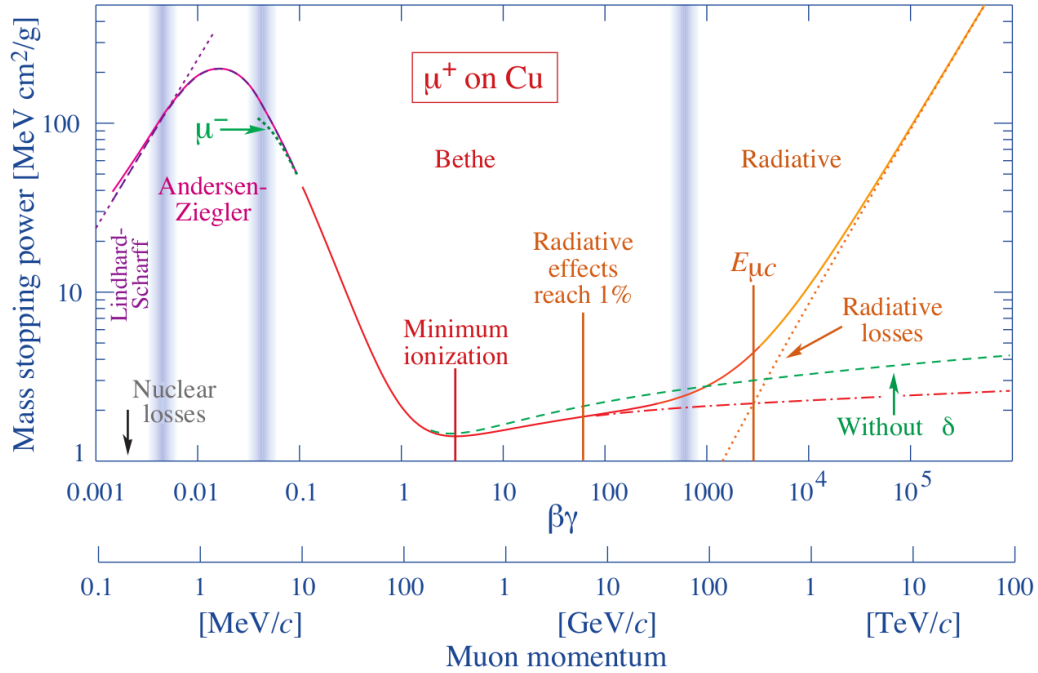


Figure 3.8: The predicted energy loss of a μ^+ in copper. The region of particle momentum relevant to MicroBooNE runs from approximately 100 MeV to 5 GeV, which is described by the Bethe-Bloch formula. Figure from Ref. [22].

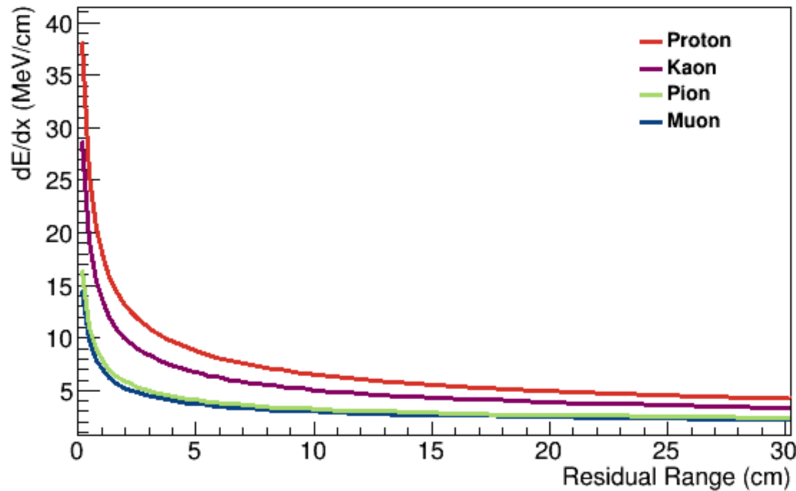


Figure 3.9: The rates of energy loss predicted by the Bethe-Bloch formula for protons, charged pions, kaons, and muons. The residual range is the distance from the end of a particle's trajectory. The rapid increase in dE/dx the final few cm of a particles track is called the “Bragg Peak”. Figure from Ref. [122].

Muons

Figure 3.9 shows that muons and charged particles ionise argon less intensely than protons and kaons, leading to the classification as minimum ionising particles (MIPs). Particle identification algorithms targeting muons, such as the one described in Section 4.4, typically compare the dE/dx along tracks to the expected values for muons. A muon can decay, with the dominant mode being $\mu^- \rightarrow e^- + \bar{\nu}_e + \nu_\mu$, though in MicroBooNE a muon will often exit active volume before doing this. The electron produced in this decay is called a “Michel electron”, and will typically create a short track of its own. A simulated muon, with Michel electron, is shown in Figure 3.10.

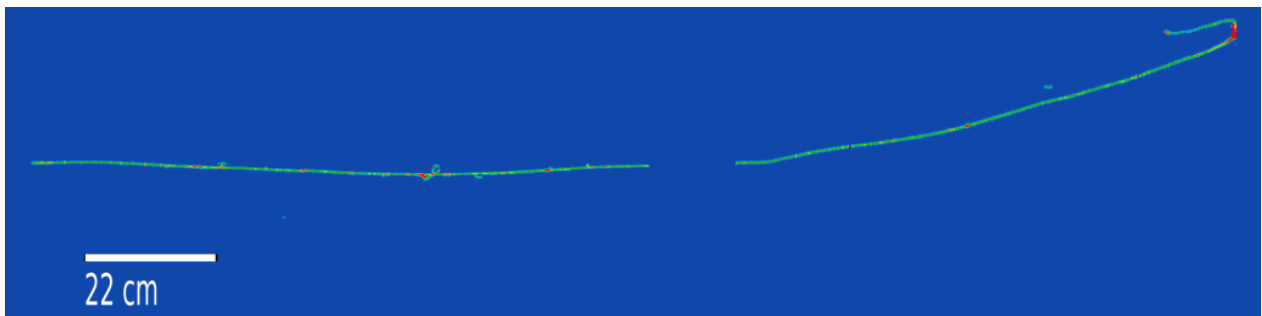


Figure 3.10: Event display of a simulated μ^- with 1 GeV of momentum, travelling left to right. The gap near the middle of the track is due to unresponsive TPC wires. The “hook” at the end of the track is produced by the Michel electron.

Protons

The primary method for the identification of protons is to measure the value of dE/dx along tracks, which will be larger than that of muons and charged pions. In the event displays in this thesis, heavier ionisation is indicated by orange/red colouration. An event display of a single simulated proton is shown in Figure 3.11.

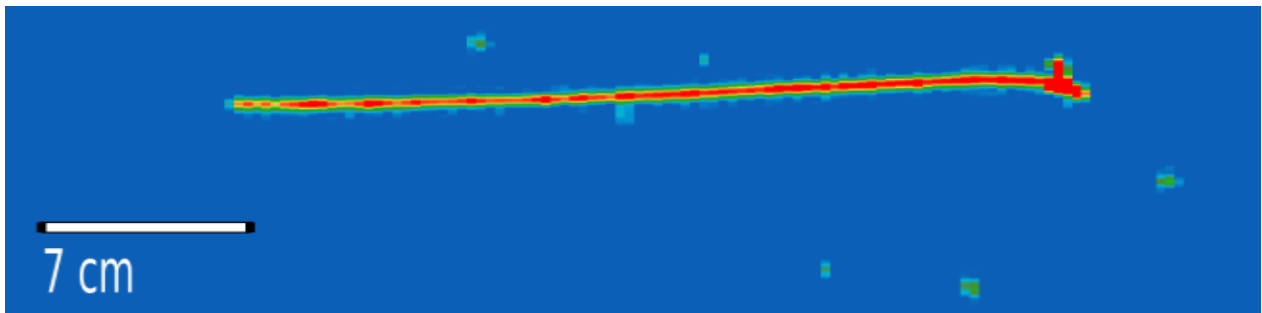


Figure 3.11: Event display of simulated proton with 1 GeV of momentum, travelling left to right. The red colour of the track indicates intense ionisation of the argon.

Charged Pions

Charged pions are challenging to separate from muons owing to their similar masses, and therefore similar dE/dx profiles, as shown by Figure 3.9. The presence of a charged pion in a neutrino interaction is often deduced through combinatoric arguments: in a CC ν_μ interaction, unless a very hard scatter occurs, the majority of the kinematic budget is transferred to the muon, with the remainder shared between the hadrons and nuclear remnant. As a result, the muon typically produces a much longer track than any charged pions, and it is assumed the longest MIP-like track is the muon, and any additional MIP-like tracks are charged pions. The presence of secondary interactions with other nuclei in the detector can also distinguish pions from muons, as the other nuclei in the detector are more transparent to muons owing to their lack of participation in the strong interaction. An example of a charged pion track is shown in Figure 3.12.

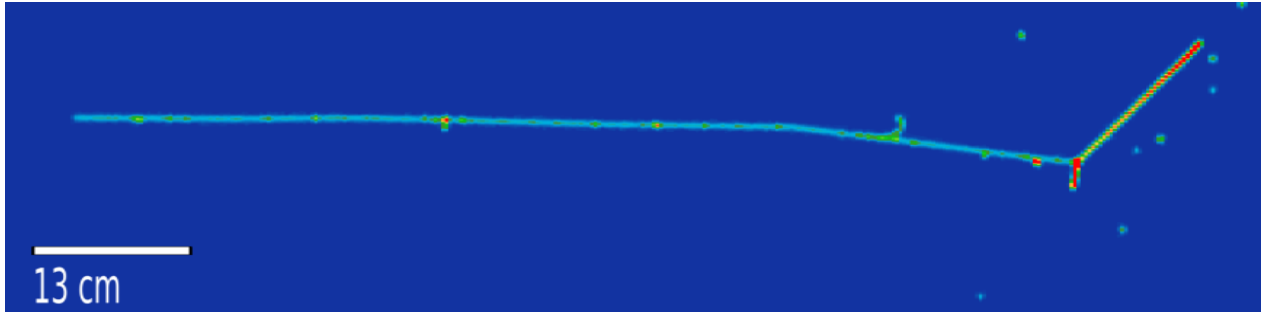


Figure 3.12: Event display of simulated π^+ with 1 GeV of momentum, travelling left to right. The π^+ underwent a scatter with a nucleus, producing a pair of protons, visible as the “split” in the track.

Charged Kaons

Kaons produce a track like signature, with an expected rate of energy loss greater than that of MIPs, but less than that of protons. Unlike the other particles, these will often decay within the detector, with its two leading decay modes being:

$$K^+ \rightarrow \mu^+ + \nu_\mu, \quad (3.3)$$

$$K^+ \rightarrow \pi^+ + \pi^0, \quad (3.4)$$

resulting in a track with a “kink”. If the kaon comes to rest before decaying, the μ^+ or π^+ are always produced with 236 MeV or 205 MeV of momentum respectively [22], and the detection of a secondary track with momentum near one of these values can indicate the parent track is a charged kaon. A charged kaon, decaying to a muon, which subsequently decays to a Michel electron, is shown in Figure 3.13.

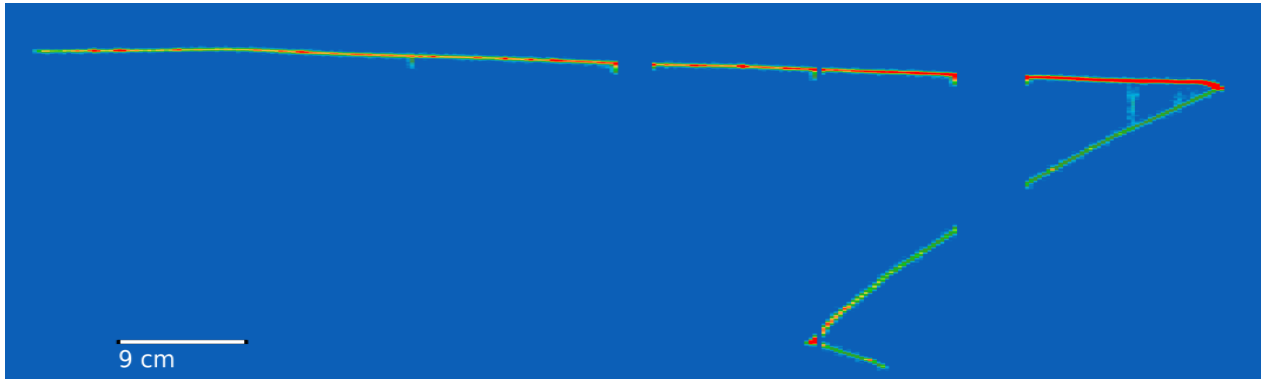


Figure 3.13: Event display of simulated K^+ with 1 GeV of momentum, travelling left to right. The K^+ undergoes a decay on the right hand side of the display to a μ^+ , which subsequently decays to a Michel electron.

Electrons/Photons

Sufficiently energetic photons will undergo pair production, resulting in an electron-positron pair, and energetic electrons can produce photons through bremsstrahlung. An electromagnetic shower is produced when an electron/photon undergoes bremsstrahlung/pair production, with the resulting photons/electrons/positrons undergoing pair production/bremsstrahlung themselves, and so on, producing a signature like the one seen in Figure 3.14. This process is illustrated in Figure 3.15.

Photons and electrons are distinguished through the intensity of energy loss near the start of the shower: an electron shower will begin with a single electron, while the photon, after converting, begins with a pair of electrons. Thus a photon shower will deposit energy in the detector at approximately twice the rate of an electron induced shower, an effect that can be seen in Figure 3.16.

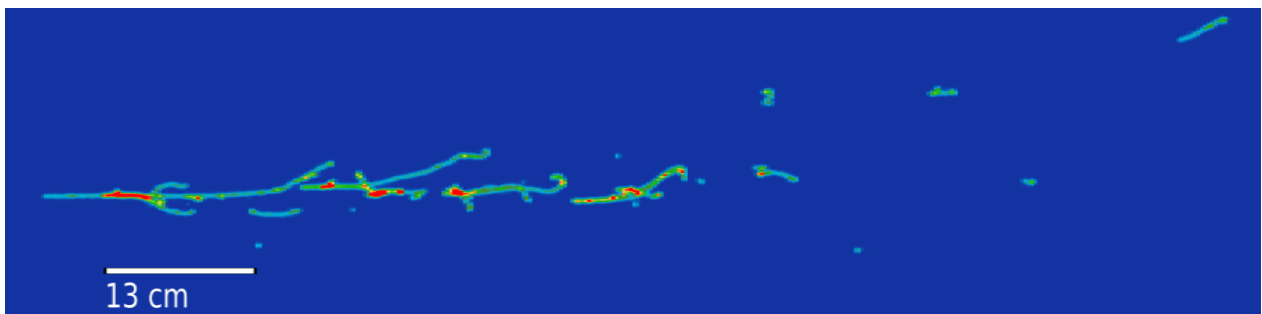


Figure 3.14: Event display of simulated electron with 0.5 GeV of momentum, travelling left to right. The electron produces a shower through repeated bremsstrahlung and pair production by the photons produced in the bremsstrahlung.

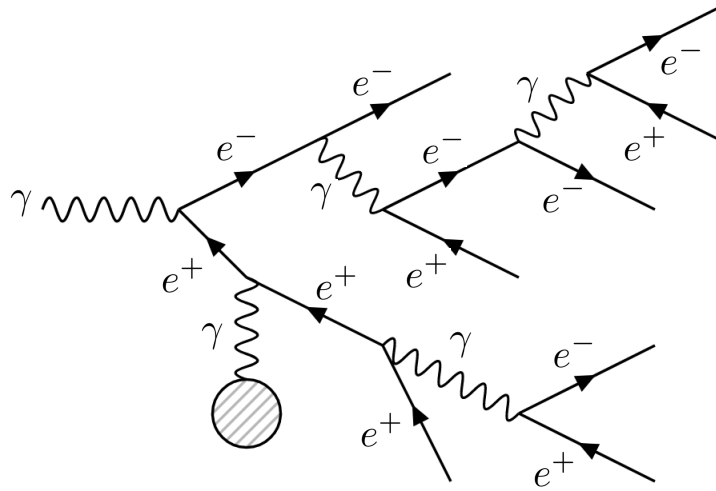


Figure 3.15: Feynman diagram describing the development of an electromagnetic shower. The shaded circle represents some perturbing factor, such as an atomic electron belonging to the medium the photon is propagating through.

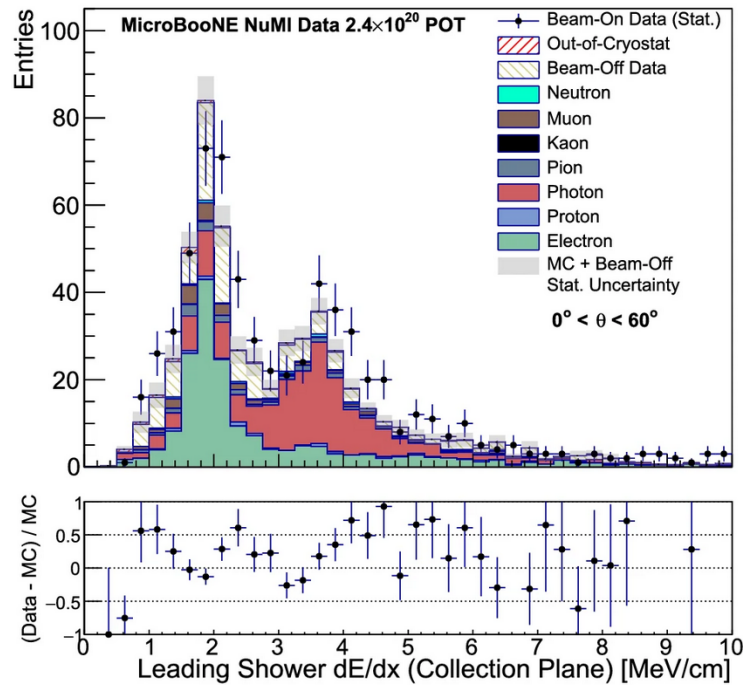


Figure 3.16: The average dE/dx of electromagnetic showers detected by MicroBooNE, compared with simulation predictions. A peak at around 2 MeV/cm is produced by electrons, while the secondary peak at 4 MeV/cm is the result of photons. Figure from Ref. [124].

Neutral Pions

The neutral pion decays electromagnetically to a pair of photons, before travelling any measureable distance in MicroBooNE. The result is a pair of separated showers pointing at the neutrino interaction vertex. If the kinematics of the showers are estimated from their length and directions, their invariant mass may be calculated and compared with that of the π^0 . An event display of a π^0 inside MicroBooNE is shown in Figure 3.17.

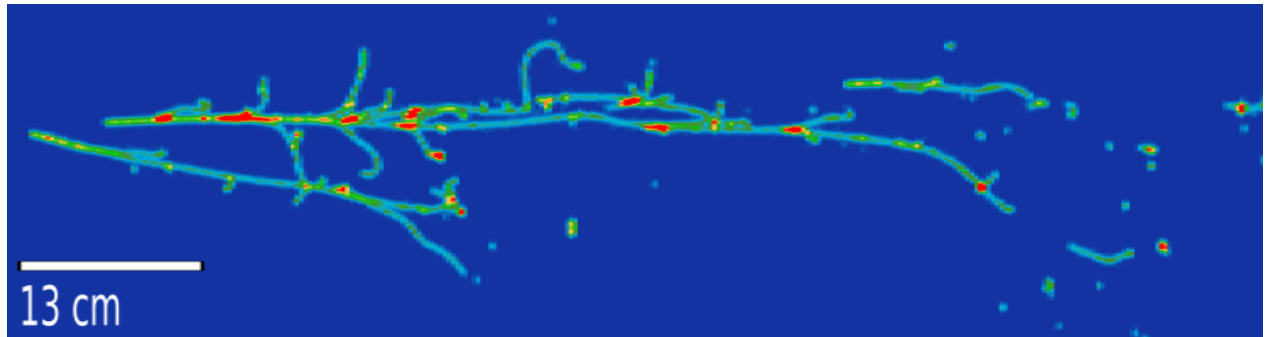


Figure 3.17: Event display of simulated π^0 with 1 GeV of momentum, travelling left to right. The π^0 immediately decays to a pair of photons, each creating an electromagnetic shower.

3.3 The BNB and NuMI Beams

Fermilab currently operates two accelerator driven neutrino beams: the Booster Neutrino (BNB) [115, 116] and Neutrinos from the Main Injector (NuMI) [117] beams. The composition in terms of neutrino energy and flavour of these beams differs greatly for several reasons which will be explained below.

The starting ingredient of both neutrino beams is a proton beam produced by an accelerator, in the case of the BNB this is the Booster ring, which produces protons at an energy of 8 GeV, and for NuMI this is the Main Injector, which operates at an energy of 120 GeV. The beams produce timed pulses of protons, called spills, with approximately 5×10^{12} protons in each spill from the BNB, and 3×10^{13} from NuMI. The total number of protons hitting the target in a data taking period, or POT (protons on target), is the measure of detector exposure simulation predictions are normalised to.

The proton beam is aimed at a target, made of beryllium in the BNB and graphite in NuMI, and the protons interact with the nuclei in the target producing, among other particles, charged pions (and kaons). These pions are produced with a wide range of energies and directions, and a must be refocused along the beam direction. Downstream of the target is a focusing horn (or pair of horns in the case of NuMI), which employs a magnetic field to steer the pions towards the beam axis, while also deflecting away pions with the wrong charge and other particles such as protons. After the focusing horns there is a decay volume,

in which the pions decay to neutrinos with the following branching fractions [22]:

$$\text{BF}(\pi^+ \rightarrow \mu^+ + \nu_\mu) = 99.9977\%, \quad (3.5)$$

$$\text{BF}(\pi^+ \rightarrow e^+ + \nu_e) = 0.0001\%, \quad (3.6)$$

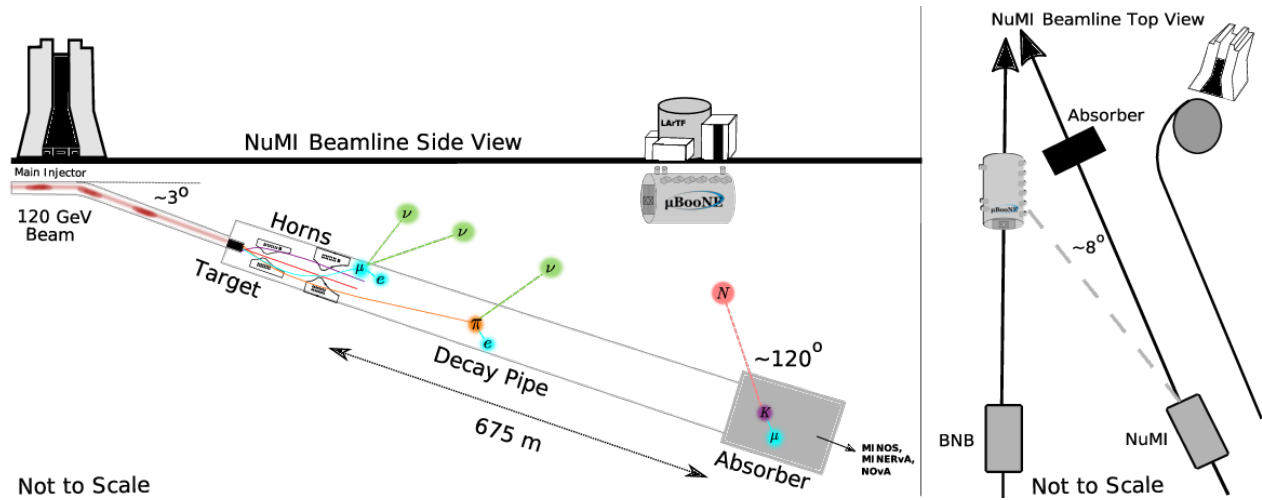
and similar for the decays of π^- to $\bar{\nu}_\mu$ and $\bar{\nu}_e$. The decay volume is terminated by an absorber, which blocks any undecayed pions and other particles produced in the collisions of the protons in the target. The layout of the NuMI beam is illustrated in Figure 3.18b. The term “beam” is somewhat misleading, as this usually conjures images of a highly collimated and highly monoenergetic stream of particles. However, the reliance on meson decays, which direct their products randomly, and the fact the neutrinos themselves cannot be steered with magnets, results in a very broad range of directions and energies, as illustrated in Figures 3.19 and 3.20 below.

A powerful feature of the focusing horn is that by reversing the direction of the currents, and therefore the direction of the magnetic field, inside the horn, a neutrino dominated beam may be transformed into an anti-neutrino dominated beam. These two settings are called Forward Horn Current (FHC) and Reverse Horn Current (RHC). The BNB has only been operated in its neutrino mode during MicroBooNE’s data taking periods, while the NuMI beam has run in a mixture of both running modes. The FHC and RHC fluxes arriving at MicroBooNE from NuMI are shown separately in Figures 3.20a and 3.20b respectively.

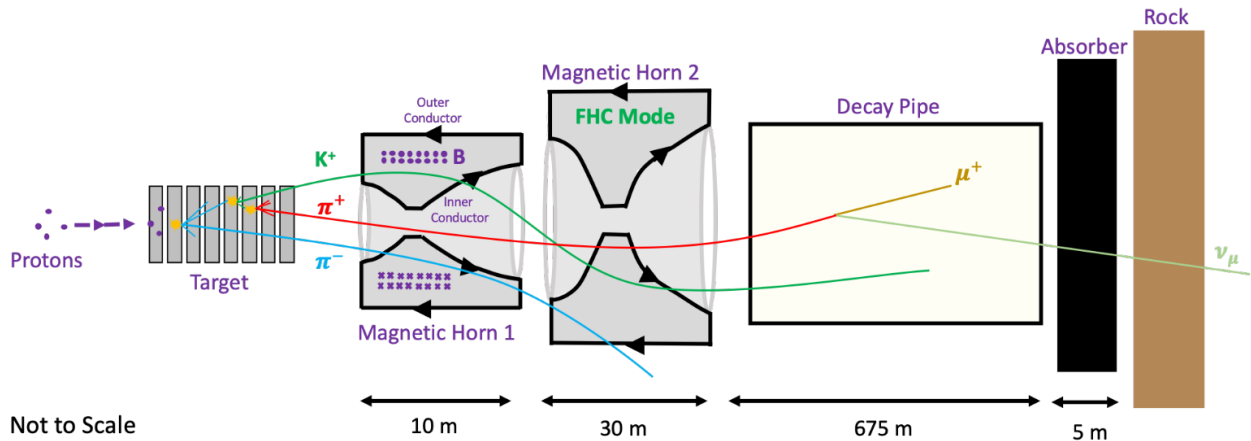
The MicroBooNE detector is placed on-axis relative to the BNB, while the detector is approximately 8° off axis relative to the NuMI target, though the detector receives neutrinos from the entire NuMI decay volume which is 675 m in length, illustrated in Figure 3.18a. This significantly modifies the shape and composition of the flux: a comparison of Figure 3.19 to Figure 3.20 shows the contamination of anti-neutrinos in the neutrino mode beam, and vice versa for the anti-neutrino mode beam (wrong-sign contamination) is far larger in the NuMI beam. NuMI also contains a higher percentage of electron neutrinos, a consequence of the more energetic proton beam that feeds it: the interactions of the higher energy protons in the target produce a larger quantity of kaons, which decay to electron neutrinos with a larger branching fraction than pions [22].

MicroBooNE Data Taking Periods

MicroBooNE has been collecting data since October 2015, with the BNB run exclusively in its neutrino mode, while NuMI has been operated in a mixture of both modes. MicroBooNE’s data taking can be split into five periods, dated in Table 3.2. Each run requires a separate set of Monte Carlo simulation samples, as the conditions and performance of the detector have varied slightly from run to run. In this thesis, data collected during Run 1 and Run 3 will be analysed. During these running periods, MicroBooNE received 3.72×10^{20} POT from the BNB, 2.18×10^{20} POT from NuMI operated in neutrino mode, and 4.93×10^{20} POT from NuMI operated in anti-neutrino mode. The measurement of the CCQE-like Λ production



(a) MicroBooNE’s location relative to the NuMI beamline. The left hand panel shows a side on view, while the right panel is a bird’s eye view. Figure from Ref. [125].



(b) Schematic of the a typical neutrino beam. Figure from Ref. [125].

Figure 3.18: The 120 GeV proton beam is collided with a target to produce charged π mesons, then are focused by a magnetic horn and fed into a decay pipe. MicroBooNE is located alongside this decay pipe, and while most of the neutrino flux arrives from near the target, neutrinos from the entire decay pipe reach the detector.

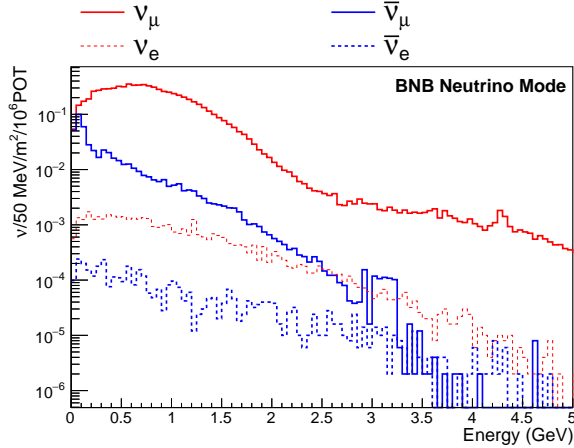
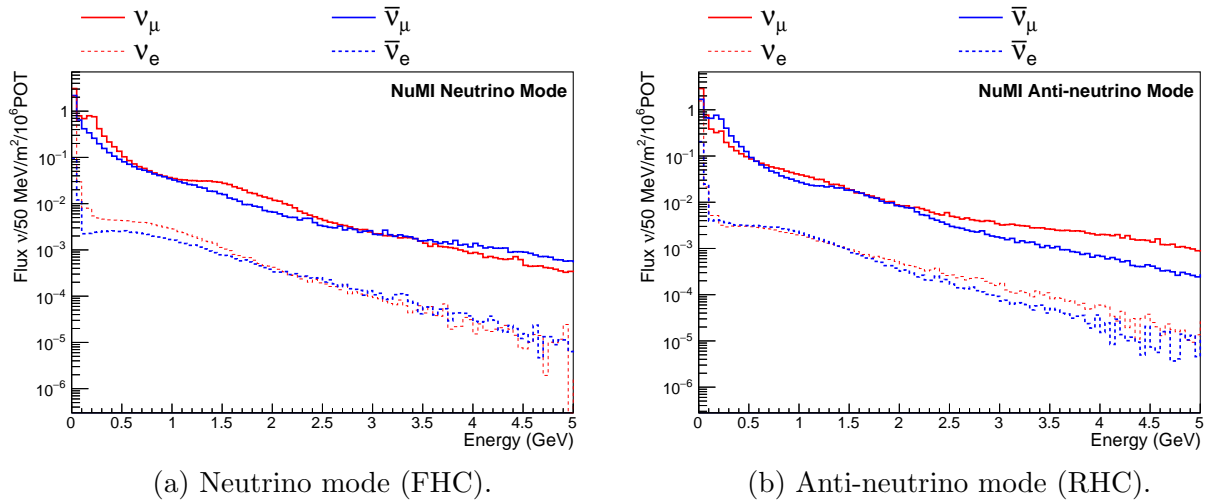


Figure 3.19: The predicted neutrino/anti-neutrino fluxes produced by the Booster Neutrino Beam at MicroBooNE’s location. Figure from Ref. [73].



(a) Neutrino mode (FHC).

(b) Anti-neutrino mode (RHC).

Figure 3.20: The fluxes produced by the NuMI beam at MicroBooNE. Note a wider range of energies is shown than in figure 3.19.

cross section will be performed with the NuMI flux, a decision that will be justified in Section 4.1.3.

Run Period	NuMI FHC Operation	NuMI RHC Operation
1	23 Oct. 2015 - 2 May 2016	29 Jun. 2016 - 29 Jul. 2016
2	14 Nov. 2016 - 20 Feb. 2017	11 Nov 2016 - 14 Nov 2017 20 Feb 2017 - 7 July 2017
3	N/A	7 Nov. 2017 - 6 Jul. 2018
4	26 Feb. 2019 - 6 Jul. 2019	20 Oct 2018 - 26 Feb 2019
5	29 Oct. 2019 - 20 Mar. 2020	N/A

Table 3.2: MicroBooNE’ data taking periods. N/A indicates no data with the beam operating in that mode was collected during that run. Data from the FHC portion of Run 1, and the RHC portion of Run 3 will be analysed in this work.

3.4 Event Simulation

3.4.1 Neutrino Fluxes

The fluxes are simulated using the GEANT 4³ [126] software package, which has been adapted by the neutrino experiments studying the NuMI beam, MINERvA, NOvA, and MicroBooNE, into the `g4numi` package. This simulates the impingement of the proton beam onto the target, the production of any resulting particles and their reinteractions elsewhere in the beamline geometry, and their decays to neutrinos. The `g4numi` package employs the `FTFP_BERT` hadron interaction models, which utilises the FRITOF pre-compound model [127] for hadron energies above 4 GeV and the Bertini cascade model [128] below this energy.

The event generators do not try to simulate interactions throughout the entire space between the decay volume and the MicroBooNE cryostat. Instead the neutrinos passing through a window approximately $30\text{ m} \times 30\text{ m}$ in size, a few meters away from the cryostat, are stored. A single neutrino may then be described by the position at which it passes through this window and its momentum. Information about the parentage of the neutrino is also stored for the purpose of propagating systematic uncertainties, but not required for the simulation. Files containing many millions of simulated neutrinos passing through this window are then passed to the neutrino interaction simulation.

³Geometry and Tracking.

3.4.2 Neutrino Interactions

The default neutrino event generator used by MicroBooNE is GENIE [63], which simulates the entire set of interaction processes described in Section 1.5, with the CCQE-like hyperon production process handled through the Llewelyn-Smith model, without FSI. Other processes such as neutrino-electron scattering are also simulated. The usage of NuWro [65] as an alternative event generator will be discussed in Section 3.4.6. These processes are all modelled using Monte Carlo simulation techniques, similar to those described in Chapter 2.

The output of this stage is a list of particles that were produced in the neutrino interaction, including the daughter nucleus, which are fed into the GEANT 4 particle propagation program at the beginning of the next stage. In addition to this list of particles, information describing the interaction process is stored, such as whether the interaction was CC or NC, QEL or RES etc., along with some quantities such as the squared four momentum transfer. This information may be used to fine tune the generator model without simulating new events through reweighting procedures, which will be discussed in Chapter 5. Multiple neutrino interactions may occur within in a single beam spill, an effect known as pileup, with two or more neutrino interactions from the NuMI flux occurring in the TPC volume approximately 1% of the time.

The GENIE model used in this thesis was tuned using T2k and MINERvA data, as described in Ref. [129]. A list of the models used for the major interaction channels is presented in Table 3.3, which comprise the G18_10a_02_11a tune.

Process	Model	Notes
Nuclear Model	LFG	
CC QE	Nieves [130]	Includes RPA corrections that suppress the cross section at low Q^2 . A Coulomb correction for the interaction between the outgoing lepton and the nuclear remnant is applied.
NC EL	Ahrens [131]	
RES	Berger-Sehgal [61, 62, 132, 133]	BS used both CC and NC interactions.
CC MEC	Valencia [134–136]	
NC MEC	GENIE Empirical [137]	
DIS	Bodek-Yang [138–140]	Applicable energy range overlaps with that of the Berger-Sehgal RES model. RES model is used for hadronic invariant masses below 1.9 GeV. Above 1.9 GeV the BY DIS model is used, with hadroniation simulated with the KNO model.
COH	Berger-Sehgal [141]	BS used for both CC and NC interactions. The BS Coherent model is distinct from the BS resonance model.
FSI	hA2018	Empirical model created by GENIE developers, tuned to pion scattering data.

Table 3.3: The neutrino interaction models used by GENIE in this thesis. The tuning of these models to T2K and MINER ν A data is described in Ref. [129].

3.4.3 Particle Propagation

The GEANT 4 [126] software package is employed to propagate the particles produced in the initial neutrino-nucleon interaction through the detector geometry, simulating secondary interactions and decays, and the calculating the quantity of energy deposited through ionisation. GEANT 4 employs a semi-classical propagation algorithm similar to the FSI

simulation described in Section 2.3.2: the distances particles travel before they interact/decay are selected by random number generation to replicate the quantum nature of such processes, though they are then transported to the interaction point as classical particles. Similarly, for particle-nucleus interactions, GEANT 4 will transport the incident particle through the nucleus semi-classically. The Bertini cascade model [128] is used for hadron-nucleus interactions.

The trajectories of ionisation electrons are not individually simulated, instead the pattern of charge liberated is projected onto the wire planes, with smearing to account for the diffusion of the electrons as they travel. The propagation of individual scintillation photons is not simulated either, instead the probability of a scintillation photon produced at a given point in the TPC reaching each PMT is estimated using a pre-generated photon library. This library was produced by splitting the TPC into small volumes, and using simulation to estimate the probability of a photon produced in each from reaching each of the PMTs.

3.4.4 Detector Response

The previous stage creates a record of where in the detector ionisation occurred, and simulating the resulting wire signals is the responsibility of the detector response simulation. This stage also simulates the scintillation light from the argon recorded by the photomultiplier tubes. The currents induced in the wires are simulated using the 2D Garfield program [119, 142]. After this stage, the processes of creating simulated data and analysing real data converge.

3.4.5 Cosmic Rays

As a surface level detector, MicroBooNE receives a significant cosmic ray flux, and a activity created by cosmic rays may be mistakenly reconstructed as a neutrino interaction. The background resulting from the detector triggers activating when no neutrino interaction is present is modelled using data collected with the external trigger described in Section 3.2.3. Cosmic rays will also produce activity in the detector that will be visible in the data collected when triggering on a real neutrino interaction. This can result in reconstruction algorithms mistaking a cosmic ray for a neutrino vertex, resulting in the real neutrino interaction being ignored⁴. The presence of cosmic rays can impact the quality of the reconstructed neutrino vertices, such as obscuring the vertex when viewed from one of the planes, or their unwanted inclusion as an additional track.

MicroBooNE employs a novel technique for simulating the effect of cosmic rays called “overlaying”: real data collected by the detector using the EXT trigger (without the neutrino beam) is combined with simulated neutrino interactions, giving a data driven model of the

⁴MicroBooNE’s reconstruction algorithms, by default, will only reconstruct single neutrino vertex per beam spill.

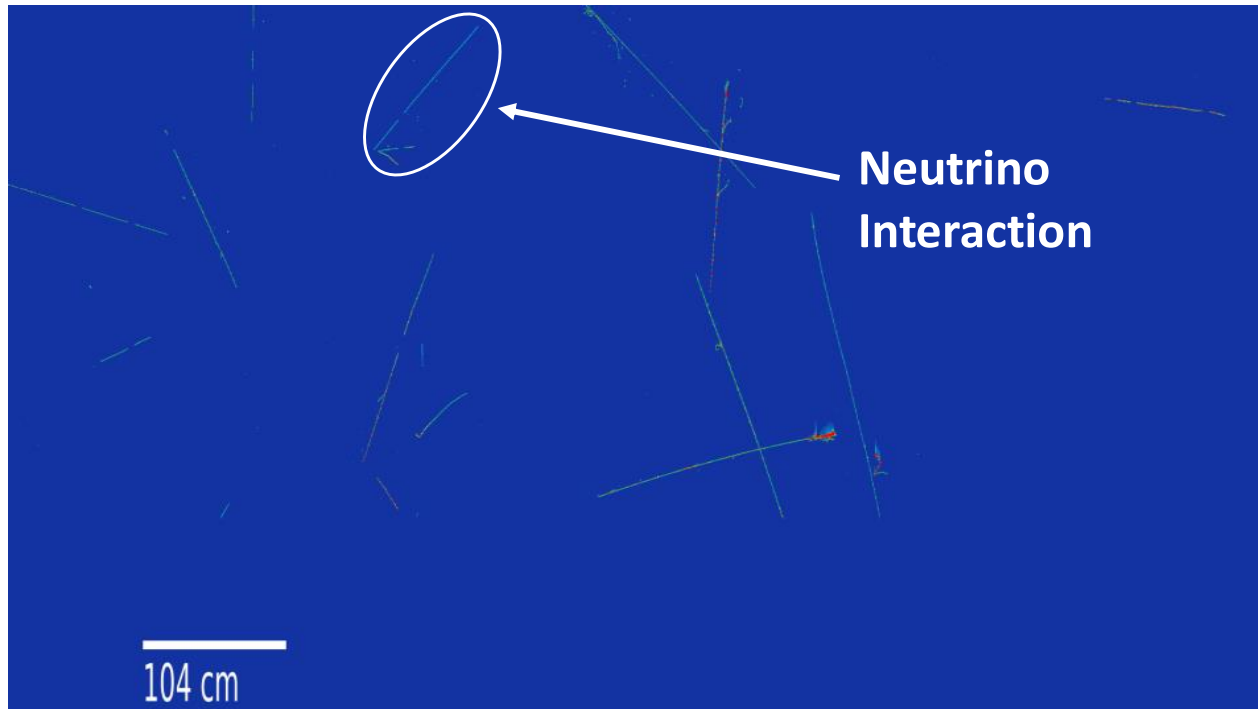


Figure 3.21: An event produced using overlaying, showing the activity received by an entire TPC plane. All of the tracks not labelled as the neutrino interaction are from a data event collected using the EXT trigger.

cosmic ray background. All of the Monte Carlo simulation samples used in the analysis described in this thesis, unless otherwise stated, use overlaying. Separate data sets are used for the EXT and to provide the cosmic background for the overlaying to prevent any bias when estimating the background due to cosmic rays.

3.4.6 NuWro An Alternative Event Generator

GENIE is used as the primary neutrino event generator in MicroBooNE, however NuWro is also capable of simulating neutrino interactions with a realistic flux in a computerised replica of a real detector. To study any model dependence appearing in the analysis described in the subsequent chapters of this thesis, NuWro will be employed as an alternative neutrino event generator, with neutrino interactions simulated by NuWro in the MicroBooNE geometry passed through the same simulation and reconstruction chain.

Validation

To test the flux and geometry modelling inside NuWro, events are simulated in the MicroBooNE cryostat with the NuMI flux, and compared to those produced with GENIE.

This will result in different predictions as the interaction models, and therefore cross sections, employed by the two generators are not the same. In order to perform a useful comparison, the cross section must be removed as a factor. To accomplish this, the cross sections for muon neutrino/anti-neutrino CCQE interactions from both generators are calculated, as shown in Figure 3.22, and their ratio is used to produce a weight:

$$w = \frac{\sigma_{\text{GENIE}}(E_\nu, \text{flavour})}{\sigma_{\text{NuWro}}(E_\nu, \text{flavour})}. \quad (3.7)$$

This can be used to reweight the CCQE event rates predicted by NuWro. The resulting distributions correspond to what NuWro will predict if using an identical total cross section to GENIE for the CCQE channel.

The NuWro CCQE events, reweighted with Equation 3.7, are compared with GENIE CCQE events in Figure 3.23. Both generators produce consistent predictions, indicating the NuWro flux/geometry simulation of MicroBooNE is functioning correctly.

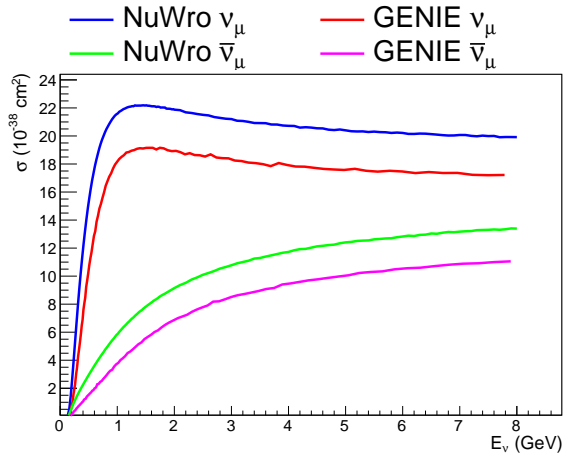


Figure 3.22: Total $\nu_\mu/\bar{\nu}_\mu$ CCQE cross sections predicted by GENIE and NuWro.

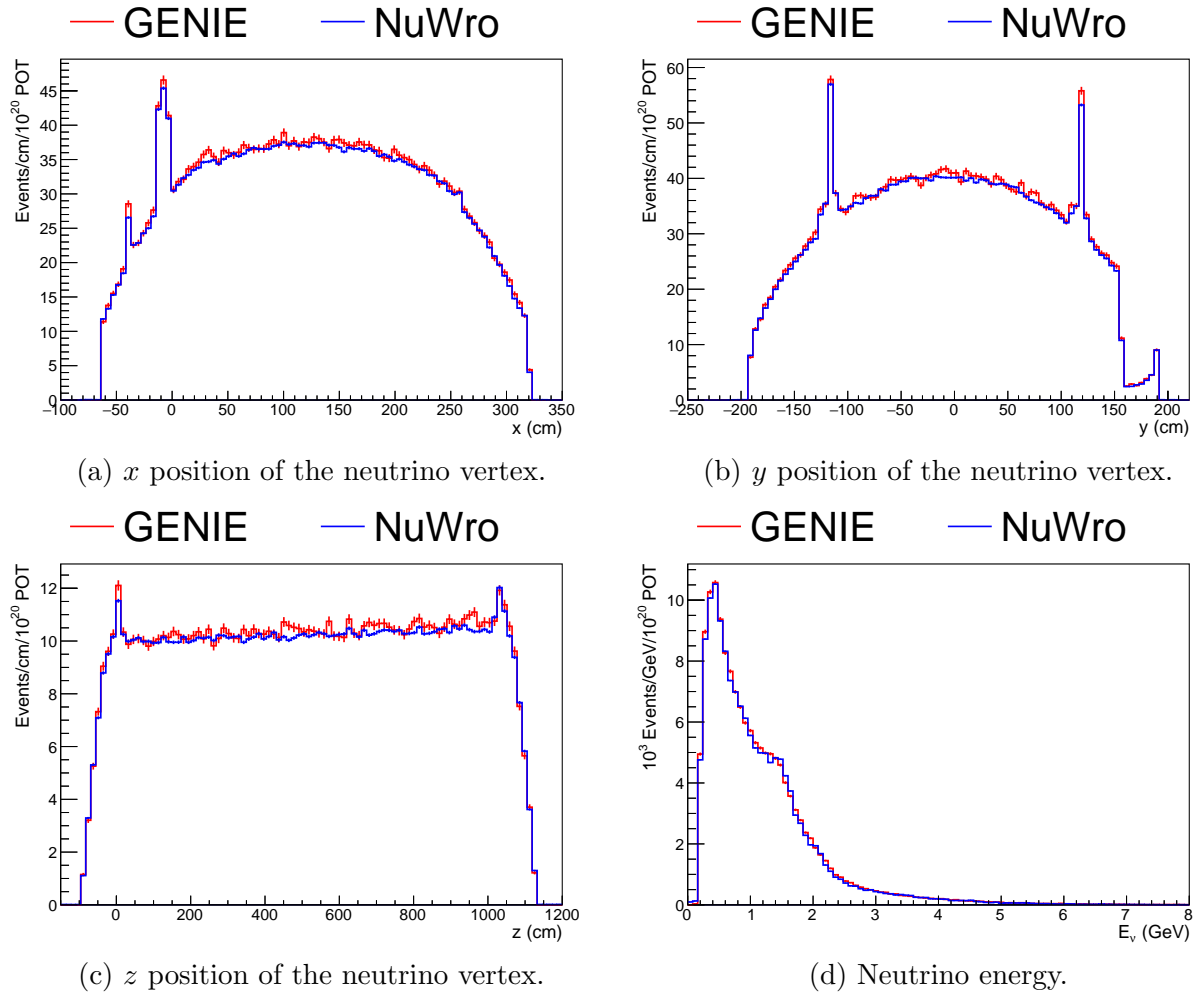


Figure 3.23: Comparisons of GENIE and NuWro CCQE events simulated with the NuMI flux in the MicroBooNE cryostat geometry, with the NuWro events reweighted using Equation 3.7.

3.5 Reconstruction

3.5.1 Hit Finding

The wire signals are filtered to remove noise and a deconvolution algorithm is applied [119, 120], leaving a record of the estimated charge arriving at each wire as a function of time, similar to the “deconvolved wire activity” in Figure 3.24. A series of Gaussian distributions are fitted to this activity, and stored in the event record as “hits”, which are passed along to the second stage of reconstruction.

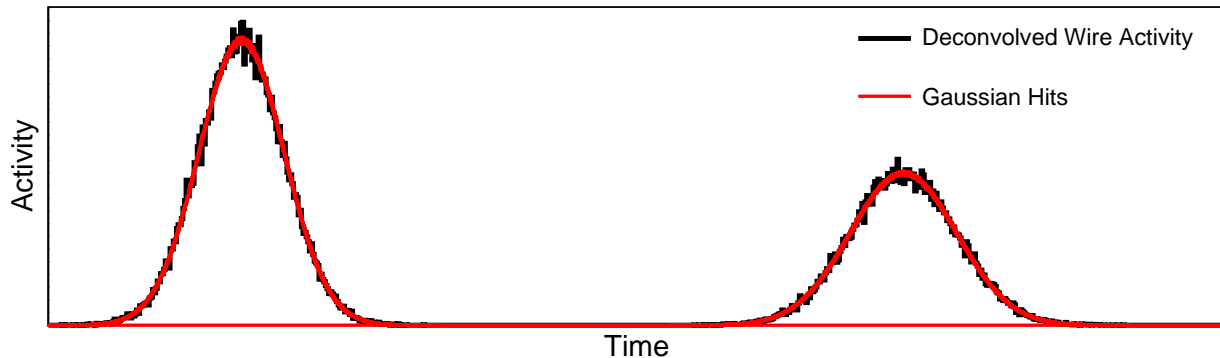


Figure 3.24: Fitting of Gaussian hits to the deconvolved wire signals, probably resulting from a pair of particles, one further from the anode than the other.

3.5.2 Tracks, Showers, and Vertices

MicroBooNE employs the Pandora [143] multi-algorithm framework to identify the signatures of tracks and showers within the hits, and select a potential neutrino interaction vertex. First the hits on each plane are grouped into objects called clusters, based on their proximity. The clusters are identified as track-like or shower-like, before the information from the three planes is correlated to combine the three two dimensional images into a single three dimensional picture. The timing information plays a key role in this process: electrons liberated at a given point in the detector will arrive at all three planes almost simultaneously, producing a hits with similar time coordinates. Inconsistencies between these matched clusters are identified, and hits added and removed from clusters, and the combinations of matched clusters permuted until they are resolved. A track and a shower is then fitted to each group of matched clusters, and a score indicating which topology the clusters bear the greatest similarity to is generated. This is the Pandora track/shower classification score. This process is performed twice, once to remove unambiguous cosmic ray tracks, and then to identify the candidate neutrino vertex and associated particles:

Cosmic Pass

The track-focused reconstruction algorithms are applied, and the similarity of the resulting tracks to cosmic rays is assessed. All hits associated with unambiguous cosmic rays are removed and not analysed in the neutrino pass.

Neutrino Pass

The hits surviving the cosmic pass are reconstructed into tracks and showers. The location of a neutrino vertex is determined based on the position and direction of nearby clusters. A hierarchy of reconstructed particles is created, starting with the neutrino vertex, with its

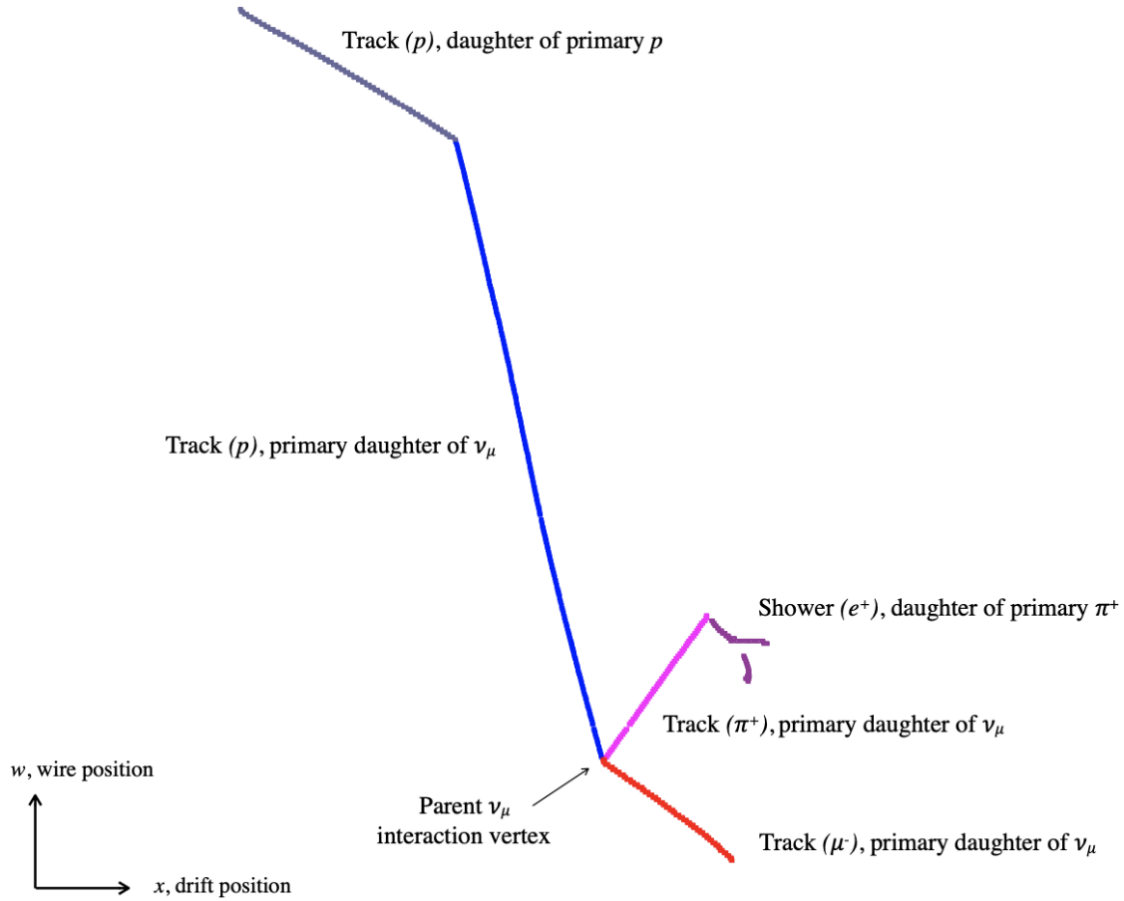


Figure 3.25: Reconstructed particle hierarchy produced by Pandora. A neutrino vertex is produced, to which three daughter tracks are associated, in this case three tracks. One track has a track-like daughter of its own, and another a shower. Figure from Ref. [143].

children being the reconstructed tracks and showers attached to it. These reconstructed particles may in turn have their own children. An example of a reconstructed particle hierarchy produced by Pandora for a neutrino interaction is shown in Figure 3.25. Only particles included in the hierarchy associated with the neutrino vertex will be considered by the event selection described in Chapter 4.

3.5.3 Truth Matching

For the purposes of developing the selection, it is useful to correlate reconstructed features with individual simulated particles in the MC simulation samples, a process known as truth matching. This is performed by tracking which simulated particles deposited energy in each

hit, and recording how many hits belonging to a track that each particle deposited energy in. A track is then matched to the simulated particle that left energy in the largest number of hits belonging to that track. It should be noted that this is not a one to one correspondence; multiple particles may deposit energy in a single hit, and a single simulated particle may deposit energy in hits belonging to several reconstructed tracks.

Chapter 4

Event Selections

4.1 Signal Definition

4.1.1 Which Decay Mode?

The Λ baryon possesses two primary hadronic decay modes [22]:

$$\text{BF}(\Lambda \rightarrow p + \pi^-) = 63.9\% \quad (4.1)$$

$$\text{BF}(\Lambda \rightarrow n + \pi^0) = 35.8\% \quad (4.2)$$

producing different signatures in a detector. As described in Section 3.2.5, protons and charged pions create track-like signatures, while neutrons may only be observed when they undergo a secondary interaction with an argon nucleus, and the presence of a neutral pion must be deduced from the invariant mass of the pair of showers resulting from its decay.

There are two features which distinguish the Λ baryon from most other particles produced in neutrino interactions: the separation between the neutrino interaction vertex and the location at which the Λ baryon has decayed, and the kinematics of the decay. In the case of the second decay mode, these are very difficult to determine precisely. The position of the decay vertex can be inferred from the directions of the two showers in the π^0 decay, but without information about the momentum of the neutron the kinematics of the decay are unknown.

In contrast, the decay vertex is clearly visible in event displays when the Λ baryon decays to a proton and π^- , for example Figure 4.1. The lengths and directions of the tracks created by these two particles may be used to estimate their momenta, as described in Section 4.6. For this reason the analysis in this thesis will only search for Λ baryons that decay to $p + \pi^-$.

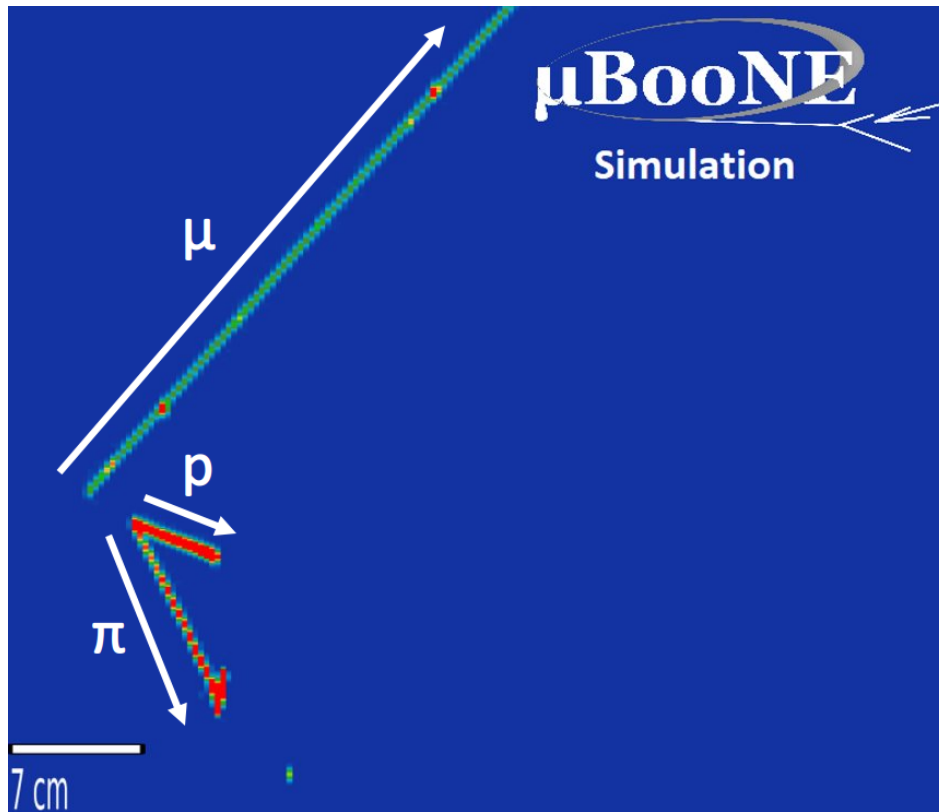


Figure 4.1: Event display of a simulated CCQE-like Λ production interaction, in which the Λ baryon decays to a proton and π^- .

4.1.2 Detection Thresholds and Phase Space

MicroBooNE is sensitive to protons with momenta above 300 MeV, and charged pions with momenta above 100 MeV, thus the measurement will only be able to observe Λ baryon decays that produce protons and pions above these thresholds. The quantity measured is therefore a *restricted phase space* cross section. The restricted phase space differential cross section, $\frac{d\sigma_*}{dp_\Lambda}$, may be defined as:

$$\frac{d\sigma_*}{dp_\Lambda} = f(p_\Lambda) \frac{d\sigma}{dp_\Lambda}, \quad (4.3)$$

where $\frac{d\sigma}{dp_\Lambda}$ is the (unrestricted) differential cross section with respect to the momentum of the Λ baryon. $f(p)$ is a function of the Λ baryons momentum, defined as:

$$f(p_\Lambda) = \frac{P(\Lambda \rightarrow p + \pi^- \text{ with } p_p > p_p^{\text{thresh}} \text{ and } p_\pi > p_\pi^{\text{thresh}})(p_\Lambda)}{\text{BF}(\Lambda \rightarrow p + \pi^-)}. \quad (4.4)$$

The numerator in this expression is the probability a Λ baryon of momentum p_Λ decays to $p + \pi^-$, with the decay products emitted with momenta above MicroBooNE's detection thresholds, $p_p^{\text{thresh}} = 0.3$ GeV, and $p_\pi^{\text{thresh}} = 0.1$ GeV. $f(p_\Lambda)$ is derived analytically in Appendix A, and is given by the following set of expressions:

$$f(p_\Lambda) = \begin{cases} 0 & \text{if } A > B \\ \frac{B-A}{2} & \text{Otherwise} \end{cases}, \quad (4.5)$$

$$A = \max \left(\frac{\sqrt{M_p^2 + |p_p^{\text{thresh}}|^2} - \gamma E_p}{\beta \gamma p}, -1 \right), \quad (4.6)$$

$$B = \min \left(\frac{-\sqrt{M_\pi^2 + |p_\pi^{\text{thresh}}|^2} + \gamma E_\pi}{\beta \gamma p}, 1 \right), \quad (4.7)$$

$$E_p = \sqrt{M_p^2 + p^2}, \quad (4.8)$$

$$E_\pi = \sqrt{M_\pi^2 + p^2}. \quad (4.9)$$

M_p and M_π are the rest masses of the proton and π^- respectively, and $p = 0.101$ GeV, is the momentum at which the proton and π^- are emitted in the Λ baryon's rest frame. β is the boost factor of the Λ baryon in the detector's frame, and $\gamma = 1/\sqrt{1-\beta^2}$. Natural units are used.

$f(p_\Lambda)$ is drawn in Figure 4.2. Four distinct regions of behaviour are visible: For Λ baryons of momenta below ≈ 0.3 GeV, the decay is never fully visible and $f(p_\Lambda) = 0$. When $0.3 \lesssim p_\Lambda \lesssim 0.5$ GeV, the decay is visible when the decay products are emitted at certain

angles in the rest frame of the Λ baryon. If $0.5 \lesssim p_\Lambda \lesssim 2$ GeV, the π^- is always above the decay threshold, and when $p_\Lambda \gtrsim 2$ GeV both decay products will always be visible and $f(p_\Lambda) = 1$.

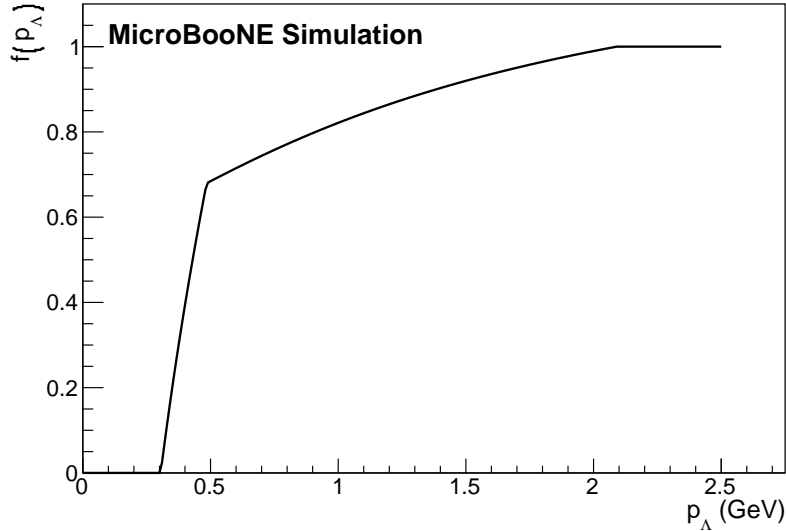


Figure 4.2: The function $f(p_\Lambda)$ featured in equations 4.4 and 4.5. The two discontinuities in gradient occur when one, and then both, of the particles produced in the decay are always above the detection threshold.

4.1.3 BNB or NuMI?

MicroBooNE receives flux from two neutrino beams, the BNB and NuMI, both of which are utilised for physics analyses, collected with separate triggers. The anti-neutrino fluxes produced by both beams, normalised to the POT corresponding to the data available for analysis, are compared in Figure 4.3. CCQE-like hyperon production is an interaction only available to anti-neutrinos and the measurement statistical uncertainties are expected to be significant in this measurement. Therefore the data with the larger anti-neutrino flux from NuMI will provide greater sensitivity, and this is the data that will be analysed in the remainder of this thesis. To maximise the available statistics, data from FHC and RHC running periods will be combined.

4.1.4 Flux-Averaging

As discussed in Chapter 3, electric and magnetic fields cannot be used to tune the energy of the neutrino beam itself, typically resulting in a broad energy spectrum. Any theoretical

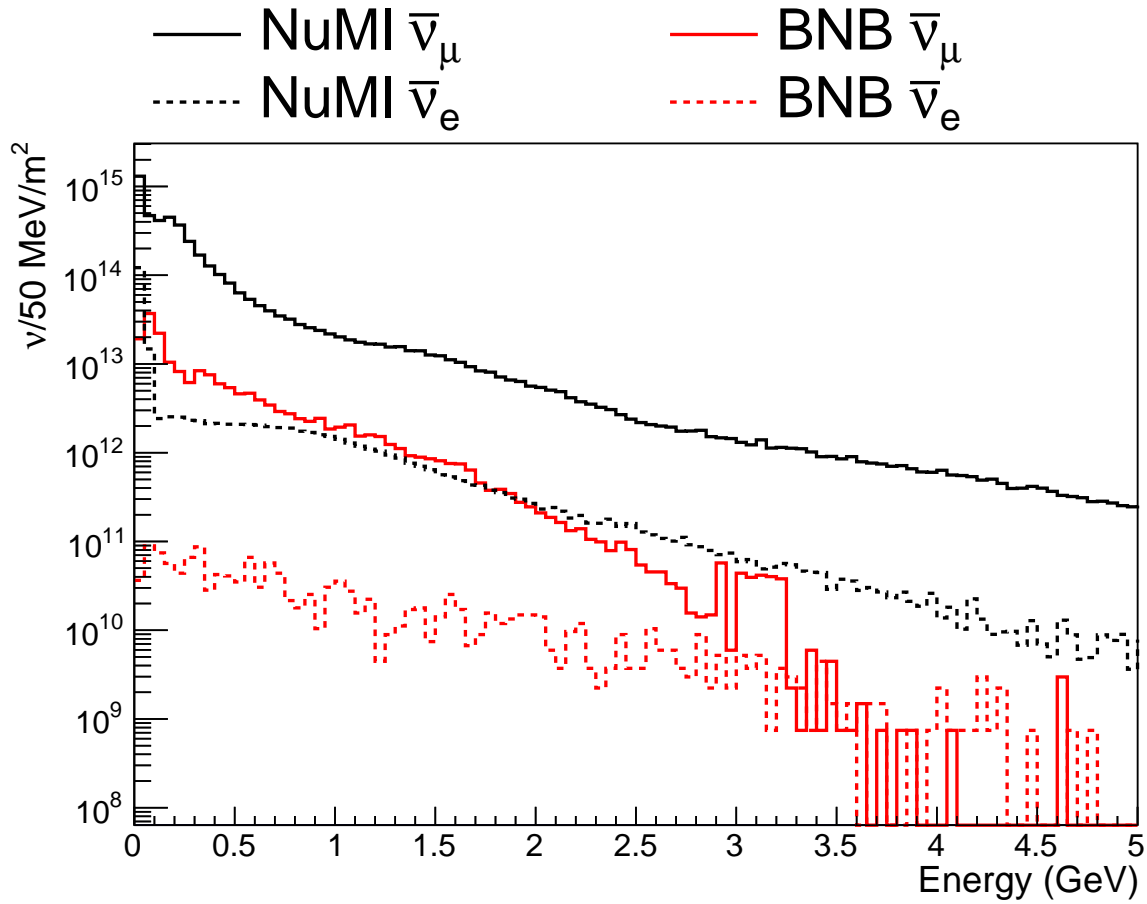


Figure 4.3: The anti-neutrino fluxes corresponding to the data from the BNB and NuMI available for analysis. 3.7×10^{20} POT of BNB flux is compared with the combined fluxes from 2.2×10^{20} POT of FHC flux and 4.9×10^{20} POT of RHC flux from NuMI. The fluctuations in the flux at higher energies are due to statistics in the flux simulation sample used to produce this graphic. The event generator samples simulated neutrinos from 500 of these files.

prediction of the cross section must be convolved with this flux to be compared with the measurement, giving a flux averaged cross section. The quantity actually measured will be a flux averaged, restricted phase space total cross section:

$$\sigma_* = \frac{\int \frac{d\sigma(E_\nu)}{dp_\Lambda} f(p_\Lambda) \Phi(E_\nu) dp_\Lambda dE_\nu}{\int \Phi(E_\nu) dE_\nu}, \quad (4.10)$$

where $\frac{d\sigma(E_\nu)}{dp_\Lambda}$ is the differential cross section for CCQE-like Λ baryon production in $\bar{\nu}_\mu$ interactions with argon nuclei at an anti-neutrino energy of E_ν , $\Phi(E_\nu)$ is the muon anti-neutrino flux from the NuMI beam at energy E_ν , and $f(p_\Lambda)$ is the phase space correction introduced in Equation 4.3. In order to calculate this quantity from a model such as the one described in Chapter 2, two pieces of information are required: the phase space correction already provided, and the shape of the anti-neutrino flux averaged over. The combining of data FHC and RHC running periods results in a uniquely shaped flux, and Appendix G gives the anti-neutrino flux corresponding to the data analysed in this thesis as a table.

4.1.5 Signal Criteria

The event selection described in this chapter targets simulated anti-neutrino interactions in the MicroBooNE detector that satisfy the following conditions:

- The interaction vertex is located within the fiducial volume (FV) described used in Ref. [144]. This comprises the TPC active volume, minus regions near the edges that suffer from a large space charge effect, and the dead region.
- A muon anti-neutrino was involved in the interaction.
- The muon anti-neutrino interaction produced a hyperon through a strangeness violating interaction, and after any FSI, a Λ baryon exited the nucleus.
- No other strange particles were produced.
- This Λ baryon subsequently decayed to a proton and π^- .
- The proton and π^- carried momenta > 0.3 GeV and > 0.1 GeV respectively.

In the case of multiple interactions occurring in the cryostat within a single beam spill, if at least one of the interactions satisfies the above conditions, the event will be classified as part of the signal. The fates of Λ baryons produced through other mechanisms will be discussed at the end of this chapter. The numbers of events from each data taking period, predicted by the GENIE and NuWro event generators, are listed in Table 4.1.

Period	CCQE Λ Events		Signal Events	
	GENIE	NuWro	GENIE	NuWro
Run 1 (FHC)	37.7 ± 0.3	51.8 ± 0.6	11.6 ± 0.2	11.5 ± 0.3
Run 3 (RHC)	85.4 ± 0.6	109.5 ± 1.2	25.9 ± 0.3	23.8 ± 0.6
Combined	123.0 ± 0.7	161.3 ± 1.4	37.4 ± 0.4	35.3 ± 0.6

Table 4.1: The number of CCQE-like Λ in the fiducial volume and signal events expected for each of the data taking periods analysed.

4.2 Monte Carlo Simulation and Data Samples

When testing the event selection and comparing to data, a sample of simulated neutrino interactions/cosmic rays from each of the categories in Sections 4.2.1- 4.2.5 is required. When generating a MC simulation sample, the beam exposure is saved in the form of a POT value, which is used to scale the MC simulation samples to the beam exposure of the data, through application of the following weight to each MC simulation event:

$$w = \frac{\text{Data POT}}{\text{MC Sample POT}}. \quad (4.11)$$

Separate samples are used to simulate the FHC and RHC data, and normalised to the POT counts for those data collection periods before being combined.

Statistical Uncertainties

To make a prediction to compare with data, events from each of the samples below are used, with the weight from Equation 4.11 applied, in addition to various other corrections, applied event by event, to fine tune the flux and event generator modelling. If the Gaussian approximation to the Poisson distribution is assumed, the uncertainty, σ , in a prediction made with weighted events is:

$$\sigma = \sqrt{\sum_i w_i^2}, \quad (4.12)$$

where w_i are the weights of the individual events. In many of the figures throughout this thesis, the uncertainties on a distribution are drawn as hatched regions, the first example of which is Figure 4.4. The uncertainties shown in this chapter are statistical only.

Λ production is a rare process, and the sources of background in the analysis are also rare processes, the Gaussian approximation may not always be appropriate. In the final cross section measurement, a Bayesian procedure for estimating the statistical uncertainties in the selection efficiency and selection background is adopted, and will be explained in Section 5.10.

4.2.1 Hyperon Only Samples

Hyperon production is a rare process, and the standard Monte Carlo simulation samples used in other MicroBooNE physics analyses contain relatively few of these events. This results in large statistical uncertainties important quantities such as estimates of the selection efficiency, and metrics of performance employed to optimise various components of the event selection.

To solve this problem, several special event samples were generated. Pure hyperon production samples were created by running the default GENIE simulation of the MicroBooNE detector with the NuMI fluxes, enabling all interaction modes. These events are filtered, leaving only those producing hyperons, which are combined with data collected with the EXT trigger and processed through the remaining stages of the simulation. With this procedure, MC simulation samples corresponding over 1000 times the POT available in the data were produced.

Running the event generator with all interaction modes active, before applying a filter, gives as a complete a picture of the hyperon production processes as possible from the neutrino event generator being run. In contrast, if only interaction modes guaranteed to produce hyperon are switched on, which is computationally more efficient, the effect of pileup on the signal will be neglected, which can lead to bias in estimates of the reconstruction efficiency and predicted background from other neutrino interactions.

No-cosmic Samples

For tuning some elements of the event selection with a large number of input parameters, most notably the selection of the tracks corresponding to the Λ baryon's decay products, there are a large number of input variables and a larger quantity of events are necessary to prevent overtraining. One way to expedite the generation of MC simulation samples is not to include cosmic rays. Pure Λ production samples with no cosmic rays are used strategically at certain points in the development of the selection. The final estimation of the selection efficiency and selected background will always be performed with overlay samples.

4.2.2 Neutron Only Samples

A significant source of irreducible background, as will be shown at the end of this chapter, results from the secondary interactions of neutrons: a neutron produced in a neutrino interaction may propagate a few cm through the argon before scattering of another argon nucleus, knocking out several charged particles. If these particles are produced with the right momenta, they will mimic the topology and kinematics of a decaying Λ baryon. This is another rare process, and as with hyperon producing events, special MC simulation samples are created to provide sufficient quantities of events to study this source of background properly.

Neutron samples are manufactured by generating neutrino interactions in the cryostat with all interaction channels active, and a filter is applied removing any events without

neutrons in the final state. These events are passed to the GEANT 4 simulation, which propagates the neutrons and other particles, simulating the aforementioned secondary interactions. A second filter is then applied to select any events containing neutrons interacting with the argon nuclei in the cryostat, in which at least two protons, two charged pions, or one of each, were produced above MicroBooNE’s detection thresholds. As with the hyperon only samples, the events selected by these filters are then mixed with EXT data and passed to the remainder of the simulation/reconstruction chain.

To avoid double counting MC simulation events, if an event is flagged as containing a neutron scatter in one of the other samples, it will be assigned a weight of zero. This does neglect the possibility of a neutron scatter and hyperon production event happening in the same spill. Approximately $\mathcal{O}(0.1\%)$ of hyperon production events also contain neutron scatters, an acceptably small fraction.

4.2.3 Background Neutrino Interactions

To include all remaining neutrino interaction processes, unfiltered samples of MC simulation events are used. Any events in this sample containing hyperons or neutron scatters are assigned weights of zero to prevent double counting.

4.2.4 Out-of-cryostat (Dirt) Samples

For the sake of computational efficiency, and as these are the neutrino interaction most likely to be detected, all of the MC simulation samples described thus far only contain interaction vertices inside the MicroBooNE cryostat. It is also possible for an interaction occurring in the surrounding matter to launch particles into the cryostat. This possibility is accounted for through the creation of out-of-cryostat, or “dirt”, samples. These are manufactured by simulating the neutrino beam, with a much larger flux window, through a model of the entire detector building, alongside some of the surrounding dirt and air. The products of the resulting neutrino interactions are passed over to the GEANT 4 simulation, which propagates them. Any events in which particles enter the cryostat are selected.

4.2.5 EXT Samples

These consist of data collected with the EXT trigger when the beam was switched off, explained in Section 3.2.3, in order to model the impact of cosmic rays mistaken for neutrino interactions. Separate samples of data collected during runs 1 and 3 are used, normalised to the respective POT values from data collected during those periods that will be analysed¹.

¹While this is real data, these events alongside those already described will be collectively referred to as “simulation”. The term “data” will only ever describe data recorded when the beam was active.

The EXT samples are normalised by comparing the number of EXT triggers used to produce them to the number of hardware triggers describing the data, yielding an equivalent POT:

$$\text{EXT POT} = \text{Data POT} \times \frac{\text{EXT Triggers}}{\text{Data Triggers}}. \quad (4.13)$$

4.3 Preselection

The event selection begins with cuts to ensure the basic elements required by later stages of the selection are present.

4.3.1 Reconstructed Vertex Location and the Fiducial Volume

The collection of data is triggered whenever a sufficient quantity of light is recorded by the PMTs within the beamgate window, and a portion of the data will not contain neutrino interactions. This source of background is greatly reduced by the reconstruction algorithms, which indicate whether a probable neutrino vertex is present in an event. The first stage of the event selection is to demand the event contains a reconstructed neutrino vertex, and that this vertex is located within the fiducial volume employed by Ref. [123]. This fiducial volume consists of a set of trapezoidal volumes, shaped to exclude the regions with the most severe SCE. Additionally, the dead region, $z \in [675 \text{ cm}, 775 \text{ cm}]$, is excluded due to a high quantity of dead channels. The location of the reconstructed vertex may be affected by the SCE, and a correction factor, described in Ref. [123] is first applied. This cut reduces the EXT and Dirt backgrounds by approximately 95%, with an estimated acceptance rate of 70% for true neutrino interactions inside the FV, and 83% for the signal.

4.3.2 Three Track Requirement

The minimal final state the signal produces comprises an anti-muon, proton, and π^- , all of which produce track-like signatures. Figure 4.4a shows the number of tracks in the neutrino hierarchy in all simulation events surviving the FV cut, compared with the signal in Figure 4.4b. By cutting events with fewer than three reconstructed tracks, a large fraction of the background may be removed. Moreover, three reconstructed tracks are the mandatory input for later steps of the event selection, including the kinematic quantities in Section 4.6, and island finding algorithm described in Section 4.7.

The three track requirement removes a large quantity of background but at a considerable cost in efficiency, indeed this cut is the largest loss of efficiency across the selection. The cause of this has been investigated and the efficiency of reconstruction of the V signature produced by the Λ decay into a pair of tracks is less than ideal. Some of the failure modes include the reconstruction of only one of the decay products, and the reconstruction of the entire decay V as a shower. Example of these can be seen in Figure 4.5. The underlying reason is thought

to be the unusual topology the signal produces, and the lack of any dedicated algorithm in Pandora to identify secondary vertices. Attempted solutions to this problem include modifying the hit record to remove the muon track, leaving only the decay V , a signature similar to that of common neutrino interactions such as CCQE, or generating an external vertex at the start of any tracks displaced away from the primary vertex and treating this as a new neutrino vertex. The development of specialised reconstruction methods is something under consideration for future generations of this analysis in MicroBooNE, but this is beyond the scope of this thesis.

Labelling Scheme

Figure 4.4 introduces a system for separating events into categories that will be used throughout the remainder of this chapter, as well as in many of the data-simulation comparisons displayed in Appendix F. This labelling method is as follows: “Signal” describes the CCQE-like Λ production signal defined in Section 4.1.5, “Other HYP” are events from other CCQE-like hyperon production processes, “Other ν ” is any other variety of neutrino interaction inside the cryostat, “Dirt” are neutrino interactions occurring outside of the cryostat, and “EXT” are events collected with the EXT trigger described in Section 3.2.3. A second labelling scheme will be introduced at the start of the next chapter to describe the specific sources of background that pass the selection in greater detail.

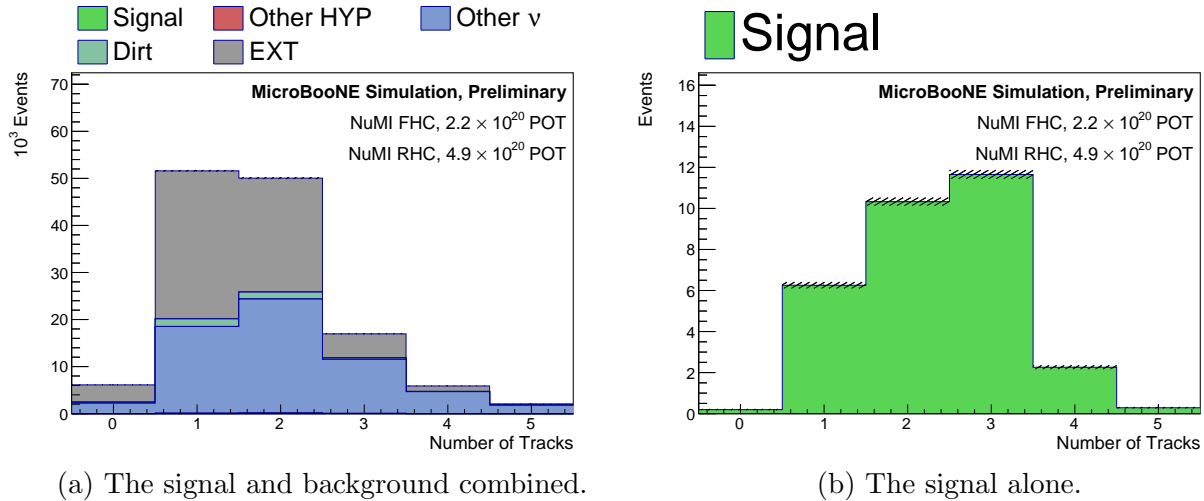
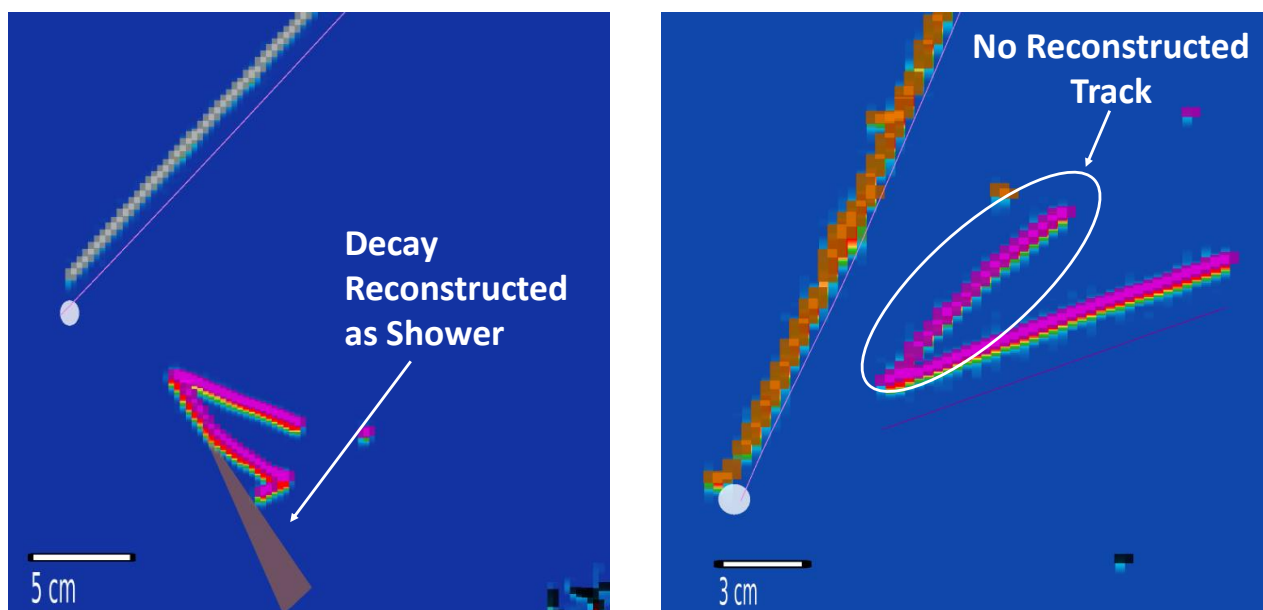


Figure 4.4: The number of reconstructed tracks associated with the reconstructed neutrino vertex, after application of the fiducial volume cut. The hatched regions on the bins indicate the statistical uncertainties. Note that the y axis of panel (a) is 10^3 events.



(a) Reconstruction of both decay products into a single shower.

(b) One of the particles produced in the Λ baryon's decay lacks a reconstructed track.

Figure 4.5: Two examples of mis-reconstruction of the Λ baryon decay vertex. This decreases the efficiency of the preselection significantly.

4.3.3 Zero Shower Requirement

Figures 4.6a and 4.6b respectively show the number of reconstructed showers in the neutrino hierarchy for all events surviving the FV cut, and for the signal alone. A source of background in this analysis comes from Σ^0 baryons, which decay to $\Lambda + \gamma$ before propagating any measurable distance in the detector. This produces a similar signature to the signal, with the addition of a shower resulting from the photon. The application of the no-shower requirement reduces the magnitude of this background by a factor of 3. The zero shower requirement is also found to reduce the sources of background from RES and DIS type interactions considerably, as these often produce large numbers of densely clustered tracks due to the higher hadron multiplicity of these interactions, often reconstructed as showers². The acceptance rates of the hyperon induced backgrounds are tabulated, cut by cut, in Tables 4.6, 4.7, and 4.8.

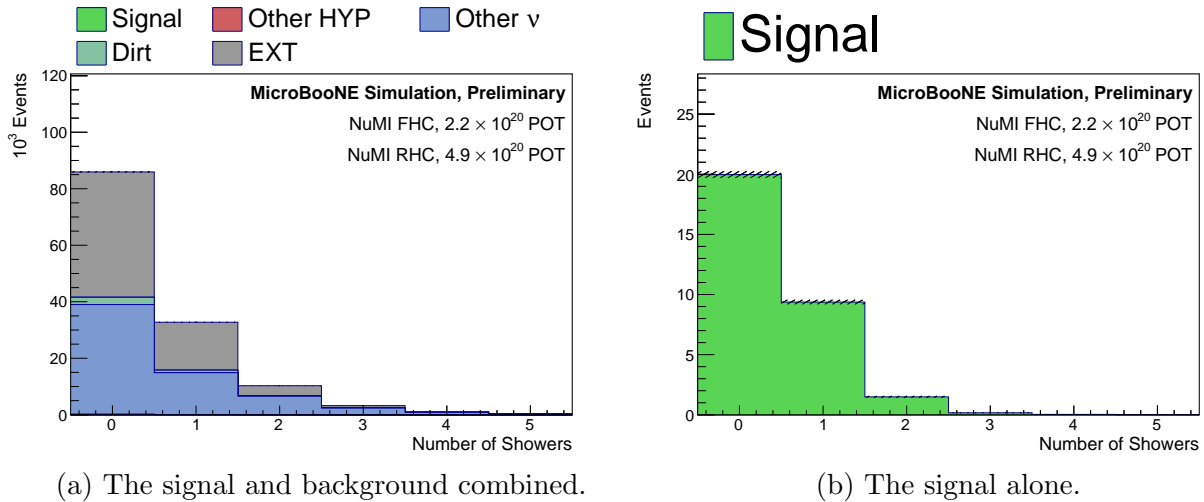
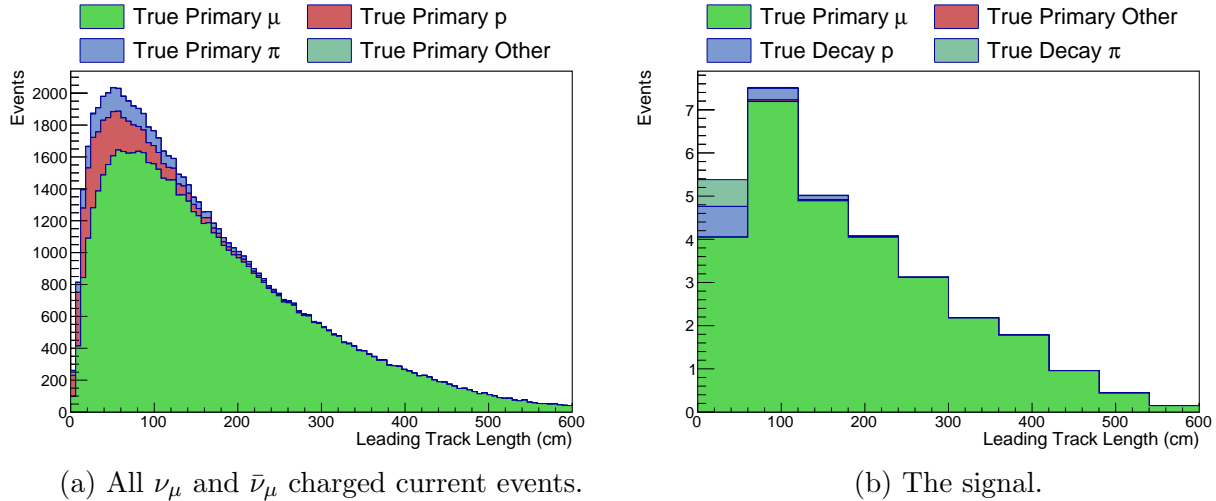


Figure 4.6: The number of reconstructed Showers associated with the reconstructed neutrino vertex, after application of the fiducial volume cut. The hatched regions on the bins indicate statistical uncertainties. Note that the y axis of panel (a) is 10^3 events.

4.4 Muon Identification

After events containing three or more tracks have been identified by the preselection, muon, proton and pion labels must be assigned to those tracks, starting with the muon. The algorithm for selection the muon track is simplistic: the longest track calorimetrically consistent with a MIP that satisfies quality requirements, outlined below, will be used. The process for analysing the calorimetry and quality requirements are described below.

²Large systematic uncertainties are applied to these sources of background regardless.

(a) All ν_μ and $\bar{\nu}_\mu$ charged current events.

(b) The signal.

Figure 4.7: The length of the longest reconstructed track in the event, with which particle creating it indicated. “True Primary X” refers to a particle of type X produced in the initial neutrino interaction.

4.4.1 Reasoning

Section 3.2.5 mentions that charged pions are difficult to distinguish from muons through calorimetry owing to their similar masses. Instead it is often assumed that if there are multiple MIP-like tracks produced in a neutrino interaction, one belongs to a muon, and the remainder must be charged pions. The kinematic budget in any neutrino interaction is shared between the muon and the hadronic system, the latter of which may be further subdivided between multiple hadrons, as well as the nuclear remnant. As a result, the muon often carries a larger quantity of kinetic energy than any individual particle in the hadronic system, enabling it to travel further through the detector. This assumption is supported by Figure 4.7a, which shows the identity of the longest track in events containing CC $\nu_\mu/\bar{\nu}_\mu$ interactions. Likewise, when the signal is considered separately in Figure 4.7b, the anti-muon is the longest track. As an additional check, Appendix F compares data to MC simulation for several variables related to the lengths and directions of the longest tracks, and indicates these quantities are well modelled.

4.4.2 The Log-likelihood Ratio PID

Figure 4.7 indicates that for some neutrino interactions, the leading track may be a proton from the primary vertex, or in the case of the signal, a proton from the decay vertex. Protons may be distinguished from charged pions and muons through analysis of the calorimetric information associated with their tracks.

Particle identification (PID) scores refer to variables that quantify the level of similarity

of a feature, in this case a track, to a certain kind of particle. The event selection employs two particle identification scores, both calculated from the dE/dx behaviour of tracks: the Log-likelihood Ratio PID score (LLR PID), described in detail in Ref. [145], and the mean dE/dx of the track, which will be explained in Section 4.5.2. A brief description of the LLR PID score is provided here.

The track is split into segments, separately for each wire plane, and for each segment the following is recorded: the value of dE/dx along that segment, the angle between the track and the direction of the wires in that plane, θ , and the distance that segment lies from the end of the track, r . These values are compared with a pair of reference tables, one from simulated protons, and another produced with simulated muons, which give the expected behaviours of dE/dx as a function of θ and r . The likelihoods of obtaining the dE/dx values along the track under each of these hypotheses are calculated, for each plane, $\mathcal{L}_i(p|dE/dx, r, \theta)$, and $\mathcal{L}_i(\mu|dE/dx, r, \theta)$, for plane $i = 0, 1, 2$. The overall likelihood under each of these hypotheses is given by the product of the likelihoods from the individual planes:

$$\mathcal{L}(p|dE/dx, r, \theta) = \prod_i \mathcal{L}_i(p|dE/dx, r, \theta). \quad (4.14)$$

To compare the likelihoods under the two hypotheses the log of their ratio is taken:

$$\text{LLR PID} = \frac{2}{\pi} \arctan \left(\ln \frac{\mathcal{L}(\mu|dE/dx, r, \theta)}{\mathcal{L}(p|dE/dx, r, \theta)} \right). \quad (4.15)$$

The arctangent function and factor of $\frac{2}{\pi}$ are applied to transform the resulting scores onto the domain $\{-1, 1\}$. The resulting scores for muons, protons, charged pions, charged kaons, and other tracks produced in neutrino interactions are drawn in Figure 4.8. Muons produce scores around 1, while protons typically score zero or less. By demanding the track scores above a certain value, chosen in the next section, the muon identification algorithm can reduce the risk of mistakenly selecting a proton.

4.4.3 Quality Cuts

Later stages of the event selection, most notably the island finding algorithm, employ the start of the muon track to identify activity in the detector associated with the primary vertex. Poor reconstruction of the start of the muon track, especially if this track started several centimetres from the primary vertex, or on the wrong side of an unresponsive wire, has a detrimental effect on the performance of these algorithms. To prevent this, the muon identification algorithm only considers tracks that begin within 1 cm of the reconstructed primary vertex. The muon track is also required to be a minimum of 10 cm in length, to ensure a sufficient quantity of calorimetric information is available. The effect of track length on PID scores will be discussed in Section 4.5.2.

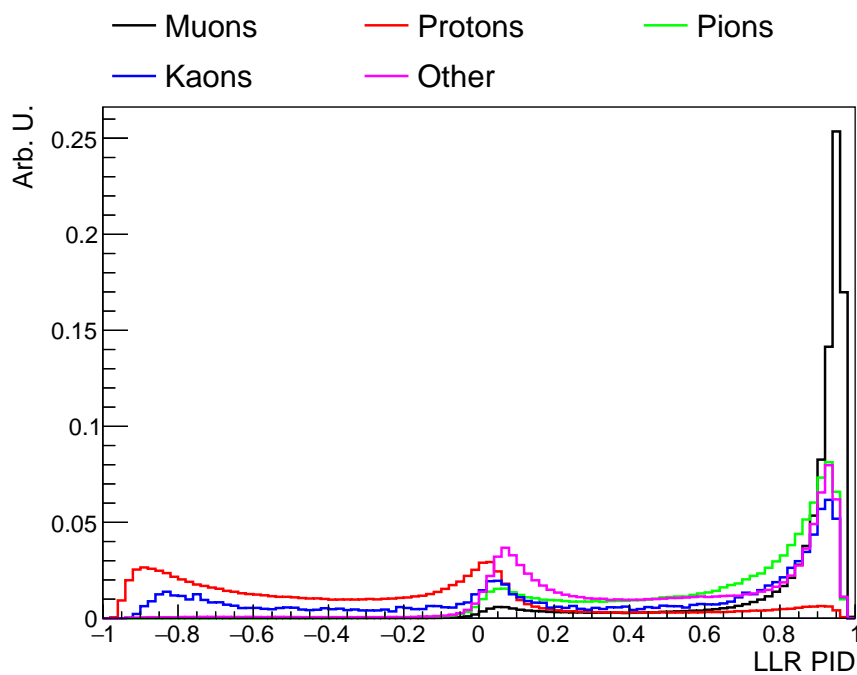


Figure 4.8: The log likelihood PID score calculated for the most common varieties of charged particles produced in neutrino interactions. No selection cuts are applied. All five distributions are normalised to 1.

4.4.4 Optimisation

To decide upon a suitable value for the LLR PID requirement, the muon ID is run repeatedly over events passing the preselection, with the minimum PID score set to different values. For a given setting, three metrics are calculated to quantify the performance of the muon ID algorithm:

$$\text{Signal Accuracy} = \frac{\text{Signal events in which the } \mu \text{ candidate is a true } \mu}{\text{Signal events with a reconstructed true } \mu \text{ track}}, \quad (4.16)$$

$$\text{Accuracy} = \frac{\text{Events in which the } \mu \text{ candidate is a true } \mu}{\text{All events with a reconstructed true } \mu \text{ track}}, \quad (4.17)$$

$$\text{Purity} = \frac{\text{Events in which the } \mu \text{ candidate is a true } \mu}{\text{Events with a } \mu \text{ candidate}}. \quad (4.18)$$

These metrics are plotted as a function of the minimum value of the LLR PID set for the muon candidate in Figure 4.9. The choice of these metrics is motivated by several factors: ensuring the muon track is chosen over one of the decay products in the case of the signal, providing a track anchored to the primary vertex for the island finding later on, and rejecting background not containing muons, such as neutral current interactions. The two accuracy scores are found to be relatively stable with respect to the choice of the PID score requirement unless a very high value is used, at which point the algorithm will fail by rejecting many true muons. The purity slightly improves as the PID requirement is increased. A value of 0.6 is chosen as the minimum PID requirement for the muon, the highest value at which the two accuracy metrics remain stable.

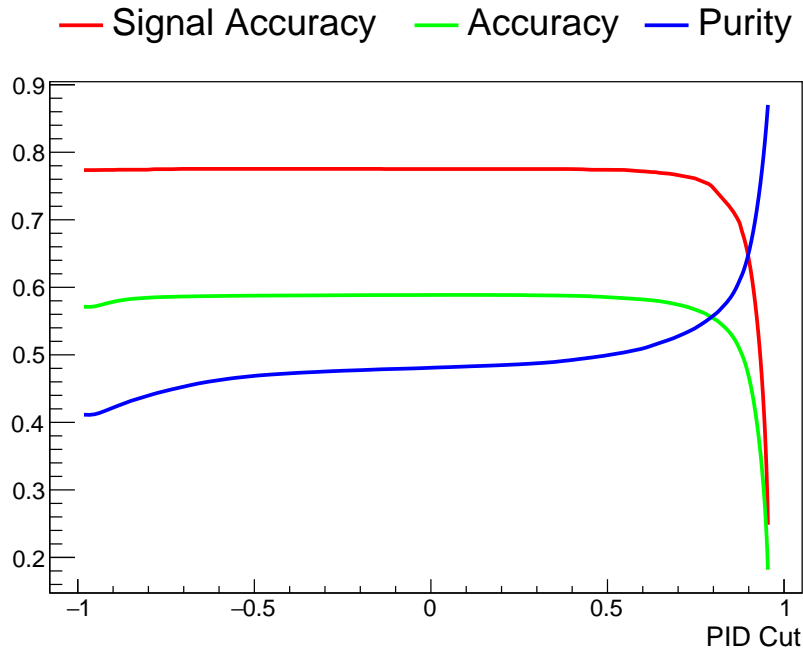


Figure 4.9: The performance metrics of the muon ID defined in equations 4.16, 4.17 and 4.18, when different values of the PID score cut are applied. The selection positions this cut at 0.6.

4.5 Selection of the Proton and Pion Tracks

To complete the picture of the signal, the selection must identify the proton and π^- produced in the Λ baryon's decay. This is more challenging than identifying the muon: there may be many other tracks attached to the primary vertex, and the secondary vertex will not be detected if one of these is mistaken for one of the Λ baryon's decay products. Furthermore, the proton and pion labels must be assigned in the correct order: the kinematic quantities computed in Section 4.6 are obtained through estimation of the momenta of the proton and pion from the lengths of their respective tracks. Separate estimators are employed for protons and pions, giving different values of momenta depending on how the labels are assigned. Techniques from multivariate analysis are employed to select these tracks.

4.5.1 Useful Variables

Several non-kinematic variables may indicate the consistency of a given pair of tracks with a Λ baryon decay: PID scores, introduced in the previous section, the proximity of the starting points of the two tracks, and the value of the Pandora track/shower separation score, first

described in Section 3.5.2. In total, seven variables are leveraged, all of which are drawn in Figure 4.10:

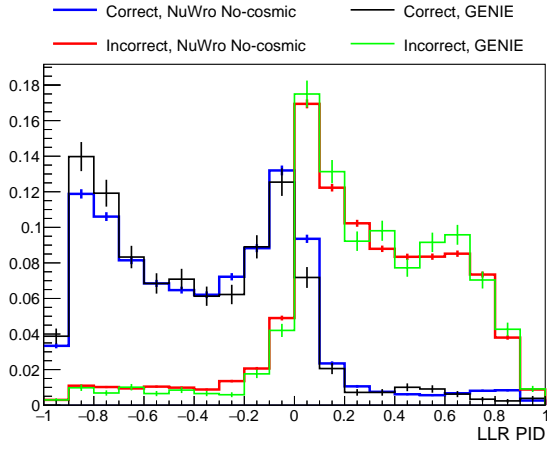
1. The separation between the starting positions of the proton/pion tracks. Both tracks should originate from a common vertex and therefore start close together.
2. The Pandora track/shower classification score of the proton track. Figures 4.10e and 4.10f show this has some power to identify the correct track combinations.
3. The Pandora track/shower classification score of the pion track.
4. The average dE/dx along the proton track, averaged across all three planes, explained in Section 4.5.2; a new PID score designed for stable performance on short tracks.
5. The average dE/dx along the pion track.
6. The LLR PID score of the proton track, previously used in the muon identification algorithm.
7. The LLR PID score of the pion track.

To tune this element of the selection, a sample of pure signal events, without cosmic ray background, were generated with NuWro³ and any events failing the preselection or muon selection were removed. For every combination of tracks (excluding the muon candidate), the seven input variables are calculated, and this information is placed into one of two datasets. These datasets are labelled as “Correct, NuWro No-cosmic” and “Incorrect, NuWro No-cosmic” in Figure 4.10, and describe the input variables when the tracks correspond to a true proton and pion produced by a decaying Λ baryon, versus any other possible combination of tracks respectively. To check these events, manufactured with a different neutrino event generator and without cosmic ray background, are still representative of the other MC simulation samples of the signal used in the other sections of this thesis, the distributions of these variables are also drawn with the default simulation samples generated with GENIE. Good agreement is found between these two samples of events. The distributions of the LLR PID, three plane mean dE/dx , and track/shower classification score are compared with data in Appendix F.

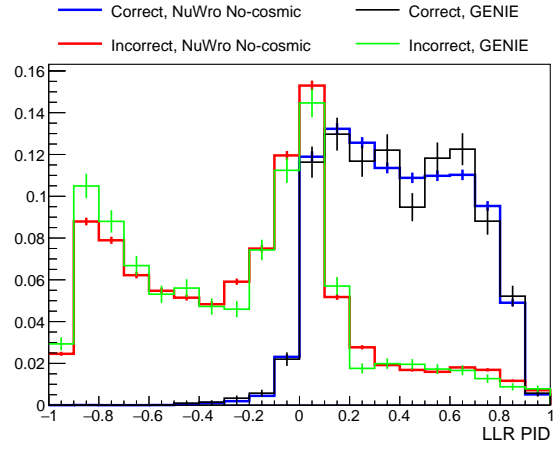
4.5.2 The Three Plane Mean dE/dx

Figure 4.11 shows the lengths of the reconstructed tracks truth matching to the proton and pion produced by the decaying Λ baryon. These tracks, especially that of the proton, are

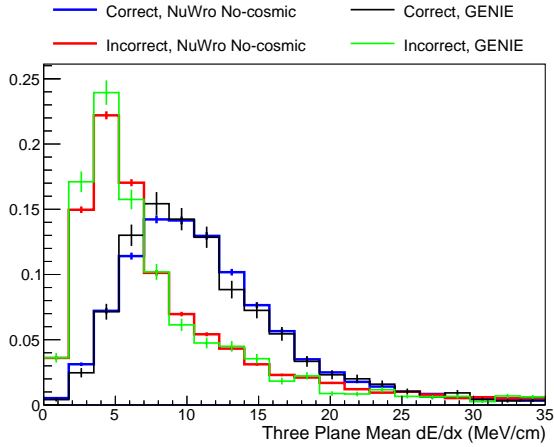
³CCQE-like hyperon production events are computationally cheaper to manufacture using NuWro as the event generator. Non including cosmic rays further reduces the computational expense, enabling the production of a larger sample of events.



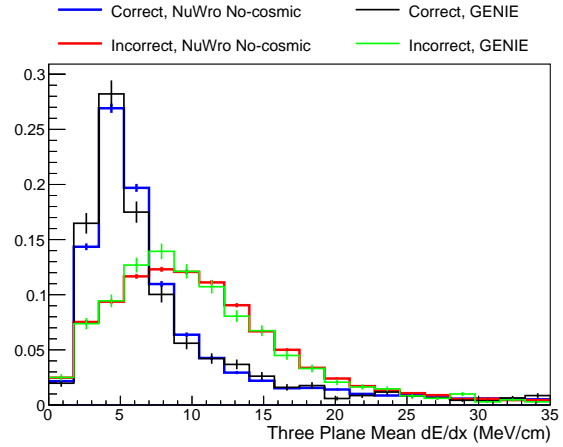
(a) Proton LLR PID.



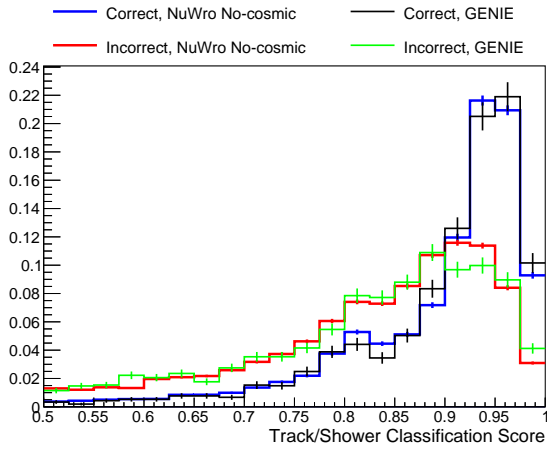
(b) Pion LLR PID.



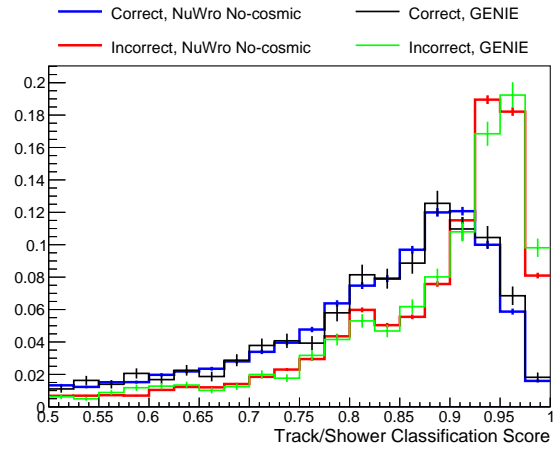
(c) Proton three plane mean dE/dx .



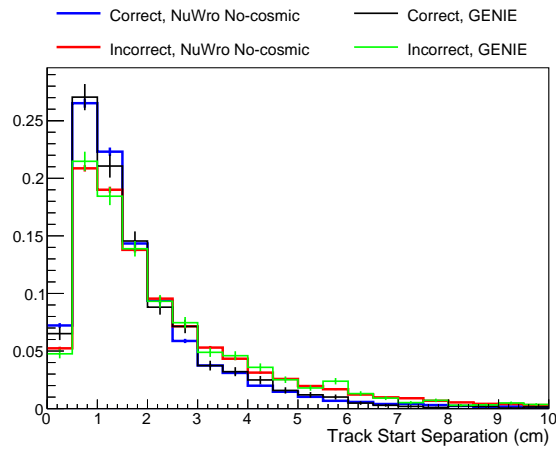
(d) Pion three plane mean dE/dx .



(e) Proton track/shower score.



(f) Pion track/shower score.



(g) Proton/pion track start separation.

Figure 4.10: The input variables leveraged to select the tracks belonging to the Λ baryon’s decay products. Events from two samples were used to produce these distributions: a pure set of Λ baryon production events, simulated with NuWro with no cosmic ray background, and the overlaid GENIE simulation events used in the rest of this thesis. The distributions labelled “correct” describe the values of the input variables when the tracks chosen correspond to a true proton and pion from the Λ baryon decay, while the distributions labelled “incorrect”, describe all of the other combinations. The vertical lines in the centres of the bins indicate statistical uncertainties.

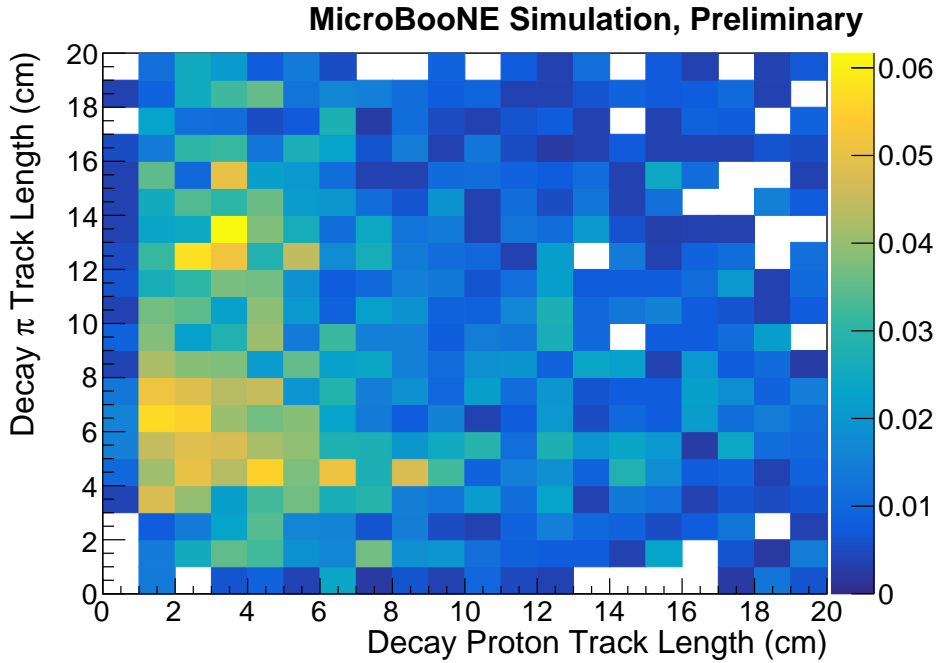


Figure 4.11: The lengths of the reconstructed tracks produced by the proton and π^- resulting from the Λ baryon's decay. The proton track is often shorter than 5 cm.

often relatively short. The more sophisticated varieties of particle identification scores such as the LLR PID may not behave in a consistent manner with such short tracks: Figures 4.12a and 4.12b show the LLR PID score for all reconstructed tracks, and all reconstructed tracks shorter than 5 cm respectively, indicating the distributions shift towards zero as the track lengths decrease.

In response to this, a new quantity to distinguish between protons and charged pions was introduced: the three plane mean dE/dx value, intended to produce more stable results with respect to track length. The mean dE/dx from a single plane is calculated with:

$$\left\langle \frac{dE}{dx} \right\rangle_i = \frac{\sum_s \left(\frac{dE}{dx} \right)_{is} x_{is}}{\sum_s x_{is}}, \quad (4.19)$$

where $i = 0, 1, 2$ indicates the wire plane, $\left(\frac{dE}{dx} \right)_{is}$ is the dE/dx recorded in the s th segment of the track in plane i , and x_{is} is the length of the s th segment of the track in plane i ⁴. The three plane score is a weighted average of the single plane scores. The following weights are used to ignore the information from wires nearly parallel to the track, when the dE/dx

⁴The splitting of the track into segments is performed separately for each plane. The number of segments is approximately equal to the number of wires the track deposits energy on.

information is known to be less reliable:

$$w_i = \begin{cases} 1 & \text{if } \sin \theta_{\text{wire}} \geq 0.05 \\ 0 & \text{if } \sin \theta_{\text{wire}} < 0.05 \end{cases}, \quad (4.20)$$

where θ_{wire} is the angle between the initial direction of the track and the wires in plane i . The three plane mean dE/dx value is given by:

$$\left\langle \frac{dE}{dx} \right\rangle_{\text{Three Plane}} = \frac{\sum_i \left\langle \frac{dE}{dx} \right\rangle_i w_i}{\sum_i w_i}. \quad (4.21)$$

In Figure 4.12, the distributions of the LLR PID and the three plane mean dE/dx are shown for all reconstructed tracks, and tracks shorter than 5 cm. The distribution of LLR PID scores changes shape drastically, and while there is some change in the distribution of the mean dE/dx value, with the exception of protons, the peaks of the distributions remain in the same location.

4.5.3 Boosted Decision Trees

To extract the maximum amount of performance from the input variables, techniques from multivariate analysis are employed. The Toolkit for Multivariate Analysis [146] (TMVA) from Root provides several suitable algorithms, designed to solve binary classification problems, with utilities to train them before testing their performance as part of the event selection. These algorithms include the Linear (Fisher) Discriminant, Boosted Decision Trees, and Multilayer Perception.

Response Scores and Binary Classification

In abstract terms, the binary classification problem is the attempted separation of a mixture of unlabelled data from category A and category B , into pure datasets of A and B . Each element of this data is described by several variables, which binary classifiers use to determine its level of similarity to either A or B . The classifiers in the TMVA package try to accomplish this by calculating a response score for each data element, which is a (complicated) function of the variables describing it. The user then assumes the data elements with response scores on one side of a cut belong to A , and the data on the other side belong to B . The LLR PID is an example of a response score, in which category A are muons, and category B are protons. The classifier is “trained” using a separate dataset in which the elements belonging to A and B are known. The parameters that affect how the classifier manipulates and combines the input data for each member into a response score can then be chosen to optimise its performance at sorting this data into A and B .

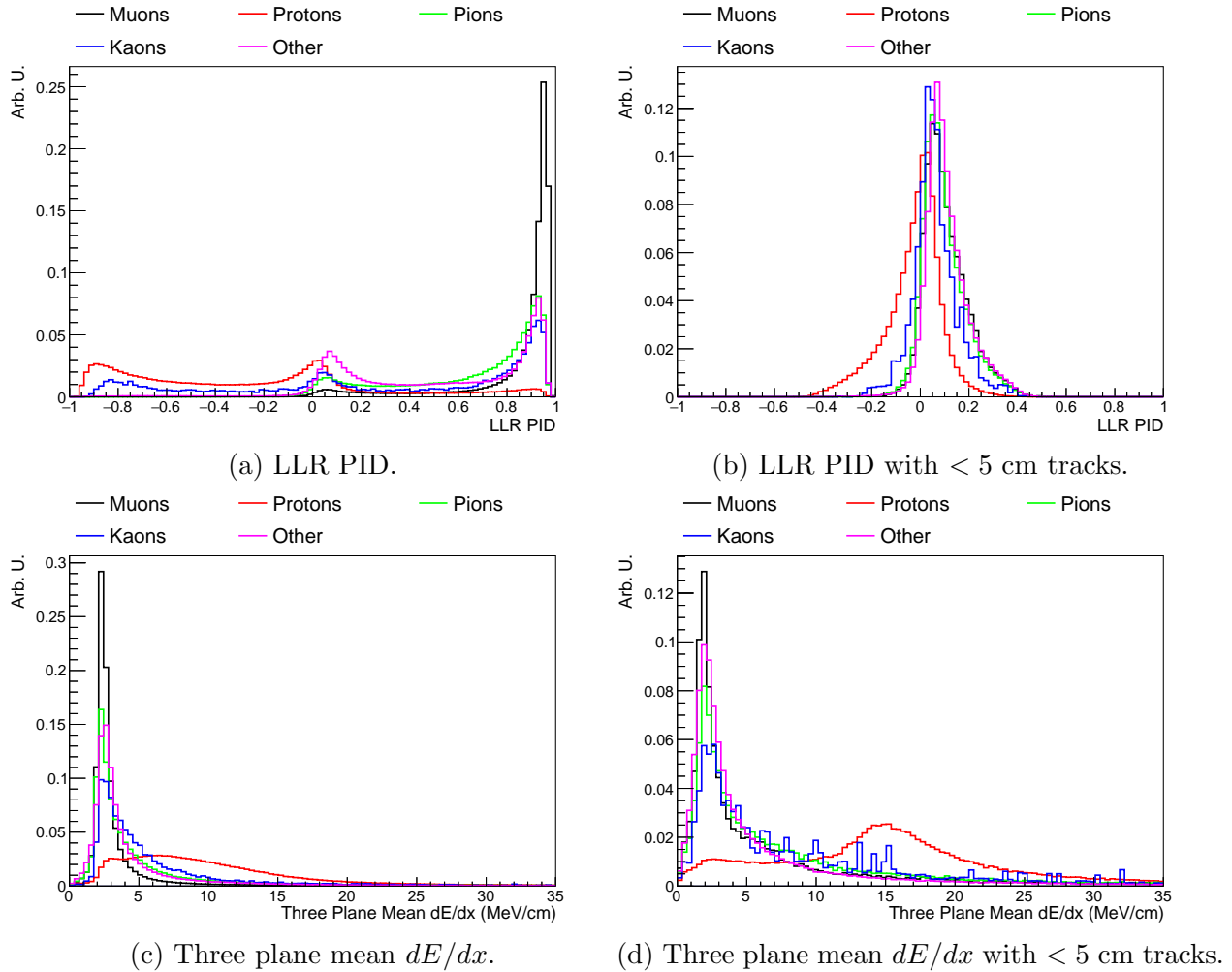


Figure 4.12: The two particle identification score employed to select a pair of tracks consistent with a proton and π^- , demonstrating the change in behaviour of the LLR PID when applied to very short tracks.

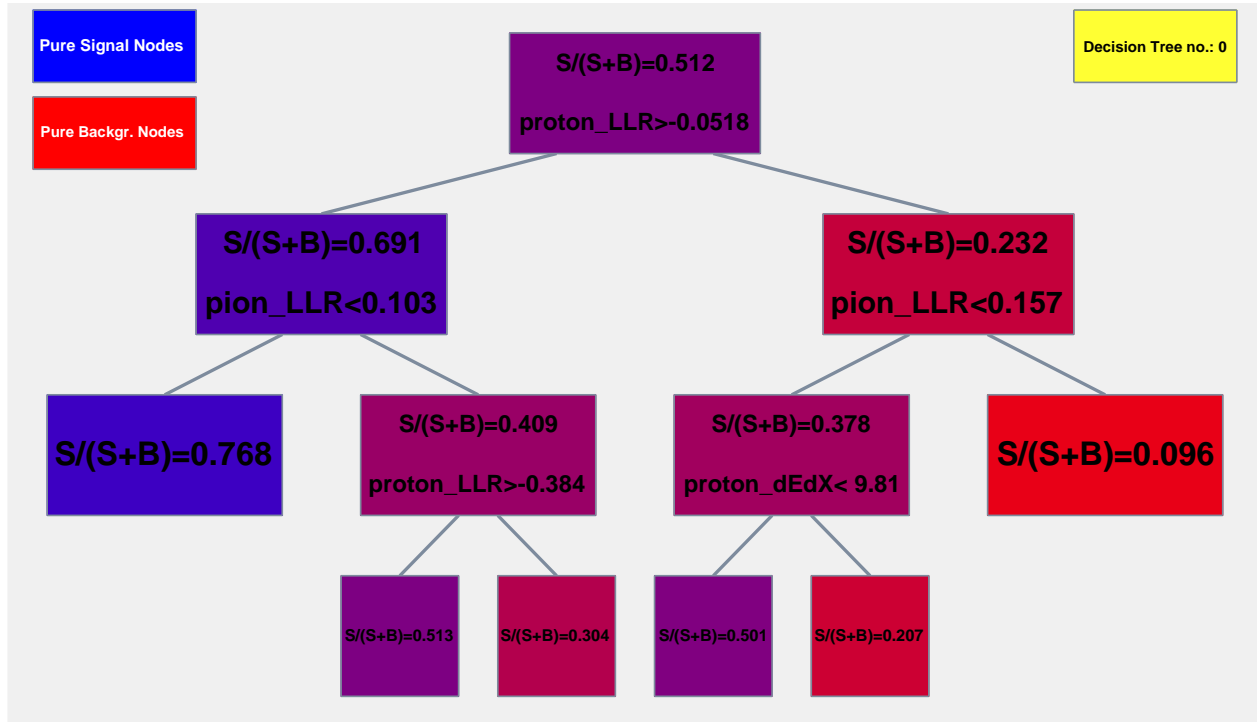


Figure 4.13: One of the decision trees used to select the proton and π^- tracks. The input variables to this tree are the proton and pion LLR PID scores, labelled as `proton_LLR` and `pion_LLR` in the figure.

Another Way to Use Response Scores

In the decay product selection, the response score is instead used to rank the different track combinations. For every possible pair of tracks, and permutation of the proton and pion labels, the response score is calculated, with the combination giving the highest response score selected. In the case of this thesis, the binary classifier is a random forest of boosted decision trees. This employs a large array of small decision trees, an example of which is shown in Figure 4.13, into which the input variables are fed. Each tree returns a weight depending on the leaf of the decision tree reached, which are added to produce a response score.

All of the possible combinations of tracks in every event in the NuWro no-cosmic data are prepared, and the first half of this data is used to optimise the BDTs, while the second half is used to check for overtraining. These two data sets are labelled as “Train” and “Test” in Figure 4.14, and are further subdivided into “Correct” and “Incorrect” as before. Figure 4.14 compares the distributions of response scores from the testing and training data sets, alongside the standard GENIE MC simulation samples studied in the rest of this thesis, all of which are statistically independent. The distributions produced by these three samples

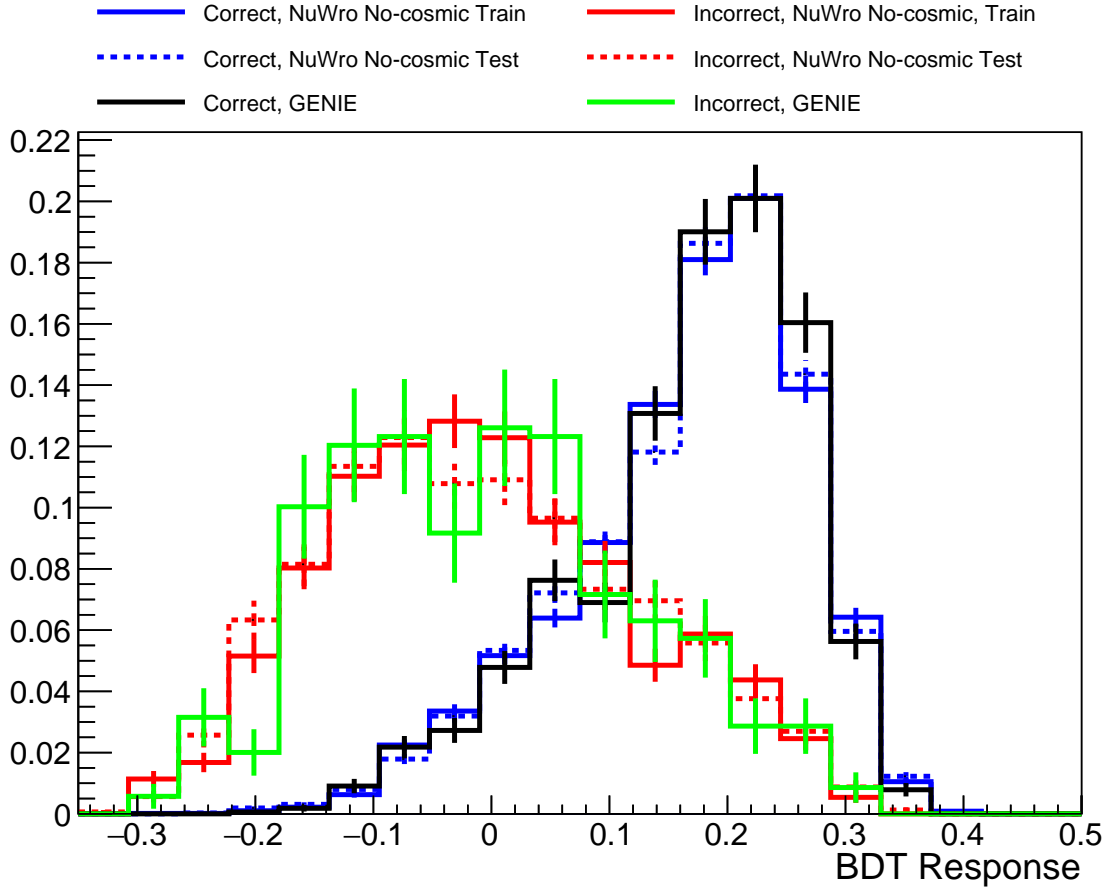


Figure 4.14: The BDT response scores of the events in the training data, split into the half used to train the BDTs (solid lines) and half used as a validation sample used by the training code (dashed lines), alongside the GENIE events used to evaluate the efficiency of the event selection.

are consistent with one another, indicating no significant overtraining has taken place. The response scores from simulation are also compared with data in Figure F.10 of Appendix F.

Input Variable Cuts

The boosted decision trees themselves only indicate which pair of tracks are the most consistent with a proton and a π^- . Another way to utilise the information in the input variables is to reject any events containing no suitable pairs of tracks. This is accomplished by applying cuts to the input variables in a similar manner to the quality cuts in the muon ID. Only combinations of tracks which satisfy the following are considered:

- The two tracks must start within 3 cm of one another.

- The proton track must have an LLR PID score < 0.1 .
- The pion track must have an LLR PID score > -0.1 .

4.5.4 Performance

The TMVA supports a smörgåsbord of binary classification algorithms, all of which produce response scores. The effectiveness of different algorithms may be compared by computing the Receiver Operating Characteristic (ROC) for each algorithm: this is performed by first calculating the response score, r , for every element of the testing data. A cut, C , is placed on the response scores and the following pair of metrics are calculated:

$$\text{Efficiency} = \frac{\text{Members of pop. } A \text{ with } r > C}{\text{All members of pop. } A}, \quad (4.22)$$

$$\text{Background Rejection} = 1 - \frac{\text{Members of pop. } B \text{ with } r > C}{\text{All members of pop. } B}. \quad (4.23)$$

The position of this cut is varied, and a graph of the efficiency versus background rejection is drawn. Figure 4.15 shows these graphs for six of the algorithms available from the TMVA. The metric indicating the overall performance is the integral of this curve, the values of which are listed in Table 4.2, with higher values indicating a more effective algorithm. The BDT offers the best performance according to this metric.

Combining this component of the event selection with the previous steps, it is possible to compute the rates at which the muon, proton, and pion are misidentified as one another. Figure 4.16 shows a confusion matrix for these three particles, with a fourth category indicating any tracks selected not belonging to the muon, proton or pion. The events used were produced with the default GENIE simulation of the signal, with a filter applied to only include events in which the proton, pion, and muon were successfully reconstructed. The confusion matrix indicates that, in the overwhelming majority of these events, the correct tracks are identified.

4.6 Kinematic Variables

It is now possible to test the consistency of the kinematics of the proton and pion with the hypothesis of a Λ baryon decay. The Λ baryon has a mass of 1115.683 ± 0.006 MeV [22], and the conservation of four momentum fixes the kinematics of its decay products⁵. Furthermore, if it is assumed the Λ baryon does not undergo an undetected scatter before decaying, the

⁵Some three body decays of the Λ have been detected, such as $\Lambda \rightarrow p + \pi^- + \gamma$, but their branching fractions are very small.

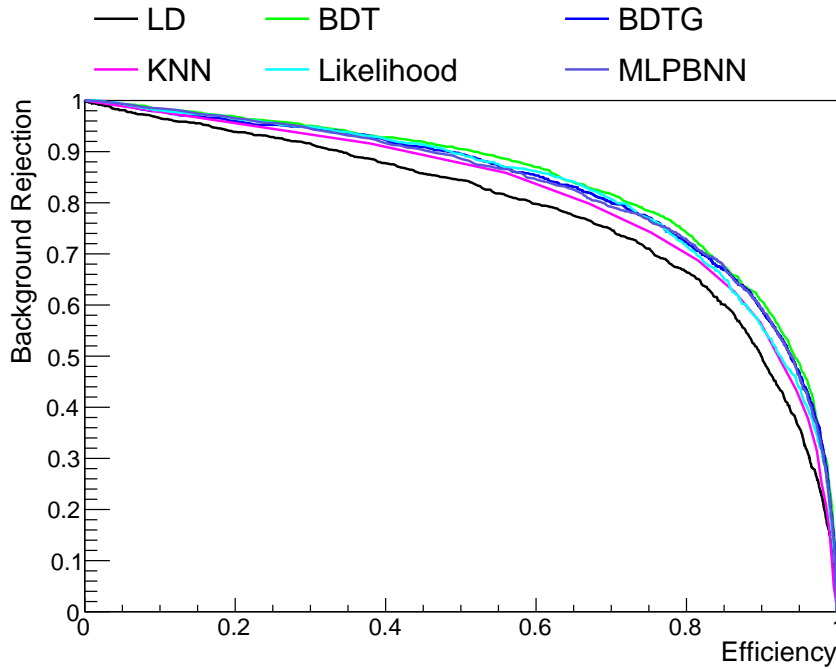


Figure 4.15: Receiver Operating Characteristic (ROC) curves for the six algorithms from the TMVA tested. The efficiency and background rejection are calculated using equations 4.22 and 4.23. The integrals of these curves indicate the performance of the selection algorithms. The algorithms tested are the Linear Discriminant (LD), Boosted Decision Trees (BDT), Gradient Boosted Decision Trees (BDTG), k -Nearest Neighbour (KNN), construction of empirical Likelihood functions (Likelihood), and Multilayer Perception (MLPBNN).

Algorithm	Integrated ROC Curve
LD	0.785
BDT	0.842
BDTG	0.832
KNN	0.815
Likelihood	0.827
MLPBNN	0.831

Table 4.2: Integrals of the ROC curve produced by different algorithms tested. The BDT produces the largest integrated ROC curve, indicating the best performance.

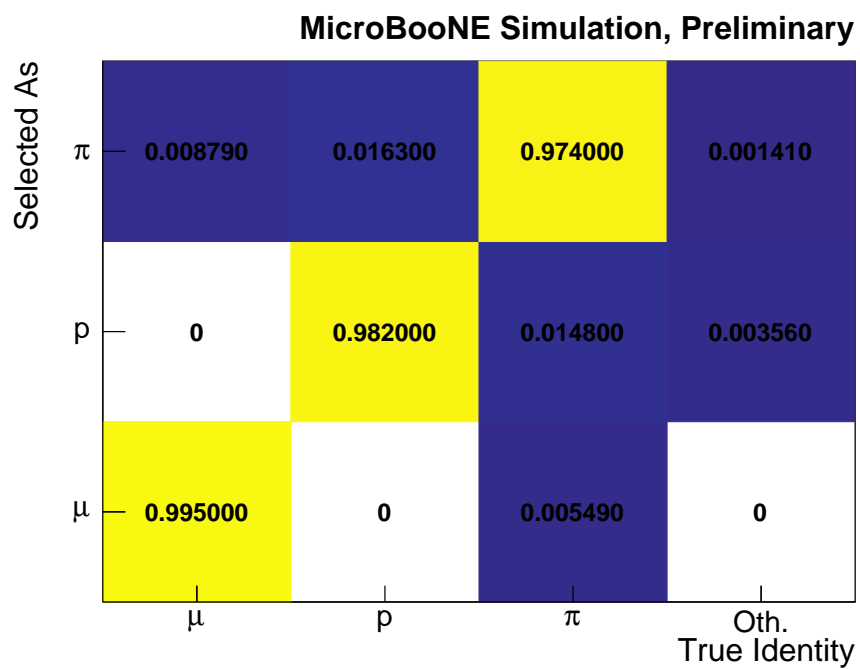


Figure 4.16: Confusion matrix indicating the number of signal events in which the track truth matching the anti-muon is selected as the muon track, decay proton track, decay pion track, or not used (“other”), and similar for the other particles in the signal topology. Only events in which all three particles were reconstructed are considered.

sum of the three momenta of the decay products can indicate the direction of the Λ baryon, which may be compared with other geometric information from the event. These observations inspire two variables leveraged by the event selection: the reconstructed invariant mass of the proton and pion, discussed in Section 4.6.2, and the “Angular Deviation”, introduced in Section 4.6.3.

4.6.1 Proton and Pion Momentum Estimation

The momenta of the proton and pion are estimated from the lengths of their respective tracks. The estimated momentum of the proton is given the formulae:

$$E_p = 29.9R_p^{0.586}, \quad (4.24)$$

$$p_p = \sqrt{E_p^2 + 2M_pE_p}, \quad (4.25)$$

acquired by fitting to data from [147], where R_p is the length of the proton’s track, $M_p = 0.9383$ GeV is the mass of the proton, and p_p is the magnitude of the three momentum of the proton. For charged pions:

$$p_\pi = (15.0 + 0.00435R_\pi - 14.7R_\pi^{-0.117}), \quad (4.26)$$

where R_π is the length of the pion track. This is the result of a fit to the ranges and momenta of simulated charged pions in the MicroBooNE cryostat. The directions of the proton and pion are taken to be the directions of the first segments of their tracks.

Range-based estimators of particle kinematic are susceptible to bias if the particle in question exits the detector, as is often the case with the muon. Since the proton and pion often do not travel very far in the detector, it is assumed that this bias is not significant. 93% of Λ baryon decays are fully contained by the TPC in MC simulation events, suggesting the containment assumption is acceptable.

Two additional sources of bias must be acknowledged: secondary interactions, and unwanted inclusion of activity created by another particle in the clusters the track is fitted to. Secondary interactions both transfer some energy from the particle to a nucleus or other particles, but will also change the direction of the particle, and the reconstructed track may stop at this point, leading to underestimation of its momenta. The estimators of particle momenta are all generated through performing fits using the track lengths and momenta of simulated particles, and secondary interactions are included in this simulation. Systematic uncertainties are also applied to the cross sections for secondary interactions of protons, charged pions, and Λ baryons, with argon nuclei, described in Section 5.6.

Figure 4.17 compares the true momentum of protons and charged pions to their reconstructed momentum obtained with Equations 4.25 and 4.26, indicating good consistency between the true and reconstructed momenta. The estimation of the momenta for pions is

somewhat worse than that of protons, though this is expected as a larger fraction of pions will exit the detector, owing to their minimum ionising property.

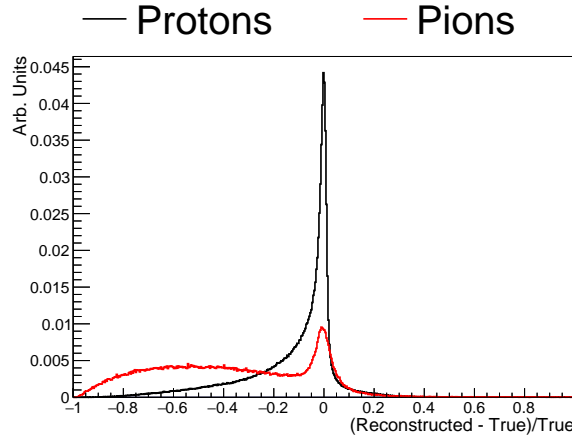
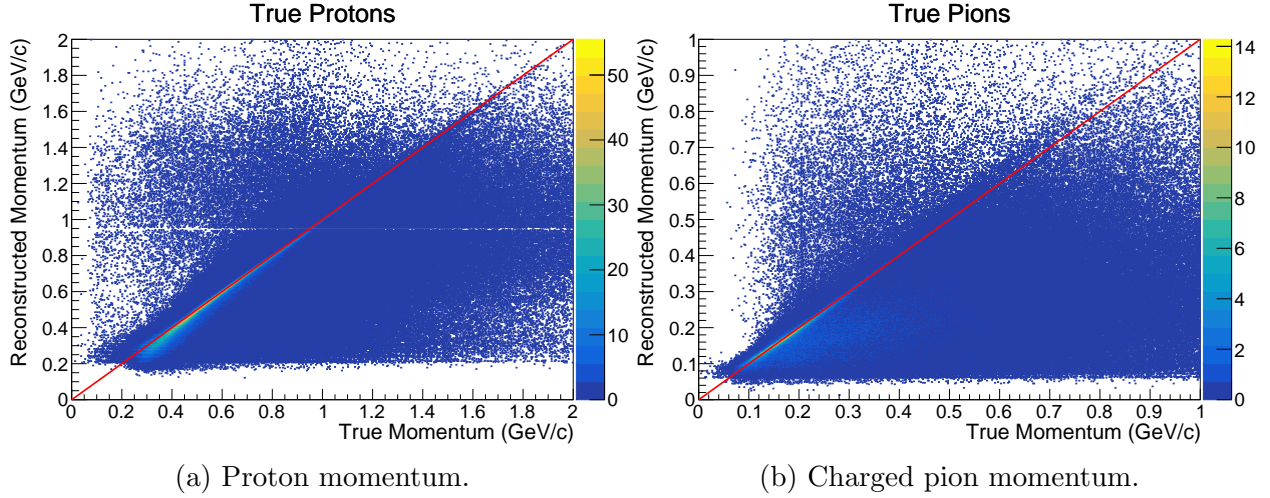


Figure 4.17: The performance of the estimators of proton and charged pion momenta. The red lines in panels indicate when true = reconstructed.

4.6.2 Reconstructed Invariant Mass

The decay products of the Λ baryon will always have a combined invariant mass of 1.115 GeV, which can be compared to the four momenta of the proton and pion calculated from their directions and momenta. The reconstructed invariant mass, W , is given by:

$$W = \sqrt{M_p^2 + M_\pi^2 + 2E_p E_\pi - 2p_p p_\pi \cos \theta}, \quad (4.27)$$

in any frame of reference. $E_p = \sqrt{M_p^2 + p_p^2}$, $E_\pi = \sqrt{M_\pi^2 + p_\pi^2}$, and θ is the opening angle between the proton and pion. Figure 4.18 shows the reconstructed invariant masses of MC simulation events that have passed the preselection and been assigned muon, proton, and pion candidates, calculated using Equation 4.27. The proton/pion tracks from signal events yield reconstructed invariant masses close to the true mass of the Λ baryon, while other processes producing proton/pion pairs (or particles mistaken for proton pion pairs) are not subjected to the same kinematic constraint, and therefore give reconstructed invariant masses distributed over a much wider range of values. The background is then reduced by placing cuts on this variable: any events with $W < 1.09$ GeV or $W > 1.14$ GeV.

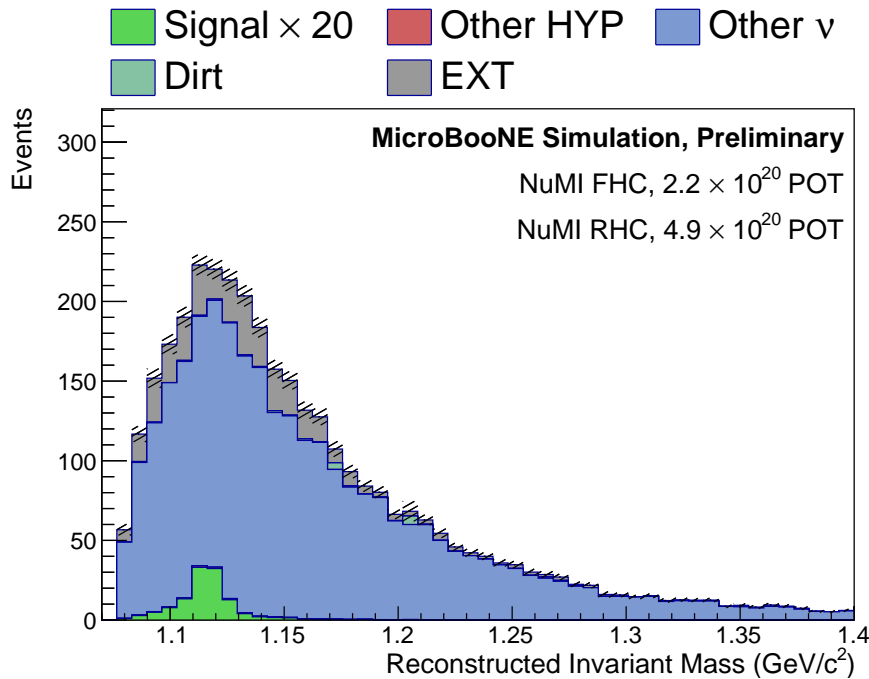


Figure 4.18: The distributions of the reconstructed invariant mass of the signal and background. The signal strength has been multiplied by 20 for visibility.

4.6.3 Angular Deviation

The Λ baryon carries no electric charge and does not ionise the argon, and will travel along a straight line from the neutrino interaction vertex to the point at which it decays, unless it undergoes a hard scattering process. The line joining the primary vertex to the decay vertex will therefore be parallel to the momentum vector of the Λ baryon. This observation inspires a second kinematic variable utilised by the event selection: the “angular deviation”, the calculation of which is illustrated in Figure 4.19. The angular deviation is defined to be the angle between the momentum vector of the Λ baryon, the sum of the momenta of

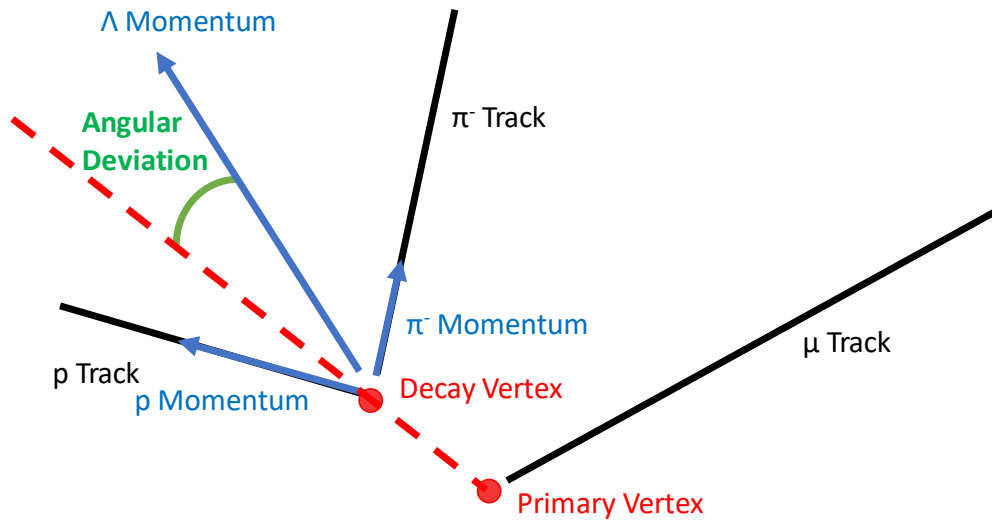


Figure 4.19: Calculation of the angular deviation.

the proton and pion, and the line joining the reconstructed primary vertex to the decay vertex. The location of the decay vertex is determined through a fitting procedure outlined in Appendix C. The distributions of the angular deviation variable, calculated for the signal and the background from MC simulation, are shown in Figure 4.20. As expected, signal events yield values close to zero, while the background is spread across a wide range of angles. The event selection rejects any events with angular deviations larger than 14° .

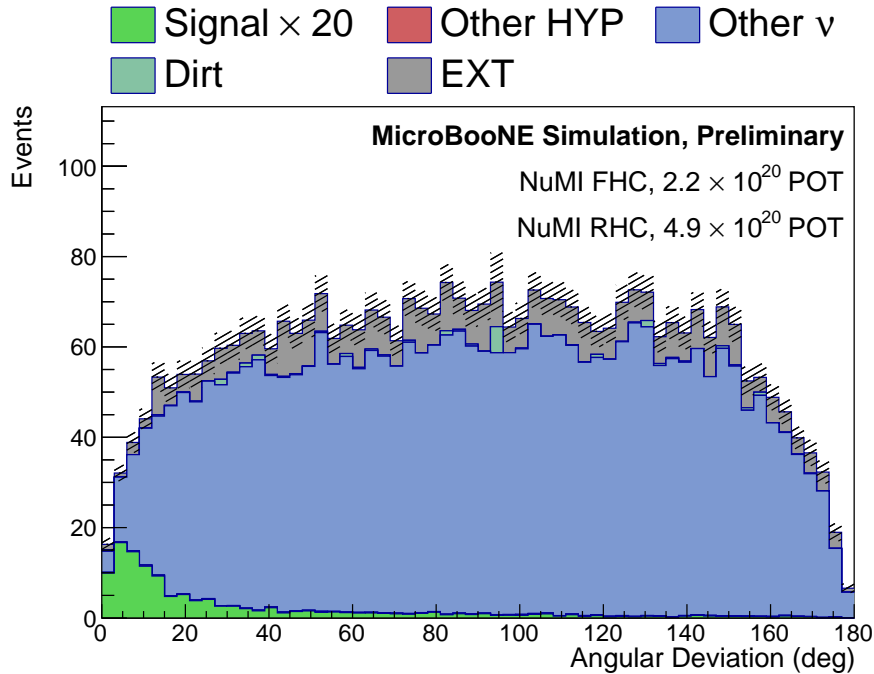


Figure 4.20: Distributions of the angular deviation for the signal and background. The signal strength has been multiplied by 20 for visibility.

4.7 Island Finding

The feature that distinguishes Λ baryon production from all but a few specific sources of background is that the Λ baryon will travel a short distance before decaying, without creating a trail of ionisation. The resulting signature is a displaced secondary vertex formed by the proton and pion, illustrated in Figure 4.23. This contrasts with the situation expected from background events, in which the proton and pion tracks correspond to two particles also created at the primary vertex. This section describes how the event selection exploits this feature to reject background events.

4.7.1 Reconstructed Decay Length

The most straightforward, but as it will turn out, not the most powerful, way to exploit the displaced vertex is calculate the distance between the reconstructed primary vertex and the decay vertex generated in Section 4.6.3. The resulting distance is denoted as the Reconstructed Decay Length, the distributions of which are compared in Figure 4.22. Intuitively, one would expect the majority of background events to possess reconstructed decay lengths of 3 mm (the resolution of the MicroBooNE detector) or less. Figure 4.22

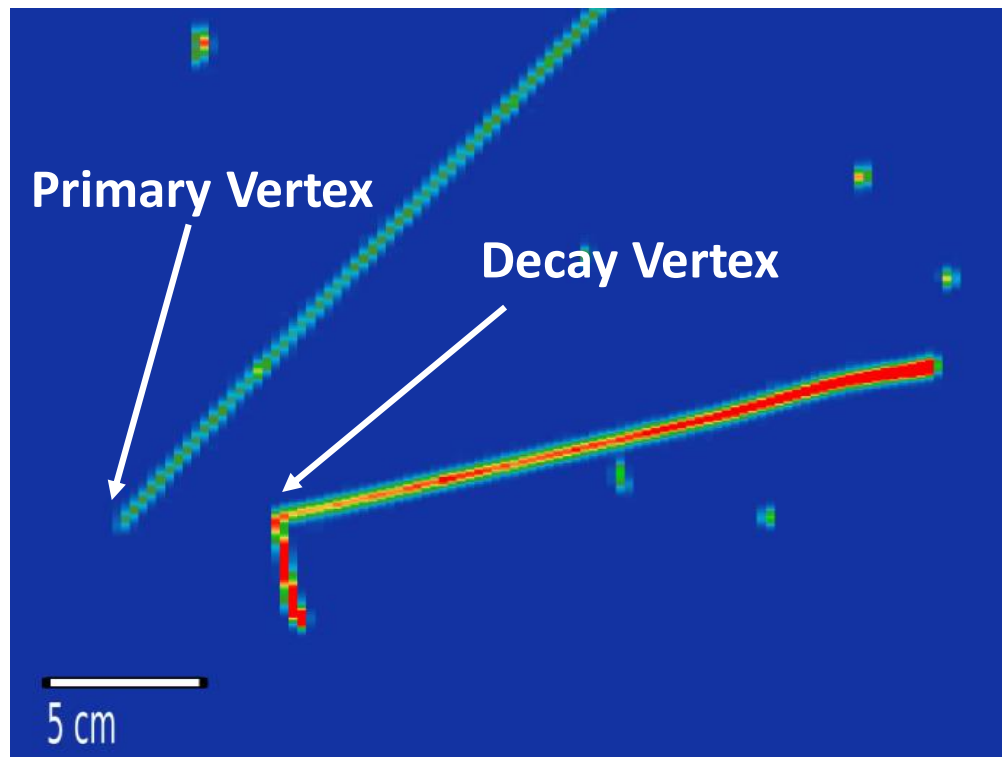


Figure 4.21: Event display of a $\mu + \Lambda$. The separation between the primary vertex and decay vertex distinguishes Λ production from most sources of background.

indicates this is not correct, the reconstructed decay lengths of many background events are larger than this, diminishing the background rejection power of this variable.

It was concluded the poor performance of the reconstructed decay length is due to the difficulty of placing the starting positions of tracks, near the primary vertex, with high precision. There can be some ambiguity as to which hits belong to which track, and some reconstructed tracks can start several centimetres from the primary vertex as a result, leading to the impression of a displaced vertex if only the reconstructed track objects are considered. Figure 4.23 is an example of such an event. However, if the original record of the charge arriving at each wire as a function of time (the coloured boxes in event displays), is inspected visually, it becomes apparent that the tracks join at the primary vertex. This is the information analysed by the island finding algorithm.

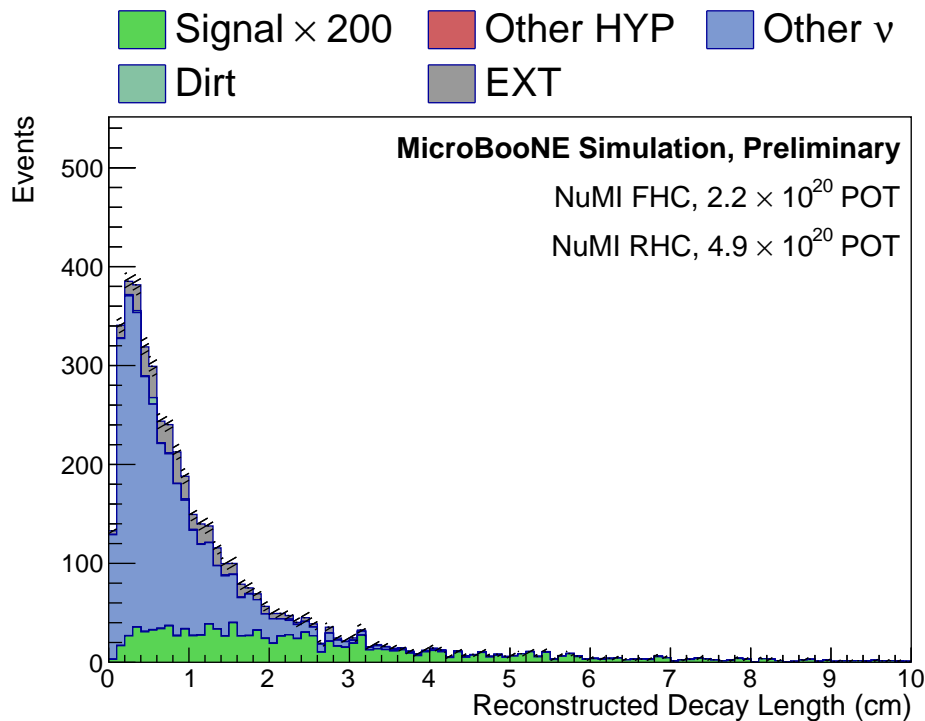


Figure 4.22: The reconstructed decay length of the signal and background, without applying the cuts to the kinematic variables. The signal strength has been multiplied by 200 for visibility.

4.7.2 Island Finding Algorithm

The event displays in this thesis show the activity recorded by the wires inside the MicroBooNE TPC, after application of deconvolution and noise removal algorithms. The bins

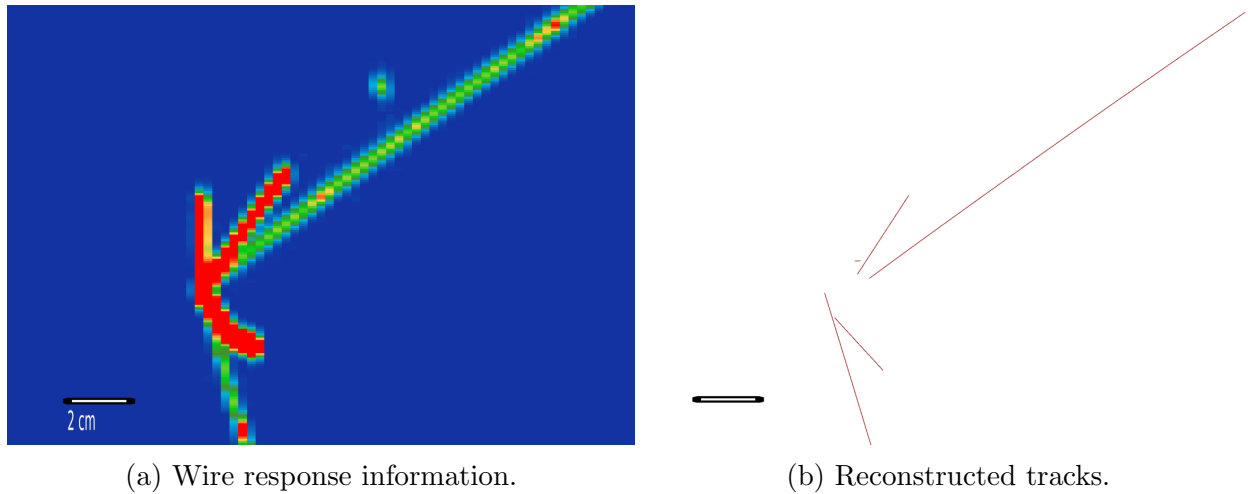


Figure 4.23: A background event that possesses a reconstructed decay length of 1.5 cm. Inspection of the track objects alone, shown in panel (b), suggests two pairs of particles located at separated vertices. Inspection of the wire activity in panel (a), does not support this.

along the x axis correspond to the different wires, and the y axis indicates time, discretised into 1 ns intervals, called “ticks”. The island finding algorithm analyses this information instead of the reconstructed tracks. Each plane is analysed separately, and the basic method for a single plane is as follows:

1. Convert the wire activity into a two dimensional histogram, in which the binning along the horizontal axis corresponds to the different wire channels, and the binning on the vertical axis is the discretised timing information (ticks). The height of each bin is the strength of the signal (ie. the number of electrons) recorded by a given wire at a given tick. This information, for the signal event from Figure 4.21, and the background event from Figure 4.23, are shown in Figure 4.24a and 4.25a.
2. The electrons liberated by a charged particle crossing the detector will spread out transversely and longitudinally, leading to a small amount of signal recorded at time ticks and on wires neighbouring a central peak, with an approximately Gaussian shape. To counteract this effect on the resolution, a filter is applied, emptying any bins recording activity below a preset threshold, and produces a list of all bins above the threshold. The surviving bins are drawn in Figures 4.24b, and 4.25b.
3. To identify bins belonging to a track, the starting positions the muon, proton, and pion tracks are used. The track is an object constructed in three dimensions, and described with Cartesian coordinates. The following relations transform Cartesian coordinates

to wire-time coordinates:

$$\text{Plane 0 Wire} = A_w(-y \sin 60 + z \cos 60) + C_0 \quad (4.28)$$

$$\text{Plane 1 Wire} = A_w(y \sin 60 + z \cos 60) + C_1 \quad (4.29)$$

$$\text{Plane 2 Wire} = A_z z + C_2 \quad (4.30)$$

$$\text{Time} = A_t x + C_t \quad (4.31)$$

where $A_w = 3.33/\text{cm}$, $C_0 = 338.1$, $C_1 = 2732.1$, $C_2 = 4799.1$, $A_t = 18.21/\text{cm}$, and $C_t = 818.4$. A_w is approximately the reciprocal of the spacing between the wires in MicroBooNE, and the other values were obtained through empirical fits to simulated, point-like energy depositions in the detector. As the wire activity is affected by the space charge effect, the starting positions of the tracks prior to correcting for the SCE are used. The starting positions, after transforming into wire/time coordinates, are used to find a “seed” bin for each track.

4. Using the bins that survive the filtering, a list of bins corresponding to each particle’s “island” is created, first by adding filled bins next to the seed bin, before recursively checking the bins neighbouring those, and so on, until no new bins can be added.
5. If two particles belong to the same island, the resulting lists of bins will be identical⁶. The results of this final stage are shown in Figures 4.24c and 4.25c.

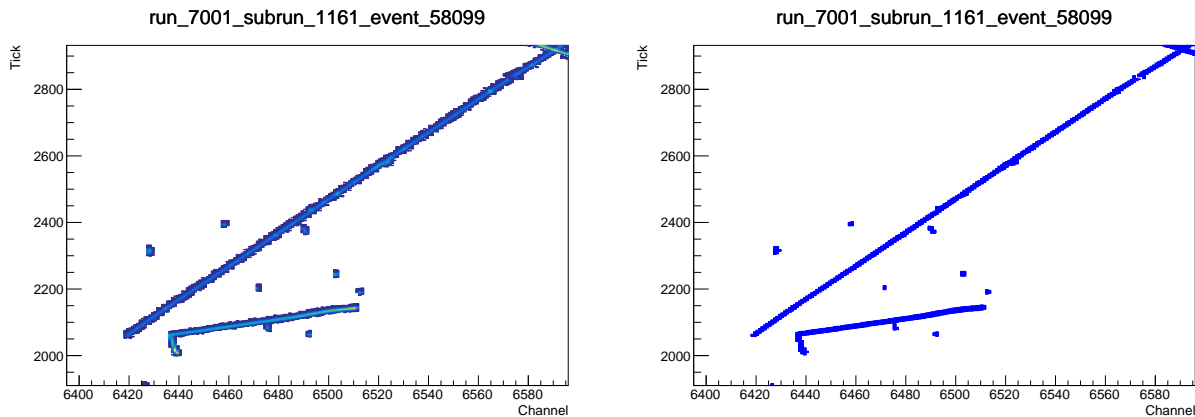
4.7.3 Selection Criteria

The algorithm reports a pass/fail result for each plane separately. A pass is reported, if the muon produces one island, and the proton and pion both belong to a second, separate island. Anything but this exact outcome, for example three islands, one for each particle, will reported as a fail. In addition to this requirement, both islands must have a minimum size of 50 bins. Lastly, the island finding algorithm is equipped with a list of unresponsive wires, and will automatically return a fail if one of the seed bins is separated from the others by an inactive wire, as this would disrupt the merging of islands.

How Many Planes?

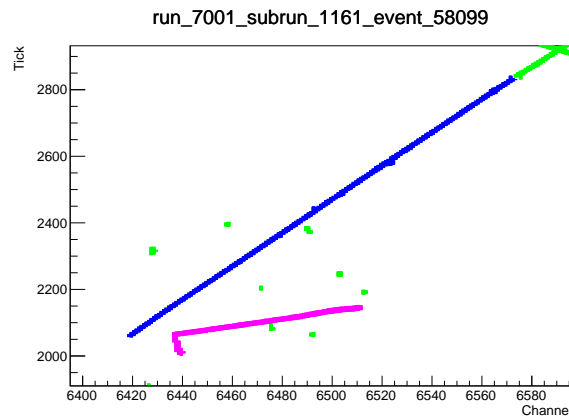
Thus far the discussion has only considered a single plane. A choice must be made regarding how many planes must be assigned a pass before selecting the event. Several performance metrics, when requiring a pass from one, two, or all three planes, are listed in Table 4.3. While a better purity is obtained when using the information from two or three planes, there is a considerable drop in efficiency. The metric optimised is the product of the efficiency and

⁶In practice, if the island for at least one of the particles has already been generated, it is computationally more efficient to check if the seed bins of any new particles already belong to it.



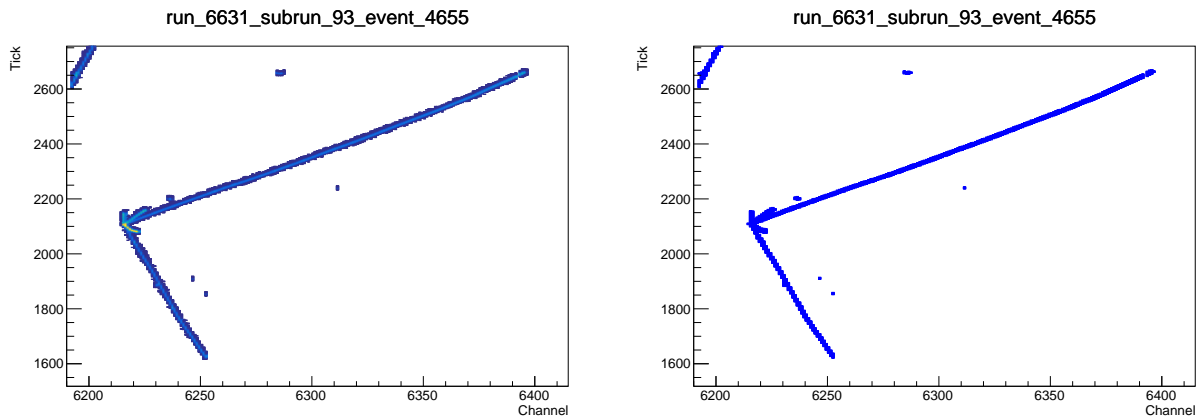
(a) Original wire response data.

(b) After filtering.



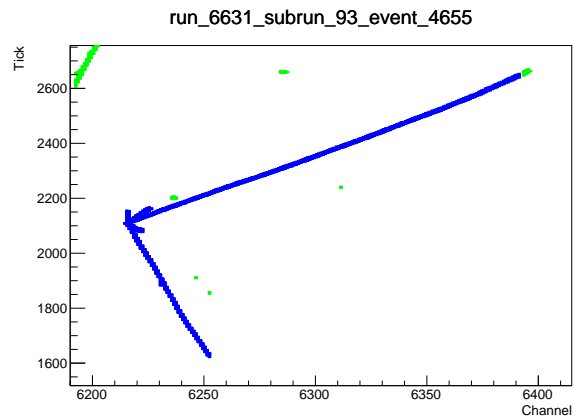
(c) After creating islands. The blue region is the island belonging to the muon. The proton and pion form a single island, coloured pink. The green regions correspond to activity not belonging to any island. This is an inactive wire located around channel 6580 which prevents growth of the muon island. The effect of unresponsive wires is addressed in Section 4.7.3.

Figure 4.24: Stages of the island finding algorithm, applied to the signal event in Figure 4.21.



(a) Original wire response data.

(b) After filtering.



(c) After creating islands.

Figure 4.25: Stages of the island finding algorithm, applied to the background event shown in Figure 4.23. In this event, the islands from the muon, proton, and pion candidates all overlap.

Planes	Efficiency	Purity	$E \times P$	$S/\sqrt{S+B}$
1	0.903	0.471	0.425	1.09
2	0.711	0.540	0.384	1.04
3	0.288	0.647	0.186	0.72
Decay Length Cut	0.747	0.247	0.184	0.712

Table 4.3: The performance of the island finding algorithm demanding a pass in 1, 2, or all three planes, indicating requiring a pass in a single plane gives the best results. The efficiency is fraction of events already passing the rest of the selection that also pass the island finding test. For purposes of comparison, the optimal $E \times P$ from applying a cut to the reconstructed decay length is included, with the values shown corresponding to a cut at 2.1 cm.

purity, indicating only a single passing plane should be required. This ability to analyse all three planes separately is one of the strengths of the island finding method. The optimal performance when applying a cut to the reconstructed decay length is also listed, which achieves both a lower purity and efficiency.

4.8 Summary

4.8.1 Performance

A brief overview of the selection algorithms is given in Table 4.4, in the order the cuts are applied. Table 4.5 lists the number of signal events predicted to survive each cut, with the resulting selection efficiencies, when simulating the signal with the GENIE and NuWro generators, along with the number of background events selected by the default GENIE simulation. These statistics are obtained applying the selection criteria sequentially. Prior to any event selection, the total background that must be removed is $\mathcal{O}(1 \text{ million})$ events, which is decreased to $\mathcal{O}(1)$ events by the end of the selection, a background suppression factor of $\sim 10^6$. The sources of background that remain are mostly irreducible, and will be described in Sections 4.8.2, 4.8.3, and 4.8.4.

In the predicted background rates and efficiencies in Tables 4.5- 4.8 the uncertainties are assumed to be approximately Gaussian. The uncertainties in the selected signal and background passing a given cut are calculated using Equation 4.12. When estimating the efficiency, the uncertainty in the total signal or background prior to applying any cuts, is taken to be zero.

As this is a measurement with a small number of selected MC simulation events, especially

for the background, the Gaussian approximation in the MC simulation statistics may not be appropriate. A more careful treatment using Bayesian statistics to account for the asymmetry in the uncertainties in the efficiency and predicted background is used in the final measurement, and will be explained in Section 5.10.

The numbers of events passing each cut, with the signal modelled using both GENIE and NuWro, are shown in Table 4.5, along with the selection efficiencies. The efficiencies calculated when modelling the signal using the two generators differ by approximately 2.5σ . Table 4.5 does not indicate any single cut is responsible. There are two possible reasons for this: a statistical fluctuation or model dependence (or a combination of the two), the latter hypothesis is investigated in Section 4.8.5. This effect is handled through additional systematic uncertainties. The results of applying the event selection to the neutrino mode and anti-neutrino mode MC simulations separately are tabulated in Appendix B.

Cut Name	Section	Description
Fiducial Volume	4.3.1	Reject events outside the FV used in [123], in the dead region ($675 \text{ cm} < z < 775 \text{ cm}$), or within 10 cm of TPC edges.
Three Tracks	4.3.2	Remove any events with fewer than three reconstructed tracks.
No Showers	4.3.3	Remove any events with reconstructed showers.
Muon ID	4.4	The muon candidate is the longest track satisfying the following criteria: LLR PID score > 0.6 , track length $> 10 \text{ cm}$, and starting within 1 cm of the primary vertex. Reject the event if no tracks satisfy these requirements.
Lambda ID	4.5	Select the pair of tracks with the highest BDT response score. Only consider combinations of tracks in which the proton candidate has LLR PID score < 0.1 , the pion candidate has LLR PID score > -0.1 , and the tracks start within 3 cm of one another. If no combination of tracks satisfy the above, reject the event.
Invariant Mass	4.6.2	Select events with $1.09 < \text{reconstructed invariant mass} < 1.14 \text{ GeV}$.
Angular Deviation	4.6.3	Select events with angular deviation $< 14^\circ$.
Island Finding	4.7	Select events passing the island finding test in at least on view.

Table 4.4: List of the selection cuts and algorithms, in the order they are applied.

Cut Name	GENIE Signal	NuWro Signal	GENIE Eff	NuWro Eff	GENIE BG
No Cuts	37.4 ± 0.4	35.2 ± 0.6	1 ± 0	1 ± 0	1863000 ± 1000
Fiducial Volume	31.0 ± 0.3	29.5 ± 0.6	0.829 ± 0.009	0.84 ± 0.02	133800 ± 200
Three Tracks	14.3 ± 0.2	13.1 ± 0.4	0.381 ± 0.006	0.373 ± 0.011	26020 ± 80
No Showers	11.8 ± 0.2	10.7 ± 0.4	0.314 ± 0.006	0.303 ± 0.010	15200 ± 70
Muon ID	9.17 ± 0.18	8.1 ± 0.3	0.245 ± 0.005	0.231 ± 0.009	9640 ± 60
Lambda ID	6.03 ± 0.15	5.2 ± 0.2	0.161 ± 0.004	0.148 ± 0.007	3410 ± 30
Invariant Mass	5.46 ± 0.15	4.7 ± 0.2	0.146 ± 0.004	0.135 ± 0.007	1375 ± 17
Angular Deviation	2.8 ± 0.1	2.21 ± 0.16	0.075 ± 0.003	0.063 ± 0.005	41 ± 3
Island Finding	2.5 ± 0.1	1.9 ± 0.15	0.068 ± 0.003	0.055 ± 0.004	2.8 ± 0.3

Table 4.5: The results of the various selection cuts. The uncertainties are statistical only, and calculated under a Gaussian approximation.

4.8.2 Response to Other Sources of Hyperons

A potential source of background is other events that produce hyperons in the final state, such as the CCQE-like Σ^0 production channel described in Chapter 2, the production of resonances that decay to Λ and Σ^0 baryons, and DIS hyperon production. To study the effect of the selection on these categories of events, three categories of “signal-like” background are defined by imposing the requirements on the Λ baryon’s decay products described in Section 4.1.5 to these other Λ baryons, and demanding the neutrino interaction occurred in the fiducial volume. In the case of events producing Σ^0 baryons, the decay conditions apply to the Λ resulting from the $\Sigma^0 \rightarrow \Lambda + \gamma$ decay. A small additional quantity of this background is due to Λ s that decay below MicroBooNE’s detection thresholds. Tables 4.6, 4.7, and 4.8, show the responses of the event selection to these sources of background. These tables show the acceptance rates for these sources of background are much lower than that of the signal, primarily due to the zero shower requirement. The total hyperon production background is 1.7 ± 0.2 events.

Direct Σ^0		
Cut	Events	Acc.
No Cuts	19.2 ± 0.3	1 ± 0
Fiducial Volume	15.9 ± 0.2	0.83 ± 0.01
Three Tracks	6.88 ± 0.15	0.358 ± 0.008
No Showers	2.36 ± 0.09	0.123 ± 0.005
Muon ID	1.67 ± 0.08	0.087 ± 0.004
Lambda ID	1.01 ± 0.06	0.053 ± 0.003
Invariant Mass	0.87 ± 0.05	0.045 ± 0.003
Angular Deviation	0.49 ± 0.04	0.026 ± 0.002
Island Finding	0.43 ± 0.04	0.0222 ± 0.0019

Table 4.6: Response of the selection to the “signal-like” Σ^0 background. This source of background is defined as Σ^0 baryons produced through the CCQE-like interaction described in Chapter 2, with the interaction inside the fiducial volume, and in which the Λ produced in the Σ^0 decay subsequently decays to a proton and π^- with momenta above MicroBooNE’s detection thresholds.

Resonant Hyperon		
No Cuts	Events	Acc.
None	40.7 ± 0.4	1 ± 0
Fiducial Volume	34.4 ± 0.4	0.844 ± 0.009
Three Tracks	22.7 ± 0.3	0.556 ± 0.007
No Showers	8.92 ± 0.18	0.219 ± 0.004
Muon ID	5.03 ± 0.13	0.123 ± 0.003
Lambda ID	2.04 ± 0.09	0.050 ± 0.002
Invariant Mass	1.20 ± 0.07	0.029 ± 0.002
Angular Deviation	0.63 ± 0.05	0.015 ± 0.001
Island Finding	0.44 ± 0.04	0.011 ± 0.001

Table 4.7: Response of the selection to the “signal-like” resonant hyperon production background. This source of background is defined as hyperons baryons produced through the RES interaction mode described in Section 1.5.2, with the interaction inside the fiducial volume, and in which the Λ produced subsequently decays to a proton and π^- with momenta above MicroBooNE’s detection thresholds.

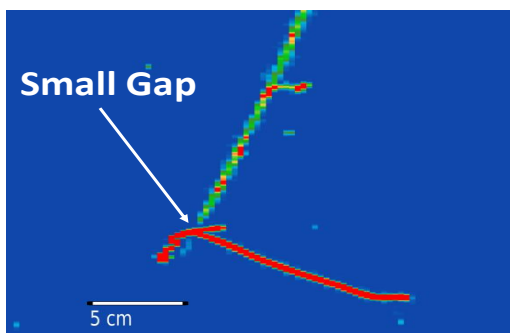
DIS Hyperon		
Cut	Events	Acc.
No Cuts	122.8 ± 0.7	1 ± 0
Fiducial Volume	103.5 ± 0.6	0.843 ± 0.005
Three Tracks	75.7 ± 0.6	0.617 ± 0.004
No Showers	15.8 ± 0.2	0.129 ± 0.002
Muon ID	9.3 ± 0.2	0.075 ± 0.002
Lambda ID	3.28 ± 0.11	0.0267 ± 0.0009
Invariant Mass	1.52 ± 0.07	0.0123 ± 0.0006
Angular Deviation	0.74 ± 0.05	0.0060 ± 0.0004
Island Finding	0.52 ± 0.04	0.0042 ± 0.0004

Table 4.8: Response of the selection to the “signal-like” DIS hyperon production background. This source of background is defined as hyperons baryons produced through the DIS interaction mode described in Section 1.5.3, with the interaction inside the fiducial volume, and in which the Λ produced subsequently decays to a proton and π^- with momenta above MicroBooNE’s detection thresholds.

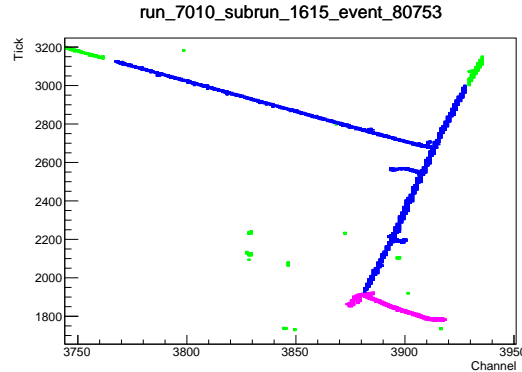
4.8.3 The Mis-reconstruction Background

A portion of the background MC simulation events selected are events containing problems with the reconstruction. Two examples of this background can be seen in Figures 4.26 and 4.27. In the first event, the muon deposits energy on a relatively small number of wires, and a small gap between the muon and the activity left by the other particles is created at the primary vertex, with the island finding algorithm misidentifying these other particles as a secondary vertex. Placing a restriction on the angle of the muon track relative to the x axis (the vertical direction in event displays) was tested when tuning the island finding method to target this failure mode. Ultimately the best performance for the entire selection was found when this cut was not included, and Figure 4.26 is only MC simulation event in which this failure occurred. The stringent quality requirements applied to the muon candidate in Section 4.4.3 help to prevent this type of failure.

The second example, Figure 4.27, is the result of activity from a cosmic ray muon being mistakenly included in the neutrino slice, alongside the true neutrino interaction. The cosmic



(a) Wire activity.



(b) With islands.

Figure 4.26: One of the MC simulation events selected because of reconstruction failure. In this event, the muon deposits energy on a small number of wires, and a gap appears in the wire activity at between the muon track and the other particles created in the primary interaction. The island finding algorithm mistook this for a secondary vertex.

ray muon was selected as the muon candidate, and then a pair of the tracks produced in the proximate neutrino scatter were selected as the Λ baryon decay. As with Figure 4.26, this is the only MC simulation event in which this specific failure mode was seen.

In total, there are only 9 MC simulation events of this type in the samples from both running modes. The computation of systematic uncertainties with so few events is problematic, and manufacturing enough MC simulation events to estimate the uncertainties through conventional methods is impractical. In the next chapter, two approaches will be explored to solve this problem: removing the background using visual scans of event displays, and employing data from a sideband to perform a constraint procedure. When scaled to the POT of the data to be analysed, this background is predicted to be 0.9 ± 0.4 events.

4.8.4 The Neutron Background

A source of non-hyperon induced background results from the secondary interactions of neutrons: when a neutron is produced in the primary neutrino-nucleus interaction, it may undergo a collision with another argon nucleus after travelling a few centimetres, knocking out several charged particles. This can also create the characteristic V shaped pair of tracks expected from a decaying Λ baryon, for example Figure 4.28. This source of background is reduced by the kinematic variable cuts, since the neutron-Ar scatter is not subject to the kinematic constraints that will apply to the decay of a Λ baryon, an effect illustrated by the distributions of reconstructed invariant mass and angular deviation for these events in Figure 4.29. The predicted magnitude of the neutron background in the event selection is 0.3 ± 0.1 events.

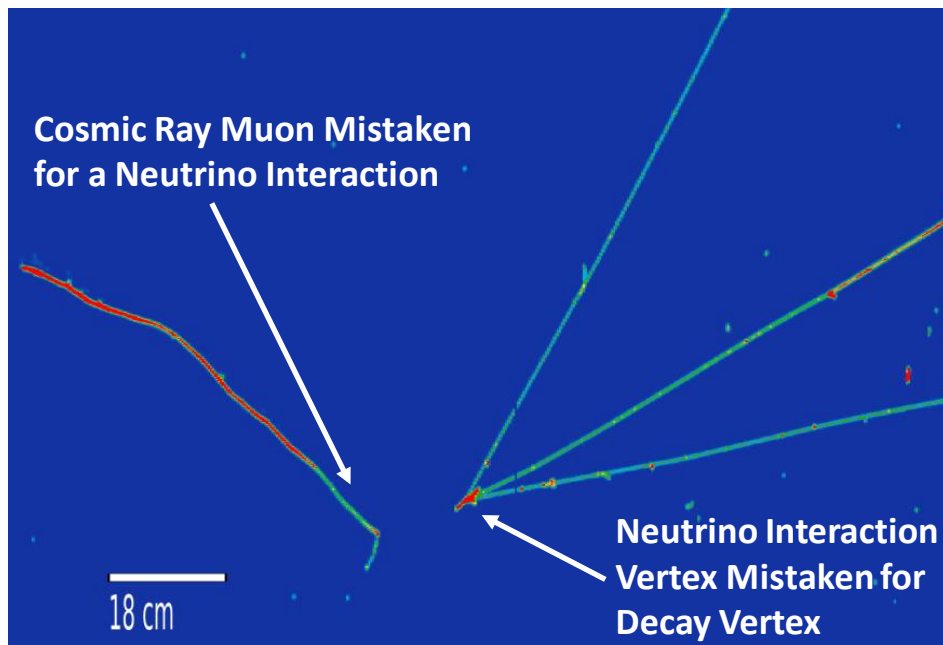


Figure 4.27: A second MC simulation event selected due to a reconstruction failure. The track on the left hand side is a cosmic ray particle undergoing a scatter a short distance into the TPC, with the vertex of this scatter mistaken for a neutrino interaction. The true neutrino interaction was nearby, and reconstructed as the Λ decay vertex.

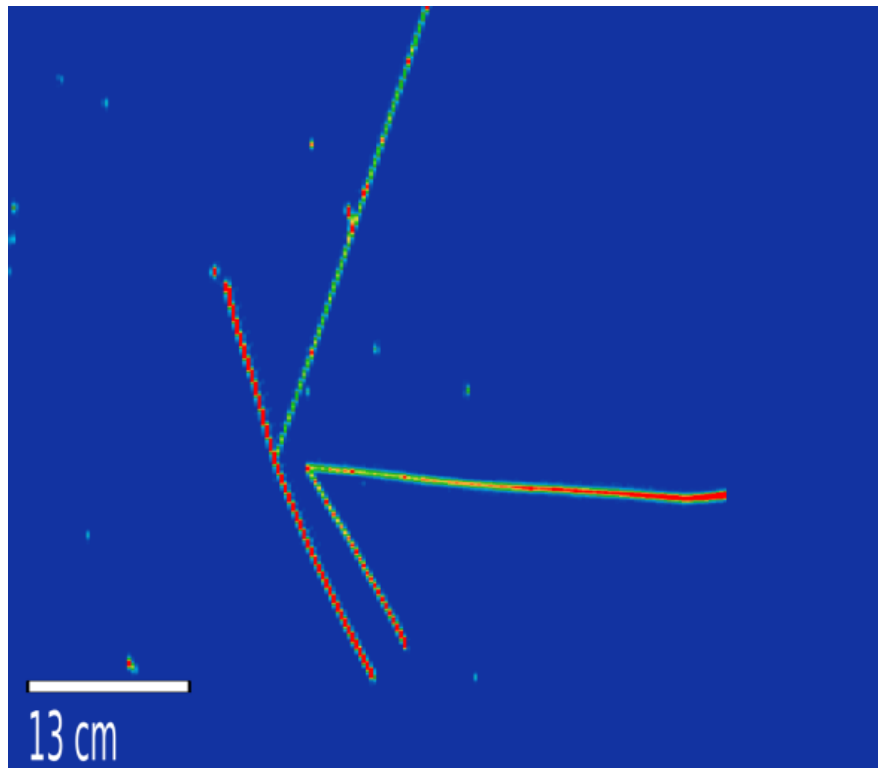


Figure 4.28: An example of a selected background MC simulation event containing a neutron scatter, in this case a $n + \text{Ar} \rightarrow p + \pi^\pm + X$ interaction was mistaken for a decaying Λ baryon.

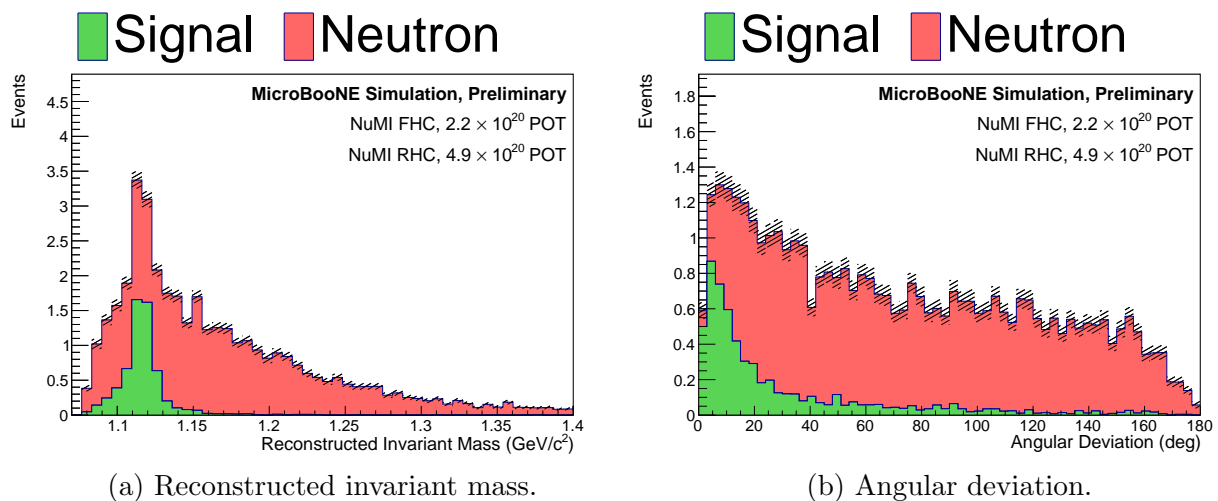


Figure 4.29: Kinematic variables introduced in Section 4.6, shown for the signal and neutron induced background.

4.8.5 Phase Space Dependence

Neutrino event generators employ radically different models of hyperon production, and the data in Figures 2.2 and 2.3 does not significantly restrict the values of the input parameters. GENIE is employed as the primary event generator by MicroBooNE and thus the majority of distributions in this thesis are produced using this generator, as are the estimates of the selection efficiency in the final cross section calculation.

To check for model dependence in the calculation of the selection efficiency, this quantity is calculated as a function of several variables using Λ baryon production events simulated with the GENIE and NuWro event generators, shown in Figures 4.30-4.34. The uncertainties are statistical only, and in the case of the event rates, they are calculated with the Gaussian approximation. The uncertainties on the selection efficiencies are quite asymmetric due to the small number of MC simulation events in each bin, and the Gaussian approximation fails. Instead a Bayesian calculation is used, the same approach applied in the final cross section extraction, explained in Section 5.10.

Figures 4.30- 4.34 reveal considerable non-uniformity in the selection efficiencies, though GENIE and NuWro both exhibit similar shapes. This suggests the difference in the selection efficiencies for the two generators is a combination of complex non-uniformity across several different variables, and statistics. This effect will be addressed when discussing the systematic uncertainties.

Variable Dependant Efficiency?

A technique employed by many measurements of cross sections is to handle this shape dependence through either a forward convolution (forward folding) or deconvolution method (unfolding). Both methods involve calculating a response matrix, M , to encode information about the detector response as a function of some variable:

$$M_{ij} = P(\text{Signal event in reconstructed bin } j | \text{Signal event in true bin } i), \quad (4.32)$$

$$= \frac{\text{Signal events from true bin } i \text{ in reconstructed bin } j \text{ after selection}}{\text{Signal events in true bin } i \text{ before selection}}, \quad (4.33)$$

which can be used to model the effect of shape dependence on the cross section. The variable the MC simulation events are binned in is usually chosen to be something in which there is an intuitive reconstructed analogue, such as outgoing particle energy or direction.

The large statistical uncertainties on the efficiencies in Figures 4.30- 4.33 suggest there would be very large statistical fluctuations in the elements of this matrix, something that could be remedied with a much larger quantity of MC simulation events for the signal, but the time and computational expense to generate these renders this impractical. Instead a single bin unfolding procedure is used, described in Chapter 5, with uncertainties included in the selection efficiency.

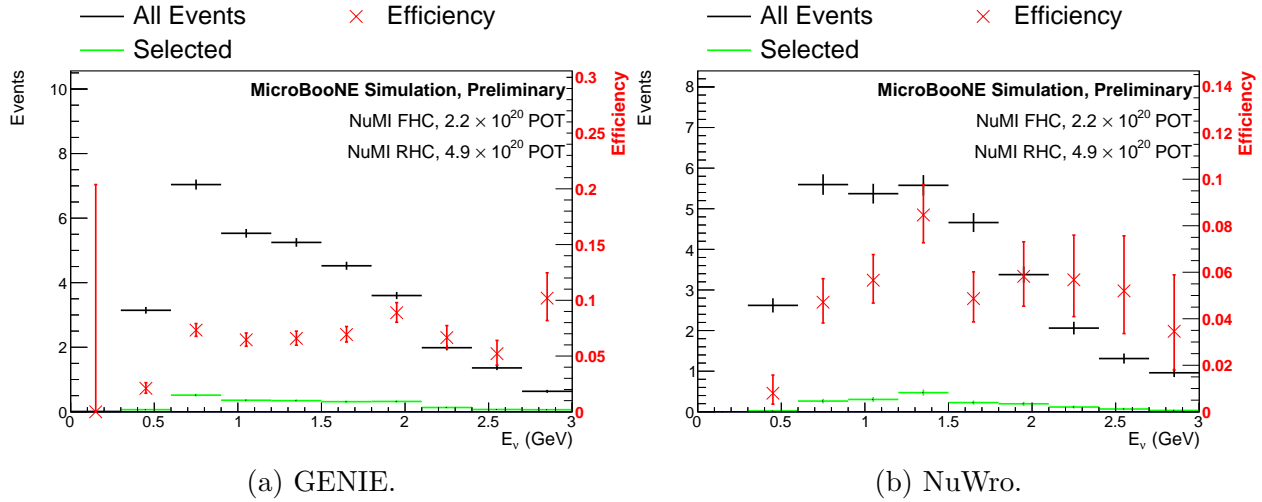


Figure 4.30: Selection efficiency calculated as a function of the muon anti-neutrino’s energy.

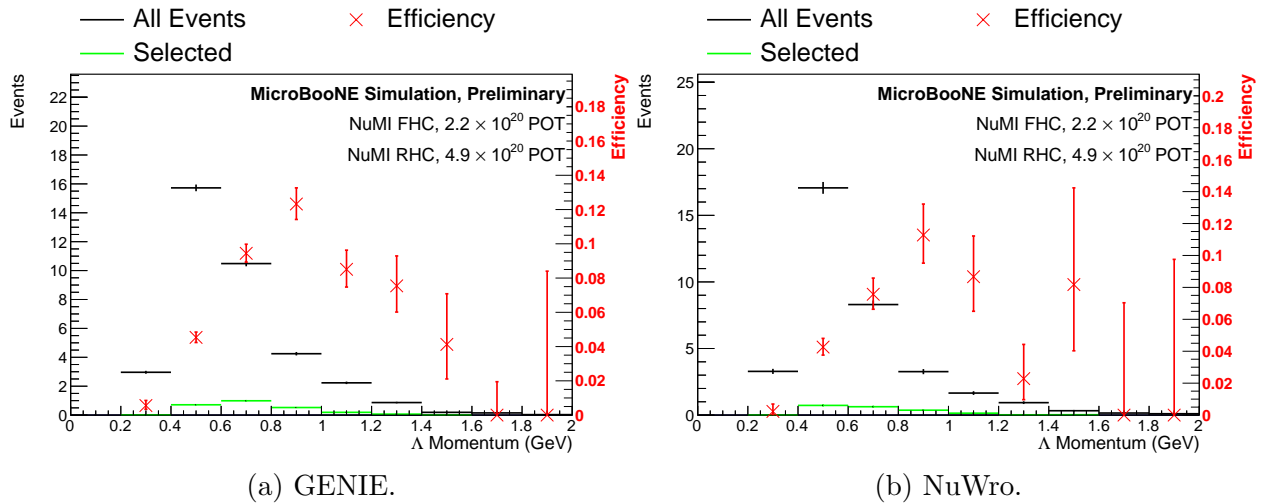


Figure 4.31: Selection efficiency calculated at different values of the Λ baryon’s momentum.

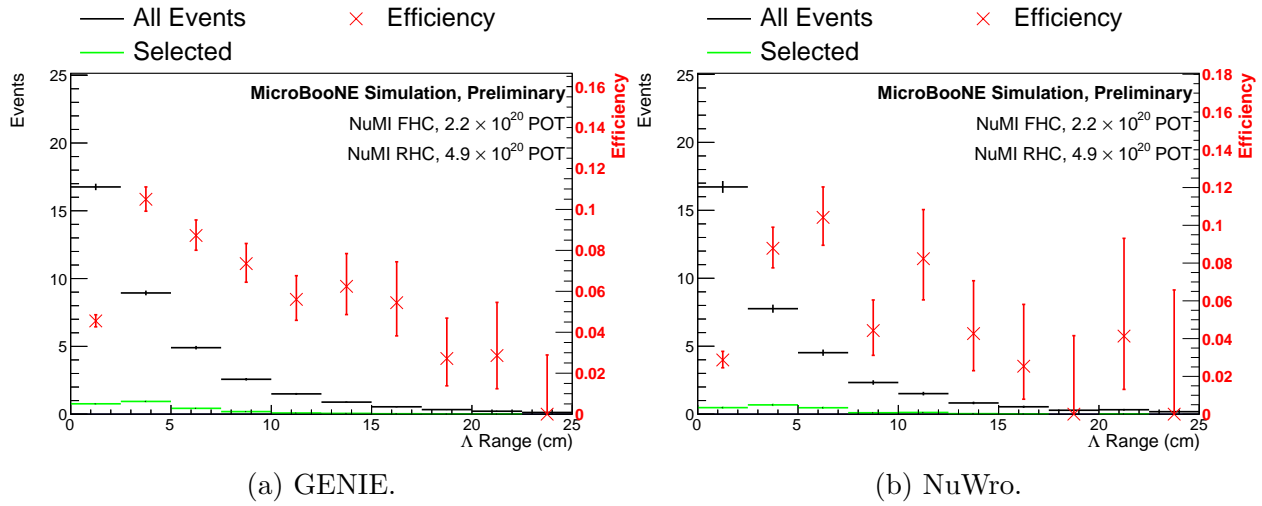


Figure 4.32: Selection efficiency calculated for different values of the Λ baryon's range.

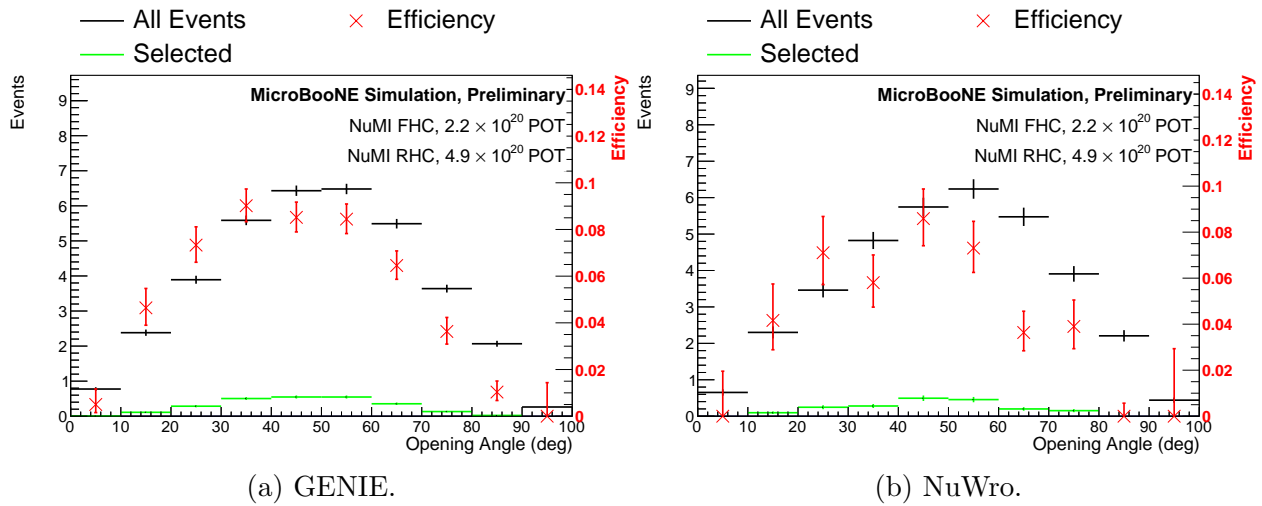


Figure 4.33: Selection efficiency calculated for different values of the opening angle of the Λ baryon's decay.

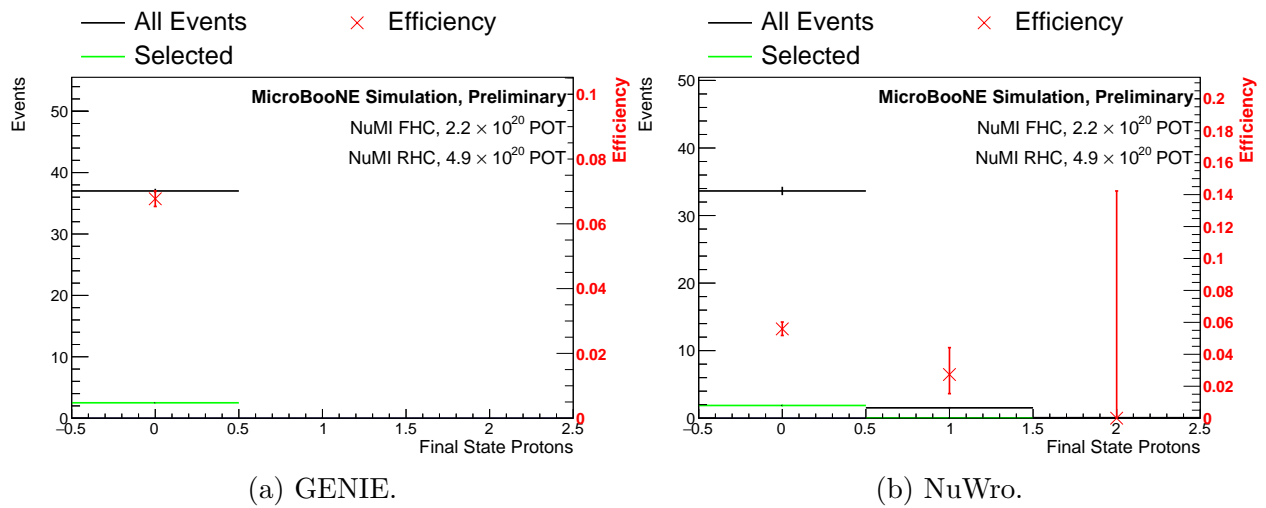


Figure 4.34: Selection efficiency calculated for different values of the opening angle of the Λ baryon's decay.

Chapter 5

Systematic and Statistical Uncertainties

5.1 Introduction

After applying the event selection, the remaining number of events from the data, N_{obs} , is used to estimate the cross section:

$$\sigma_* = \frac{N_{\text{obs}} - B}{T\Phi\Gamma\epsilon}, \quad (5.1)$$

where σ_* is the flux averaged, partial phase space cross section introduced in Section 6.3, B is the predicted number of background event surviving the event selection, ϵ is the selection efficiency, Φ is the total $\bar{\nu}_\mu$ flux corresponding to the data analysed, $\Gamma = 0.639 \pm 0.005 = \text{BF}(\Lambda \rightarrow p + \pi^-)$ [22], and T is the number of argon nuclei in the fiducial volume.

Every quantity in this equation, save for N_{obs} , is estimated from MC simulation and therefore creates systematic bias. Furthermore, B and ϵ are estimated from MC simulation samples of finite statistics, and introduce MC simulation statistical uncertainties. Lastly, N_{obs} will carry its own statistical uncertainty. This chapter details the calculation of these statistical and systematic uncertainties, and their propagation into the final measurement.

The systematic uncertainties are estimated by comparing the predictions of the default simulation with systematic variations, sets of predictions in which some parameters of the physics models have been altered. In this chapter, the predicted signal and background will be presented as a five binned histogram, such as Figure 5.1, in which each bin gives the number of events selected from simulation belonging to each of the following five categories:

1. The CCQE-like Λ production signal.
2. Other events producing Λ baryons, including the RES and DIS processes.
3. Events producing other hyperons, dominated by the CCQE-like Σ^0 channel.

4. The neutron scatter background from Section 4.8.4.
5. The mis-reconstruction background described in Section 4.8.3.

This histogram can then be drawn alongside the systematic variations, to confirm they affect the predicted signal and background in the manner expected, and to establish which sources of uncertainty are the most significant.

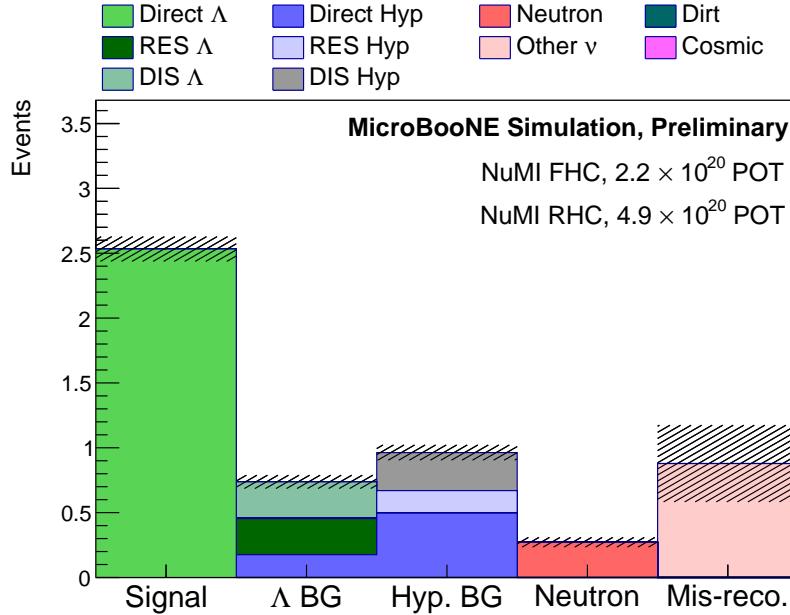


Figure 5.1: The predicted rates of the signal and four categories of background, prior to applying the sideband constraint or hand scan corrections introduced in Section 5.3.

The main product of the systematic uncertainty calculations is a fractional covariance matrix between the selection efficiency, ϵ , the total muon anti-neutrino flux, Φ , and the number of selected background events, B . This matrix is used to generate systematic shifts in the parameters in cross section formula, in a procedure which will be described in greater detail in Section 5.10. The contribution to this matrix from each of the main categories of systematic uncertainty will be shown. The systematic uncertainties in the number of targets and the branching fraction of the $\Lambda \rightarrow p + \pi^-$ decay are negligible compared with the other sources of uncertainty in the measurement.

5.2 Treatments

All of the systematic uncertainties are calculated by constructing systematic variations, copies of variables and distributions in which some parameters of the MC simulation

have been changed from their default values. These are then compared with the default simulation prediction, and one another, to estimate the resulting systematic uncertainties in the measurement. Many simulation parameters affect multiple quantities in the cross section formula, and it is necessary to calculate the covariance matrix of all the quantities in Equation 5.1 to which systematic uncertainties apply. The same arguments apply to the signal and rates of predicted background in Figure 5.1. The following treatments are three approaches to calculate the covariance, $\text{Cov}(X, Y)$, of two generic quantities of interest, X and Y . The choice of procedure depends on the underlying physics parameters being varied, and will be explained in subsequent sections. Two closely related quantities are the fractional covariance, $\text{FCov}(X, Y)$, and the fractional uncertainty, $\text{FE}(X)$:

$$\text{FCov}(X, Y) = \frac{\text{Cov}(X, Y)}{XY}, \quad (5.2)$$

$$\text{FE}(X) = \sqrt{\text{FCov}(X, X)}. \quad (5.3)$$

These are often more informative if there exists a large disparity between the magnitudes of the quantities the covariance matrix relates to.

Multisim Technique

This approach is often applied if the uncertainties from several parameters that are known to be correlated are being evaluated. So named because to include the effect of their correlations, multiple input parameters are varied in parallel, often sampled from some multidimensional distribution. For two of the quantities calculated in n variations, their covariance is estimated with:

$$\text{Cov}(X, Y) = \frac{1}{n-1} \sum_{i=1}^n (X_i - \bar{X})(Y_i - \bar{Y}), \quad (5.4)$$

where X_i is the predicted value of X in the i th universe, and $\bar{X} = \frac{1}{n} \sum_{i=1}^n X_i$.

Two Universe Unisim

This method is applied for continuous parameters assumed to be approximately uncorrelated with the other inputs into the MC simulation predictions. A single parameter is increased/decreased by a single standard deviation, and the resulting values of X and Y , $X_{+/-}$ and $Y_{+/-}$ are calculated. The covariance of X and Y is:

$$\text{Cov}(X, Y) = \frac{(X_+ - X_-)(Y_+ - Y_-)}{4}. \quad (5.5)$$

Alternative Model

Some inputs to the MC simulation cannot be varied continuously, and often the approach is to compare the predictions when employing different models instead. The default values of

X and Y are compared with its predictions when employing some alternative model, X' and Y' , with the resulting covariance:

$$\text{Cov}(X, Y) = (X' - X)(Y' - Y). \quad (5.6)$$

Brief Note: Combining Runs

In this thesis, data from MicroBooNE runs 1 and 3 will be analysed, and all distributions contain the combined predictions from both runs unless otherwise indicated. This approach continues in this chapter, including when calculating the systematic variations. By combining the predictions from both data taking periods, *before* applying one of Equations 5.4, 5.5, or 5.6, any correlations of the uncertainties between the two data taking periods are included.

5.3 Low Simulation Statistics Background

At the end of the previous chapter, it was discovered that a portion of the background events surviving the selection were due to failures in reconstruction, and not the result of any specific physics processes. This leads to difficulties when calculating the systematic uncertainties in the size of this background, as there are only 9 MC simulation events of this type available in the entire set of MC simulation samples available for analysis. The responses of these 9 events to the various uncertainty propagation techniques described in the remainder of this chapter are unlikely to be representative of this background as a whole. Worse still, to estimate the uncertainties related to the modelling of the detector response, only a subset of these events are available, and this category of uncertainties is included through counting the number of events from samples with different detector models that survive the event selection. This leads to extremely coarse estimation of these uncertainties: if n MC simulation events are selected from the sample using the default model, the resolution at which the fractional uncertainty may be estimated is $1/n$.

The features that lead the selection of these events only appear after reconstruction, and the technique of manufacturing high purity samples using filters in the manner of the hyperon and neutron samples is rendered impractical by the computational expense. Two other solutions to this problem are explored in this chapter: employing data from a sideband and performing a constraint procedure, and visual inspection of the selected MC simulation events to identify and remove events of this type, reducing the problematic background to a level at which the related uncertainties are no longer important. In the discussions of the systematic uncertainties in Sections 5.4 to 5.8, sideband constraint method will be used. The calculations of the covariance matrices with the visual scanning method are displayed in Appendix E.

5.3.1 Sideband Constraint

Two variables arise from the event selection that can provide signal-poor regions predicted to contain relatively large quantities of the mis-reconstruction background: the invariant mass of the Λ baryon candidate, W , and the angular deviation, α . With the assumption that the mis-reconstruction background is not the result of any specific physics process, one expects the uncertainties in the predicted rates of this background inside and outside the signal region to be correlated, and therefore a measurement of this background in these sidebands can constrain the quantity inside the signal region.

Preparing the Data

The sideband data is generated by applying the full event selection to the data with the kinematic cuts inverted to remove the signal region. Joint distributions of the angular deviation and invariant mass, drawn separately for the signal and background, are shown in Figures 5.2a and 5.2b. The signal and two sideband regions are illustrated, defined as:

$$\text{Near Sideband} := 1.08 < W < 1.3 \text{ GeV and } \alpha < 50^\circ, \quad (5.7)$$

$$\text{Far Sideband} := \text{All other values of } W \text{ and } \alpha. \quad (5.8)$$

The signal region is $1.09 < W < 1.14 \text{ GeV}$, and $\alpha < 14^\circ$, removed by the inverted kinematic selection cuts. Two bins are chosen to minimise statistical uncertainties in the fit whilst retaining some information about the shapes of the distributions of different sources of background in α and W . The data from these sidebands is compared with the predictions from the default MC simulation predictions in Figure 5.3a. The pale pink component, labelled “Other ν ”, is the mis-reconstruction background to be fitted.

Fitting Procedure

To fit to this data, a scaling parameter, k , is introduced. This modifies the size of the mis-reconstruction background by the same factor for both bins, with $k = 1$ giving the result from the default MC simulation prior to applying the fit. The predicted number of events in the b th sideband bin, R_b , is the sum of sum of six components:

$$R_b(k) = S_b + B_b^{\text{Hyperon}} + B_b^{\text{Neutron}} + B_b^{\text{Dirt}} + B_b^{\text{EXT}} + kB_b^{\text{Mis-reco}}, \quad (5.9)$$

where S_b is the signal, B_b^{Hyperon} the predicted number of events in the sideband bin from the hyperon production background, B_b^{Neutron} the predicted number of events from the neutron background, B_b^{Dirt} and B_b^{EXT} the predicted backgrounds from the Dirt and EXT samples, and B_b^{Other} the mis-reconstruction events. The last term is scaled by k . k is then varied to perform a least-squares fit, minimising the following metric:

$$\chi^2(k) = \sum_{b=1,2} \frac{(R_b(k) - D_b)^2}{\sigma_b^2}, \quad (5.10)$$

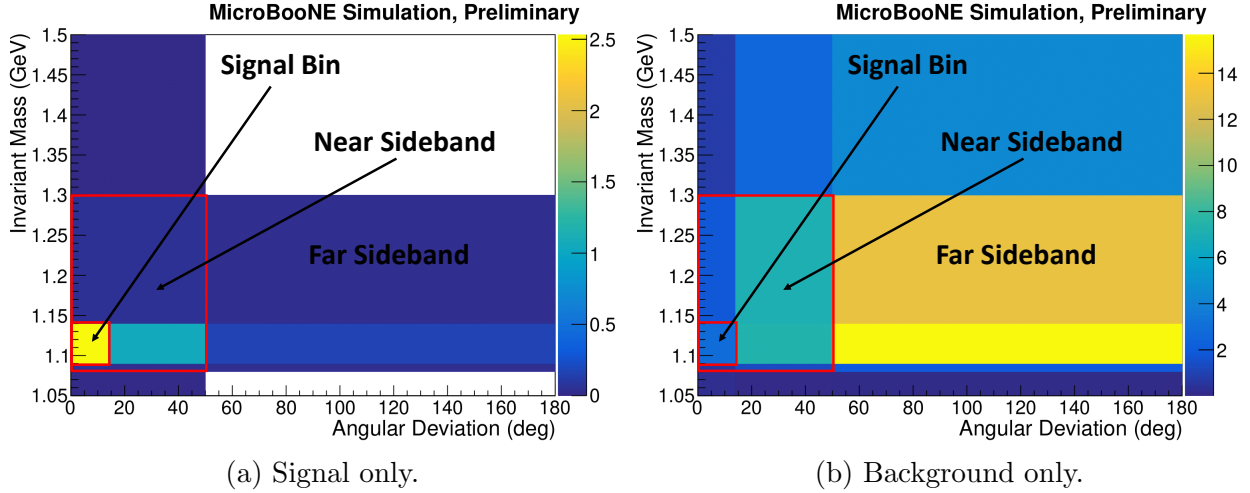


Figure 5.2: Two dimensional distributions of MC simulation events in the variables used to construct the two sidebands.

where D_b is the number data events in bin b . σ_b^2 is the sum of the squared of the data and MC simulation statistical uncertainties, assuming the Gaussian approximation to the Poisson distribution:

$$\sigma_b^2 = D_b^2 + \sum w_b^2 \quad (5.11)$$

where $\sum w_b^2$ is the sum of the squared weights of the MC simulation events in bin b , which are multiplied by k if they belong to the mis-reconstruction background.

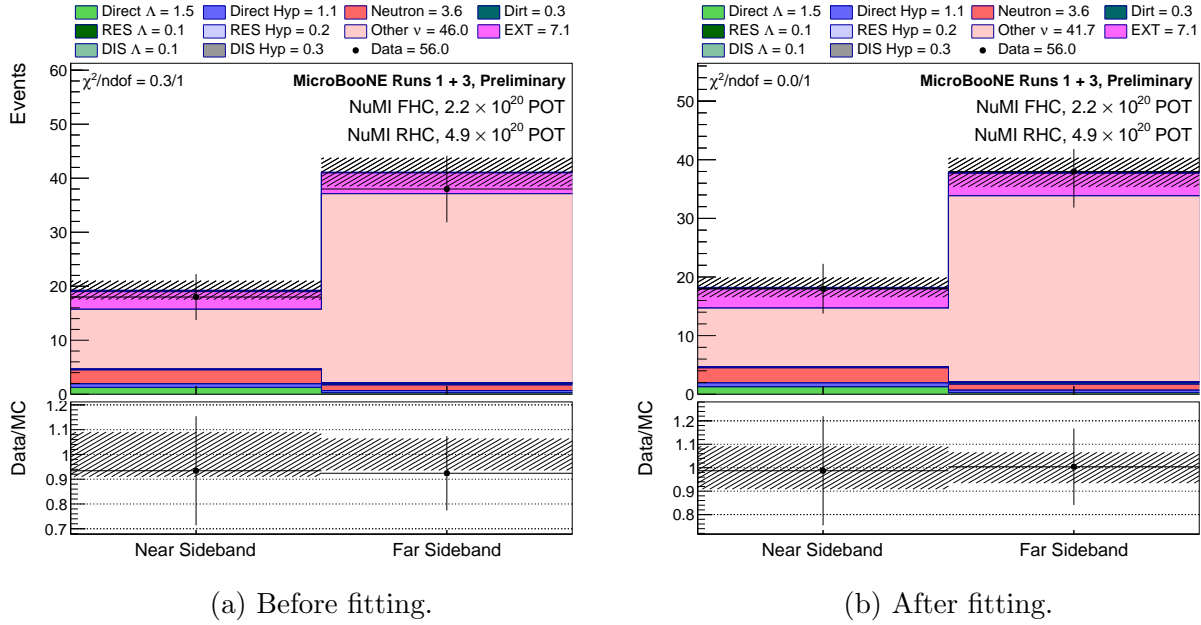
The MINUIT [148] algorithm is employed to minimise the value of $\chi^2(k)$, obtaining a best fit of $k = 0.90 \pm 0.17$. The uncertainty is due to the statistics of the data and MC simulation in the sideband. The predicted event rates in the sideband bins, after rescaling the mis-reconstruction background by k , are shown in Figure 5.3b. The uncertainty in k is added to the final uncertainty budget in Section 5.8.2.

Systematic Uncertainties

To produce systematic variations for the mis-reconstruction background, a separate fit is performed in every systematic universe, yielding a separate scaling variable, k_i , for each. In systematic universe i , Equation 5.9 becomes:

$$R_{bi}(k_i) = S_{bi} + B_{bi}^{\text{Hyperon}} + B_{bi}^{\text{Neutron}} + B_{bi}^{\text{Dirt}} + B_b^{\text{EXT}} + k_i B_b^{\text{Mis-reco}}. \quad (5.12)$$

The terms from the signal, hyperon and neutron backgrounds, and the dirt background are all given by their i th systematic variation, obtained through reweighting and other methods described in the later sections of this chapter, indicated by the i subscript. The mis-reconstruction background is kept at its default value, B_b^{Other} , and scaled by k_i . B_b^{EXT} is



(a) Before fitting.

(b) After fitting.

Figure 5.3: The data from the sideband compared with MC simulation predictions, before and after performing the fit. The fit involves rescaling the component of the MC simulation labelled “Other ν ”.

obtained from data collected when the beam was inactive and therefore does not possess any systematic variations.

As before, a least squares fit is performed, minimising the value of $\chi^2(k_i)$ from Equation 5.10, comparing $R_{bi}(k_i)$ to the data in the sideband bins to obtain k_i . The *sideband constrained* predicted background from mis-reconstruction in the signal bin, in universe i , is the magnitude of this background predicted by the default MC simulation multiplied by k_i . This method enables calculation of systematic uncertainties without requiring a large number of events in the signal bin to be reweighted. The downsides of this approach are the additional statistical uncertainty introduced by the fit, and the reliance on the assumption that systematic uncertainties in the fitted background are completely correlated across the signal region and the sideband.

5.3.2 Visual Scanning

The second method explored, attempts to remove the mis-reconstruction background entirely, obviating the need for accurate systematic uncertainties, through the visual inspection of event displays (hand scanning).

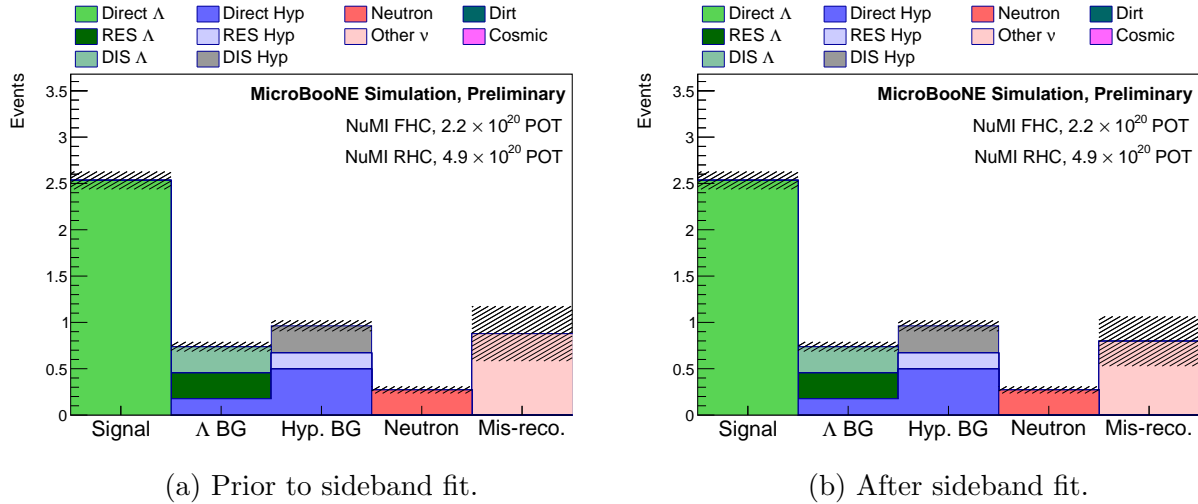


Figure 5.4: The breakdown of predicted backgrounds before and after applying the sideband constraint to the final bin. The other source of background are not modified. The hatched regions indicate uncertainties, and are statistical only.

Simulation Based Study

In order to assess the efficiency, background rejection power, and reliability of visual scanning, a study with MC simulation events was first performed. A sample of 150 events, comprising a mixture of the five categories of events passing the automated selection, was prepared. The numbers of events from each category are listed in Table 5.1. These events were placed in a random order with no labelling to indicate which category of background they belonged to. In the case of the mis-reconstruction background, the kinematic cuts were removed to provide a larger sample of events to use. Event displays of all 150 events were produced using a visualisation tool developed as part of the island finding algorithm, first seen in Figure 4.24c from the previous chapter. Examples of these images for the signal and mis-reconstruction background, taken from set of events used in this study, are shown in Figures 4.24c, 4.25c, and 4.26b. The island finding algorithm analyses each plane in isolation, while the (human) scanners were provided with the images of all three planes, and asked to confirm whether the information from the plane(s) the island finding algorithm labelled as containing secondary vertices was corroborated by the other planes. They would then indicate if they thought the event was likely to contain a Λ baryon or not. Table 5.1 lists the number of events from each category were selected by each scanner.

This method is very effective at removing the mis-reconstruction background, achieving an average reduction of 90%, though there is some variation in how many events from the various backgrounds they selected. This variability will be accounted for through the inclusion of an additional systematic uncertainty, explained in Section 5.8.1. The averaged selection efficiencies of the scanners, shown in Table 5.1, are used to reweight the MC simulation

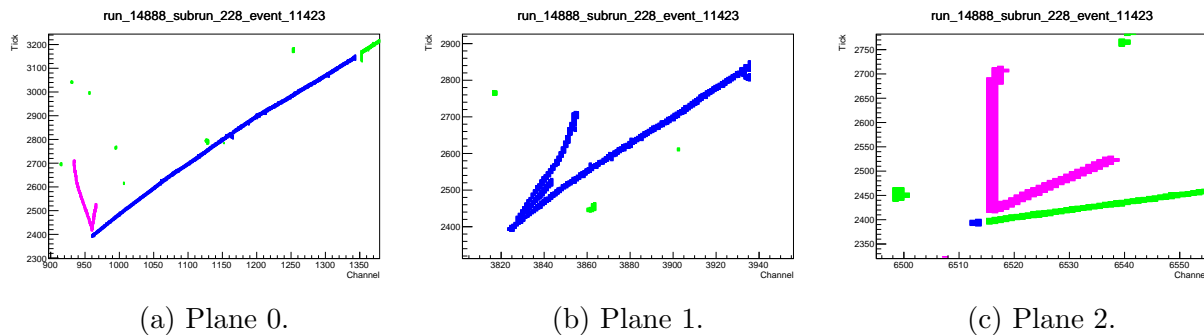


Figure 5.5: Visual output of the island finding algorithm given to the hand scanners, showing a signal event. The island finding algorithm rejected Planes 1 and 2, the former on due to the size of the muon island, though there is a clear secondary vertex in all three images.

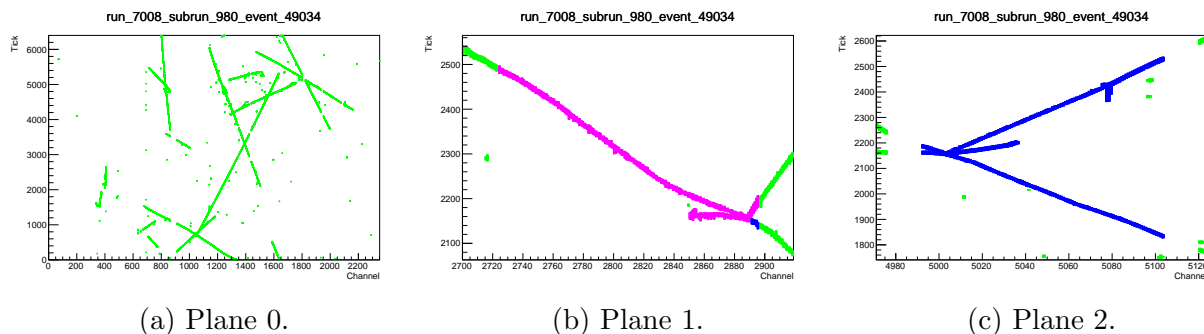


Figure 5.6: Visual output of the island finding algorithm given to the hand scanners, showing a BG event. The island finding algorithm indicated the presence of a secondary vertex in Plane 1. A result not supported by information in the other two planes.

predictions for each of the five categories of backgrounds, creating a set of predictions that can be compared with data that has undergone the same visual scan. The application of the visual scanning technique to data, including how blindness is maintained, will be described in Chapter 6.

The predicted rates of the signal and four categories of background, before and after applying hand scanning weights, are shown in Figure 5.7. When estimating the systematic uncertainty on the mis-reconstruction background, the same methods used for the signal and hyperon/neutron induced backgrounds will be applied. As this background is almost eliminated, inaccurate calculation of the corresponding uncertainties should not be a significant effect.

	Signal	Λ BG	Hyp. BG	Neutron	Mis-reco.
Total Events	40	11	19	30	50
Scanner 1	33	1	10	2	1
Scanner 2	37	10	14	16	6
Scanner 3	38	11	18	16	1
Scanner 4	34	4	7	4	8
Scanner 5	39	10	18	29	10
Average Selection Eff.	0.91	0.65	0.71	0.45	0.10
Automated Selection	2.5	0.7	1.0	0.3	0.9
Automated + HS	2.3	0.5	0.7	0.1	0.1

Table 5.1: The total events from each category used in the visual scanning study, compared with the number selected by each scanner. The bottom most pair of rows indicate the number of events of each type predicted to pass the purely automated selection from the previous chapter, and the automated selection combined with visual scanning.

5.4 Neutrino Flux

The neutrino flux is simulated with the `g4numi` package, which outsources the modelling of collisions between the protons from the Main Injector beam and the nuclei in the target to GEANT 4 [126], as described in Section 3.4.1. This introduces three sources of uncertainty:

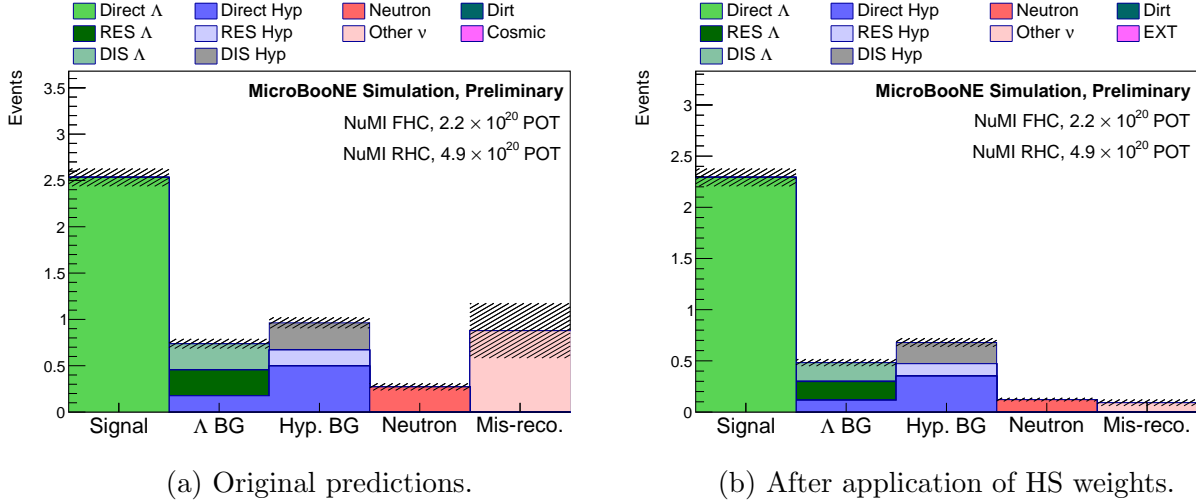


Figure 5.7: The breakdown of predicted backgrounds before and after correcting with the results of the hand scan. The hatched regions indicate statistical uncertainties.

the cross sections of the hadron production processes, the geometry model of the beam assembly, and the POT counting.

For the first two categories, the uncertainties are propagated by first calculating the flux arriving at the window, ϕ , for each flavour of neutrino/anti-neutrino as a function of the neutrino energy, E_ν , and the angle between the neutrino's direction and the NuMI beam axis, θ . Alternative beam simulations are then run, and the flux in alternative universe i , ϕ_i , is calculated. The ratio of this alternative flux to the default provides the following weight:

$$w_i(E_\nu, \theta, f) = \frac{\phi_i(E_\nu, \theta, f)}{\phi(E_\nu, \theta, f)}, \quad (5.13)$$

where $f = \nu_\mu, \bar{\nu}_\mu, \nu_e, \bar{\nu}_e$. The inclusion of the angle is necessary as MicroBooNE receives flux from the entire length of the NuMI decay volume, up to and including the absorber, and the production of neutrinos is dominated by different physics processes at different elements of the beamline.

Aside from changing the total muon anti-neutrino flux appearing in the denominator of the cross section formula, the quantity of selected background events depends on the shape and intensity of the fluxes. Figure 4.30 also indicates some dependence of the selection efficiency on the shape of the anti-neutrino energy spectrum.

Transforming to NuMI Coordinates

All positions and directions in this thesis use the coordinate system of Figure 3.4, in which the z direction points along the axis of the BNB, the drift field is parallel to the x axis, and the y axis is vertical. Before calculating the flux weights, the following rotation is applied to

the directions of the neutrinos:

$$R = \begin{bmatrix} 0.921 & 0.022 & 0.389 \\ 0 & 0.998 & -0.0584 \\ -0.389 & 0.0538 & 0.919 \end{bmatrix}, \quad (5.14)$$

reorienting the coordinate system such that the z axis is now parallel to the direction of the NuMI beam.

5.4.1 Hadron Production

The neutrino flux depends on the hadron yield, which is sensitive to a number of effects: the fraction of protons interacting to produce charged mesons, which mesons are produced, and the rates at which they are re-absorbed elsewhere in the beam assembly.

To propagate these uncertainties, the Package to Predict Flux (PPFX), developed by L. Aliaga Soplin for the MINERvA collaboration [149], is employed. This software constrains the neutrino flux using data from the MIPP [150], NA49 [151–153], and NA61 [154] experiments, which studied various $p + C$ scattering processes. The MIPP experiment was conducted using the Fermilab Main Injector Beam and a spare NuMI target. PPFX compares the cross sections and predicted hadron yields from the `g4numi` beam simulation to this data, providing corrections and correlated uncertainties in the hadron yield. Corrections to the predicted hadron yield are in turn used to adjust the neutrino flux arriving at MicroBooNE using information about the neutrino parentage.

The uncertainties are propagated by producing 600 variations using the corrections and correlated uncertainties from PPFX, and calculating the flux, Φ_i , in each. The fractional uncertainties in the muon neutrino and anti-neutrino fluxes resulting from the hadron production modelling are presented in Figure 5.8 as functions of E_ν and θ .

Total uncertainty in the muon anti-neutrino flux from the hadron production modelling is approximately 23%. Figure 4.30 indicates the selection efficiency has some dependence on the shape of the flux; calculating the efficiency in the hadron production variations yields an uncertainty of less than 1%. Figure 5.9 shows number of signal events and background events predicted by simulation, alongside the hadron production variations, the uncertainty in the predicted signal is approximately 11%. The small size of the uncertainties in the selection efficiency and predicted signal compared with that of the total flux can be understood by identifying the portion of the flux that creates the signal, shown in Figure 5.10: energies above 1 GeV and small angles. Comparison with Figure 5.8 reveals this is the region in which the hadron production uncertainties are the smallest.

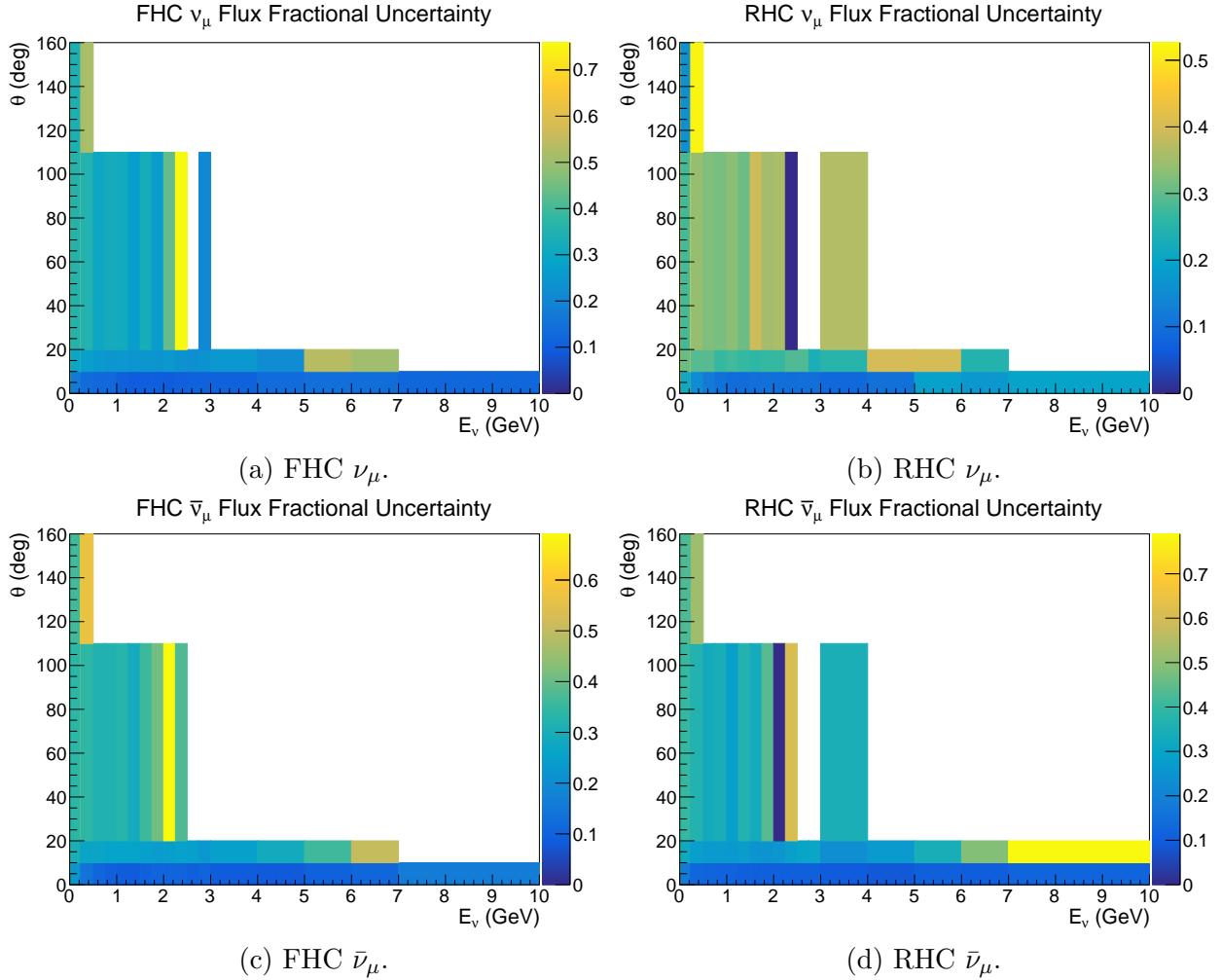


Figure 5.8: The fractional uncertainties in the neutrino flux as a function of E_ν and θ . The choice of binning is along the θ axis is to separate the flux into components arriving from different pieces of the beamline assembly: the first pair of divisions are from the target and horns, the third, much wider set of bins, from the decay pipe, and the final set from the absorber.

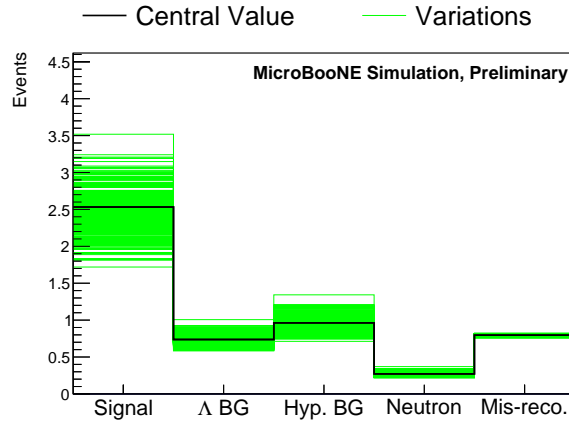


Figure 5.9: Selected signal and background in different hadron production universes. The uncertainty in the selected signal is approximately 11%.

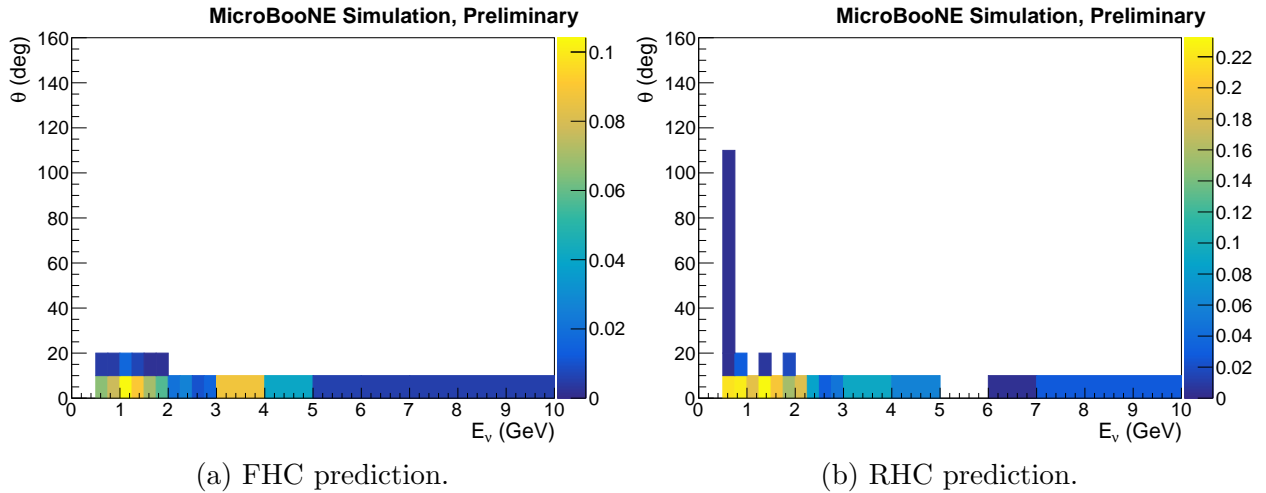


Figure 5.10: Neutrino energies and angles of the selected signal events, using the same binning scheme as Figure 5.8. The signal primarily comes from anti-neutrinos of energies around 1 GeV with small angles, where the flux uncertainties are small.

5.4.2 Beamline Geometry

The beam simulation requires a model of the beamline geometry, with which the interactions of proton beam and resulting hadrons are modelled. The exact positions and properties of the elements of the geometry are only known to a certain level of precision. 10 sources of uncertainty from the beamline model parameters are considered, listed in Table 5.2. The uncertainties in the flux, selected signal, and selected background from the beamline geometry are all found to be around 1% or less. The systematic variations when applying the sideband constraint procedure are presented in Figure D.1 of Appendix D.

Simulation Param	Variation Size
Horn Current	± 2 kA
Beam spot size	± 0.2 mm
Target z position	± 7 mm
Water on horns	± 1 mm
Horn 1 x position	± 3 mm
Horn 1 y positions	± 3 mm
Horn 2 x position	± 3 mm
Horn 2 y position	± 3 mm
Beam x position	± 1 mm
Beam y position	± 1 mm

Table 5.2: Beamline geometry parameters varied and their uncertainties.

5.4.3 POT Counting

The simulation samples are normalised to POT recorded by toroidal monitors around the proton beam, which have an operational uncertainty of 2% [149]. This applied by increasing and decreasing the MC simulation predictions, with the exception of the bad reconstruction background if the sideband constraint method is applied (where the data constraint is used to estimate this uncertainty instead), by $\pm 2\%$. This introduces uncertainties of 2% in the predicted background and flux in the cross section formula.

5.4.4 Summary of Flux Uncertainties

The fractional uncertainties in the quantity of signal events and different categories of background resulting from the 12 categories of flux uncertainties are compared in Figure 5.11; hadron production modelling is the dominant component. The final fractional covariance matrices for ϵ , Φ , and B , after applying the hand scanning and sideband constraint procedures, are shown in Tables 5.3b and 5.3a.

	ϵ	Φ	B
ϵ	0.00005	-0.00116	-0.00023
Φ	-0.00116	0.05339	0.01255
B	-0.00023	0.01255	0.00460

(a) Applying the sideband constraint.

	ϵ	Φ	B
ϵ	0.00005	-0.00116	-0.00040
Φ	-0.00116	0.05339	0.01887
B	-0.00040	0.01887	0.00933

(b) With visual scanning.

Table 5.3: Total fractional covariance matrix of the selection efficiency, $\bar{\nu}_\mu$ flux, and selected background events, combining all background neutrino flux uncertainties.

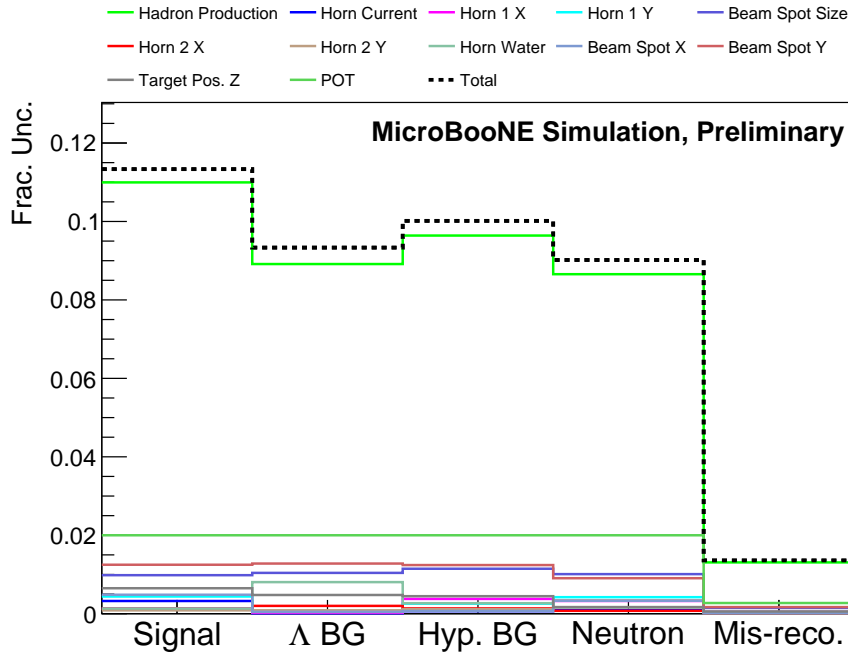


Figure 5.11: Fractional uncertainties in the predicted signal and different sources of background from the flux modelling, when applying the sideband constraint procedure to the mis-reconstruction background.

5.5 Background Cross Sections

The quantity of background events predicted to survive the event selection is subtracted from the number of events observed in the data to obtain an estimate of the number of signal events in the cross section calculation. This quantity depends on the cross sections of processes producing these background interactions, to which uncertainties are applied.

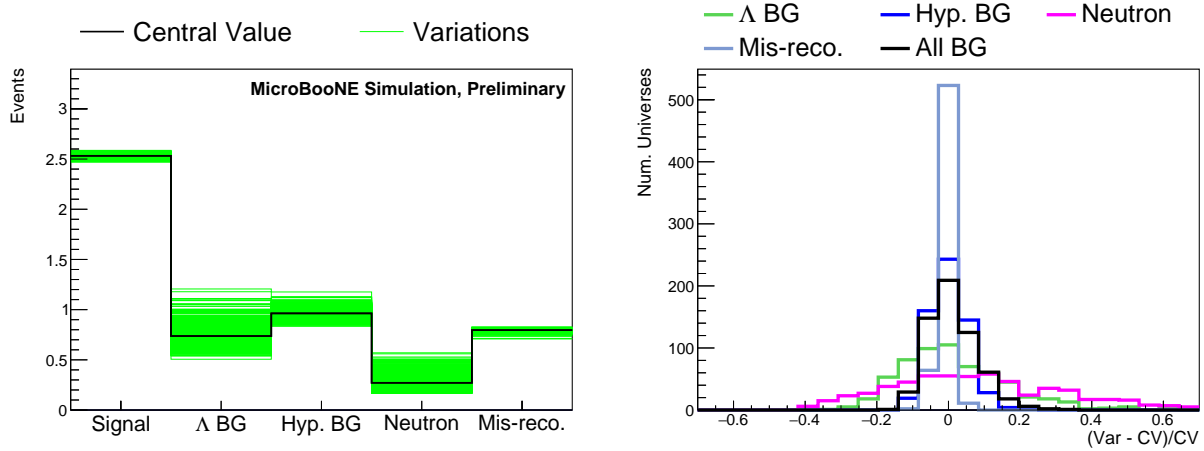
5.5.1 The MicroBooNE Cross Section Tune and Uncertainties

Ref. [129] describes the creation of a new tune of the GENIE [63] neutrino event generator created by MicroBooNE after performing fits of 44 cross section model parameters, listed in Table 5.4, to MINERvA and T2K cross section measurements. These include the vector and axial masses and non-resonant background in the RES interaction, and several parameters of the Bodek-Yang DIS model. These quantities are varied in parallel to produce a set of 600 variations, drawn alongside the central value prediction in Figure 5.12a. This reveals two effects warranting further investigation: the slight variation in the predicted signal despite the lack of variations in the CCQE-like Λ cross section, and the appearance of an upward shift in the neutron background. The latter is understood by calculating the fractional change in the predicted background for every universe, and drawing the distribution of resulting values, shown in Figure 5.12b. All of the resulting distributions have their maxima close to zero, indicating the parameter sets sampled for the reweighting are centred around those used in the default simulation.

The small variation in the predicted signal is in fact due to the small fraction of signal events in which another interaction occurred within the cryostat in the same beam spill. This second interaction is assigned a systematic weight, and the weight for the entire event is the product of the weights of the individual interactions. The uncertainties in the RES and DIS backgrounds are calculated to be 35% and 25% using this reweighting procedure.

Name	Parameter	Name	Parameter
MaCCQE	CCQE axial mass	NormCCMEC	CC MEC normalisation
CouLombCCQE	Nuclear Coulomb potential	NormNCMEC	NC MEC normalisation
MaNCEL	NC elastic axial mass	FracPN_CCMEC	Fraction of CC MEC interactions on $p + n$
EtaNCEL	NC elastic η parameter	FracDelta_CCMEC	Fraction of CC MEC interactions involving Δ excitation
MaCCRES	CC resonant axial mass	NonRESBGvpCC1pi	
MvCCRES	CC resonant vector mass	NonRESBGvpCC2pi	
MaNCRES	NC resonant axial mass	NonRESBGvpNC1pi	
MvNCRES	NC resonant vector mass	NonRESBGvpNC2pi	
AhtBY		NonRESBGvnCC1pi	
BhtBY		NonRESBGvnCC2pi	
CV1uBY	Bodek-Yang model parameters	NonRESBGvnNC1pi	
CV2uBY		NonRESBGvnNC2pi	
AGKYxF1pi	Hadronization model parameters	NonRESBGvbarpCC1pi	
AGKYpT1pi		NonRESBGvbarpCC2pi	
MFP_pi		NonRESBGvbarpNC1pi	
MFP_N		NonRESBGvbarpNC2pi	
FrCEx_pi		NonRESBGvbarnCC1pi	
FrInel_pi		NonRESBGvbarnCC2pi	
FrAbs_pi		NonRESBGvbarnNC1pi	
FrCEx_N		NonRESBGvbarnNC2pi	
FrInel_N			
FrAbs_N			
		RDecBR1gamma	Branching ratio for Δ radiative decay
		RDecBR1eta	Branching ratio for Δ decay to η

Table 5.4: The parameters varied in the GENIE multisim reweighting.



(a) Predicted signal and background surviving the selection, with variations. (b) Fractional changes in the selected background.

Figure 5.12: Selected and signal in different generator multisim variations. The fractional differences between the variations and the central value predictions are recorded in histograms in panel (b) to check for any offsets, which would indicate problems with the reweighting procedure. None are seen.

5.5.2 Alternative Models and CCQE RPA

For some interaction processes, several competing models exist, with no measurements to indicate which provides the best description of the physics. Table 5.5 contains a list of such processes for which uncertainties are estimated by comparing the predictions of competing models. These processes are not significant sources of background in this analysis, and these uncertainties are included for completeness. The systematic variations are displayed in Appendix D.2.

Another, miscellaneous uncertainty applying to the cross sections of background neutrino interactions is the strength of the RPA corrections in the Nieves CCQE model [130]. RPA corrections are not a continuous effect, and weights are instead obtained by interpolating between the predictions with and without the corrections¹. Again, this uncertainty is included here for completeness.

¹The interpolations can be seen in Figure 3 of Ref. [129]

Parameter	Default	Alt. Model
CCQE vector form factor	BBA 07	Dipole
CCQE axial FF	Dipole	z expansion
CCCOH normalisation	$1 \times$ default cross section	$2 \times$ default cross section
NCCOH normalisation	$1 \times$ default cross section	$2 \times$ default cross section
Δ radiative decay angle	Isotropic distribution in θ	$\cos^2(\theta)$ distribution
Δ hadronic decay angle	Isotropic distribution in θ	Rein-Seghal model
MEC decay angle	Isotropic distribution in θ	$\cos^2(\theta)$ distribution
MEC differential cross section	Tuned GENIE empirical model	Valencia model

Table 5.5: Alternative models used to estimate event generator systematics not included in the multisims.

5.5.3 CCQE Hyperon Cross Sections

As shown in Chapter 2, there is little existing data on the physics of CCQE-like hyperon production. A 100% uncertainty is applied to all sources of background due to direct hyperon production interactions, primarily Σ^0 baryon production. The resulting effect on the predicted mixture of backgrounds is shown in Figure 5.13.

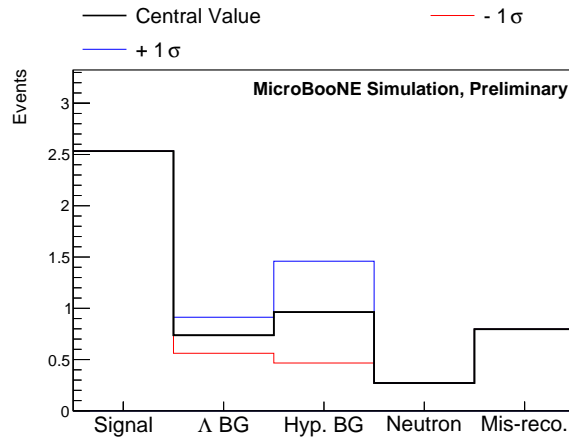


Figure 5.13: Selected signal and background when varying the CCQE-like hyperon production cross sections.

5.5.4 Summary of Background Cross Section Uncertainties

A breakdown of the systematic uncertainties due to the cross sections of background neutrino interactions is shown in Figure 5.15. The alternative model uncertainties discussed in Section 5.5.2 are all very small compared with the other uncertainties. The multisim variations assign uncertainties of around 30% to the RES and DIS driven hyperon background, which combined with the 100% uncertainty applied to the direct hyperon production background, yields uncertainties of 30% and 50% in the sources of background producing hyperons. The final fractional uncertainties in the selected background are 26% and 35% when applying the sideband constraint and visual scanning procedures respectively, with the covariance matrices shown in Tables 5.6a, and 5.6b. The larger *fractional* uncertainty obtained when applying the visual scanning method does not necessarily indicate worse overall performance, as the quantity of background has been reduced.

	ϵ	Φ	B
ϵ	0.00003	0	-0.00005
Φ	0	0	0
B	-0.00005	0	0.06710

(a) Applying the sideband constraint.

	ϵ	Φ	B
ϵ	0.00003	0	-0.00003
Φ	0	0	0
B	-0.00003	0	0.12533

(b) With visual scanning.

Table 5.6: Total fractional covariance matrix of the selection efficiency, $\bar{\nu}_\mu$ flux, and selected background events, combining all background cross section uncertainties.

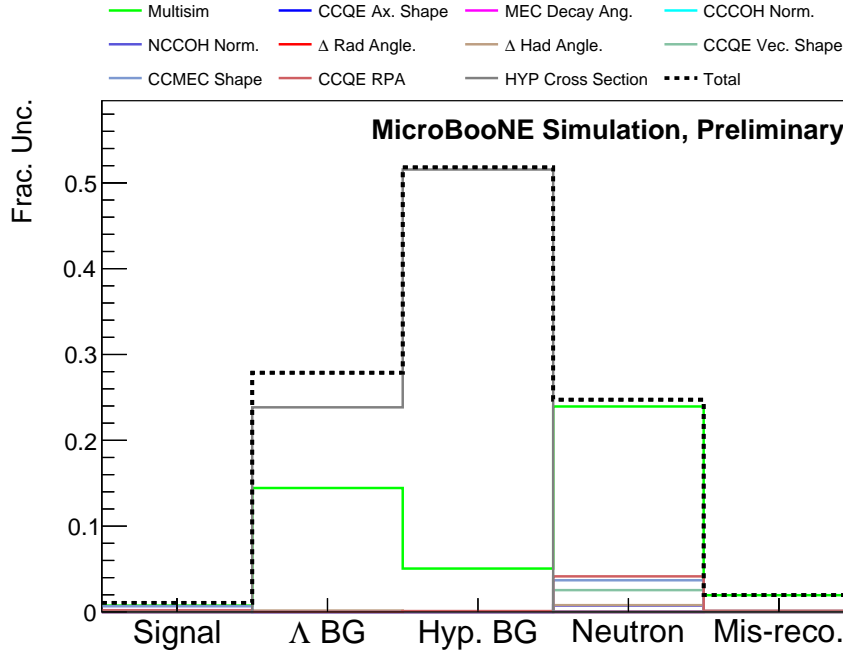


Figure 5.14: Breakdown of fractional uncertainties.

Figure 5.15: Summary of the systematic uncertainties due the cross sections of other neutrino interactions. The dominant sources of uncertainty are the multisim systematics, and the effect these have on the RES and DIS driven hyperon production backgrounds, and the 100% uncertainty applied to the direct hyperon production background.

5.6 Secondary Interactions

After the neutrino interaction has been simulated with GENIE/NuWro, the outgoing particles are propagated through the detector geometry by the GEANT 4 [126] software package. This element of the modelling requires the cross sections of particle-argon interactions. The uncertainties associated with the interactions of five particles with argon nuclei are considered: protons, π^\pm , Λ baryons and neutrons. Uncertainties in the muon-argon scattering cross sections are not included; the rate at which these occur is relatively small as the muon does not participate in the strong interaction, and the muon is not used to calculate any kinematic quantities in the event selection. These uncertainties affect both the selection efficiency, as the event selection is expected to perform worse if the decay products of the Λ rescatter, and the predicted background in the cross section calculation.

Reweighting GEANT 4 Trajectories

With the exception of the neutron uncertainty, the Geant4Reweight [2] package is utilised to propagate these uncertainties. Weights are calculated from the trajectory simulated by GEANT 4 in a procedure described in detail in Ref. [2]. An overview of the method is given here. GEANT 4 simulates two categories of interactions for hadrons: the incident hadron may scatter elastically, exchanging some momentum with a nucleus, leaving both particles intact, or the hadron may propagate into the nucleus, in which case GEANT 4 performs a full cascade simulation. These two categories of processes are labelled by GEANT 4 as elastic and *reaction* respectively.

The path of a particle may be split into a sequence of steps, with the end process of the particle, be that a scatter or decay (or exit from the geometry), occurring at the end of the final step. Weights are generated by calculating the ratios of survival/interaction probabilities at every step of the particle's trajectory. The probability of a particle traversing a distance L of material of number density ρ without interacting is:

$$P_{\text{surv}}(L, \sigma) = e^{-\sigma\rho L}, \quad (5.15)$$

when σ is the total cross section of all interactions. The interaction probability is therefore $1 - P_{\text{surv}}(L, \sigma)$. The weight is then:

$$w = \left(\frac{1 - P_{\text{surv}}(L_N, \sigma'_N)}{1 - P_{\text{surv}}(L_N, \sigma_N)} \right) \left(\frac{\prod_{i=1}^{N-1} P_{\text{surv}}(L_i, \sigma'_i)}{\prod_{i=1}^{N-1} P_{\text{surv}}(L_i, \sigma_i)} \right), \quad (5.16)$$

$$= \frac{1 - e^{-\sigma'_N \rho L_N}}{1 - e^{-\sigma_N \rho L_N}} \exp \left[\rho \sum_{i=1}^{N-1} L_i (\sigma'_i - \sigma_i) \right]. \quad (5.17)$$

Where σ'_N is the alternative interaction cross section being reweighted to. The energy dependence of the cross section has been suppressed for the efficiency of notation. In the case of reweighting individual inelastic exclusive processes, which is performed for charged pions, an additional weight is applied to account for the different probabilities of different final interactions: $w_{\text{int}} = \frac{\sigma'_{\text{int}}}{\sigma_{\text{int}}}$, where σ_{int} is the exclusive cross section for the interaction in the default simulation, σ'_{int} , the alternative model. This assumes a homogeneous medium of constant density ρ . GEANT 4 is programmed to always begin a new step when a particle reaches a boundary between different materials in the detector geometry. In the following uncertainty calculations, only the cross sections of particle-argon scattering are reweighted.

5.6.1 Protons

The version of Geant4Reweight supported by MicroBooNE's software framework during the analysis only supported variations in the total elastic and total reaction cross section². These

²Newer releases of Geant4Reweight are able to reweight exclusive final states of proton interactions, as well as neutrons.

two cross sections are varied simultaneously, to produce a set of 1000 variations, shown in Figure 5.16, with a 20% uncertainty assumed for each cross section. It was decided not fit these cross sections to external data, as the resulting uncertainty with the default setting of 20% is relatively small compared with the other source of uncertainty in this analysis.

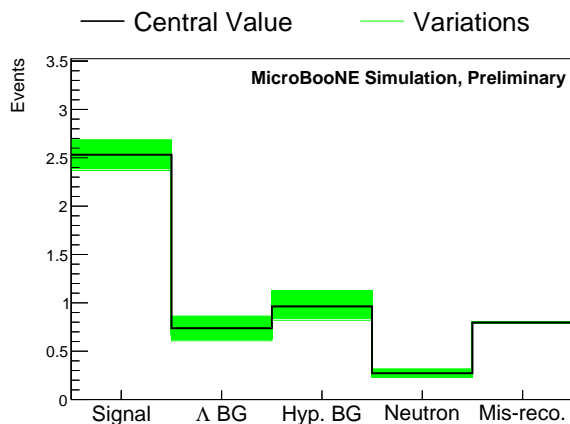


Figure 5.16: Selected signal and background in different proton-argon cross section universes.

5.6.2 Λ Baryons

As with protons, only the total elastic and reaction cross sections for Λ baryons are reweightable. There are no measurements of Λ baryon scattering on argon nuclei, and as with the proton scattering cross sections, 20% input uncertainties are assumed, and the resulting uncertainties on the predicted signal and background are small. The variations are shown in Figure 5.17, and modify the signal and hyperon backgrounds, leaving the neutron and misreconstruction backgrounds unaffected.

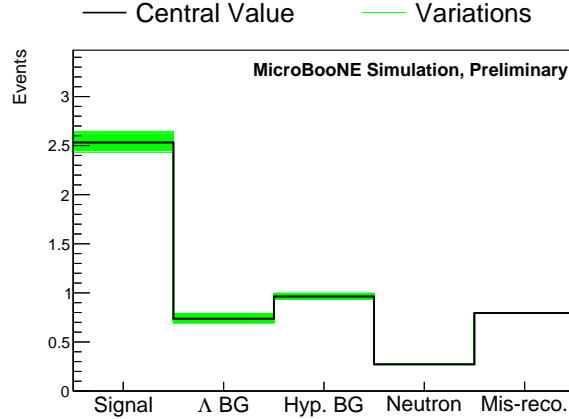


Figure 5.17: Selected signal and background in different Λ -argon cross section universes.

5.6.3 Charged Pions

The variations were generated using a multi-dimensional Gaussian parameterised by a covariance matrix obtained by performing a global fit to available charged pion-nucleus cross section data, fitting several exclusive channels simultaneously.

External Data Fits

Many measurements of pion-nucleus scattering cross sections exist, however their coverage of targets, energies, and final states is very sporadic. To overcome this issue, a global fit to the available data was performed, using measurements of cross sections for targets ranging from He-4 to lead. Measurements of the six exclusive channels exist, listed in Table 5.7. Except for the elastic process, G4 does not store cross sections for these exclusive channels, instead the cross sections are estimated by repeatedly simulating pion-nucleus collisions and recording the rates at which the different final states in Table 5.7 are produced, shown in Figure 5.18.

To perform the fit, a parameter is assigned to each of the six processes in Table 5.7³, which scales the G4 predictions of that channel by the same amount for every target, uniformly across all pion energies. These parameters are fitted by minimising the following χ^2 function:

$$\chi_k^2 = \frac{1}{N_k - p_k} \sum_i^{N_k} \left(\frac{\sigma_i^{\text{Data}} - \sigma_i^{\text{MC}}}{\Delta\sigma_i^{\text{Data}}} \right)^2 \quad (5.18)$$

$$\chi^2 = \frac{1}{N_C + f - 1} \left(\sum_k \chi_k^2 + f\chi_{\text{Total}}^2 \right) \quad (5.19)$$

³No fit to π^- double charge exchange is performed due to a lack of measurements. An uncertainty of 50% is assumed.

σ_i^{Data} are the measurements in the fit, with uncertainties $\Delta\sigma_i^{\text{Data}}$, and σ_i^{MC} the corresponding G4 predictions. Equation 5.18 gives the χ^2 from a single exclusive channel, with N_k measurements, and p_k parameters directly affecting that channel. Equation 5.19 sums together the χ^2 values from the individual channels, with the exception of the total cross section data. A weight f , is applied to the total cross section data to control the “importance” of this data in the fit. If the end user considers the cross sections of exclusive channels unimportant this can be increased. The factor outside of the brackets in Equation 5.19 ensures $\chi^2 \rightarrow 1$ when the average difference between the data and simulation predictions is approximately one standard deviation. As an example, the data available for fitting for the combined cross sections for absorption and charge exchange are presented in Figure 5.19. Tables 5.8 and 5.9 are the covariance matrices yielded by this fit. Future versions of this analysis should try to incorporate measurements on argon from experiments such as ProtoDUNE [155].

Channel	Definition
Elastic (Elast)	$\pi^\pm + N \rightarrow \pi^\pm + N$
Absorption (Abs)	$\pi^\pm + N \rightarrow N'$
Inelastic (Inel)	$\pi^\pm + N \rightarrow \pi^\pm + N'$
Charge Exchange (Cex)	$\pi^\pm + N \rightarrow \pi^0 + N'$
Double Charge Exchange (DCex)	$\pi^\pm + N \rightarrow \pi^\mp + N'$
Pion Production (Prod)	$\pi^\pm + N \rightarrow n\pi + N'$

Table 5.7: List of pion reinteraction channels. The total reaction cross section is sum of the cross sections for absorption, inelastic, charge exchange, double charge exchange, and pion production.

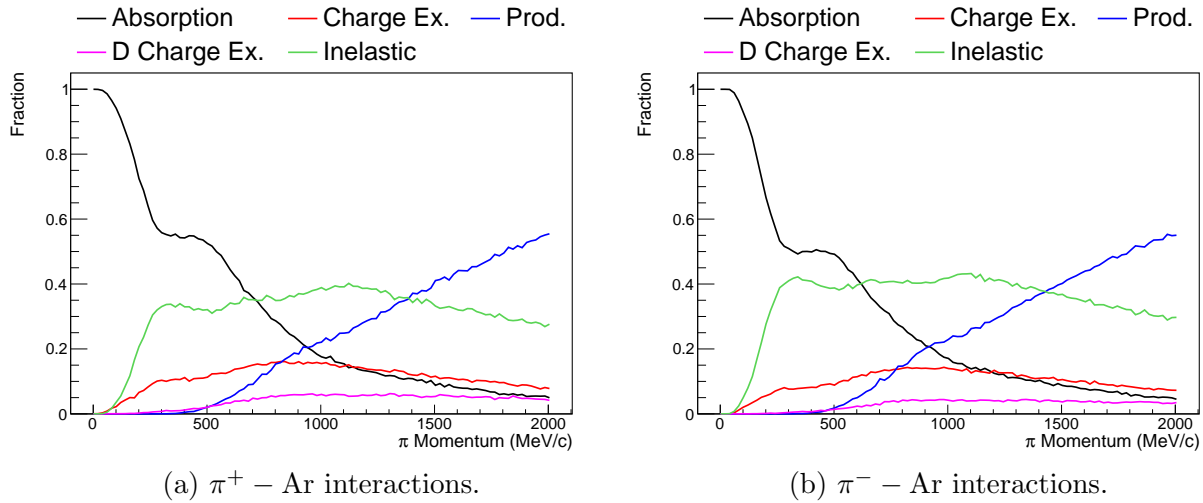
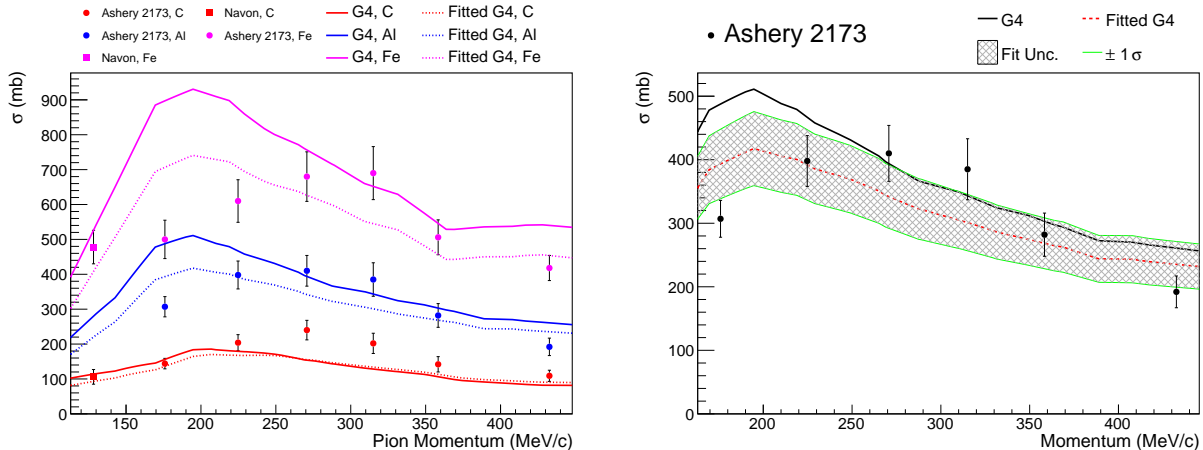


Figure 5.18: Fraction of total pion reaction cross section for five of the exclusive channels listed in Table 5.7, estimating by repeatedly simulating pion-argon collisions.



(a) Data from all targets compared with G4 (b) Data for Al, with fit and uncertainty band. predictions before and after fitting.

Figure 5.19: Data for the combined cross sections of π^+ absorption and charge exchange compared with GEANT 4 predictions, before and after performing the fit. The shaded band in panel (b) shows the uncertainty.

	Abs	Cex	DCex	Inel	Prod	Elast
Abs	0.0116	-0.0126	-0.00580	-0.00371	0.00257	-0.00221
Cex	-0.0126	0.178	-0.0489	-0.0372	-0.000498	0.00564
DCex	-0.00580	-0.0488	0.224	-0.00864	-0.00263	0.0103
Inel	-0.00371	-0.0372	-0.00864	0.0538	-0.0265	-0.0203
Prod	0.00257	-0.000498	-0.00263	-0.0265	0.0247	0.0116
Elast	-0.00221	0.00564	0.0103	-0.0203	0.0116	0.0325

Table 5.8: Covariance matrix obtain from the six parameter fit the the π^+ cross section data.

	Abs	Cex	Inel	Prod	Elast
Abs	0.00726	-0.00579	-0.00326	0.00180	0.00182
Cex	-0.00580	0.146	-0.0481	0.00518	0.00743
Inel	-0.00326	-0.0481	0.0440	-0.0210	-0.0229
Prod	0.00180	0.00518	-0.0210	0.0214	0.0134
Elast	0.00182	0.00743	-0.0229	0.0134	0.0244

Table 5.9: Covariance matrix obtain from the six parameter fit the the π^- cross section data.

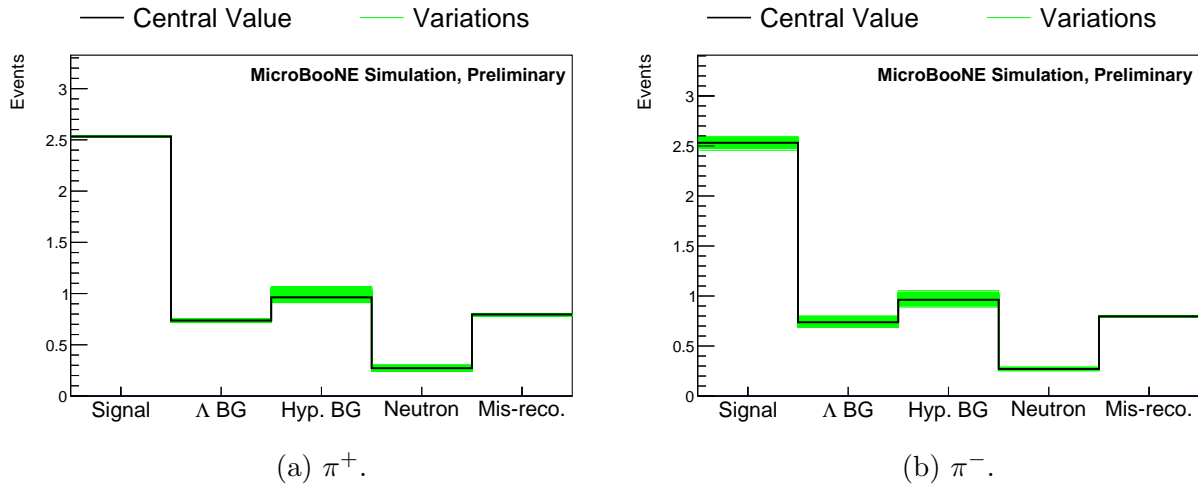


Figure 5.20: Selected signal and background in different charged pion-argon cross section universes.

5.6.4 Neutrons

The event selection will sometimes mistake a pair of charged particles produced in the interaction of a neutron, another process that creates displaced vertices, for a Λ baryon decay. The magnitude of this background is proportional to the cross sections of these secondary interactions. The release of Geant4Reweight available during the development of this analysis does not support neutron reweighting, and as this is predicted to be a relatively small source of background, a simpler approach of assigning a 26% uncertainty to this background was adopted instead of a full reweighting treatment. The 26% uncertainty was obtained from fits to data from the CAPTAIN experiment [156], described below.

CAPTAIN Data

A single neutron total cross section dataset exists for argon in the relevant range of neutron energies, measured by the CAPTAIN collaboration [156], which is compared to GEANT 4 calculations in Figure 5.21. A single parameter fit using MINUIT [148] was performed by scaling the total cross section prediction uniformly across all energies to minimise a χ^2 score. The resulting uncertainty is approximately 26%.

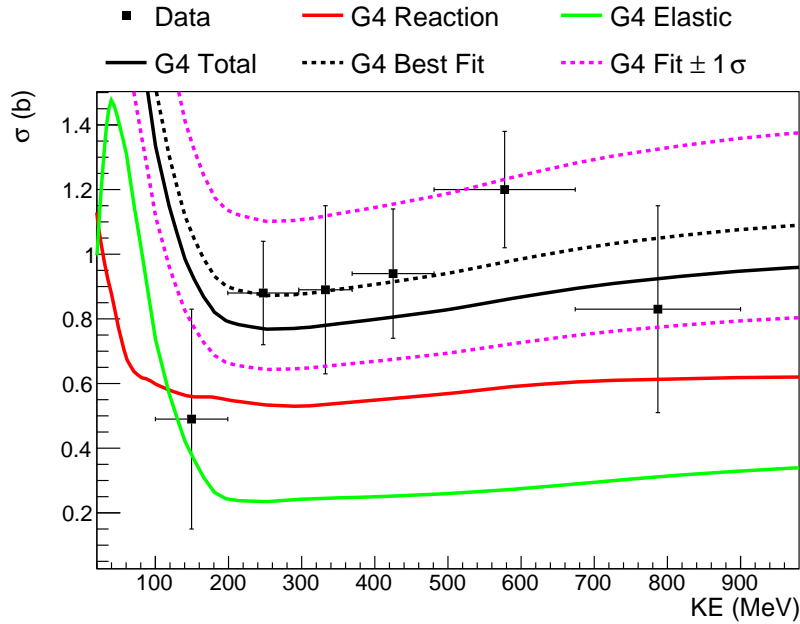


Figure 5.21: Neutron scattering data from the CAPTAIN experiment compared with Geant 4 predictions and single channel best fit.

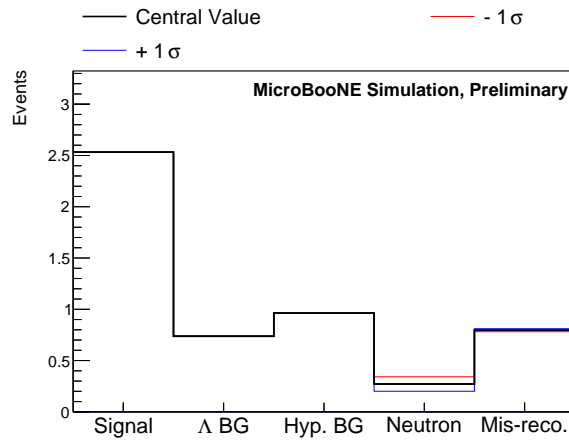


Figure 5.22: Selected signal and background in different neutron-argon cross section universes.

5.6.5 Summary of Secondary Interaction Uncertainties

Comparing the effects of the secondary interaction uncertainties, the largest contribution to the uncertainty in the selection efficiency are the proton-argon interaction cross sections,

	ϵ	Φ	B		ϵ	Φ	B
ϵ	0.00071	0	0.00087	ϵ	0.00071	0	0.00110
Φ	0	0	0	Φ	0	0	0
B	0.00087	0	0.00548	B	0.00110	0	0.00412

(a) Applying the sideband constraint. (b) With visual scanning.

Table 5.10: Total fractional covariance matrix of the selection efficiency, $\bar{\nu}_\mu$ flux, and selected background events, combining all secondary interaction uncertainties.

and in the background the neutron-argon cross section. The final fractional covariance matrices, after applying the hand scanning and sideband constraint procedures, are shown in Tables 5.10b and 5.10a.

It is worth acknowledging the overlap between the physics describing the yields of hadrons from the beam, secondary interactions of hadrons within nuclear remnant in the primary interaction, and secondary interactions. Ideally, the same uncertainties would be applied to all three of these elements of the modelling. This is difficult to implement as these stages of the simulation are performed with different pieces of software. Moreover, the flux simulation is already equipped with data driven uncertainties provided by an experiment that directly measured the hadron yield from the same beam setup (MIPP).

5.7 Detector Response

After propagating particles through the detector geometry with `GEANT 4`, a simulation of the detector response is run. This introduces uncertainties in the quantity of light reaching the PMTs, the size and shape of the signals recorded by the wires, along with effects more difficult to categorise such as the SCE. The selection efficiency and selected background may be sensitive to these effects.

5.7.1 Detector Variations

In contrast with the other uncertainties, the detector response uncertainties are not estimated through reweighting. Instead, sets of MC simulation events with different detector response models are produced, called “detector variations”. These are manufactured by first generating a single set of events with the default flux, event generator, and `GEANT 4` simulations, then passing these events through the default detector response model, and nine alternative models, before reconstructing them. This creates 10 copies of the same events in which the “true” physics is identical, with different detector responses simulated. The systematic

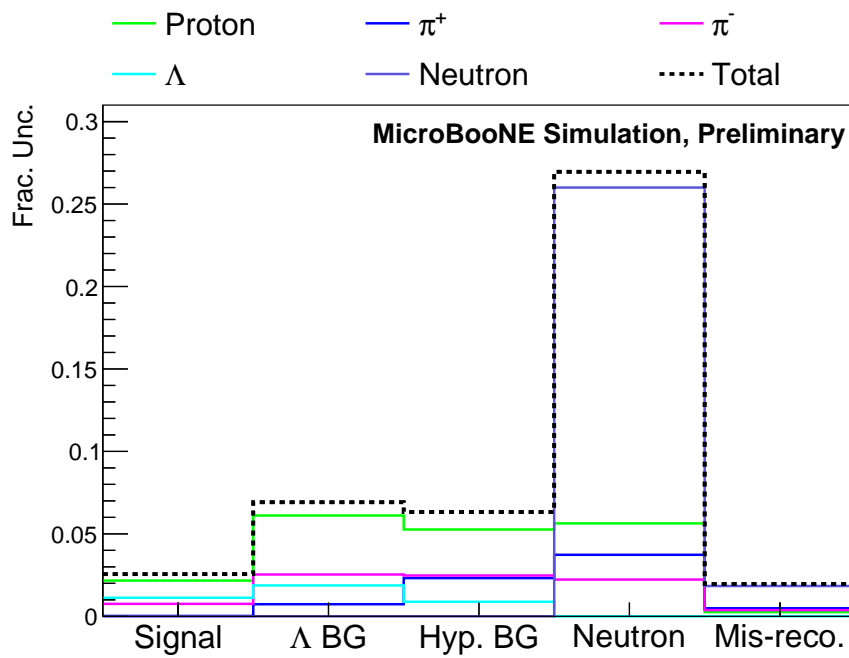


Figure 5.23: Fractional uncertainties in the predicted signal and different sources of background from secondary interaction cross sections, when applying the sideband constraint procedure to the mis-reconstruction background.

uncertainties in the cross section measurement resulting from the detector response modelling may then be established by passing the default simulation and nine detector variations through the event selection and applying the alternative model formula for elements of the covariance matrix, Equation 5.6. Detector variations for the hyperon-only, neutron-only, and background neutrino interaction samples are generated. There are no detector variations for the dirt, as these events have a separate data-driven uncertainty described in Section 5.8.4, and the EXT contribution is estimated from real data and therefore does not require systematic uncertainties. The uncertainties may be broadly grouped into four categories: wire response, light yield (LY), space charge, and recombination, described in Table 5.11.

Variation Name	Description
Drift Direction Wire Response θ_{YZ} Wire Response θ_{XZ} Wire Response $y - z$ Plane Wire Response	Modified shape of the Gaussian hits as a function of track position and direction.
Alternative Space Charge	Modified space charge correction map.
Reduced LY	Reduce quantity of photoelectrons by 25%.
Position Dependent LY	Light yield calculation includes Rayleigh scattering.
Attenuation of LY	Include attenuation effects in LY calculation.
Alternative Recombination	Different electron-ion recombination correction in dE/dx calculation.

Table 5.11: Set of alternative detector models used to estimate related uncertainties.

Statistical Consistency

MC simulation samples are manufactured using a batch computing system, splitting the samples into portions of around 50 events, and which are processed in parallel on many CPUs. One of the advantages of this approach is if an error occurs in the processing of an event, the error is contained to that batch and the remainder of the sample is unaffected.

This is important when estimating uncertainties by comparing separately processed samples, as the final reconstructed detector variations will contain slightly different subsets of the original sample of events simulated to the GEANT 4 stage. If the sets of events from

the default simulation and detector variations are not identical, statistical fluctuations may be mistaken detector response uncertainties. This is prevented by generating a list of events present in the default sample and all nine variations, and only using this subset of events to estimate the uncertainties. Since only a portion of the events in the MC samples are used, the POT estimate for each sample has to be corrected to correspond to the events actually used:

$$\text{POT} = \text{Default Sample POT} \times \frac{\text{N Events In All Samples}}{\text{N Events in Default Sample}} \quad (5.20)$$

5.7.2 Light Yield

The primary function of the light collection system in MicroBooNE is to provide precise timing information utilised by the triggers. The uncertainties resulting from the light yield simulation are estimated to be very small, around 1%. The variations are shown in Appendix D.3.

5.7.3 Wire Response

The modelling of MicroBooNE's detector response was studied extensively in Ref. [157], through comparisons of cosmic-ray data collected by the detector when the beam was inactive to MC simulation using the CORSIKA [158] air shower simulation. The hit charge and hit width distributions were calculated as a function of four variables: the location of the hit in the direction perpendicular to the wire planes, the location of the hit in the plane parallel to the wires, the direction of the track in the $x - z$ plane, and the direction of the track in the $y - z$ plane. These comparisons were used to produce four sets of corrections to the hit charge and width. Four sets of MC simulation samples, one with each of these corrections applied, are compared to the default simulation in Figure 5.24. The resulting uncertainties in the selection efficiency and selected background are all 5% or less.

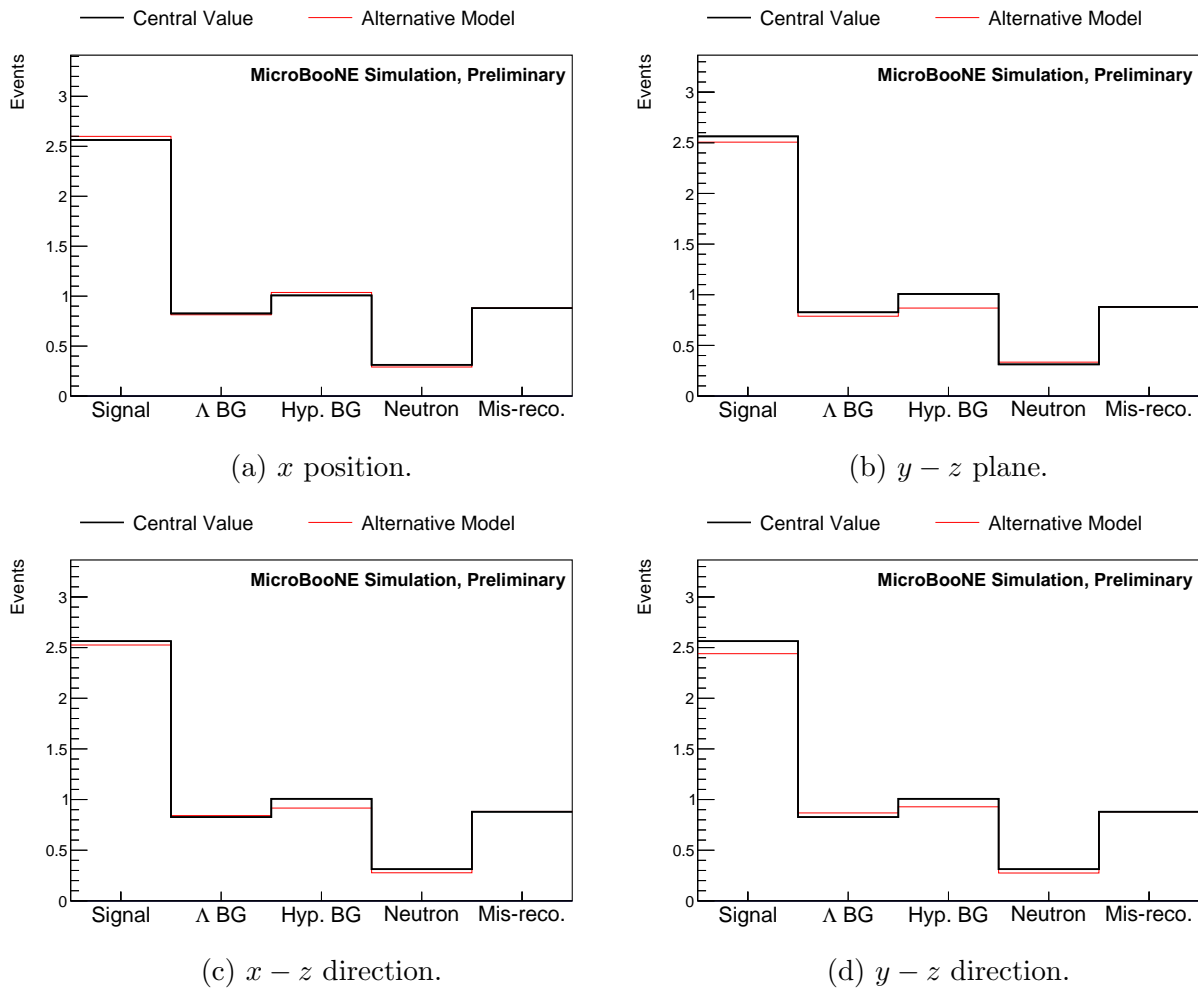


Figure 5.24: Predictions of the signal and background, comparing the default model (central value) to the predictions with the wire response corrections applied (alternative model).

5.7.4 Recombination Model

Recombination refers to the process in which the electrons liberated during the passage of a charged particle through the detector combine with nearby argon ions, thereby reducing the quantity of charge reaching the wires. Alternative settings for the recombination model were obtained through fitting predicted dE/dx values recorded by the wires to calibration data. The predicted rates of signal and background with this alternative model are compared with the default simulation in Figure 5.25. The resulting uncertainties are all small.

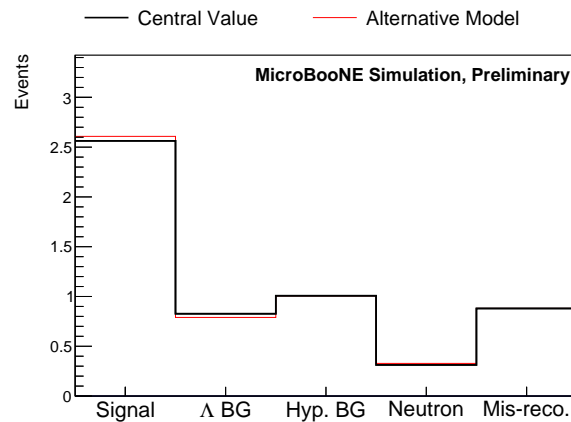


Figure 5.25: The alternative recombination model compared with the default simulation.

5.7.5 Space Charge

The space charge effect was studied by MicroBooNE using cosmic-ray muons in Ref. [123], and with a UV laser system in Ref. [159]. These were used to estimate the severity of the space charge effect by comparing the locations of hits in the detector from the muons/laser to their expected positions under the assumption the muons/laser photons travelled through the detector in straight lines. These were used to create a data-driven alternative space charge map, in which the space charge corrections near the edges of the TPC are estimated with cosmic ray muons, and near the centre they are estimated with the UV laser method. The data-driven SCE map is used as the alternative model, compared to the default in Figure 5.26.

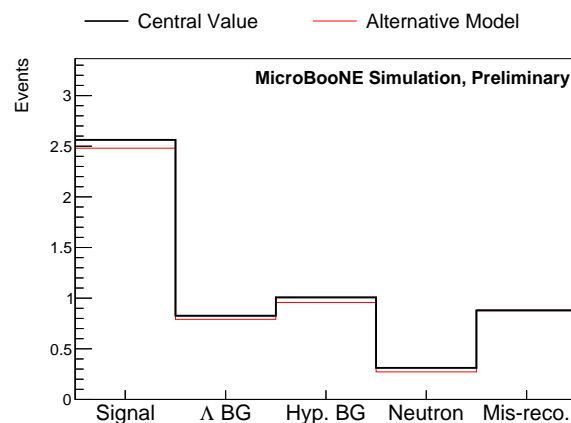


Figure 5.26: Extraction of the systematic uncertainties from the space charge map.

	ϵ	Φ	B		ϵ	Φ	B
ϵ	0.00469	0.00000	0.00414	ϵ	0.00469	0.00000	0.00552
Φ	0.00000	0.00000	0.00000	Φ	0.00000	0.00000	0.00000
B	0.00414	0.00000	0.00658	B	0.00552	0.00000	0.02412

(a) Applying the sideband constraint. (b) With visual scanning.

Table 5.12: Total fractional covariance matrix of the selection efficiency, $\bar{\nu}_\mu$ flux, and selected background events, combining all secondary interaction uncertainties.

5.7.6 Detector Uncertainties Summary

A breakdown of the systematic uncertainties belonging to the detector response model is shown in Figure 5.27. The contributions to the fractional covariance matrices of the selection efficiency, flux, and selected background, from the detector response uncertainties are shown in Tables 5.12a, and 5.12b; the detector response is the largest source of uncertainty in the selection efficiency, apart from the cross section shape discussed in the next section.

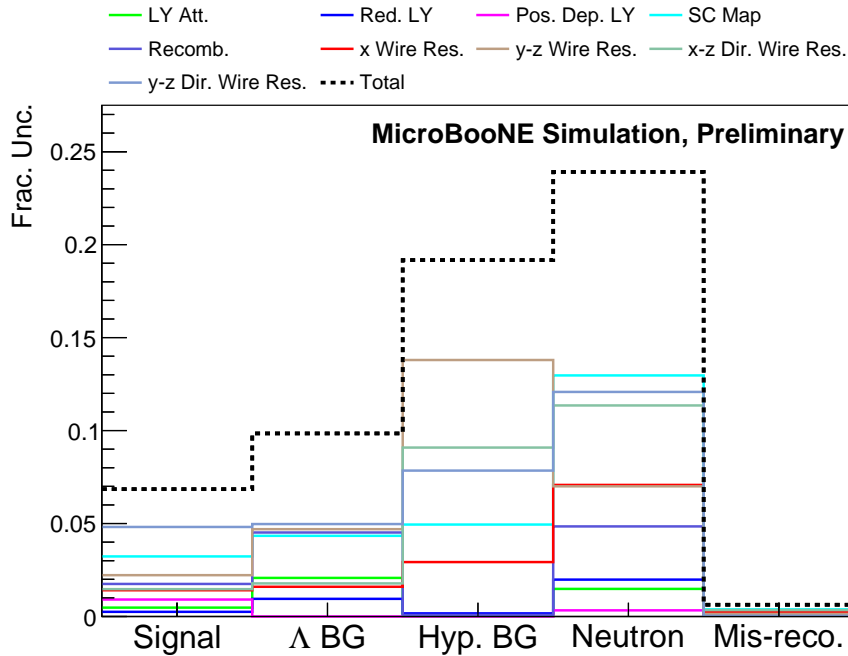


Figure 5.27: Fractional uncertainties in the selected signal and different sources of background from the detector response modelling.

5.8 Miscellaneous

Several other sources of systematic bias are considered that do not fall into one of the categories already discussed. These include the efficiency and background rejection power of the visual scanning, the statistical uncertainty in the sideband fit, and the shape of the signal cross section and the effect this has on the selection efficiency.

5.8.1 Visual Scanning

Five hand scanners were used to establish the reliability of hand scanning as a method to remove the bad-reconstruction background after applying the automated event selection, by reviewing a sample containing a mixture of the signal and the four categories of background surviving the automated event selection from the previous chapter. The results of this study are reported in Table 5.1. To estimate the systematic uncertainty, a set of systematic variations are constructed from the results of each scanner, by applying the following weights to the MC simulation events passing the automated selection:

$$w_{ib} = \frac{\text{Events from category } b \text{ selected by scanner } i}{\text{Total events from category } b \text{ in the HS sample}}. \quad (5.21)$$

b corresponds to one of the five categories of selected background, and $i = \{1 \dots 5\}$. The prediction in the i th universe for the b th bin in Figure 5.28 is obtained by multiplying the prediction from Figure 5.1 by w_{ib} . The resulting covariances of the selected backgrounds are estimated by applying the multisim technique to these five predictions.

While the visual scanning is extremely effective at removing the mis-reconstruction background, and removes some of the other backgrounds too, at a relatively little cost in the efficiency, this method does introduce significant systematic uncertainties. The sensitivity will be compared to the result obtained when applying the sideband constraint method. The application of the visual scan to data, including how blindness is maintained, will be explained in Section 6.2.

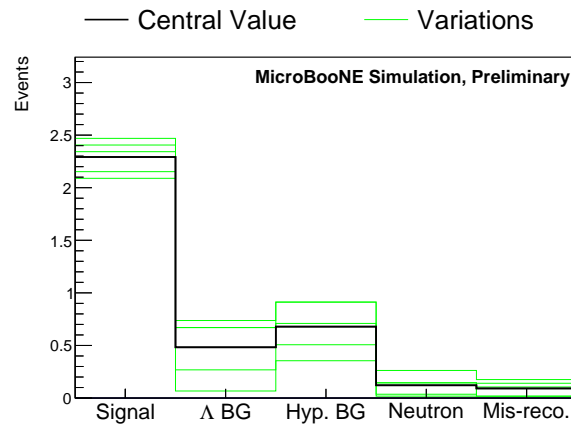


Figure 5.28: Variations obtained from the hand scanning weights, compared with the central value prediction when using the hand scanning technique.

5.8.2 Sideband Fit Uncertainty

An additional uncertainty must be applied to the mis-reconstruction background to account for the limited data and MC simulation statistics available in the sideband region. The scale to be applied to the mis-reconstruction background in the central value universe was 0.90 ± 0.17 , and so an uncertainty of $0.17/0.9 \approx 19\%$ is required. The resulting variations are shown in Figure 5.29.

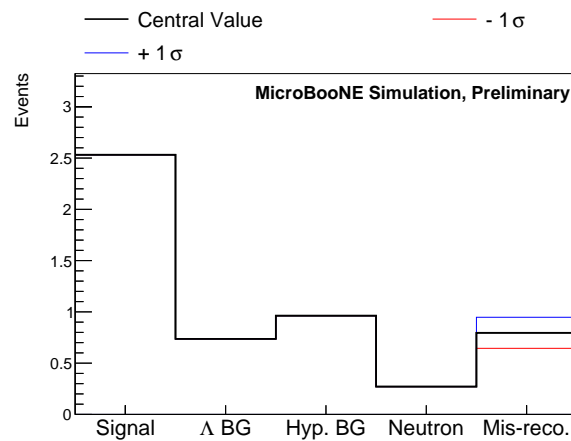


Figure 5.29: Variations employed to propagate the sideband fit statistical uncertainty.

5.8.3 Signal Selection Efficiency

At the end of Chapter 4, the selection efficiency was calculated with two event generators, GENIE and NuWro, with GENIE performing better. A study of the dependence of the selection efficiency also shows some shape dependence. The uncertainties in the efficiencies calculated with both generators do not rule out a statistical fluctuation as the explanation for the difference efficiencies, but as a precaution an additional uncertainty in the selection efficiency is applied to account for any possible model dependence.

Two methods for obtaining this uncertainty were explored: calculating the differential cross sections with extreme variations in several model parameters, and estimating the resulting changes in the efficiency, and using the difference in efficiency when employing NuWro and GENIE to simulate the signal as an uncertainty. Whichever provides the more conservative value will be used.

M_A and Binding Energy Variations

The shapes of the cross section were calculated in terms of four different variables: Q^2 , Λ baryon momentum, $\cos\theta_\mu$, and neutrino energy, for both event generators. The cross section shape curves for the momentum of the Λ baryon are presented in Figure 5.30. These distributions were used to reweight the predictions of the generators, giving alternative efficiency values. The largest change in efficiency was obtained by varying the hyperon-nucleus potentials, with the extreme values obtained from the four variations being 5.3% and 6.2%, compared with a nominal efficiency from the NuWro MC simulation sample of 5.5%.

The selection efficiencies calculated using interactions in the MicroBooNE cryostat simulated with GENIE and with NuWro were found to be 6.8% and 5.5% at the end of Chapter 4. The relative difference between the selection efficiencies between the two generators, $(0.068 - 0.055)/0.068 \approx 19\%$, is used instead to be conservative.

5.8.4 Out-of Cryostat Contribution

While event selection rejects all out-of-cryostat neutrino interactions in the MC simulation samples, this component does appear the data to simulation comparisons in Appendix F, and in the sideband. It is very computationally expensive to apply the reweighting treatments to these events as they often contain $\mathcal{O}(10 - 100)$ simulated neutrino interactions in every beam spill. Instead, a simple scaling uncertainty is applied to this component of any prediction, obtained by performing fits to dirt rich sidebands. The extracted uncertainty is $\pm 71\%$.

The small quantity of dirt in the sideband means the fit yields slightly different values when the dirt contribution is varied, which in turn affects the estimation of the misreconstruction background in the signal region. The systematic uncertainty in the misreconstruction background from this effect is 0.6%. When using the visual scan technique, this uncertainty is zero.

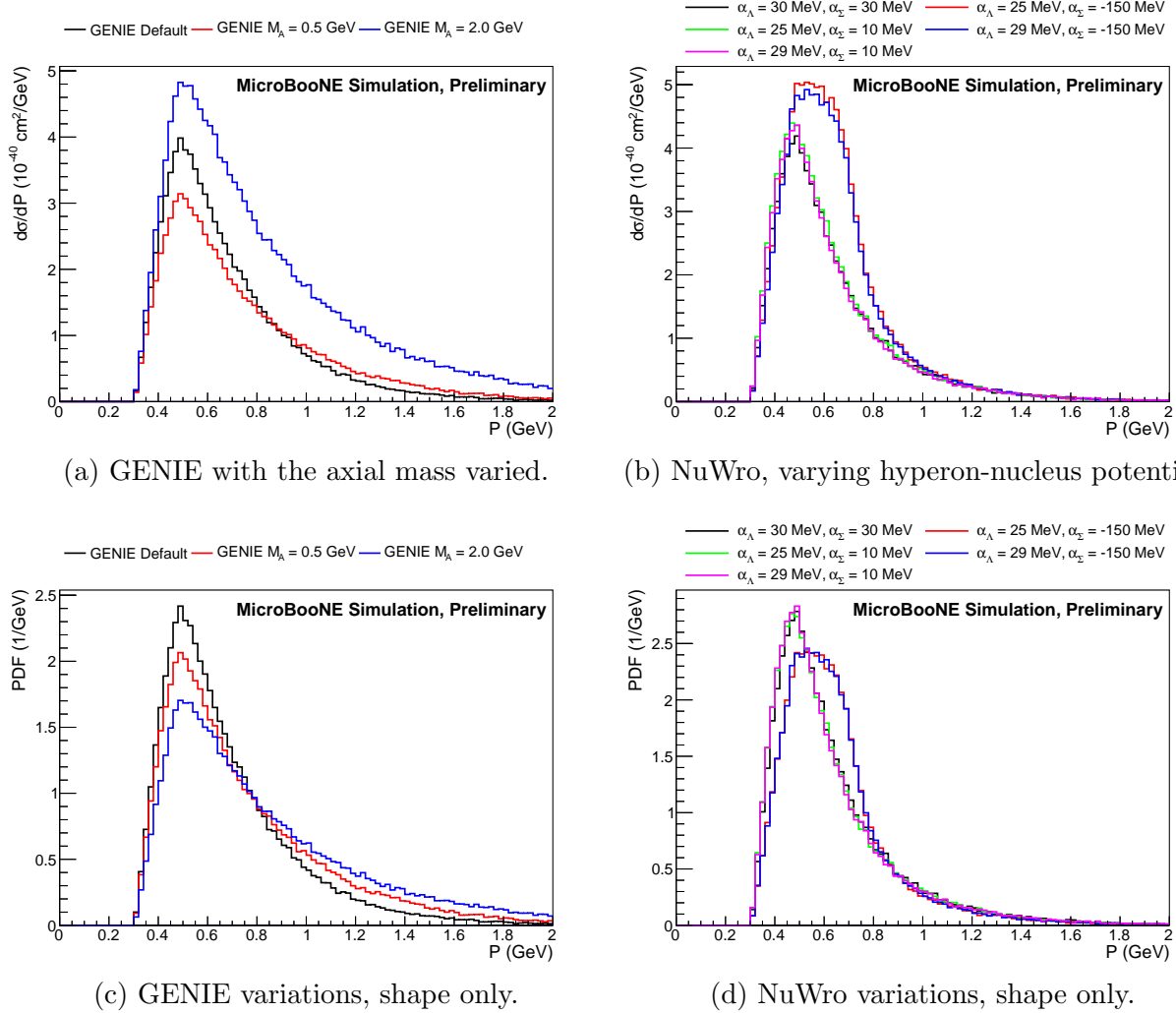


Figure 5.30: The shapes of the cross section curves for the signal, after applying the phase space correction. The black curves in both plots give the default simulation settings for the two generators used in this analysis, and used in the efficiency estimates. In the case of GENIE, the default axial mass is 0.96 GeV, which is compared to the predictions when using axial masses of 0.5 GeV and 2.0 GeV. The hyperon-nucleus potentials were varied for NuWro. The values used in the simulation samples in this thesis are $\alpha_\Lambda = 30$ MeV and $\alpha_\Sigma = 30$ MeV. These are old default settings from NuWro prior to the release of NuWro 21, chosen for consistency with Ref. [160].

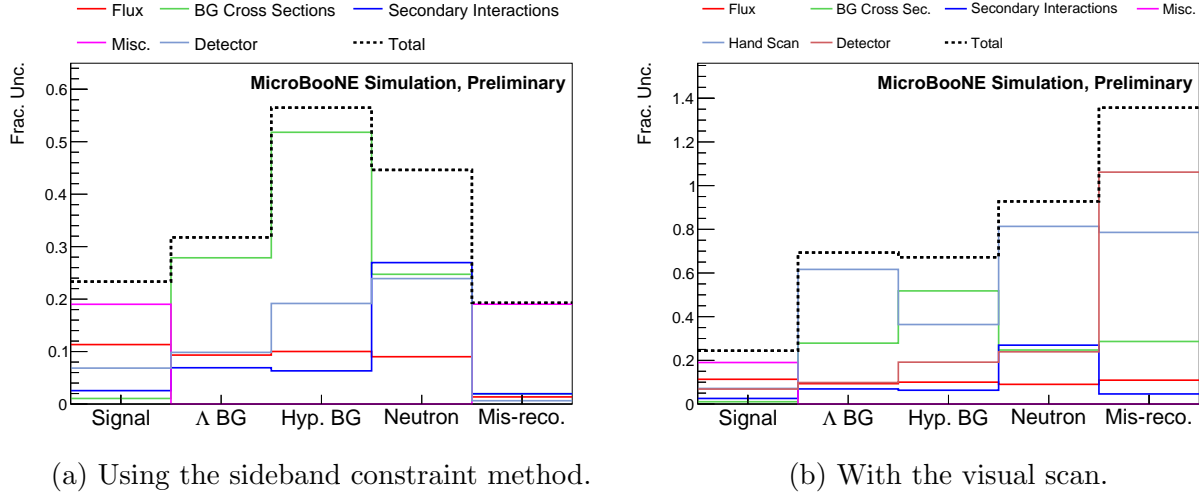


Figure 5.31: Breakdown of fractional uncertainties into the main categories described above, along with MC simulation statistical uncertainties, estimated with a Gaussian approximation.

5.9 Summary of Systematic Uncertainties

The fractional uncertainties in the number of events from the signal and different categories of background predicted by MC simulation, broken down into the main categories from the previous sections, are shown in Figure 5.31. The largest source of uncertainty in the selected signal is the shape of the signal cross section, with the total uncertainty in the number of signal events predicted by the GENIE model being approximately 24%. The visual scan does not introduce a significant uncertainty into the signal efficiency, but does become one of the dominant uncertainties in the estimation of the background; this procedure was found to be less reliable when applied to the different sources of background. Very small systematic uncertainties in the mis-reconstruction background are obtained when applying the constraint procedure, though this is partially counteracted by the statistical uncertainty in the fit itself.

The final fractional covariance matrices, encoding all systematic uncertainties between the selection efficiency, flux, and selected background, are shown in Tables 5.13a, and 5.13b. When applying the sideband constraint procedure, the final fractional uncertainty in the selected background events is 30%, compared with 60% when applying the visual scanning method. However, these are fractional uncertainties, and when combined with the reduction in background expected from the visual scan, the uncertainties in the total selected background are equal to one significant figure at ± 0.8 events. The final uncertainty in the selection efficiency⁴ is approximately 20%, and the uncertainty in the muon anti-neutrino flux around 23%.

⁴The uncertainty in the efficiency, and the predicted signal are not equal, as the flux uncertainties do not have to respect unitarity.

	ϵ	Φ	B		ϵ	Φ	B
ϵ	0.04163	-0.00116	0.00473	ϵ	0.04572	-0.00116	0.03237
Φ	-0.00116	0.05339	0.01255	Φ	-0.00116	0.05339	0.01887
B	0.00473	0.01255	0.08721	B	0.03237	0.01887	0.33123

(a) Applying the sideband constraint. (b) With visual scanning.

Table 5.13: Total fractional covariance matrix of the selection efficiency, $\bar{\nu}_\mu$ flux, and selected background events, combining all systematic uncertainties.

Neglected Effects

Given the MC simulation predicts the number of events selected to be ~ 5 , and therefore the fractional data statistical uncertainty will be around $1/\sqrt{5} \sim 45\%$, small sources of systematic uncertainty may be ignored. The following uncertainties are neglected: the uncertainty in the density of argon and volume of the fiducial volume, both of which affect the number of targets in the cross section calculation, and the branching fraction for $\Lambda \rightarrow p + \pi^-$, the uncertainty in which is $< 1\%$.

Sidebands

In addition to the systematic uncertainties, sidebands were constructed from two variables, the invariant mass of the Λ candidate, and the angular deviation. To construct the distribution of one of these variables, the full event selection minus the kinematic variable cuts was applied. The cut to one the two kinematic variables would be applied, and the resulting distribution of the other was drawn. This was performed for data using the NuMI flux, and the BNB flux, and the results are shown in Figure F.12. The signal region is kept blind in the case of the NuMI flux. No unexpected features are seen in these sideband distributions. Event displays of the events in these sidebands were inspected for any Λ production-like interactions, which would indicate dangerous mis-modelling of the selected background. None were found.

5.10 Cross Section Extraction

The calculations of all relevant systematic uncertainties have been described. These are now combined with the statistical uncertainties to produce estimates of sensitivity. As already described, the statistical uncertainties in this analysis are non-Gaussian, and to try and propagate the effects of asymmetric uncertainties the uncertainties into the final cross section measurement, a procedure based around generating pseudo-experiments was adopted. The

cross section is repeatedly calculated with:

$$\sigma_* = \frac{N - (B + B_0\alpha_B)}{T(\Phi + \Phi_0\alpha_\Phi)\Gamma(\epsilon + \epsilon_0\alpha_\epsilon)}, \quad (5.22)$$

similar to Equation 2.17, but with the following alterations: N , B and ϵ are sampled from distributions to incorporate their statistical uncertainties, which will be described in Sections 5.10.1 and 5.10.2. $\alpha_\epsilon, \alpha_\Phi$, and α_B are systematic shifts, sampled from a three dimensional Gaussian distribution, parameterised by their fractional covariance matrix, which are multiplied by their respective predictions from the default MC simulation, ϵ_0 , Φ_0 , and B_0 . All six parameters are varied simultaneously, and the resulting distribution in the values of σ_* , provides the sensitivity to the cross section. More precisely, this is the Bayesian posterior probability distribution of the signal cross section. The decision to use Bayesian statistics in this analysis is primarily motivated by the lack of any readily available frequentist estimators of the MC simulation statistical uncertainty that will correctly interpret individually weighted events.

5.10.1 Data Statistical Uncertainties

The number of events observed in the data is a single observation, N_{obs} , of a Poisson distributed random variable, with a mean value N . The effect of the statistical uncertainty in the number of data events observed can therefore be propagated through application of Bayes' theorem to the Poisson distribution, obtaining a posterior distribution for N with:

$$P(N|N_{\text{obs}}) = \frac{P(N_{\text{obs}}|N)P(N)}{\int_a^b P(N_{\text{obs}}|N)P(N)dN}. \quad (5.23)$$

The function $P(N)$ is the prior distribution of N . A uniform prior over the interval $[a, b] = [0, 20]$ is used. Examples of the posterior distribution $P(N|N_{\text{obs}})$, when $N_{\text{obs}} = 0 \dots 7$, are shown in figure 5.32.

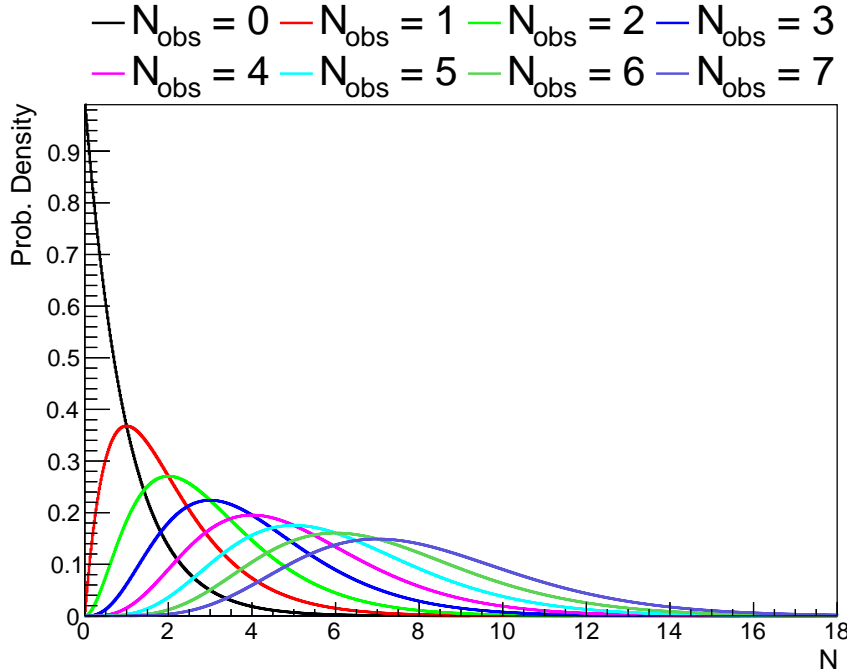


Figure 5.32: The Bayesian posterior probability distributions describing the data statistical uncertainties for different values of N_{obs} , calculated with Equation 5.23.

5.10.2 Monte Carlo Statistical Uncertainties

As with the data, the MC events have relatively low statistics for some sources of background and the resulting statistical uncertainties cannot be assumed to be Gaussian. The TEfficiency class from Root [161], is employed to calculate the Bayesian posterior distributions of the selection efficiency, and selected background. It can be shown that, when the Beta distribution is used as a prior, the Bayesian posterior distribution of the efficiency, $P(\epsilon)$, is given by:

$$P(\epsilon) = \text{Beta}(\epsilon, a, b), \quad (5.24)$$

$$a = \alpha + k, \quad (5.25)$$

$$b = \beta + n - k. \quad (5.26)$$

α and β are the parameters of the Beta distribution. $\text{Beta}(x, 1, 1)$ is the uniform distribution with $x \in [0, 1]$. k is the number of selected events and n the total number of events in the sample. As a weighed, inhomogeneous sample of MC simulation events is used, these

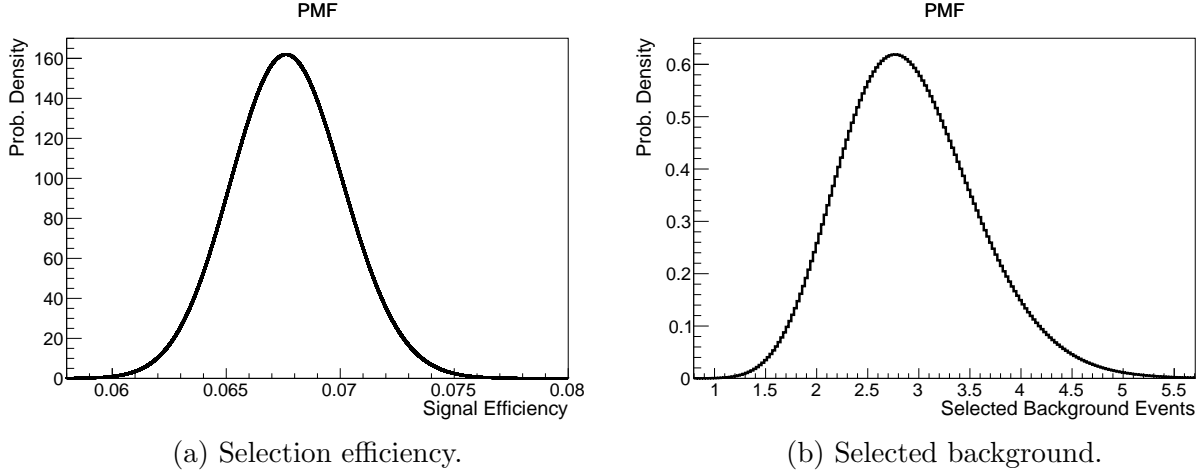


Figure 5.33: Bayesian posterior probability distributions used to describe the MC statistical uncertainties on the signal selection efficiency and selected background. In this instance, the sideband constraint method was used. Similar curves are produced when employing the hand scanning procedure, except the background prediction is centred around 1.5 events.

quantities become:

$$k = \hat{\epsilon}\hat{N}, \quad (5.27)$$

$$\hat{\epsilon} = \frac{\sum_{\text{sel}} w_i}{\sum_{\text{all}} w_i}, \quad (5.28)$$

$$\hat{N} = \frac{(\sum_{\text{all}} w_i)^2}{\sum_{\text{all}} w_i^2}, \quad (5.29)$$

$$n = \hat{N}. \quad (5.30)$$

$\sum_{\text{all}} w_i$ indicates a summation of the weights of all of the events in the population, while $\sum_{\text{sel}} w_i$ only includes events passing the selection. The above formulae may be used to separately calculate the signal selection efficiency and the background acceptance. Multiplying the latter by the total predicted background before any event selection is applied gives the posterior distribution of the number of selected background events.

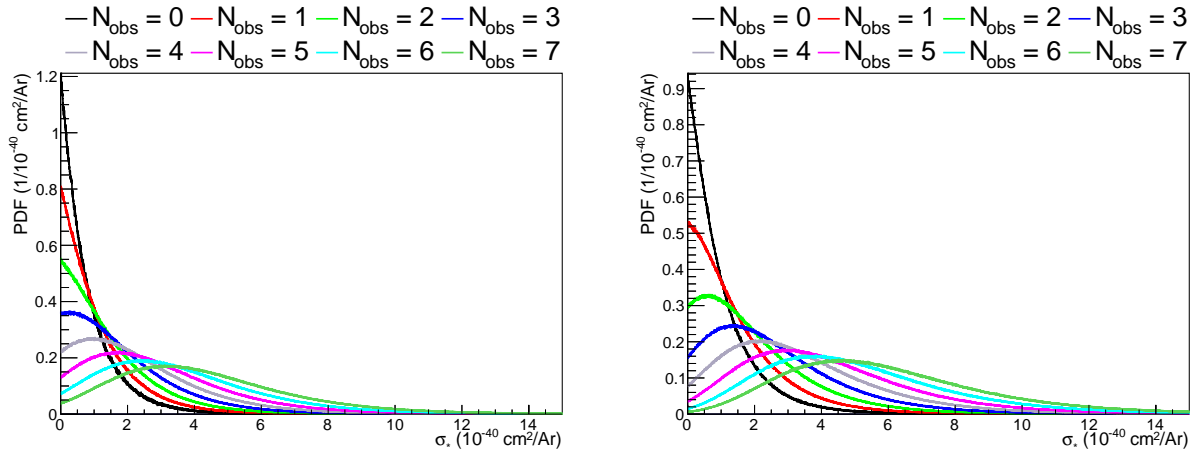
Visual Scanning and Sideband Constraint

In the predicted signal and background distributions, shown in earlier sections of this chapter, the effects of the visual scanning and sideband constraint are incorporated into the central value predictions by applying weights to the selected events. The effects of these corrections

are propagated into posterior distributions by multiplying the terms in the numerator of Equation 5.28 by the same weights.

5.10.3 Sensitivity

The final posterior probability distributions of the cross section, applying both the sideband constraint and hand scanning procedures, and incorporating all sources of uncertainty described, are shown in Figure 5.34, and indicate the sensitivity of the measurement. The data will be unblinded in the next chapter, and the procedure for extracting a cross section value and uncertainty from these distributions will be described.



(a) Employing the sideband constraint procedure.

(b) Applying visual scanning method.

Figure 5.34: Bayesian posterior probability distributions of the partial phase space cross section. The curves when using the hand can procedure yield larger values of σ_* for the same values of N_{obs} due to the small number of predicted background events and lower selection efficiency when using this method.

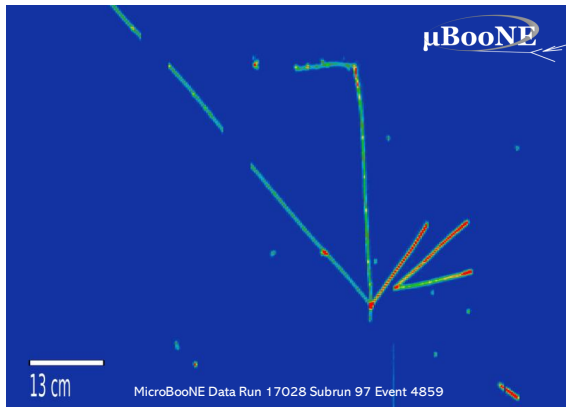
Chapter 6

Result and Summary

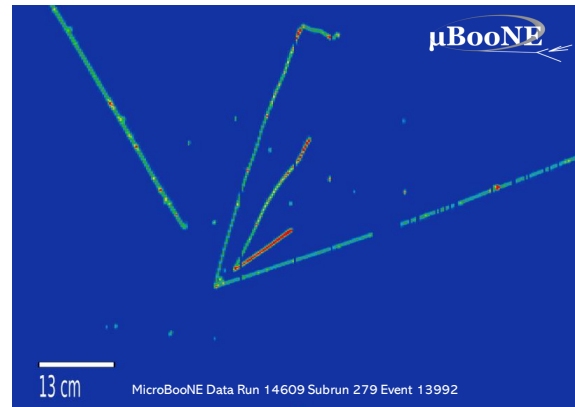
6.1 Selected Data

During the development of the event selection and systematics calculations, the data was kept blind save for the data to MC simulation comparisons in Appendix F, all of which were used to confirm the event selection leverages well modelled quantities, and are insensitive to the signal cross section. The complete event selection was never applied to data. After the decision to unblind the data was made, the automated event selection was applied to the data, and identified five Λ candidates. Event displays of these five events are shown in Figure 6.1. This information was not shared until the visual scanning, described in the next section, was completed to maintain blindness.

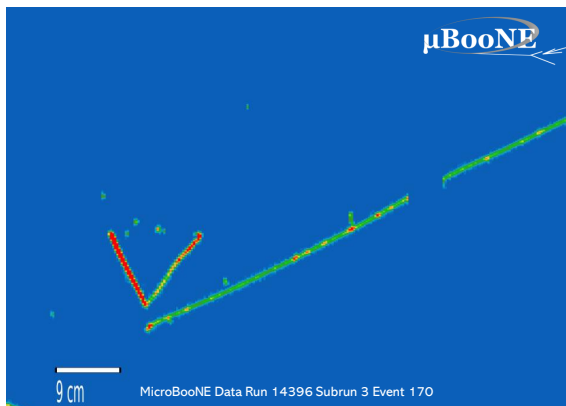
If an interpretation of these event displays has to be made, Figures 6.1c, and 6.1e, show CCQE-like Λ production interactions, while Figures 6.1a, and 6.1b contain RES/DIS Λ production events, especially given both contain L-shaped tracks which are potentially charged kaons, and Figure 6.1d is a CCQE-like Σ^0 event, in which the trail of ionisation pointing to the bottom left of the display is a photon that was not reconstructed. This is an interpretation only and should be viewed with some scepticism.



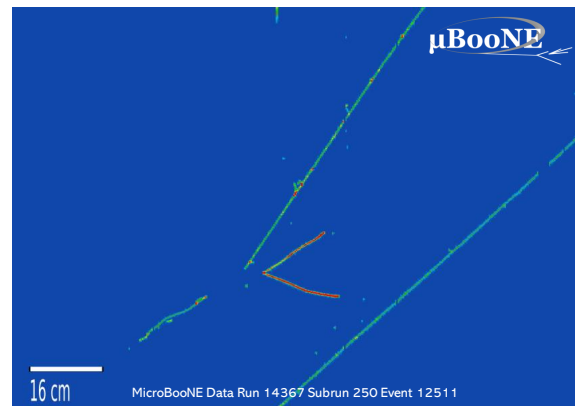
(a) Run 17028 subrun 97 event 4859.



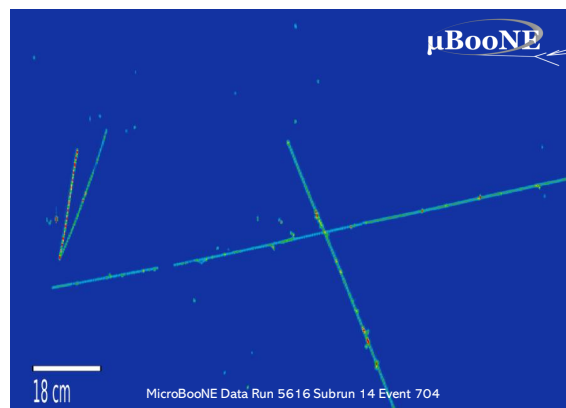
(b) Run 14609 subrun 279 event 13992.



(c) Run 14396 subrun 3 event 170.



(d) Run 14367 subrun 250 event 12511.



(e) Run 5616 subrun 14 event 704.

Figure 6.1: The Λ candidates identified in the data by the automated selection.

Run	Subrun	Event	Sc. 1	Sc. 2	Sc. 3	Sc. 4	Sc. 5
17028	97	4859			✓		✓
14609	279	13992	✓		✓		
14396	3	170	✓	✓	✓	✓	✓
14367	250	12511	✓	✓	✓	✓	✓
5616	14	704	✓	✓	✓	✓	✓

Table 6.1: The events selected from the data by each of the five scanners.

6.2 Visual Scan of Data

In order to compare data to the predictions made using the visual scanning technique, the same visual scan must be applied to the selected data. To preserve blindness, the events from the data selected by the automated event selection were mixed with MC simulation events. As with the test study described in Section 5.3.2, the MC simulation events contain a mixture of signal and the different varieties of background, and the events were scrambled and stripped of identifying labels. The process of preparing these events was automated, and 50 – N simulation events mixed with the N selected data events, concealing both the number of data events in the sample, and which events were simulation and which were data. An additional benefit of including simulation events is that the performance of the scanners on this new set of simulation events may be compared with the results of the test study to check for consistency. These comparisons are shown in Figure 6.2. All results are consistent within two standard deviations. The results of the visual scanning for the five data events are listed in Table 6.1.

Combing Different Scan Results

The final sensitivity is reported in Section 5.10 in the form of Bayesian posterior probability distributions, with a different distribution describing the result for different numbers of events observed after the final unblinding. The visual scanners reported different numbers of selected events and these distributions must therefore be combined somehow. This is performed by calculating a weighted average of the distributions in Figure 6.3a:

$$P_{\text{VS}}(\sigma_*) = \frac{1}{5} (2P_3(\sigma_*) + 2P_4(\sigma_*) + P_5(\sigma_*)), \quad (6.1)$$

in which $P_N(\sigma_*)$ is the posterior distribution for $N_{\text{obs}} = N$ events in Figure 6.3a.

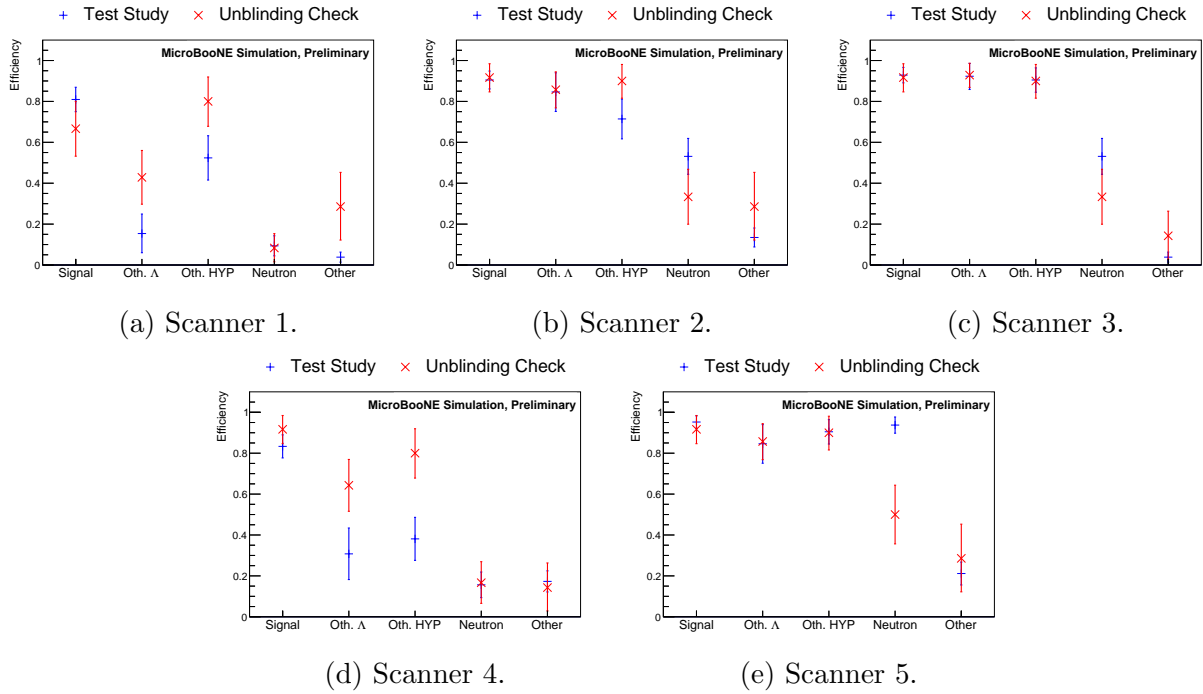
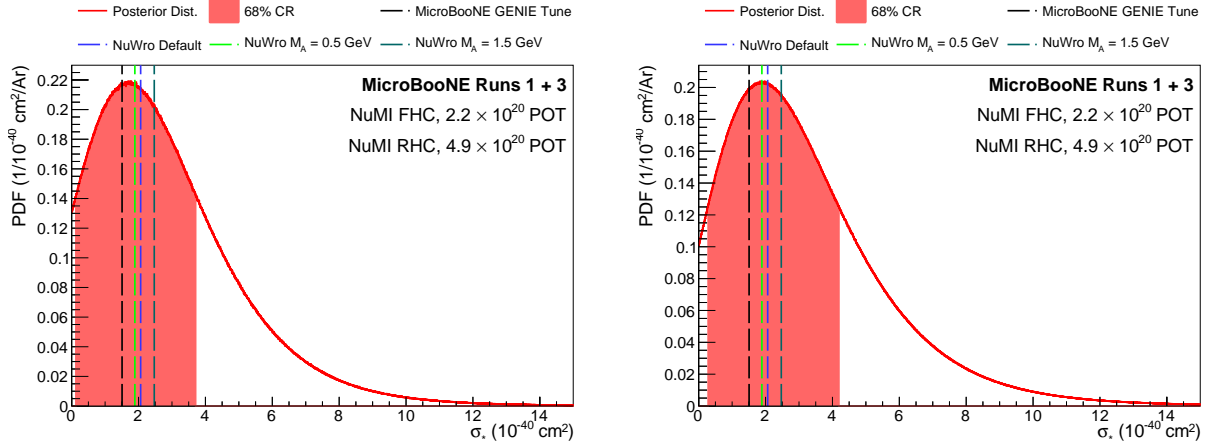


Figure 6.2: The uncertainties are obtained by applying the Bayesian method described in Section 5.10.2. As a rough method to quantify the level of agreement, a reduced χ^2 score is calculated, giving $\chi_n^2 = 35.8/25$, which yields a p value of 0.06. This indicates a weak but not unacceptable level of agreement. The uncertainties in this calculation are the sum in quadrature of the “inner” pair of uncertainties.



(a) Using the sideband constraint method.

(b) Applying the visual scanning method.

Figure 6.3: Final partial phase space cross section distributions. The extracted cross sections are $\sigma_*^{\text{SC}} = 1.8_{-1.6}^{+2.0} \times 10^{-40} \text{ cm}^2/\text{Ar}$ and $\sigma_*^{\text{VS}} = 2.0_{-1.7}^{+2.2} \times 10^{-40} \text{ cm}^2/\text{Ar}$ respectively.

6.3 Cross Section Measurement

Starting with the modal bin, a 68% Bayesian credible interval is constructed by successively adding bins of decreasing height from the posterior distribution until an interval with a probability content of 68% is obtained. Quoting the limits of this interval alongside the modal value of the posterior distributions yields to the following pair of cross section values:

$$\sigma_*^{\text{SC}} = 1.8_{-1.6}^{+2.0} \times 10^{-40} \text{ cm}^2/\text{Ar}, \quad (6.2)$$

$$\sigma_*^{\text{VS}} = 2.0_{-1.7}^{+2.2} \times 10^{-40} \text{ cm}^2/\text{Ar}, \quad (6.3)$$

when employing the sideband constraint and visual scanning methods respectively. The final posterior distributions using the two methods, with the credible intervals indicated as the red filled regions, are shown in Figure 6.3. The results of the two methods are consistent with one another. Predictions from the GENIE and NuWro generators are indicated by the vertical lines. All generator predictions are consistent with these measurements.

6.4 Distributions

While this analysis is not equipped with sufficient statistics to measure differential cross sections, it is possible to compare the positions of the individual data events in terms of interesting variables to the distributions predicted by MC simulation, and check for any unexpected features. Five variables are shown: the reconstructed invariant mass of the Λ baryon candidate, the reconstructed momentum of the Λ baryon candidate, the opening

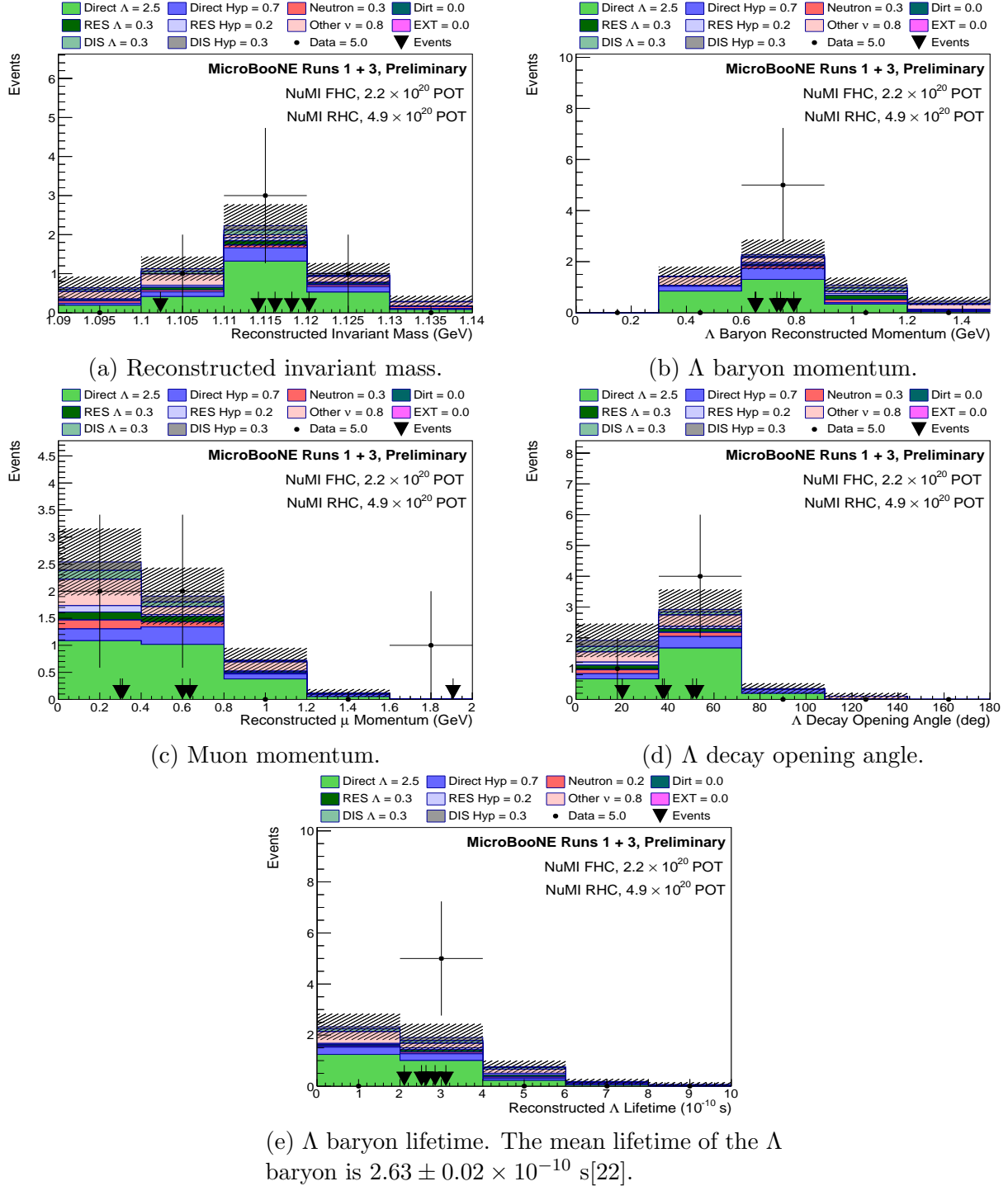
angle between the proton and π^- tracks, the reconstructed momenta of the muon candidate, and the estimated lifetime of the Λ baryon. The muon's momentum is estimated from its range and is calculated using the tables published by the Particle Data Group in [162]. One potentially noteworthy feature is the single event (shown in Figure 6.1e) in which the estimated muon momentum is approximately 1.9 GeV, located in a region in which the MC simulation predicts almost no events. Though this should be viewed with some caution as this is only a single event.

6.5 Outlook

The sensitivity of the measurement is limited by statistics, and the greatest improvement in sensitivity can be obtained through analysis of more data or performing the measurement in an experiment with a larger active mass/anti-neutrino flux. This analysis should be performed using data from all of MicroBooNE's data taking periods, which correspond to approximately 1.0×10^{21} POT of neutrino mode flux, and 1.5×10^{21} POT of anti-neutrino mode flux. Inclusion of these datasets would result in an approximately fourfold increase in statistics. It is also worth emphasising the exportability of the methodology described in this thesis; SBND and DUNE will employ the LArTPC technology with similar readout, but are expected to obtain much larger quantities.

The low statistics nature of the analysis means certain sources of uncertainty, such as the shape of the cross section, are not very significant. Future, more sensitive analyses will need to employ more sophisticated cross section extraction procedures, such as deconvolution. Aside from analysing a larger dataset, the greatest improvement in the sensitivity of this analysis is likely to come from improvements in reconstruction: the version of Pandora employed in this analysis is optimised to analyse single vertex topologies, as these are of the greatest importance to oscillation measurements. Development of a dedicated reconstruction algorithm targeting events containing secondary vertices, such as Λ baryon production or neutron reinteractions, may be beneficial.

Beyond the LArTPC detector paradigm, measurements of hyperon production in electron-nucleus scattering data may be of use, as these will be subjected to many of the same nuclear effects, and could be used to better understand the RES and DIS driven hyperon production processes, which are not limited to neutrino interactions. Inspired by a measurement by MINERvA [163], measurements of hyperon production from free protons in hydrocarbon targets could be used to study the more subtle effects such as the second class current.



(e) Λ baryon lifetime. The mean lifetime of the Λ baryon is $2.63 \pm 0.02 \times 10^{-10}$ s[22].

Figure 6.4: Distributions of the data compared with MC simulation predictions for several variables. The black triangles indicate the positions of the five individual data events. The uncertainties in the mis-reconstruction background were estimated with the sideband constraint procedure from Section 5.3.1.

References

- [1] C. Thorpe *et al.* “Second class currents, axial mass, and nuclear effects in hyperon production”. *Phys. Rev. C* 104.3 (2021), p. 035502.
- [2] J. Calcutt *et al.* “Geant4Reweight: a framework for evaluating and propagating hadronic interaction uncertainties in Geant4”. *JINST* 16.08 (2021), P08042.
- [3] P. Abratenko *et al.* “First Measurement of Quasielastic Λ Baryon Production in Muon Antineutrino Interactions in the MicroBooNE Detector”. *Phys. Rev. Lett.* 130.23 (2023), p. 231802.
- [4] W. Pauli. “Dear radioactive ladies and gentlemen”. *Phys. Today* 31N9 (1978), p. 27.
- [5] E. Fermi. “An attempt of a theory of beta radiation. 1.” *Z. Phys.* 88 (1934), pp. 161–177.
- [6] F. Reines and C. L. Cowan. “A Proposed experiment to detect the free neutrino”. *Phys. Rev.* 90 (1953), pp. 492–493.
- [7] F. Reines and C. L. Cowan. “Detection of the free neutrino”. *Phys. Rev.* 92 (1953), pp. 830–831.
- [8] C. L. Cowan *et al.* “Detection of the free neutrino: A Confirmation”. *Science* 124 (1956), pp. 103–104.
- [9] G. Danby *et al.* “Observation of High-Energy Neutrino Reactions and the Existence of Two Kinds of Neutrinos”. *Phys. Rev. Lett.* 9 (1962), pp. 36–44.
- [10] M. L. Perl *et al.* “Evidence for Anomalous Lepton Production in $e^+ - e^-$ Annihilation”. *Phys. Rev. Lett.* 35 (1975), pp. 1489–1492.
- [11] K. Kodama *et al.* “Observation of tau neutrino interactions”. *Phys. Lett. B* 504 (2001), pp. 218–224.
- [12] N. Agafonova *et al.* “Observation of a first ν_τ candidate in the OPERA experiment in the CNGS beam”. *Phys. Lett. B* 691 (2010), pp. 138–145.
- [13] M. G. Aartsen *et al.* “Measurement of Atmospheric Tau Neutrino Appearance with IceCube DeepCore”. *Phys. Rev. D* 99.3 (2019), p. 032007.

- [14] K. Abe *et al.* “Evidence for the Appearance of Atmospheric Tau Neutrinos in Super-Kamiokande”. *Phys. Rev. Lett.* 110.18 (2013), p. 181802.
- [15] Z. Li *et al.* “Measurement of the tau neutrino cross section in atmospheric neutrino oscillations with Super-Kamiokande”. *Phys. Rev. D* 98.5 (2018), p. 052006.
- [16] P. Janot and S. Jadach. “Improved Bhabha cross section at LEP and the number of light neutrino species”. *Phys. Lett. B* 803 (2020), p. 135319.
- [17] D. Decamp *et al.* “ALEPH: A detector for electron-positron annihilations at LEP”. *Nucl. Instrum. Meth. A* 294 (1990). [Erratum: *Nucl. Instrum. Meth. A* 303, 393 (1991)], pp. 121–178.
- [18] P. A. Aarnio *et al.* “The DELPHI detector at LEP”. *Nucl. Instrum. Meth. A* 303 (1991), pp. 233–276.
- [19] B. Adeva *et al.* “The Construction of the L3 Experiment”. *Nucl. Instrum. Meth. A* 289 (1990), pp. 35–102.
- [20] K. Ahmet *et al.* “The OPAL detector at LEP”. *Nucl. Instrum. Meth. A* 305 (1991), pp. 275–319.
- [21] S. Schael *et al.* “Precision electroweak measurements on the Z resonance”. *Phys. Rept.* 427 (2006), pp. 257–454.
- [22] R. L. Workman. “Review of Particle Physics”. *PTEP* 2022 (2022), p. 083C01.
- [23] M. J. Dolinski, A. W. P. Poon, and W. Rodejohann. “Neutrinoless Double-Beta Decay: Status and Prospects”. *Ann. Rev. Nucl. Part. Sci.* 69 (2019), pp. 219–251.
- [24] R. Davis Jr., D. S. Harmer, and K. C. Hoffman. “Search for neutrinos from the sun”. *Phys. Rev. Lett.* 20 (1968), pp. 1205–1209.
- [25] Q. R. Ahmad *et al.* “Direct evidence for neutrino flavor transformation from neutral current interactions in the Sudbury Neutrino Observatory”. *Phys. Rev. Lett.* 89 (2002), p. 011301.
- [26] Y. Fukuda *et al.* “Evidence for oscillation of atmospheric neutrinos”. *Phys. Rev. Lett.* 81 (1998), pp. 1562–1567.
- [27] Z. Maki, M. Nakagawa, and S. Sakata. “Remarks on the unified model of elementary particles”. *Prog. Theor. Phys.* 28 (1962), pp. 870–880.
- [28] M. Aker *et al.* “Improved Upper Limit on the Neutrino Mass from a Direct Kinematic Method by KATRIN”. *Phys. Rev. Lett.* 123.22 (2019), p. 221802.
- [29] A. D. Sakharov. “Violation of CP Invariance, C asymmetry, and baryon asymmetry of the universe”. *Pisma Zh. Eksp. Teor. Fiz.* 5 (1967), pp. 32–35.
- [30] K. Abe *et al.* “Constraint on the matter–antimatter symmetry-violating phase in neutrino oscillations”. *Nature* 580.7803 (2020). [Erratum: *Nature* 583, E16 (2020)], pp. 339–344. arXiv: 1910.03887 [hep-ex].

- [31] <http://www.nu-fit.org/?q=node/256>. Accessed January 2023.
- [32] P. Anselmann *et al.* “First results from the Cr-51 neutrino source experiment with the GALLEX detector”. *Phys. Lett. B* 342 (1995), pp. 440–450.
- [33] W. Hampel *et al.* “Final results of the Cr-51 neutrino source experiments in GALLEX”. *Phys. Lett. B* 420 (1998), pp. 114–126.
- [34] F. Kaether *et al.* “Reanalysis of the GALLEX solar neutrino flux and source experiments”. *Phys. Lett. B* 685 (2010), pp. 47–54.
- [35] Dzh. N. Abdurashitov *et al.* “The Russian-American gallium experiment (SAGE) Cr neutrino source measurement”. *Phys. Rev. Lett.* 77 (1996), pp. 4708–4711.
- [36] J. N. Abdurashitov *et al.* “Measurement of the response of a Ga solar neutrino experiment to neutrinos from an Ar-37 source”. *Phys. Rev. C* 73 (2006), p. 045805.
- [37] J. N. Abdurashitov *et al.* “Measurement of the response of the Russian-American gallium experiment to neutrinos from a Cr-51 source”. *Phys. Rev. C* 59 (1999), pp. 2246–2263.
- [38] V. V. Barinov *et al.* “Results from the Baksan Experiment on Sterile Transitions (BEST)”. *Phys. Rev. Lett.* 128.23 (2022), p. 232501.
- [39] V. V. Barinov *et al.* “Search for electron-neutrino transitions to sterile states in the BEST experiment”. *Phys. Rev. C* 105.6 (2022), p. 065502.
- [40] A. Aguilar-Arevalo *et al.* “Evidence for neutrino oscillations from the observation of $\bar{\nu}_e$ appearance in a $\bar{\nu}_\mu$ beam”. *Phys. Rev. D* 64 (2001), p. 112007.
- [41] C. Athanassopoulos *et al.* “Evidence for anti-muon-neutrino \rightarrow anti-electron-neutrino oscillations from the LSND experiment at LAMPF”. *Phys. Rev. Lett.* 77 (1996), pp. 3082–3085.
- [42] J. M. Conrad and M. H. Shaevitz. “Sterile Neutrinos: An Introduction to Experiments”. *Adv. Ser. Direct. High Energy Phys.* 28 (2018), pp. 391–442.
- [43] A. A. Aguilar-Arevalo *et al.* “The MiniBooNE Detector”. *Nucl. Instrum. Meth. A* 599 (2009), pp. 28–46.
- [44] A. A. Aguilar-Arevalo *et al.* “Significant Excess of ElectronLike Events in the MiniBooNE Short-Baseline Neutrino Experiment”. *Phys. Rev. Lett.* 121.22 (2018), p. 221801.
- [45] P. Abratenko *et al.* “Search for Neutrino-Induced Neutral-Current Δ Radiative Decay in MicroBooNE and a First Test of the MiniBooNE Low Energy Excess under a Single-Photon Hypothesis”. *Phys. Rev. Lett.* 128 (2022), p. 111801.
- [46] A. A. Aguilar-Arevalo *et al.* “A Search for Electron Neutrino Appearance at the $\Delta m^2 \sim 1\text{eV}^2$ Scale”. *Phys. Rev. Lett.* 98 (2007), p. 231801.

-
- [47] B. Armbruster *et al.* “Upper limits for neutrino oscillations muon-anti-neutrino \rightarrow electron-anti-neutrino from muon decay at rest”. *Phys. Rev. D* 65 (2002), p. 112001.
- [48] N. Agafonova *et al.* “Final results of the search for $\nu_\mu \rightarrow \nu_e$ oscillations with the OPERA detector in the CNGS beam”. *JHEP* 06 (2018), p. 151.
- [49] A. A. Aguilar-Arevalo *et al.* “Updated MiniBooNE neutrino oscillation results with increased data and new background studies”. *Phys. Rev. D* 103.5 (2021), p. 052002.
- [50] A. P. Serebrov *et al.* “NEUTRINO4 experiment: preparations for search for sterile neutrino at 100 MW Reactor SM-3 at 6-12 Meters” (2012). arXiv: 1205.2955 [hep-ph].
- [51] A. P. Serebrov *et al.* “Search for sterile neutrinos with the Neutrino-4 experiment and measurement results”. *Phys. Rev. D* 104.3 (2021), p. 032003.
- [52] C. Giunti *et al.* “Neutrino-4 anomaly: oscillations or fluctuations?” *Phys. Lett. B* 816 (2021), p. 136214.
- [53] M Antonello *et al.* “Experimental search for the “LSND anomaly” with the ICARUS detector in the CNGS neutrino beam”. *Eur. Phys. J. C* 73.3 (2013), p. 2345.
- [54] P. Adamson *et al.* “Search for Sterile Neutrinos Mixing with Muon Neutrinos in MINOS”. *Phys. Rev. Lett.* 117.15 (2016), p. 151803.
- [55] P. Adamson *et al.* “Limits on Active to Sterile Neutrino Oscillations from Disappearance Searches in the MINOS, Daya Bay, and Bugey-3 Experiments”. *Phys. Rev. Lett.* 117.15 (2016). [Addendum: *Phys.Rev.Lett.* 117, 209901 (2016)], p. 151801.
- [56] I. E. Stockdale *et al.* “Limits on Muon Neutrino Oscillations in the Mass Range $55 \text{ eV}^2 < \Delta m^2 < 800 \text{ eV}^2$ ”. *Phys. Rev. Lett.* 52 (1984), p. 1384.
- [57] M. G. Aartsen *et al.* “Searches for Sterile Neutrinos with the IceCube Detector”. *Phys. Rev. Lett.* 117.7 (2016), p. 071801.
- [58] M. Aker *et al.* “Bound on 3+1 Active-Sterile Neutrino Mixing from the First Four-Week Science Run of KATRIN”. *Phys. Rev. Lett.* 126.9 (2021), p. 091803.
- [59] A. Diaz *et al.* “Where Are We With Light Sterile Neutrinos?” *Phys. Rept.* 884 (2020), pp. 1–59.
- [60] C. H. Llewellyn Smith. “Neutrino Reactions at Accelerator Energies”. *Phys. Rept.* 3 (1972), pp. 261–379.
- [61] D. Rein and L. M. Sehgal. “Neutrino Excitation of Baryon Resonances and Single Pion Production”. *Annals Phys.* 133 (1981), pp. 79–153.
- [62] Ch. Berger and L. M. Sehgal. “Lepton mass effects in single pion production by neutrinos”. *Phys. Rev. D* 76 (2007), p. 113004.

- [63] C. Andreopoulos *et al.* “The GENIE Neutrino Monte Carlo Generator”. Nucl. Instrum. Meth. A 614 (2010), pp. 87–104.
- [64] Y. Hayato. “A neutrino interaction simulation program library NEUT”. Acta Phys. Polon. B 40 (2009). Ed. by A. Ankowski and J. Sobczyk, pp. 2477–2489.
- [65] J. A. Nowak and J. T. Sobczyk. “Modelling CC neutrino cross sections in the few GeV energy region”. Acta Phys. Polon. B 37 (2006). Ed. by A. Zalewska, K. Golec-Biernat, and M. Skrzypek, pp. 1955–1966.
- [66] C. Bronner. “Generators for the SIS/DIS region”. JPS Conf. Proc. 12 (2016), p. 010025.
- [67] Christian Bierlich *et al.* “A comprehensive guide to the physics and usage of PYTHIA 8.3” (2022).
- [68] M. Martini *et al.* “A Unified approach for nucleon knock-out, coherent and incoherent pion production in neutrino interactions with nuclei”. Phys. Rev. C 80 (2009), p. 065501.
- [69] D. S. Ayres *et al.* “The NOvA Technical Design Report” (2007).
- [70] Y. Fukuda *et al.* “The Super-Kamiokande detector”. Nucl. Instrum. Meth. A 501 (2003). Ed. by V. A. Ilyin, V. V. Korenkov, and D. Perret-Gallix, pp. 418–462.
- [71] R. Acciarri *et al.* “Design and Construction of the MicroBooNE Detector”. JINST 12.02 (2017), P02017.
- [72] A. M. Szec. “The ArgoNeuT Experiment”. AIP Conf. Proc. 1663.1 (2015). Ed. by H. Da Motta, Jorge G. Morfin, and M. Sakuda, p. 020004.
- [73] M. Antonello *et al.* “A Proposal for a Three Detector Short-Baseline Neutrino Oscillation Program in the Fermilab Booster Neutrino Beam” (2015). arXiv: 1503.01520 [physics.ins-det].
- [74] L. Aliaga *et al.* “Design, Calibration, and Performance of the MINERvA Detector”. Nucl. Instrum. Meth. A 743 (2014), pp. 130–159.
- [75] U. Mosel. “Neutrino event generators: foundation, status and future”. J. Phys. G 46.11 (2019), p. 113001.
- [76] <https://indico.cern.ch/event/657167/contributions/2677886/>. Graphic from talk presented by Callum Wilkinson at the 17th International Workshop on Next Generation Nucleon Decay and Neutrino Detectors. Accessed February 2023.
- [77] O. Ravel. “Early cosmic ray research in France”. AIP Conf. Proc. 1516.1 (2013). Ed. by Jonathan F. Ormes, pp. 67–71.
- [78] T. D. Lee and C. N. Yang. “Parity Nonconservation and a Two Component Theory of the Neutrino”. Phys. Rev. 105 (1957). Ed. by G. Feinberg, pp. 1671–1675.

- [79] A. Fatima, M. Sajjad Athar, and S.K. Singh. “Second class currents and T violation in quasielastic neutrino and antineutrino scattering from nucleons”. *Phys. Rev. D* 98.3 (2018), p. 033005.
- [80] R. Bradford *et al.* “A New parameterization of the nucleon elastic form-factors”. *Nucl. Phys. B Proc. Suppl.* 159 (2006). Ed. by F. Cavanna, J. G. Morfin, and T. Nakaya, pp. 127–132.
- [81] B. Bhattacharya, R. J. Hill, and G. Paz. “Model independent determination of the axial mass parameter in quasielastic neutrino-nucleon scattering”. *Phys. Rev. D* 84 (2011), p. 073006.
- [82] N. Cabibbo, E. C. Swallow, and R. Winston. “Semileptonic hyperon decays”. *Ann. Rev. Nucl. Part. Sci.* 53 (2003), pp. 39–75.
- [83] Y. Nambu. “Axial vector current conservation in weak interactions”. *Phys. Rev. Lett.* 4 (1960). Ed. by T. Eguchi, pp. 380–382.
- [84] F. Schlumpf. “Beta decay of hyperons in a relativistic quark model”. *Phys. Rev. D* 51 (1995), pp. 2262–2270.
- [85] O. Erriquez *et al.* “Production of Strange Particles in anti-neutrino Interactions at the CERN PS”. *Nucl. Phys. B* 140 (1978), pp. 123–140.
- [86] O. Erriquez *et al.* “Strange particle production by antineutrinos”. *Physics Letters B* 70.3 (1977).
- [87] T. Eichten *et al.* “Observation of ‘Elastic’ Hyperon Production by Anti-neutrinos”. *Phys. Lett. B* 40 (1972), pp. 593–596.
- [88] V. V. Ammosov *et al.* “Neutral Strange Particle Exclusive Production in Charged Current High-energy Anti-neutrino Interactions”. *Z. Phys. C* 36 (1987), pp. 377–381.
- [89] G. Fanourakis *et al.* “Study of Low-energy Anti-neutrino Interactions on Protons”. *Phys. Rev. D* 21 (1980), p. 562.
- [90] J. Brunner *et al.* “Quasielastic Nucleon and Hyperon Production by Neutrinos and Anti-neutrinos With Energies Below 30-GeV”. *Z. Phys. C* 45 (1990), p. 551.
- [91] S. Farooq. “Antineutrino-induced charge current quasi-elastic neutral hyperon production in ArgoNeUT”. PhD thesis. Kansas State U., Manhattan, (2016).
- [92] V. Bernard, L. Elouadrhiri, and U. G. Meissner. “Axial structure of the nucleon: Topical Review”. *J. Phys. G* 28 (2002), R1–R35.
- [93] V Lyubushkin *et al.* “A Study of quasi-elastic muon neutrino and antineutrino scattering in the NOMAD experiment”. *Eur. Phys. J. C* 63 (2009), pp. 355–381.
- [94] A. Bodek *et al.* “Vector and Axial Nucleon Form Factors:A Duality Constrained Parameterization”. *Eur. Phys. J. C* 53 (2008), pp. 349–354.

- [95] H. De Vries, C. W. De Jager, and C. De Vries. “Nuclear charge and magnetization density distribution parameters from elastic electron scattering”. *Atom. Data Nucl. Data Tabl.* 36 (1987), pp. 495–536.
- [96] A. Bodek and J. L. Ritchie. “Further Studies of Fermi Motion Effects in Lepton Scattering from Nuclear Targets”. *Phys. Rev. D* 24 (1981), p. 1400.
- [97] A. M. Ankowski and J. T. Sobczyk. “Construction of spectral functions for medium-mass nuclei”. *Phys. Rev. C* 77 (2008), p. 044311.
- [98] S. K. Singh and M. J. Vicente Vacas. “Weak quasi-elastic production of hyperons”. *Phys. Rev. D* 74 (2006), p. 053009.
- [99] N. Metropolis *et al.* “Monte Carlo Calculations on Intranuclear Cascades. I. Low-Energy Studies”. *Phys. Rev.* 110.1 (1958), p. 185.
- [100] S. Dimopoulos, S. Raby, and F. Wilczek. “Proton Decay in Supersymmetric Models”. *Phys. Lett. B* 112 (1982), p. 133.
- [101] N. K. Glendenning. “The Hyperon Composition of Neutron Stars”. *Phys. Lett. B* 114 (1982), pp. 392–396.
- [102] I. Vidaña. “Neutron stars and the hyperon puzzle”. *EPJ Web Conf.* 271 (2022), p. 09001.
- [103] R. B. Wiringa, V. G. J. Stoks, and R. Schiavilla. “An Accurate nucleon-nucleon potential with charge independence breaking”. *Phys. Rev. C* 51 (1995), pp. 38–51.
- [104] M. Baldo, I. Bombaci, and G. F. Burgio. “Microscopic nuclear equation of state with three-body forces and neutron star structure”. *Astron. Astrophys.* 328 (1997), pp. 274–282.
- [105] T. A. Rijken, M. M. Nagels, and Y. Yamamoto. “Status of understanding the $Y N / Y Y$ -interactions meson-exchange viewpoint”. *Nucl. Phys. A* 835 (2010). Ed. by Benjamin F. Gibson *et al.*, pp. 160–167.
- [106] J. Antoniadis *et al.* “A Massive Pulsar in a Compact Relativistic Binary”. *Science* 340 (2013), p. 6131.
- [107] J. L. Rodríguez-Sánchez *et al.* “Constraining the Λ -nucleus potential within the Liège intranuclear cascade model”. *Phys. Rev. C* 98.2 (2018), p. 021602.
- [108] T. Harada and Y. Hirabayashi. “Is the Sigma-nucleus potential for Sigma- atoms consistent with the Si-28(π^- , K^+) data?” *Nucl. Phys. A* 759 (2005), pp. 143–169.
- [109] P. K. Saha *et al.* “Study of the Sigma-nucleus potential by the (π^- , K^+) reaction on medium-to-heavy nuclear targets”. *Phys. Rev. C* 70 (2004), p. 044613.
- [110] R. Acciarri *et al.* “Long-Baseline Neutrino Facility (LBNF) and Deep Underground Neutrino Experiment (DUNE): Conceptual Design Report, Volume 1: The LBNF and DUNE Projects” (2016). arXiv: 1601.05471 [physics.ins-det].

-
- [111] R. Acciarri *et al.* “Long-Baseline Neutrino Facility (LBNF) and Deep Underground Neutrino Experiment (DUNE): Conceptual Design Report, Volume 2: The Physics Program for DUNE at LBNF” (2015). arXiv: 1512.06148 [physics.ins-det].
- [112] W. Shockley. “Currents to conductors induced by a moving point charge”. *J. Appl. Phys.* 9.10 (1938), pp. 635–636.
- [113] S. Ramo. “Currents induced by electron motion”. *Proc. Ire.* 27 (1939), pp. 584–585.
- [114] B. J. P. Jones. “Sterile Neutrinos in Cold Climates”. PhD thesis. MIT, (2015).
- [115] I. Stancu *et al.* “Technical Design Report for the 8 GeV Beam” (2001).
- [116] A. A. Aguilar-Arevalo *et al.* “The Neutrino Flux prediction at MiniBooNE”. *Phys. Rev. D* 79 (2009), p. 072002.
- [117] P. Adamson *et al.* “The NuMI Neutrino Beam”. *Nucl. Instrum. Meth. A* 806 (2016), pp. 279–306.
- [118] B. Fleming. “The MicroBooNE Technical Design Report” (2012).
- [119] C. Adams *et al.* “Ionization electron signal processing in single phase LArTPCs. Part I. Algorithm Description and quantitative evaluation with MicroBooNE simulation”. *JINST* 13.07 (2018), P07006.
- [120] C. Adams *et al.* “Ionization electron signal processing in single phase LArTPCs. Part II. Data/simulation comparison and performance in MicroBooNE”. *JINST* 13.07 (2018), P07007.
- [121] C. Adams *et al.* “Design and construction of the MicroBooNE Cosmic Ray Tagger system”. *JINST* 14.04 (2019), P04004.
- [122] A. Lister. “Constraint of Systematic Uncertainties in an Electron Neutrino Search Using Muon Neutrinos at MicroBooNE”. PhD thesis. Lancaster U., (2019).
- [123] P. Abratenko *et al.* “Measurement of space charge effects in the MicroBooNE LArTPC using cosmic muons”. *JINST* 15.12 (2020), P12037.
- [124] K. E. Duffy *et al.* “Neutrino interaction measurements with the MicroBooNE and ArgoNeUT liquid argon time projection chambers”. *Eur. Phys. J. ST* 230.24 (2021), pp. 4275–4291.
- [125] K. V. J. Mistry. “First Measurement of the Flux-Averaged Differential Charged-Current Electron-Neutrino and Antineutrino Cross Section on Argon with the MicroBooNE Detector”. PhD thesis. Manchester U., (2021).
- [126] S. Agostinelli *et al.* “GEANT4—a simulation toolkit”. *Nucl. Instrum. Meth. A* 506 (2003), pp. 250–303.
- [127] H. Pi. “An Event generator for interactions between hadrons and nuclei: FRITIOF version 7.0”. *Comput. Phys. Commun.* 71 (1992), pp. 173–192.

- [128] D. H. Wright and M. H. Kelsey. “The Geant4 Bertini Cascade”. Nucl. Instrum. Meth. A 804 (2015), pp. 175–188.
- [129] P. Abratenko *et al.* “New $CC0\pi$ GENIE model tune for MicroBooNE”. Phys. Rev. D 105.7 (2022), p. 072001.
- [130] J. Nieves, J. E. Amaro, and M. Valverde. “Inclusive quasi-elastic neutrino reactions”. Phys. Rev. C 70 (2004). [Erratum: Phys.Rev.C 72, 019902 (2005)], p. 055503.
- [131] L. A. Ahrens *et al.* “Measurement of Neutrino - Proton and anti-neutrino - Proton Elastic Scattering”. Phys. Rev. D 35 (1987), p. 785.
- [132] D. Rein. “Angular Distribution in Neutrino Induced Single Pion Production Processes”. Z. Phys. C 35 (1987), pp. 43–64.
- [133] K. S. Kuzmin, V. V. Lyubushkin, and V. A. Naumov. “Lepton polarization in neutrino nucleon interactions”. Mod. Phys. Lett. A 19 (2004). Ed. by A. V. Efremov and O. V. Teryaev, pp. 2815–2829.
- [134] J. Schwehr, D. Cherdack, and R. Gran. “GENIE implementation of IFIC Valencia model for QE-like 2p2h neutrino-nucleus cross section” (2016).
- [135] J. Nieves, I. Ruiz Simo, and M. J. Vicente Vacas. “Inclusive Charged-Current Neutrino-Nucleus Reactions”. Phys. Rev. C 83 (2011), p. 045501.
- [136] R. Gran *et al.* “Neutrino-nucleus quasi-elastic and 2p2h interactions up to 10 GeV”. Phys. Rev. D 88.11 (2013), p. 113007.
- [137] T. Katori. “Meson Exchange Current (MEC) Models in Neutrino Interaction Generators”. AIP Conf. Proc. 1663.1 (2015). Ed. by H. Da Motta, J. G. Morfin, and M. Sakuda, p. 030001.
- [138] A. Bodek and U. Yang. “Axial and Vector Structure Functions for Electron- and Neutrino- Nucleon Scattering Cross Sections at all Q^2 using Effective Leading order Parton Distribution Functions” (2010). arXiv: 1011.6592 [hep-ph].
- [139] A Bodek and U. K. Yang. “Higher twist, ξ_ω scaling, and effective LO PDFs for lepton scattering in the few GeV region”. J. Phys. G 29 (2003). Ed. by K. Long and R. Edgecock, pp. 1899–1906.
- [140] A. Bodek, I. Park, and U. Yang. “Improved low Q^2 model for neutrino and electron nucleon cross sections in few GeV region”. Nucl. Phys. B Proc. Suppl. 139 (2005). Ed. by F. Cavanna *et al.*, pp. 113–118.
- [141] Ch. Berger and L. M. Sehgal. “PCAC and coherent pion production by low energy neutrinos”. Phys. Rev. D 79 (2009), p. 053003.
- [142] R. Veenhof. “GARFIELD, recent developments”. Nucl. Instrum. Meth. A 419 (1998). Ed. by M. Krammer *et al.*, pp. 726–730.

- [143] R. Acciarri *et al.* “The Pandora multi-algorithm approach to automated pattern recognition of cosmic-ray muon and neutrino events in the MicroBooNE detector”. *Eur. Phys. J. C* 78.1 (2018), p. 82.
- [144] P. Abratenko *et al.* “Cosmic Ray Background Rejection with Wire-Cell LArTPC Event Reconstruction in the MicroBooNE Detector”. *Phys. Rev. Applied* 15.6 (2021), p. 064071.
- [145] P. Abratenko *et al.* “Calorimetric classification of track-like signatures in liquid argon TPCs using MicroBooNE data”. *JHEP* 12 (2021), p. 153.
- [146] A. Hocker *et al.* “TMVA - Toolkit for Multivariate Data Analysis” (2007). arXiv: physics/0703039.
- [147] <https://physics.nist.gov/PhysRefData/Star/Text/PSTAR.html>. Accessed July 2023.
- [148] F. James and M. Roos. “Minuit: A System for Function Minimization and Analysis of the Parameter Errors and Correlations”. *Comput. Phys. Commun.* 10 (1975), pp. 343–367.
- [149] L. Aliaga Soplin. “Neutrino Flux Prediction for The Numi Beamline”. PhD thesis. William-Mary Coll., (2016).
- [150] A. V. Lebedev. “Ratio of pion kaon production in proton carbon interactions”. PhD thesis. Harvard U., (2007).
- [151] C. Alt *et al.* “Inclusive production of charged pions in p + C collisions at 158-GeV/c beam momentum”. *Eur. Phys. J. C* 49 (2007), pp. 897–917.
- [152] B. Baatar *et al.* “Inclusive production of protons, anti-protons, neutrons, deuterons and tritons in p+C collisions at 158 GeV/c beam momentum”. *Eur. Phys. J. C* 73.4 (2013), p. 2364.
- [153] G. M. Tinti. “Sterile neutrino oscillations in MINOS and hadron production in pC collisions”. PhD thesis. Oxford U., (2010).
- [154] N Abgrall *et al.* “Measurements of Cross Sections and Charged Pion Spectra in Proton-Carbon Interactions at 31 GeV/c”. *Phys. Rev. C* 84 (2011), p. 034604.
- [155] A. Abed Abud *et al.* “Design, construction and operation of the ProtoDUNE-SP Liquid Argon TPC”. JINST 17.01 (2022), P01005.
- [156] B. Bhandari *et al.* “First Measurement of the Total Neutron Cross Section on Argon Between 100 and 800 MeV”. *Phys. Rev. Lett.* 123.4 (2019), p. 042502.
- [157] P. Abratenko *et al.* “Novel approach for evaluating detector-related uncertainties in a LArTPC using MicroBooNE data”. *Eur. Phys. J. C* 82.5 (2022), p. 454.
- [158] D. Heck *et al.* “CORSIKA: A Monte Carlo code to simulate extensive air showers” (1998).

-
- [159] C. Adams *et al.* “A method to determine the electric field of liquid argon time projection chambers using a UV laser system and its application in MicroBooNE”. JINST 15.07 (2020), P07010.
- [160] J. E. Sobczyk *et al.* “Weak Production of Strange and Charmed Ground-State Baryons in Nuclei”. Phys. Rev. C 99.6 (2019), p. 065503.
- [161] <https://root.cern.ch/doc/master/classTEfficiency.html>. Accessed August 2021. Root version 6.16 used.
- [162] <https://pdg.lbl.gov/2012/AtomicNuclearProperties/>. Accessed January 2023.
- [163] T. Cai *et al.* “Measurement of the axial vector form factor from antineutrino–proton scattering”. Nature 614.7946 (2023), pp. 48–53.

Appendix A

Partial Phase Space Definition

The Λ baryon has momentum p_Λ in the rest frame of the detector (LAB) frame. The boost factor β , in natural units, is:

$$\beta = \frac{p_\Lambda}{\sqrt{p_\Lambda^2 + M_\Lambda^2}}, \quad (\text{A.1})$$

where $M_\Lambda = 1.115$ GeV [22]. To boost from the Λ baryon's rest frame (CMS) to the rest frame of the detector, the Lorentz transformation matrix is:

$$\Lambda^{-1} = \begin{bmatrix} \gamma & 0 & \beta\gamma \\ 0 & 1 & 0 \\ \beta\gamma & 0 & \gamma \end{bmatrix}, \quad (\text{A.2})$$

where $\gamma = 1/\sqrt{1 - \beta^2}$. The proton is emitted at an angle θ with respect to the boost direction in the rest frame of the Λ baryon with momentum $p = 0.101$ GeV [22]. The four momenta of the proton and pion in this frame are:

$$P_p^{\text{CMS}} = (E_p, p \sin \theta, p \cos \theta), \quad (\text{A.3})$$

$$P_\pi^{\text{CMS}} = (E_\pi, -p \sin \theta, -p \cos \theta), \quad (\text{A.4})$$

where $E_p = \sqrt{M_p^2 + p^2}$, and $E_\pi = \sqrt{M_\pi^2 + p^2}$. $p \cos \theta$ is the momentum of the proton along the boost direction, $p \sin \theta$ the momentum of the proton in the plane transverse to the boost direction. Transforming these four momenta to the rest frame of the detector:

$$P_p^{\text{LAB}} = \Lambda^{-1} P_p^{\text{CMS}}, \quad (\text{A.5})$$

$$P_\pi^{\text{LAB}} = \Lambda^{-1} P_\pi^{\text{CMS}}, \quad (\text{A.6})$$

$$P_p^{\text{LAB}} = (\gamma E_p + \beta\gamma p \cos \theta, p \sin \theta, \beta\gamma E_p + \gamma p \cos \theta), \quad (\text{A.7})$$

$$P_\pi^{\text{LAB}} = (\gamma E_\pi - \beta\gamma p \cos \theta, -p \sin \theta, \beta\gamma E_\pi - \gamma p \cos \theta). \quad (\text{A.8})$$

For the efficiency of notation, let $a_p = \gamma E_p$, $a_\pi = \gamma E_\pi$ and $b = \beta\gamma p$. The squared 3 momenta of the proton and pion in the LAB frame are:

$$|p_p^{\text{LAB}}|^2 = (a_p + b \cos \theta)^2 - M_p^2, \quad (\text{A.9})$$

$$|p_\pi^{\text{LAB}}|^2 = (a_\pi - b \cos \theta)^2 - M_\pi^2. \quad (\text{A.10})$$

To find the set of values of $\cos \theta$ for which the proton or pion are above the detection thresholds $p_p^{\text{thresh}} = 0.3 \text{ GeV}$ and $p_\pi^{\text{thresh}} = 0.1 \text{ GeV}$, solve:

$$(a_p + b \cos \theta)^2 - M_p^2 = |p_p^{\text{thresh}}|^2, \quad (\text{A.11})$$

$$\cos \theta = \frac{\pm \sqrt{M_p^2 + |p_p^{\text{thresh}}|^2} - a_p}{b}, \quad (\text{A.12})$$

and similar for the pion. The requirement that $-1 < \cos \theta < 1$ excludes the negative solution in the case of the proton and the positive solution for the pion. This leaves a pair of limits on $\cos \theta$:

$$\cos \theta > \frac{\sqrt{M_p^2 + |p_p^{\text{thresh}}|^2} - a_p}{b}, \quad (\text{A.13})$$

$$\cos \theta < \frac{-\sqrt{M_\pi^2 + |p_\pi^{\text{thresh}}|^2} + a_\pi}{b}. \quad (\text{A.14})$$

There are four distinct behavioural regions that must be considered:

Sub-Threshold Region: Neither particle is produced above threshold for any value of $\cos \theta$. This occurs when the lower limit on theta imposed by equation A.13 is greater than the upper limit imposed by equation A.14. The values of β and γ that define the boundary of this region satisfy:

$$\frac{\sqrt{M_p^2 + |p_p^{\text{thresh}}|^2} - \gamma E_p}{\beta\gamma p} = \frac{-\sqrt{M_\pi^2 + |p_\pi^{\text{thresh}}|^2} + \gamma E_\pi}{\beta\gamma p}. \quad (\text{A.15})$$

Low Energy Region: the decay products are produced above threshold for the values of $\cos \theta$ between the lower limit imposed by equation A.13 and equation A.14. The probability of the proton being emitted at an angle of θ in the rest frame of the Λ baryon is $\frac{1}{2} \sin \theta$, and so the probability the proton is emitted between θ_1 and θ_2 is $\frac{1}{2} \int_{\theta_1}^{\theta_2} \sin \theta d\theta = \frac{1}{2} (\cos \theta_1 - \cos \theta_2)$. This gives the expression for $f(p_\Lambda)$ in this region:

$$f(p_\Lambda) = \frac{1}{2} \left(\frac{-\sqrt{M_\pi^2 + |p_\pi^{\text{thresh}}|^2} + \gamma E_\pi}{\beta\gamma p} - \frac{\sqrt{M_p^2 + |p_p^{\text{thresh}}|^2} - \gamma E_p}{\beta\gamma p} \right). \quad (\text{A.16})$$

Medium Energy Region: one of the decay products is produced above the detection threshold for all values of $\cos \theta$. This occurs for the proton when lower limit in equation A.13 is equal to -1 , and for the pion when the upper limit in equation A.14 equals $+1$. Equation A.16 may be modified to account for this behaviour by defining

$$A = \max \left(\frac{\sqrt{M_p^2 + |p_p^{\text{thresh}}|^2} - \gamma E_p}{\beta \gamma p}, -1 \right), \quad (\text{A.17})$$

$$B = \min \left(\frac{-\sqrt{M_\pi^2 + |p_\pi^{\text{thresh}}|^2} + \gamma E_\pi}{\beta \gamma p}, 1 \right), \quad (\text{A.18})$$

$$(\text{A.19})$$

then $f(p_\Lambda) = B - A$. The final domain, the **High Energy Region**, begins when $A = -1$ and $B = 1$. $f(p_\Lambda)$, for all four regions can be compactly written as:

$$f(p_\Lambda) = \begin{cases} 0 & \text{if } A > B \\ \frac{B-A}{2} & \text{Otherwise} \end{cases} \quad (\text{A.20})$$

Appendix B

Selection Performance Tables

Cut Name	GENIE Signal	NuWro Signal	GENIE Eff.	NuWro Eff.	GENIE BG
None	11.60 ± 0.17	11.5 ± 0.3	1 ± 0	1 ± 0	657200 ± 600
Fiducial Volume	9.53 ± 0.16	9.4 ± 0.3	0.822 ± 0.014	0.82 ± 0.02	42480 ± 130
Three Tracks	4.46 ± 0.11	4.09 ± 0.17	0.385 ± 0.009	0.356 ± 0.015	7890 ± 50
No Showers	3.64 ± 0.10	3.25 ± 0.16	0.314 ± 0.008	0.283 ± 0.014	4832.3 ± 40
Muon ID	2.72 ± 0.08	2.42 ± 0.13	0.235 ± 0.007	0.210 ± 0.012	3040 ± 30
Lambda ID	1.91 ± 0.07	1.66 ± 0.11	0.165 ± 0.006	0.145 ± 0.010	1257 ± 17
Invariant Mass	1.65 ± 0.07	1.5 ± 0.1	0.143 ± 0.006	0.127 ± 0.009	532 ± 12
Angular Deviation	0.82 ± 0.05	0.684 ± 0.07	0.070 ± 0.004	0.059 ± 0.006	15.8 ± 1.9
Island Finding	0.72 ± 0.04	0.58 ± 0.07	0.062 ± 0.004	0.050 ± 0.006	0.85 ± 0.17

(a) Neutrino mode.

Cut Name	GENIE Signal	NuWro Signal	GENIE Eff.	NuWro Eff.	GENIE BG
None	25.9 ± 0.3	23.8 ± 0.6	1 ± 0	1 ± 0	1206100 ± 800
Fiducial Volume	21.5 ± 0.3	20.1 ± 0.5	0.832 ± 0.011	0.85 ± 0.02	91300 ± 200
Three Tracks	9.8 ± 0.2	9.1 ± 0.3	0.379 ± 0.008	0.381 ± 0.015	18130 ± 70
No Showers	8.12 ± 0.18	7.4 ± 0.3	0.314 ± 0.007	0.313 ± 0.013	10370 ± 60
Muon ID	6.44 ± 0.16	5.7 ± 0.3	0.249 ± 0.006	0.241 ± 0.012	6590 ± 50
Lambda ID	4.12 ± 0.13	3.6 ± 0.2	0.159 ± 0.005	0.150 ± 0.009	2160 ± 20
Invariant Mass	3.80 ± 0.13	3.3 ± 0.2	0.147 ± 0.005	0.138 ± 0.009	843 ± 13
Angular Deviation	1.99 ± 0.09	1.53 ± 0.14	0.077 ± 0.003	0.064 ± 0.007	24.7 ± 1.7
Island Finding	1.81 ± 0.08	1.34 ± 0.13	0.070 ± 0.003	0.057 ± 0.006	2.0 ± 0.3

(b) Anti-neutrino mode.

Table B.1: Performance of the event selection.

Appendix C

Vertex Finding

To calculate quantities such as the angular deviation from Section 4.6.3 and the reconstructed decay length in Section 4.7.1, a secondary vertex is required. MicroBooNE’s reconstruction framework, Pandora [143], does not generate secondary vertices. An initial estimate of the position of the secondary vertex may be made using the point of closest approach of the proton and pion tracks, however this can lead to misleading values of the reconstructed decay length, especially if the two tracks lie in a “T” or “X” shaped configuration. A more sophisticated algorithm was developed to penalise these outcomes, and to try and produce a metric indicating the “quality” of the secondary vertex, ie. the consistency of the vertex and tracks with a V shape. The reconstructed decay length was ultimately superseded by the island finding method, but the vertex generation algorithm remains in use.

This fitted V algorithm generates a vertex, \mathbf{v} , shown in red in Figure C.1, and a pair of “arms”, the blue lines extending out from \mathbf{V} in Figure C.1, the directions of which are given by $\hat{\mathbf{k}}_p$ and $\hat{\mathbf{k}}_\pi$. One varies the position of \mathbf{v} and the directions of the arms to match the reconstructed tracks, shown in black, as closely as possible. The lines corresponding to the fitted arms are described by the pair of vector equations:

$$\mathbf{k}_p(t) = \mathbf{v} + t\hat{\mathbf{k}}_p \quad (\text{C.1})$$

$$\mathbf{k}_\pi(t) = \mathbf{v} + t\hat{\mathbf{k}}_\pi \quad (\text{C.2})$$

The main ingredient for the fit metric is the minimum distance between a point \mathbf{x}_i along either the proton/pion track and the corresponding arm of the fitted V. The point of closest approach between \mathbf{x}_i and the fitted V is \mathbf{p} :

$$\mathbf{p} = \mathbf{v} - ((\mathbf{v} - \mathbf{x}) \cdot \hat{\mathbf{k}})\hat{\mathbf{k}} \quad (\text{C.3})$$

$$\delta = (\mathbf{p} - \mathbf{v}) \cdot \hat{\mathbf{k}} \quad (\text{C.4})$$

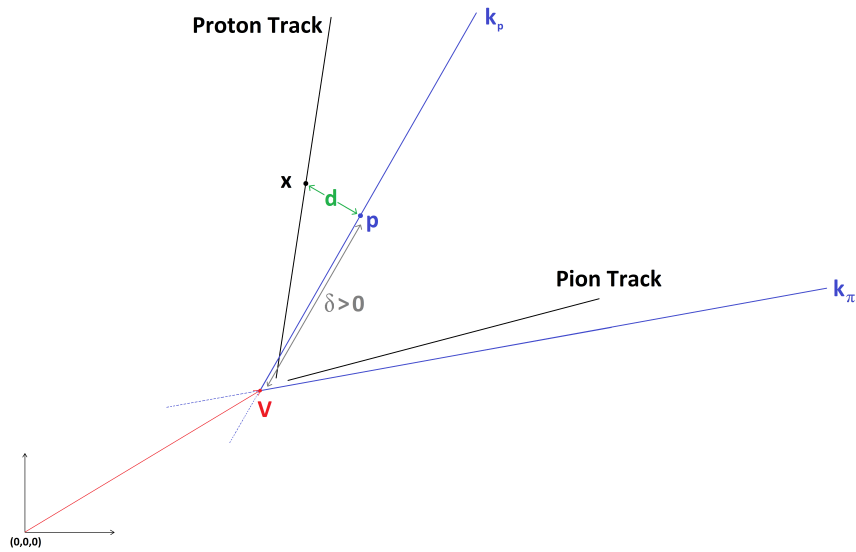
δ is an important related quantity, indicating whether \mathbf{p} lies upstream of downstream of the fitted vertex. These possibilities are shown in Figures C.1a and C.1b respectively.

The fit procedure is as follows: Initial values of \mathbf{v} , $\hat{\mathbf{k}}_p$ and $\hat{\mathbf{k}}_\pi$ are the midpoint of the line connecting the proton and pion start points and their track directions respectively. For each track generate a list of n evenly spaced points, \mathbf{x}_i and calculate the following for every point:

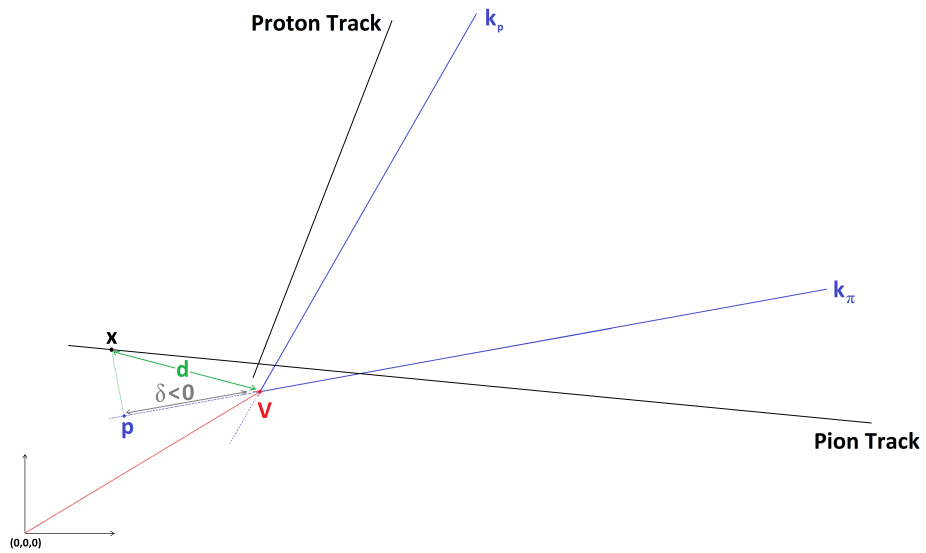
$$d_i = \begin{cases} |\mathbf{x}_i - \mathbf{p}_i| & \text{if } \delta_i \geq 0 \\ f|\mathbf{x}_i - \mathbf{v}| & \text{if } \delta_i < 0 \end{cases} \quad (\text{C.5})$$

The distance d is shown in green in Figure C.1 and the two cases correspond to placement of the vertex downstream/upstream of the vertex shown in Figures C.1a/C.1b. Placement of the vertex in configuration (b) is allowed but penalised by the fit with parameter f . The fit metric Δ^2 is the sum of the squares of these values for both branches:

$$\Delta^2 = \sum_{i=1}^n (d_{ip}^2 + d_{i\pi}^2) \quad (\text{C.6})$$



(a) $\delta > 0$. The track starts downstream of the candidate vertex.



(b) $\delta < 0$. The track starts upstream of the candidate vertex.

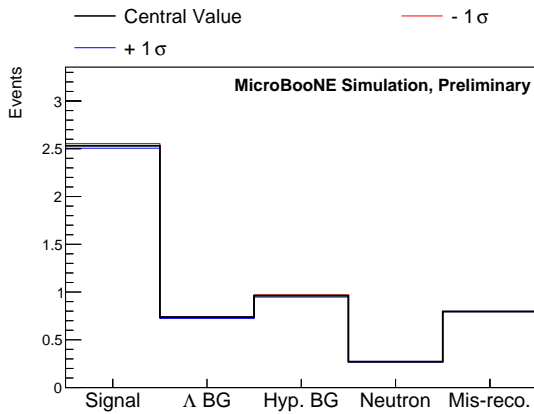
Figure C.1: Calculation of \mathbf{p} , δ and d . The Black lines are the actual reconstructed tracks from the proton and pion candidates chosen by the BDTs, the blue lines are the fitted V the secondary vertex fitter has constructed.

Appendix D

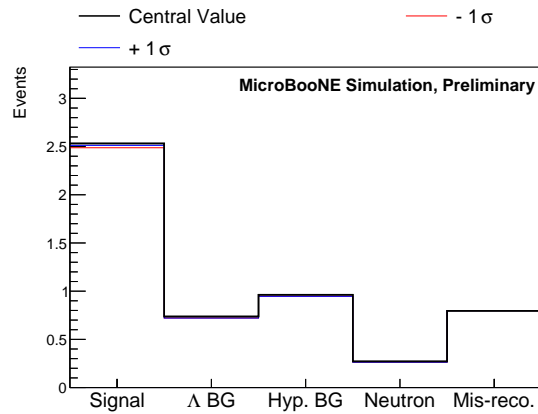
Systematics Calculations

The following sections show the systematic variations for two sources of uncertainty found to be negligible: the beamline geometry model, discussed in Section 5.4.2, the set of alternative models for the background neutrino interactions, described in Section 5.5.2, and the light yield simulation in Section 5.7.2. The sets of variations in this section involve applying the sideband constraint procedure from Section 5.3.1; the variations after applying the visual scan are presented in Appendix E.

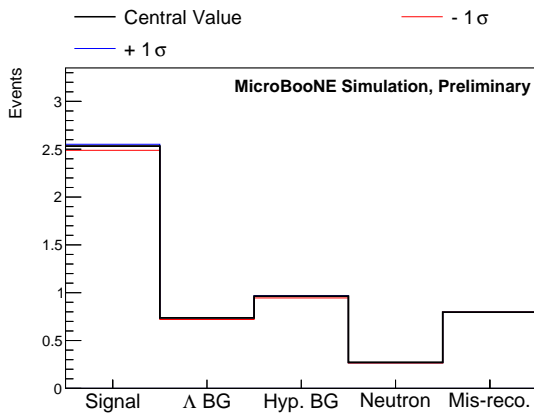
D.1 Beamline Geometry



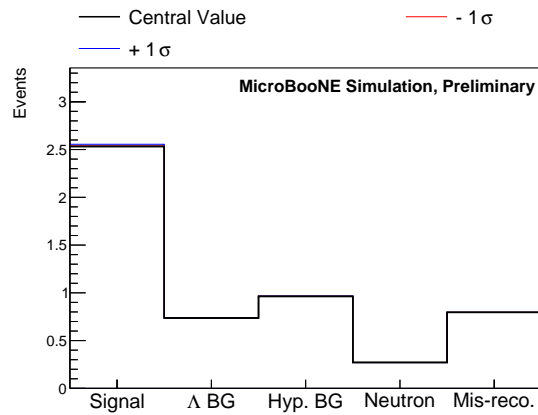
(a) Beam spot size.



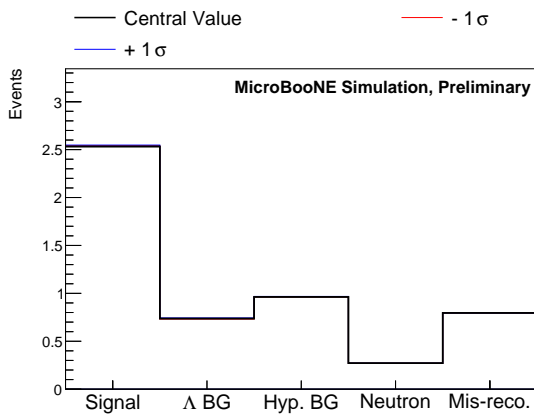
(b) Beam spot x .



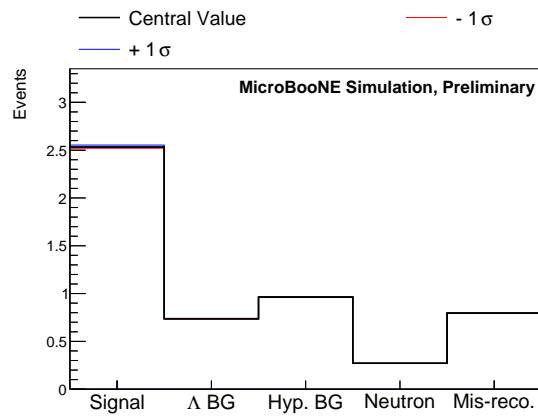
(c) Beam spot y .



(d) Horn current.



(e) Horn water.



(f) Target z position.

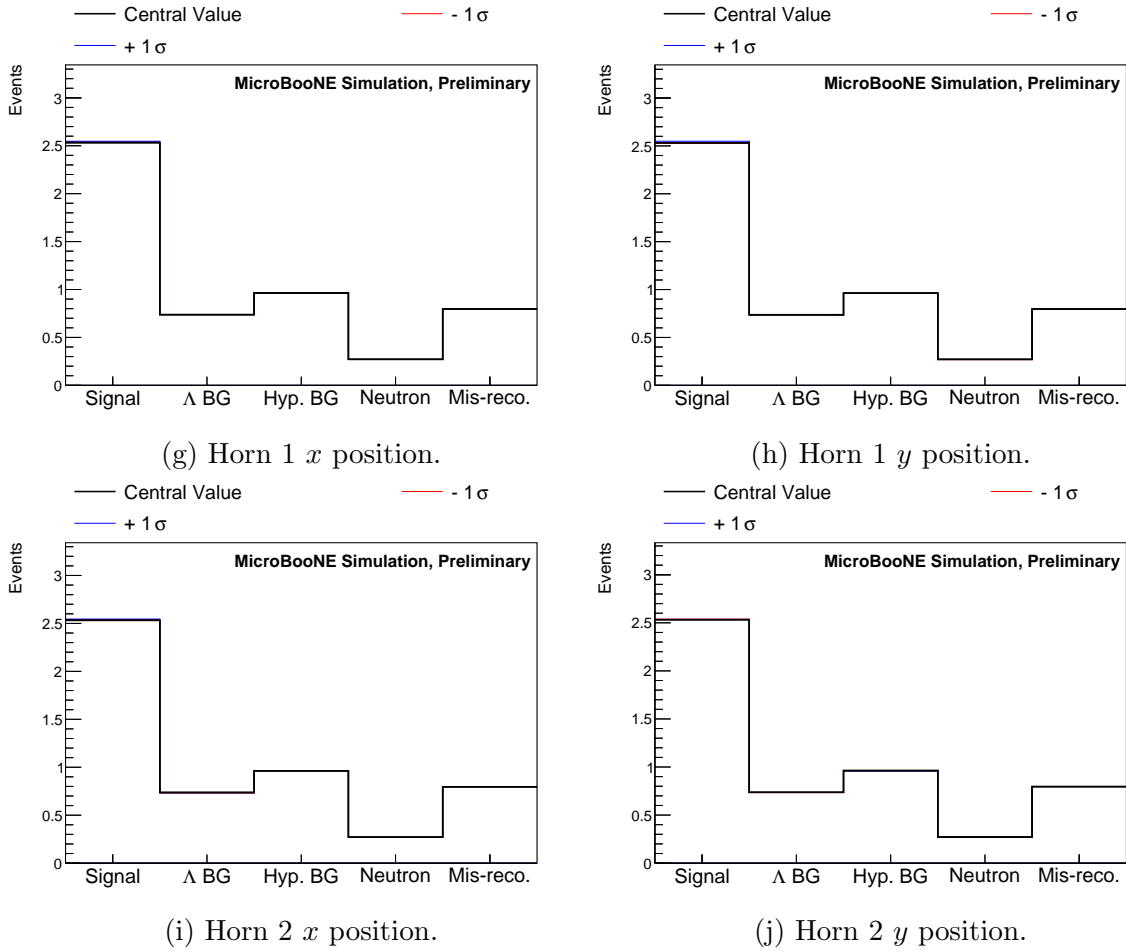
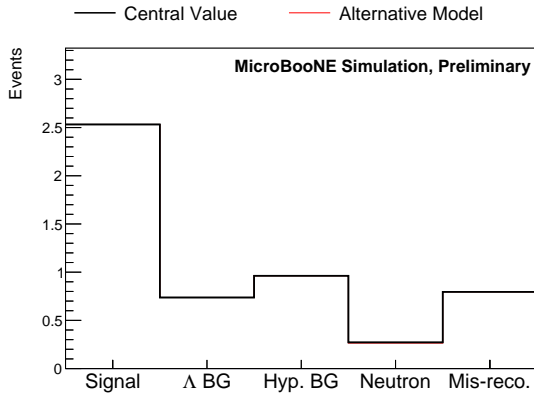
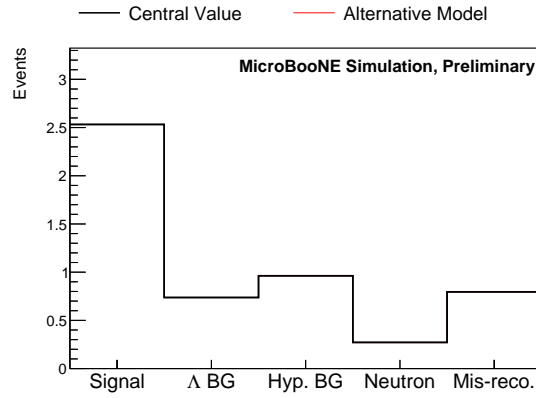


Figure D.1: Selected signal and background from the 10 beamline geometry variations.

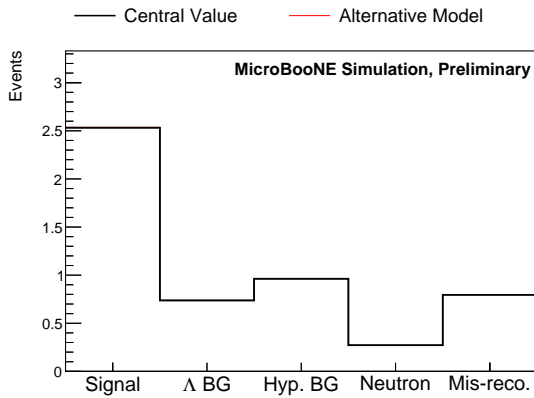
D.2 Background Cross Section Uncertainties



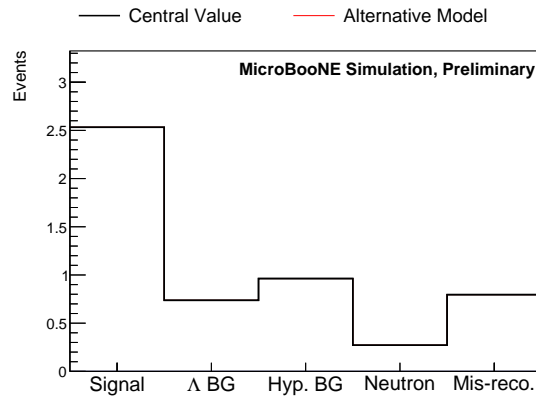
(a) CCQE Vector FF.



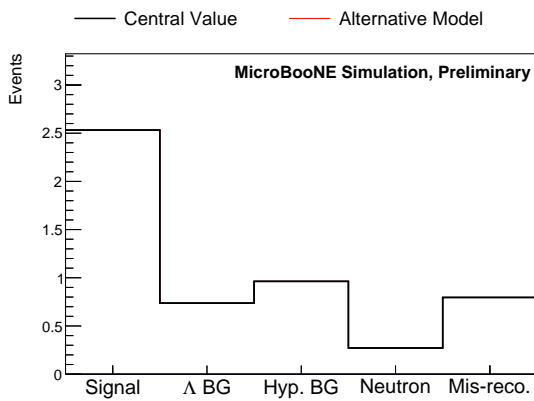
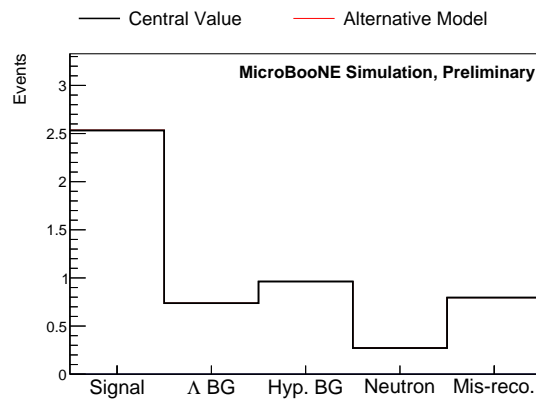
(b) CCQE axial FF.



(c) CCCOH normalisation.



(d) NCCOH normalisation.

(e) Δ radiative decay angle.(f) Δ hadronic decay angle.

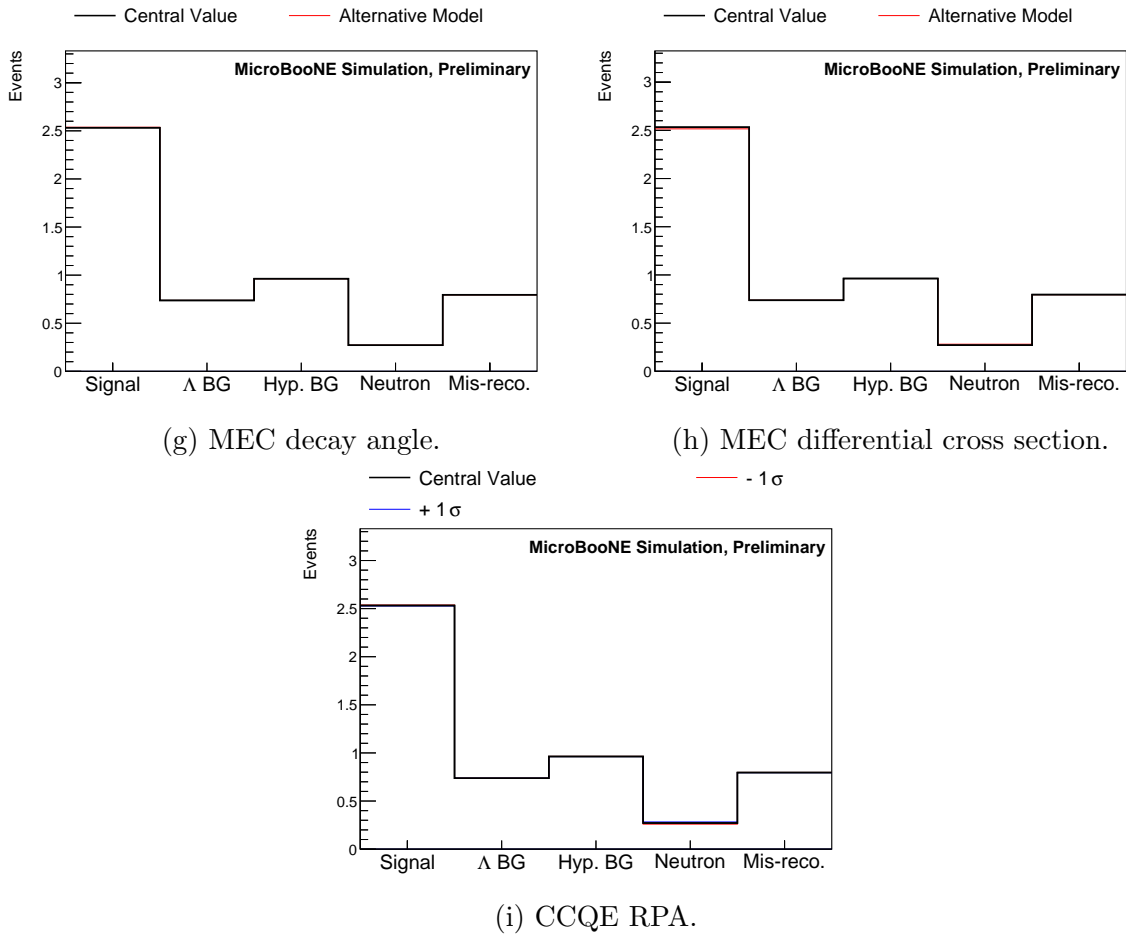
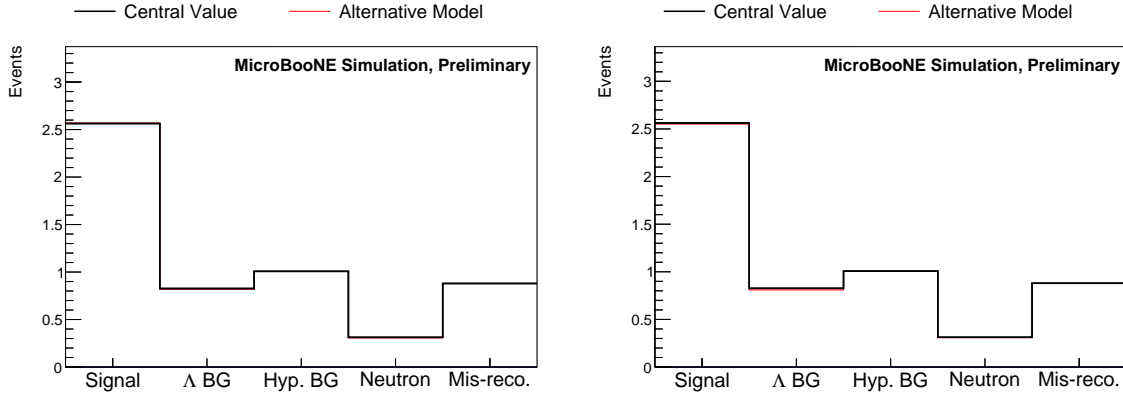


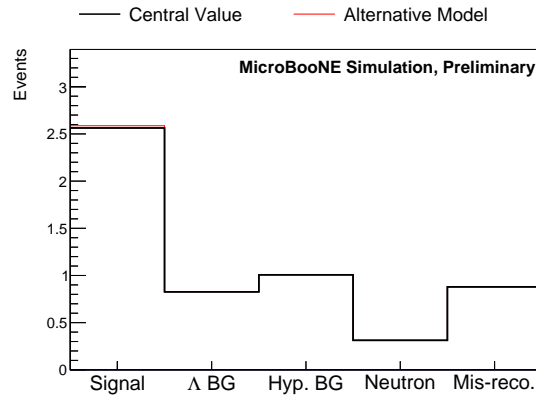
Figure D.2: Selected signal and background, calculated using the default GENIE simulation and using alternative models described in Table 5.5, and the two CCQE RPA variations.

D.3 Light Yield Simulation



(a) Reduced light yield.

(b) Attenuated light yield.



(c) Light with Rayleigh scattering.

Figure D.3: Predictions of the different light yield variations compared with the default model, employing the sideband constraint in the final bin.

Appendix E

When Applying the Visual Scan

The following sections contain the distributions calculated in Chapter 5, utilising the visual scanning method instead of the sideband constraint procedure.

E.1 Neutrino Flux

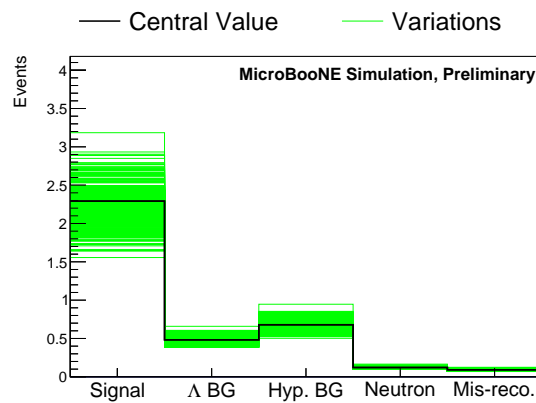
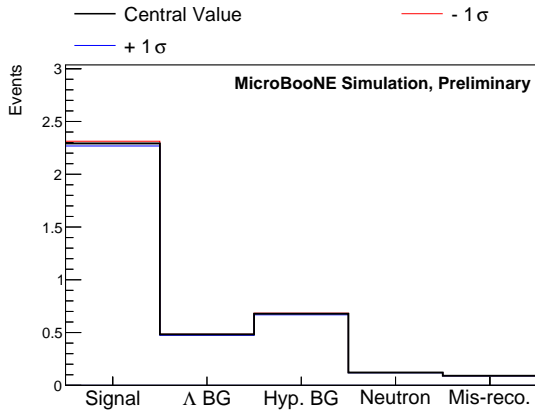
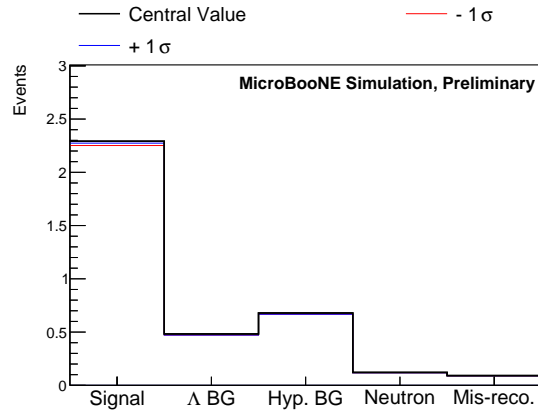


Figure E.1: Selected signal/background.

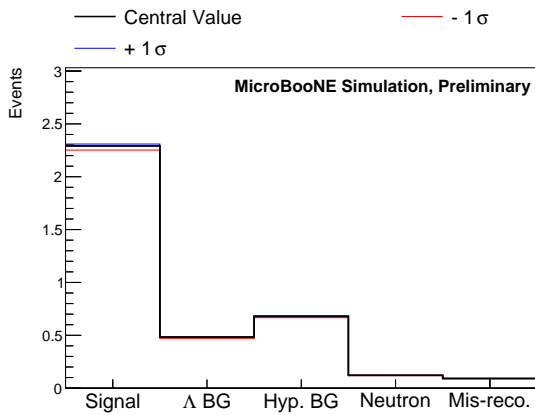
Figure E.2: Selected signal and background in different hadron production universes.



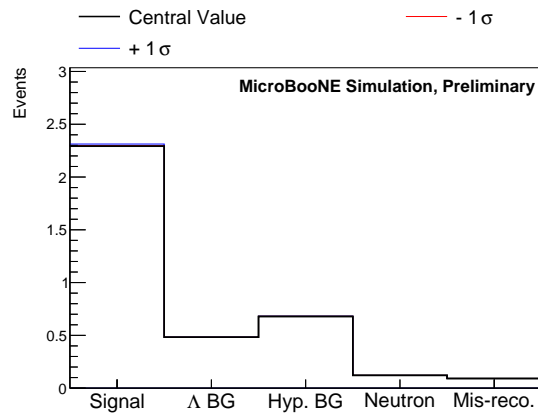
(a) Beam spot size.



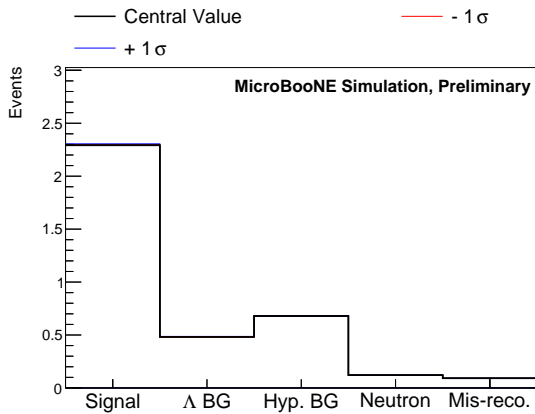
(b) Beam spot x .



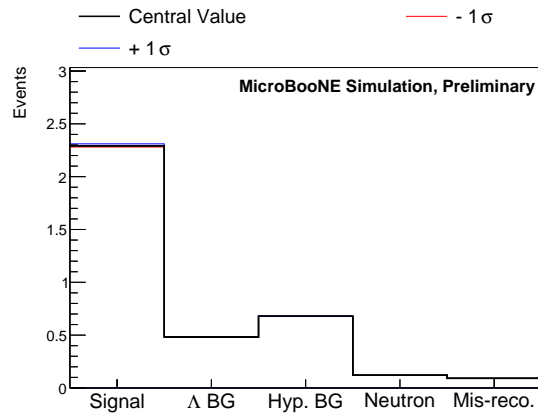
(c) Beam spot y .



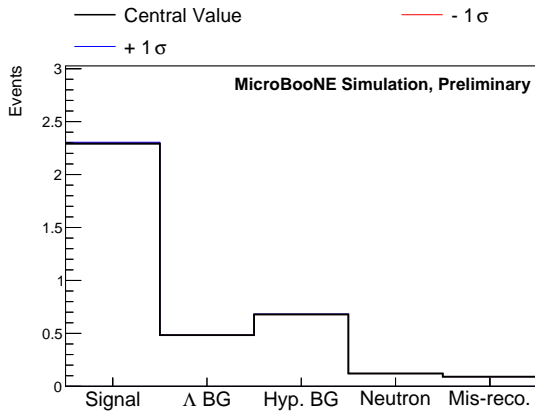
(d) Horn current.



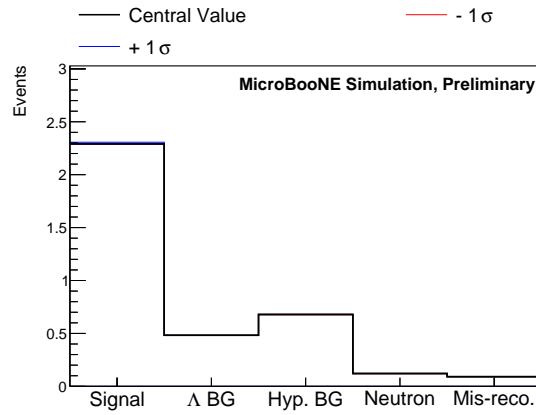
(e) Horn water.



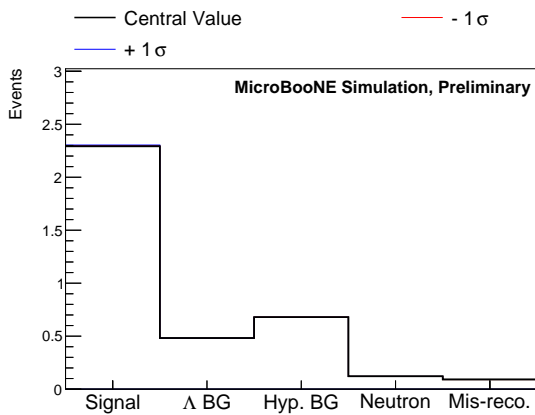
(f) Target z position.



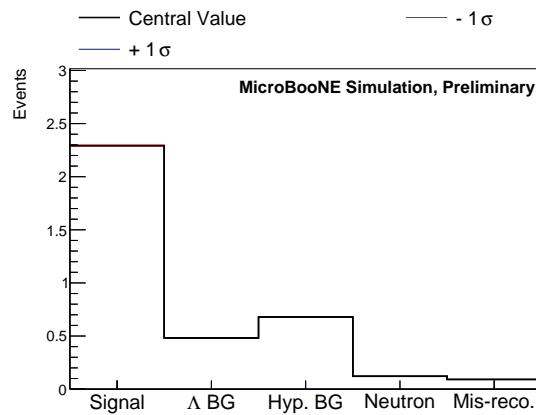
(g) Horn 1 x position.



(h) Horn 1 y position.



(i) Horn 2 x position.



(j) Horn 2 y position.

Figure E.3: Selected signal and background from the 10 beamline geometry variations.

E.2 Background Cross Sections

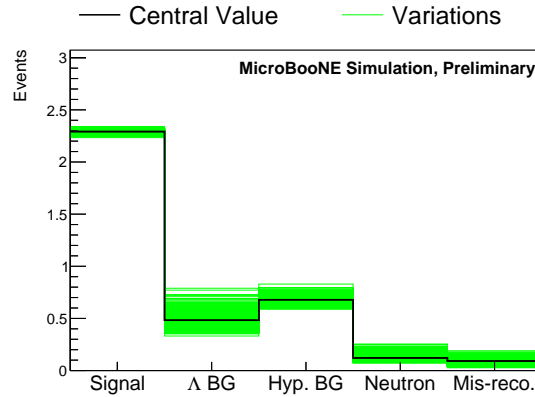


Figure E.4: Selected and signal in different generator multisim variations and the extracted fractional covariance matrix. The small variation in the signal occurs from handful of events containing a second neutrino interaction besides the Λ production in the same beam spill.

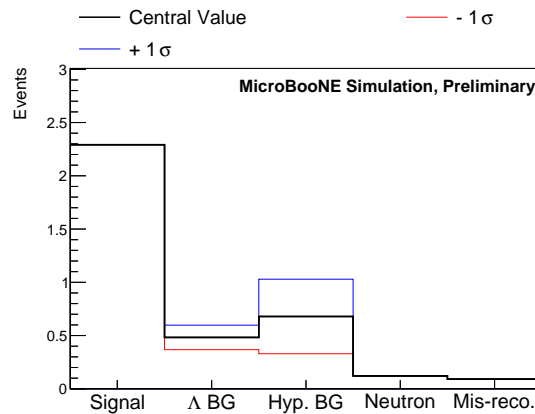
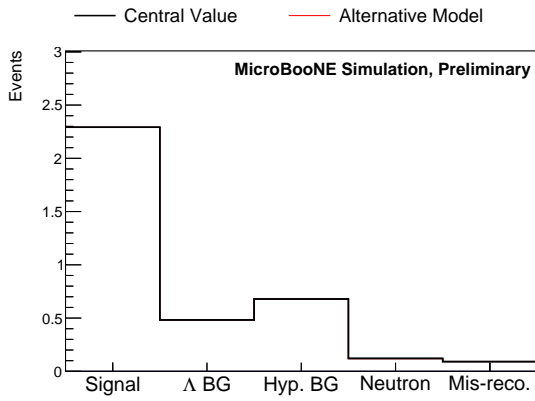
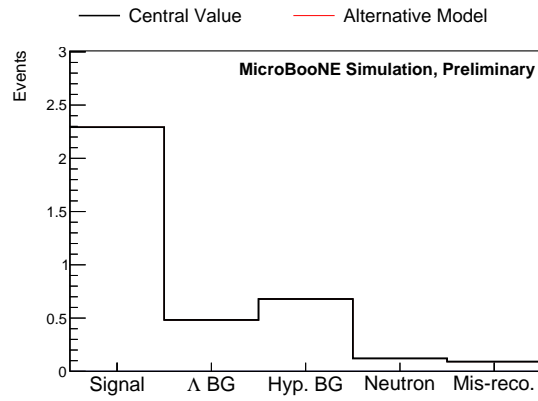


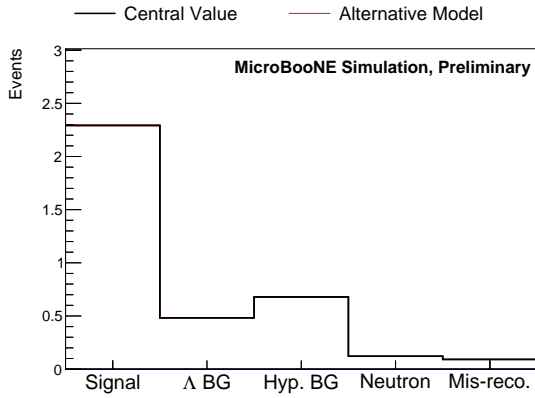
Figure E.5: Selected signal and background when varying the CCQE-like hyperon production cross sections.



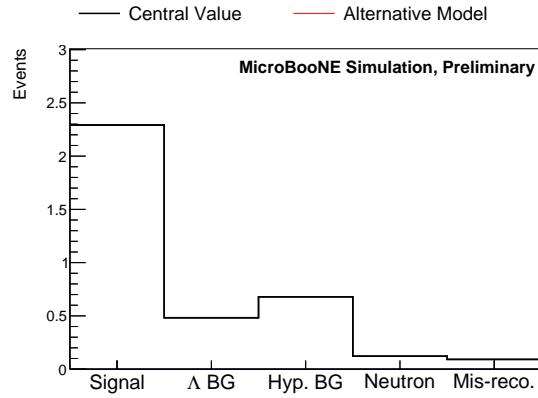
(a) CCQE Vector FF.



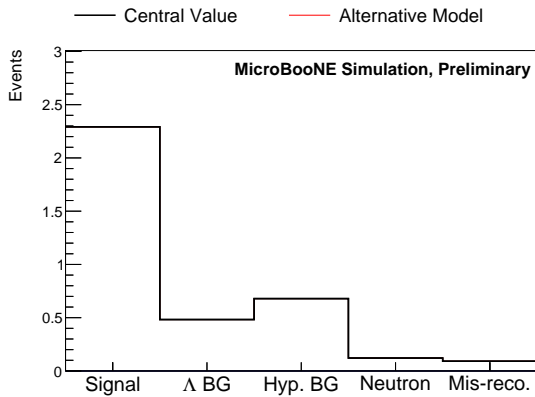
(b) CCQE axial FF.



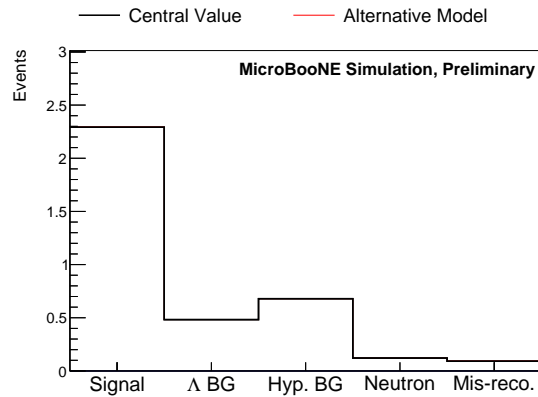
(c) CCCOH normalisation.



(d) NCCOH normalisation.



(e) Δ radiative decay angle.



(f) Δ hadronic decay angle.

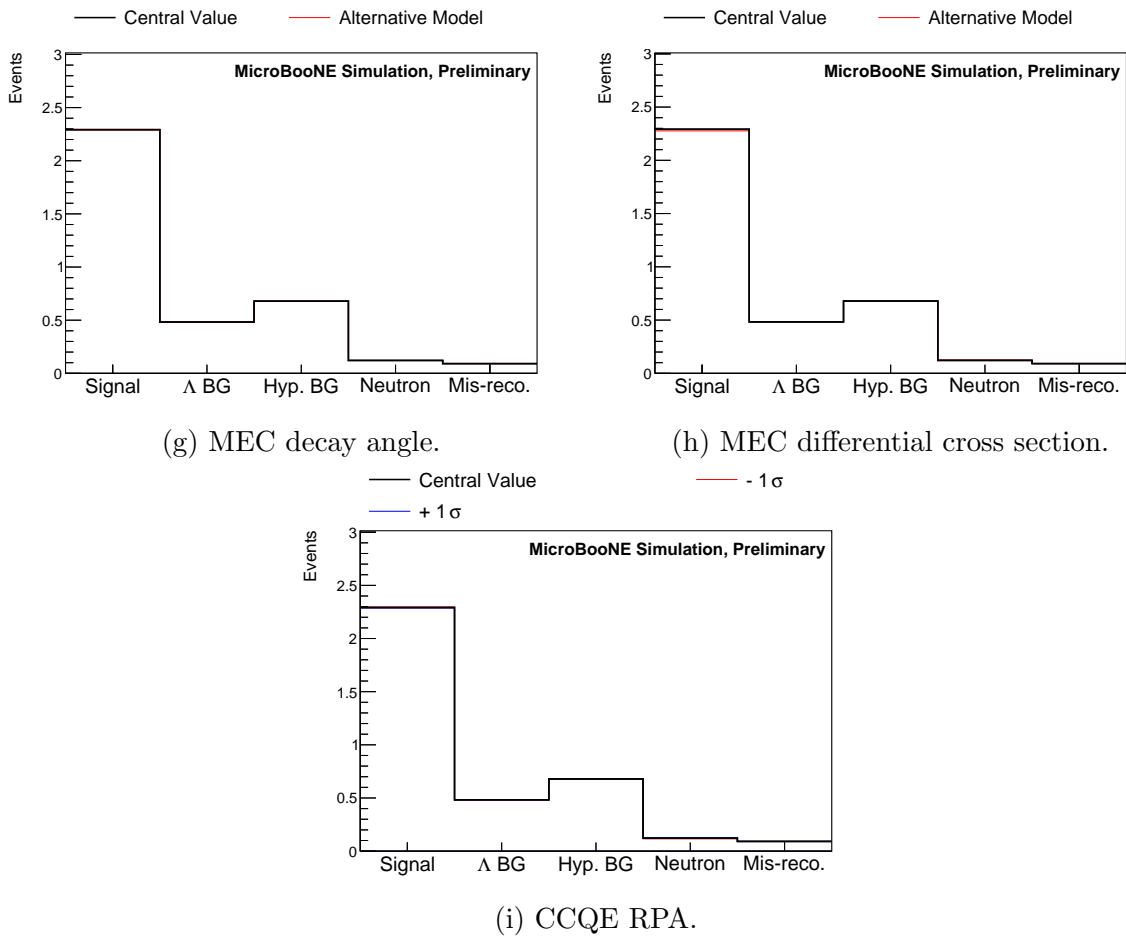


Figure E.6: Selected signal and background, calculated using the default GENIE simulation and using alternative models described in Table 5.5, and the two CCQE RPA variations.

E.3 Secondary Interactions

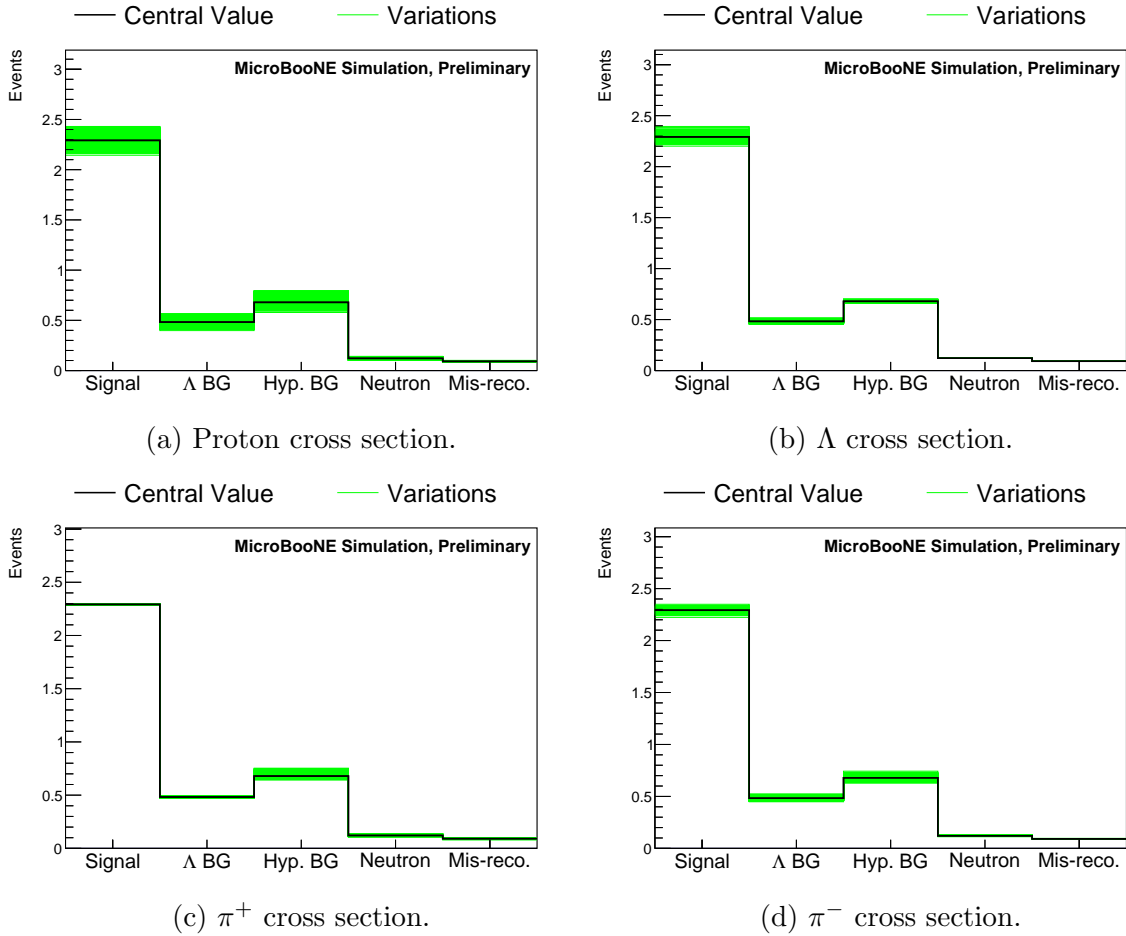


Figure E.7: Secondary interaction cross section variations.

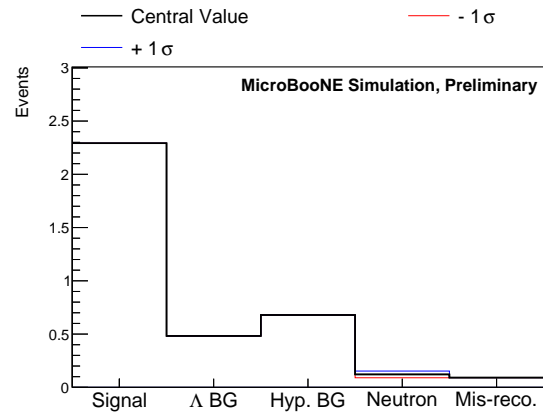
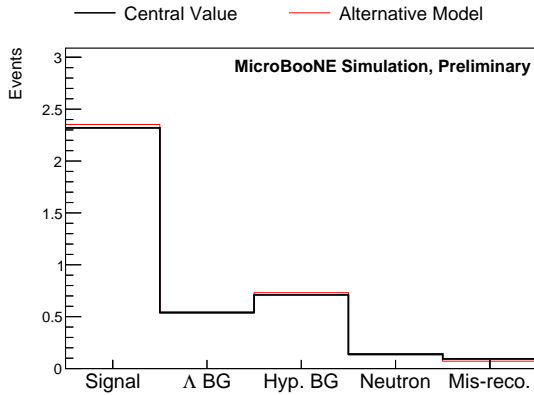
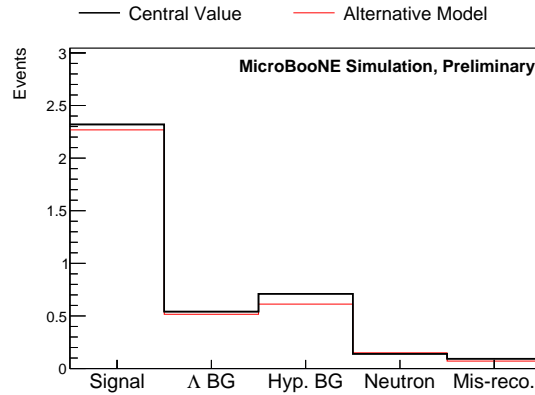


Figure E.8: Secondary neutron interaction cross section variations.

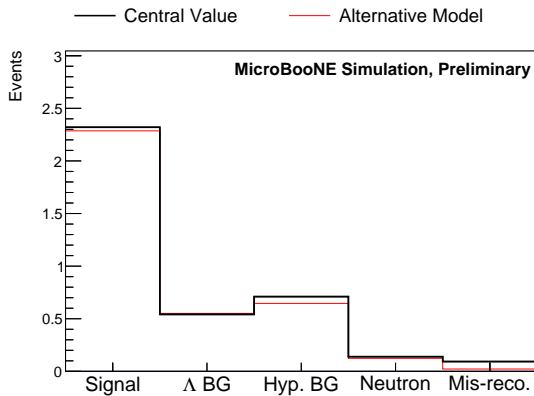
E.4 Detector Response



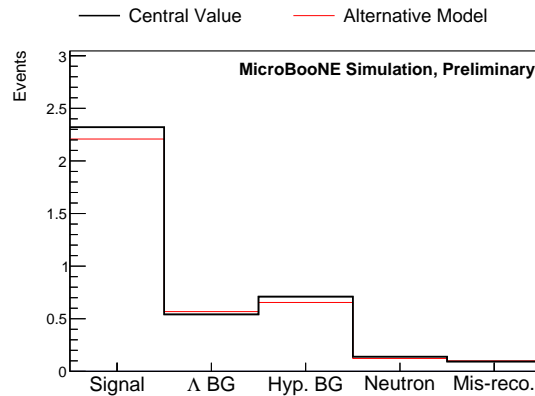
(a) Wire response in x .



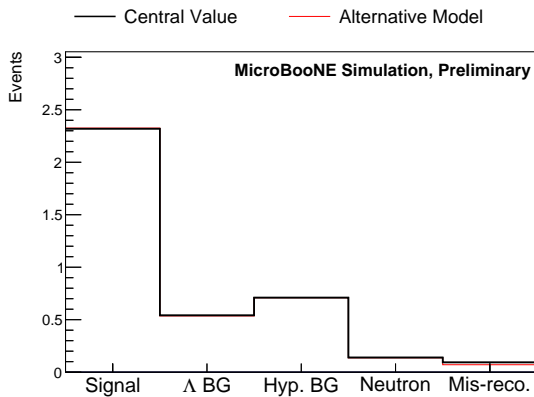
(b) Wire response in $y - z$ plane.



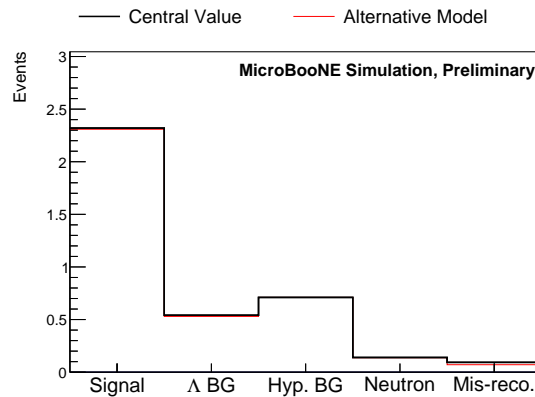
(c) Wire response in $x - z$ direction.



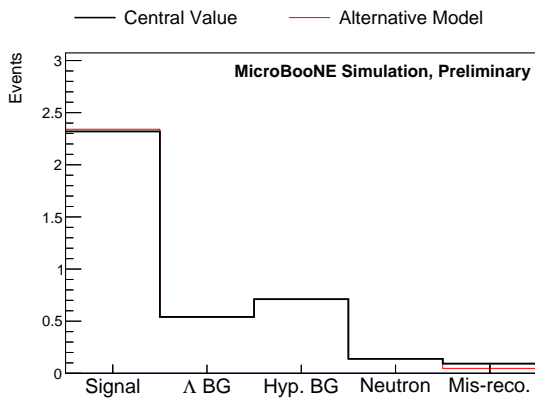
(d) Wire response in $y - z$ direction.



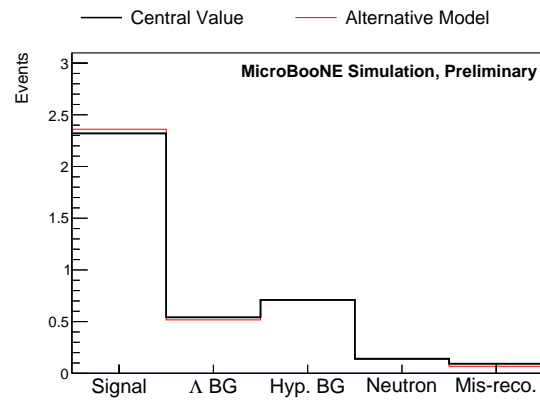
(e) Reduced light yield.



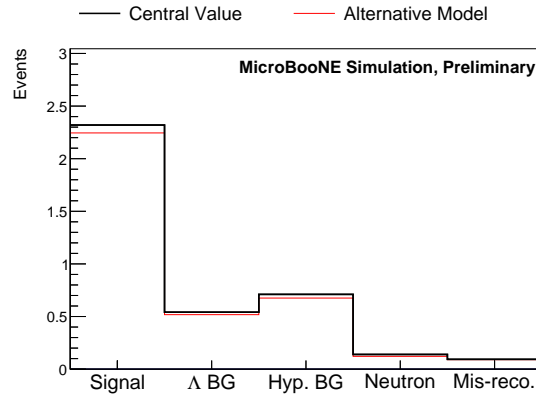
(f) Light yield attenuation.



(g) Position dependant light yield.



(h) Recombination model.



(i) Alternative space charge map.

Figure E.9: The predicted mixture of signal and background, when testing alternative models of the detector response to estimate the corresponding uncertainties after applying the visual scan.

Appendix F

Data MC Comparisons

Before unblinding the data completely, it is important to validate the predictions as thoroughly as possible. As the signal only reaches a similar size to the background near the very end of the selection, we may study the data using a looser selection without sacrificing blindness. In this section we present comparisons between data and MC, progressively applying stronger selections up to but not including the analysis BDT and connectedness test, and calculating a range of different variables to search for discrepancies.

To quantify the level of agreement between the data and MC simulation predictions, a χ^2 statistic is calculated:

$$\chi^2 = \sum_i \sum_j (X_i^{\text{Data}} - X_i^{\text{MC}}) \text{Cov}_{ij}^{-1} (X_j^{\text{Data}} - X_j^{\text{MC}}) \quad (\text{F.1})$$

where Cov^{-1} is the inverted covariance matrix containing all systematic and statistical uncertainties, X_i^{Data} is the number of data events in bin i and X_i^{MC} the prediction in bin i . Data and MC statistical uncertainties are assumed to be Gaussian and incorporated into the covariance matrix in the following way:

$$\text{Cov}_{i,i}^{\text{Data Stat}} = X_i^{\text{Data}}, \quad (\text{F.2})$$

$$\text{Cov}_{i,i}^{\text{MC Stat}} = \sum w_i^2, \quad (\text{F.3})$$

where w_i are the weights of MC events in bin i . Statistical errors do not contribute to the off-diagonal elements of the covariance matrix.

F.1 Normalisation

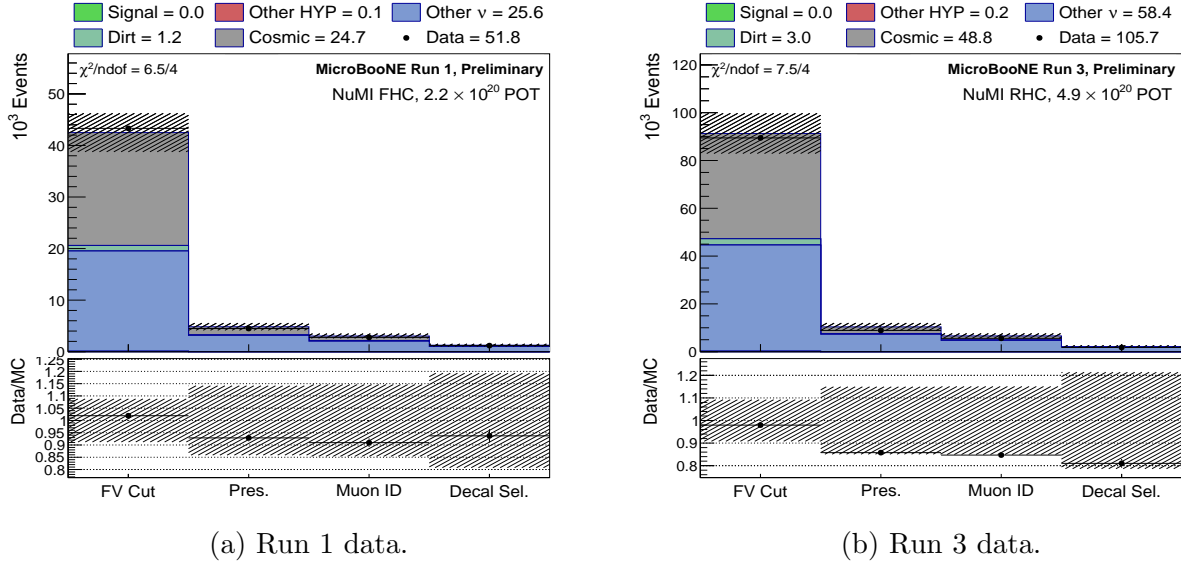
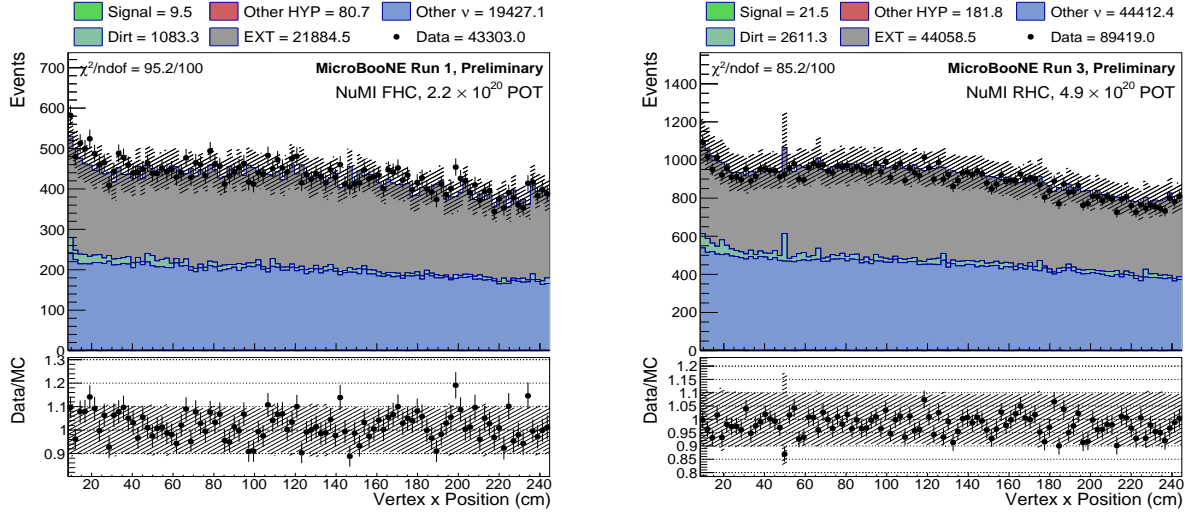


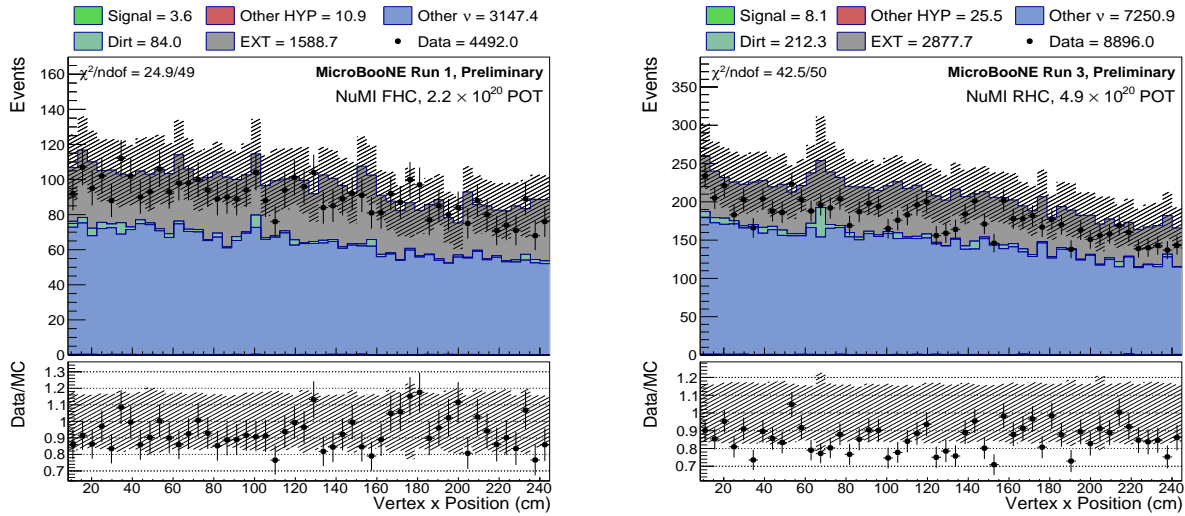
Figure F.1: Comparison of the total number of events at different stage of the event selection.

F.2 Vertex x position.



(a) Run 1 data, after applying the CV cut.

(b) Run 3 data, after applying the FV cut.

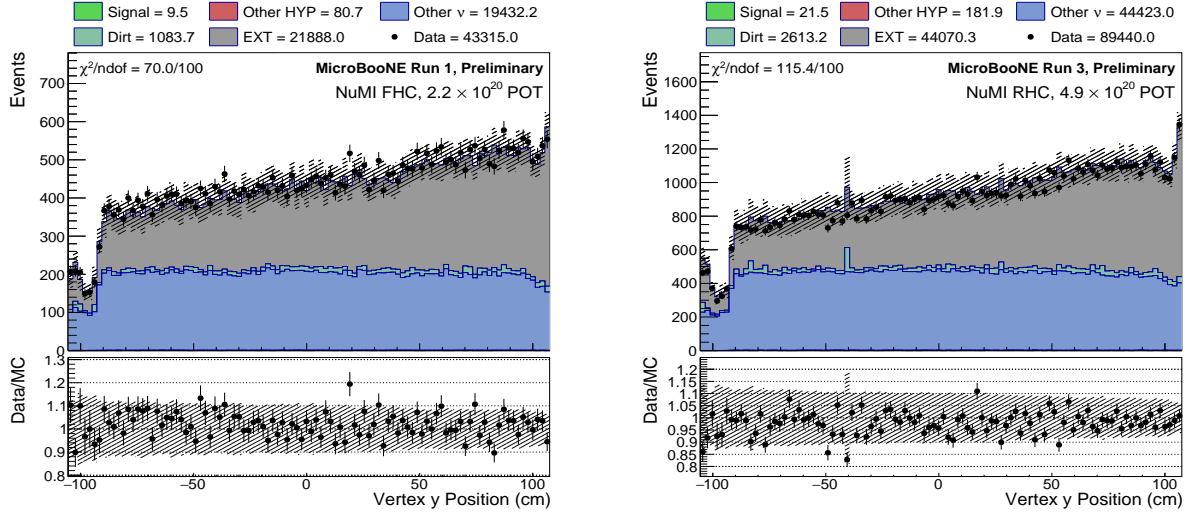


(c) Run 1 data, after applying the FV cut, three track and zero shower requirements.

(d) Run 3 data, after applying the FV cut, three track and zero shower requirements.

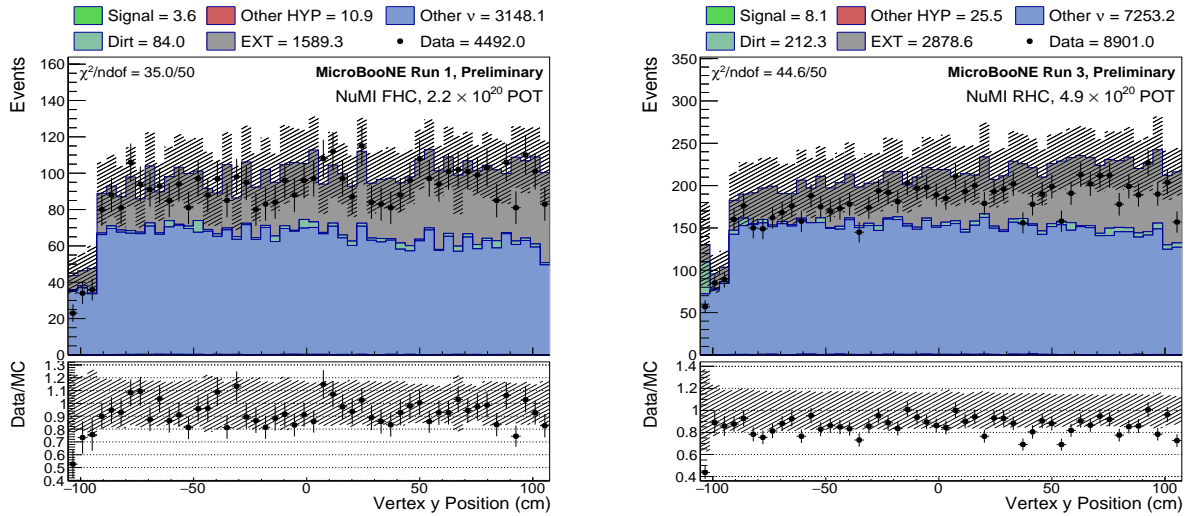
Figure F.2: Comparisons of the x vertex position distributions between data and MC simulation.

F.3 Vertex y position.



(a) Run 1 data, after applying the FV cut.

(b) Run 3 data, after applying the FV cut.

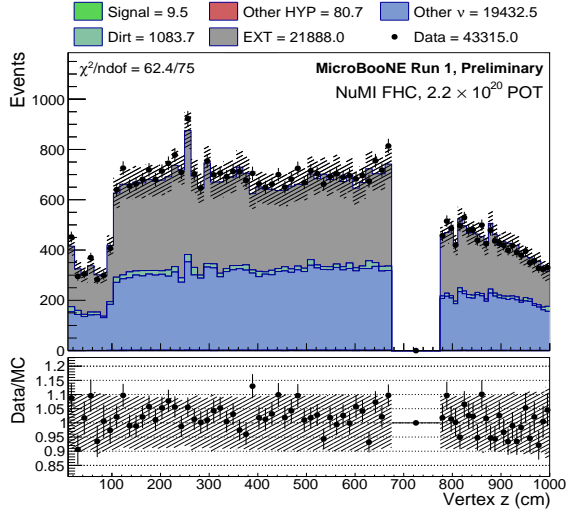


(c) Run 1 data, after applying the FV cut, three track and zero shower requirements.

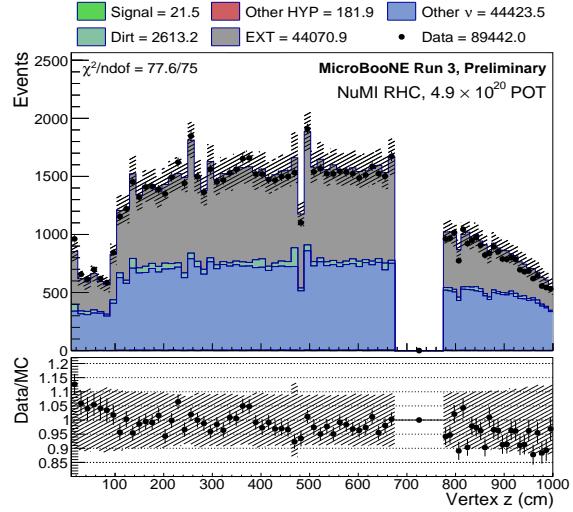
(d) Run 3 data, after applying the FV cut, three track and zero shower requirements.

Figure F.3: Comparisons of the y vertex position distributions between data and MC simulation.

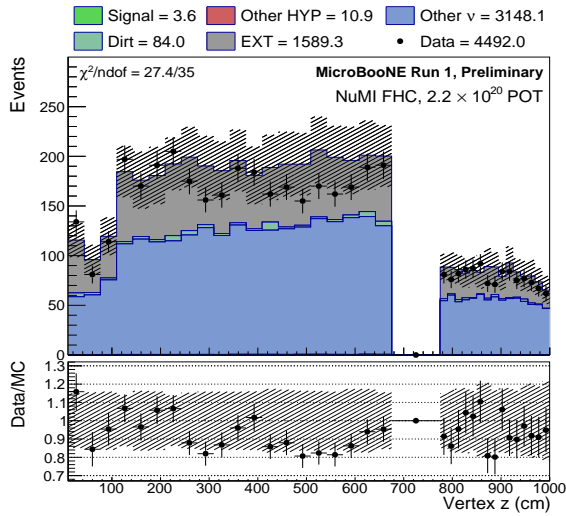
F.4 Vertex z position.



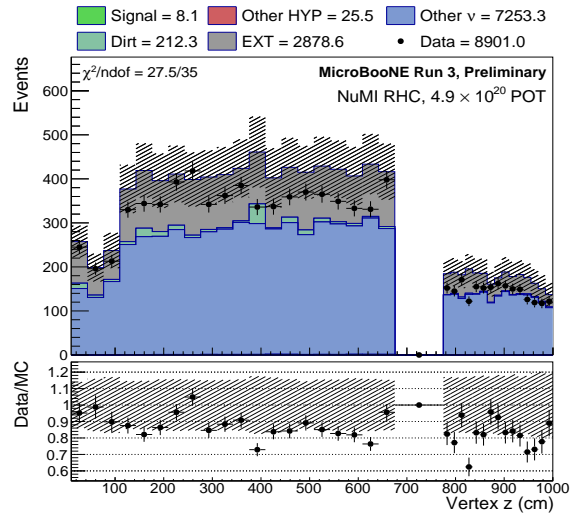
(a) Run 1 data, after applying the FV cut.



(b) Run 3 data, after applying the FV cut.



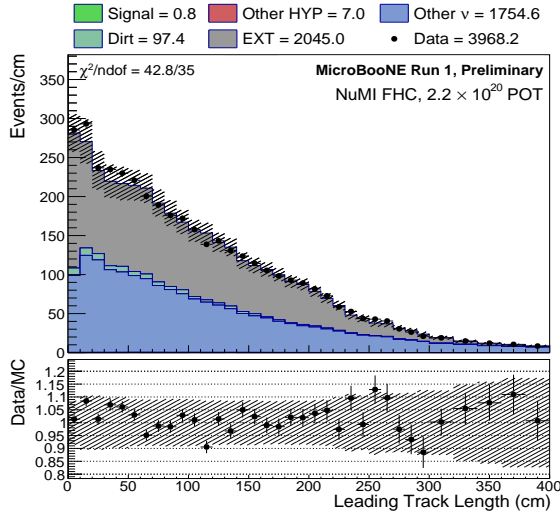
(c) Run 1 data, after applying the FV cut, three track and zero shower requirements.



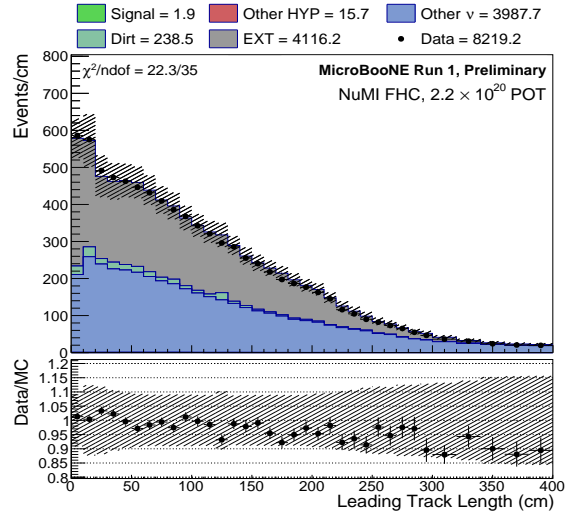
(d) Run 3 data, after applying the FV cut, three track and zero shower requirements.

Figure F.4: Comparisons of the z vertex position distributions between data and MC simulation.

F.5 Leading Track Length



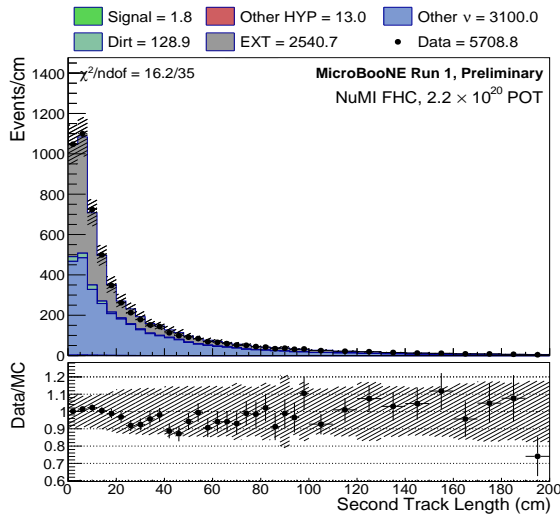
(a) Run 1 data.



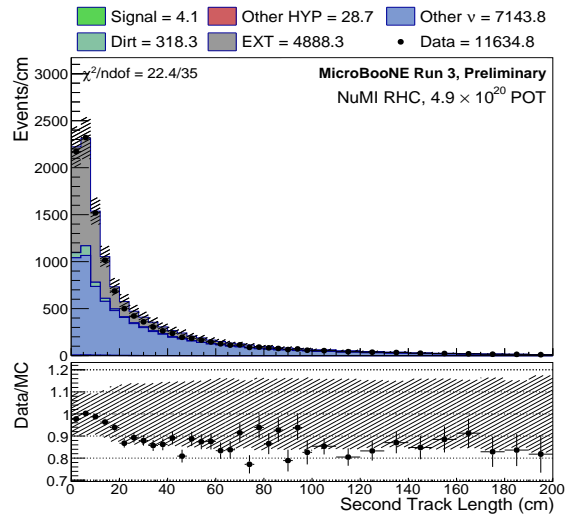
(b) Run 3 data.

Figure F.5: Comparison of the length of the longest track. The FV cut has been applied.

F.6 Second Track Length



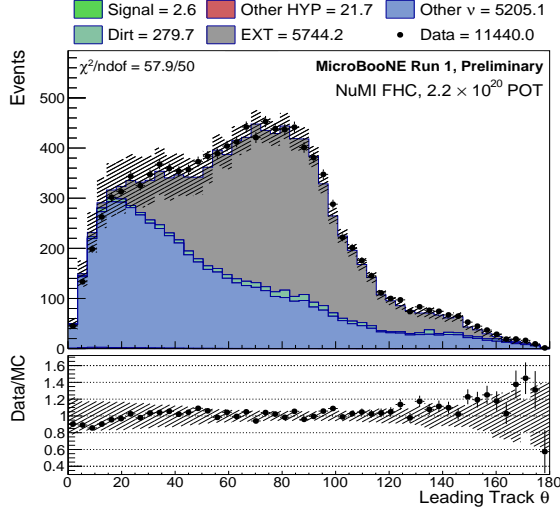
(a) Run 1 data.



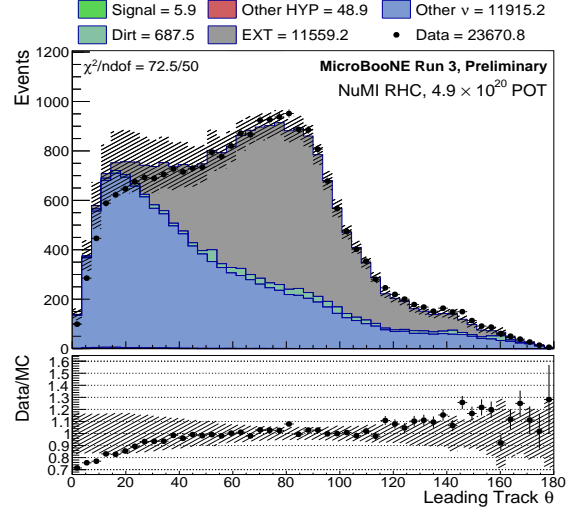
(b) Run 3 data.

Figure F.6: Comparison of the length of the second longest track. The FV cut has been applied and any events with fewer than reconstructed tracks have been removed.

F.7 Leading Track Polar Angle



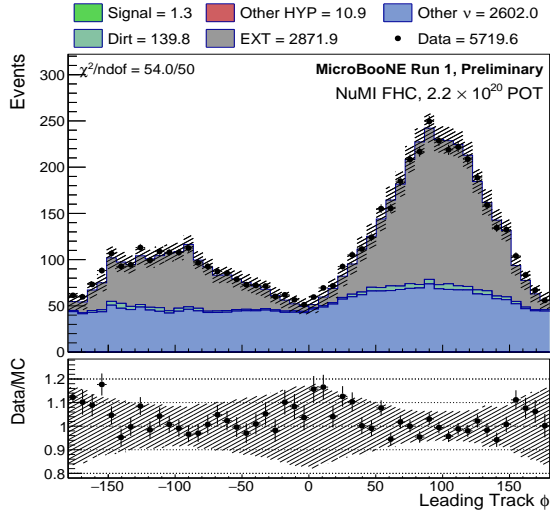
(a) Run 1 data.



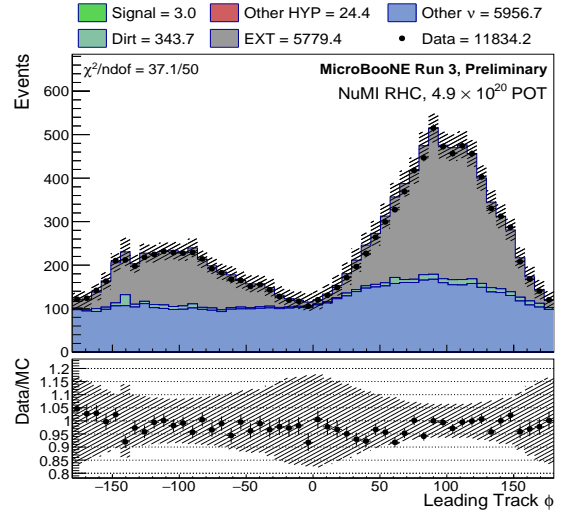
(b) Run 3 data.

Figure F.7: Comparison of the angle between the longest track and the (NuMI) beam direction. The FV cut has been applied.

F.8 Leading Track Azimuthal Angle



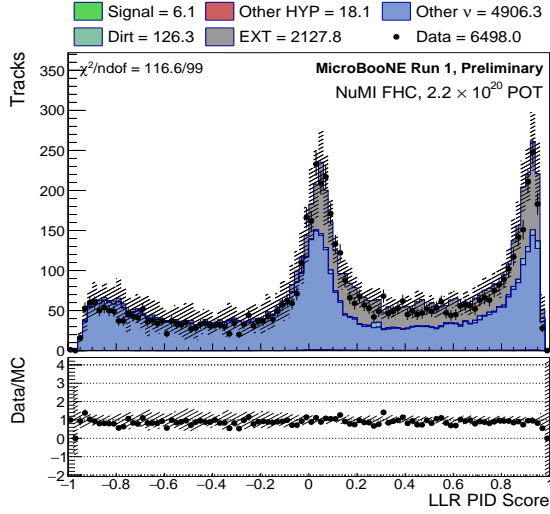
(a) Run 1 data.



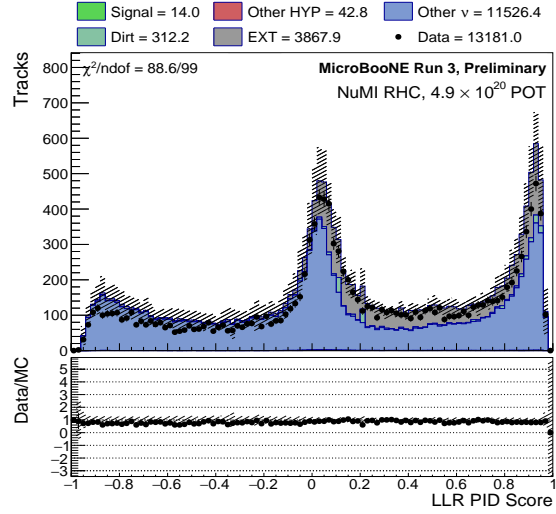
(b) Run 3 data.

Figure F.8: Comparison of the azimuthal angle of the longest track after rotating into the direction of the NuMI beam with the matrix in Equation 5.14. The FV cut has been applied.

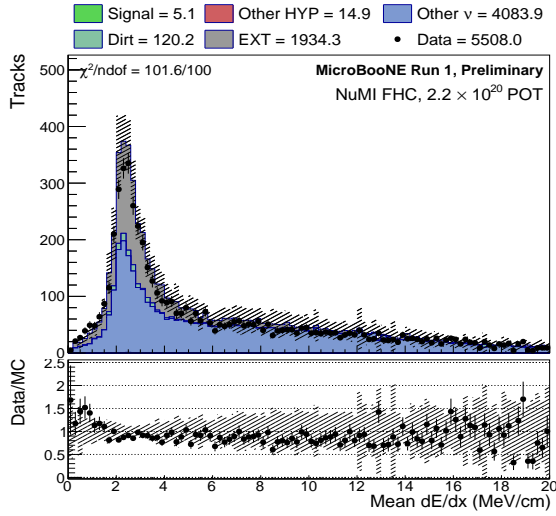
F.9 BDT Input Variables



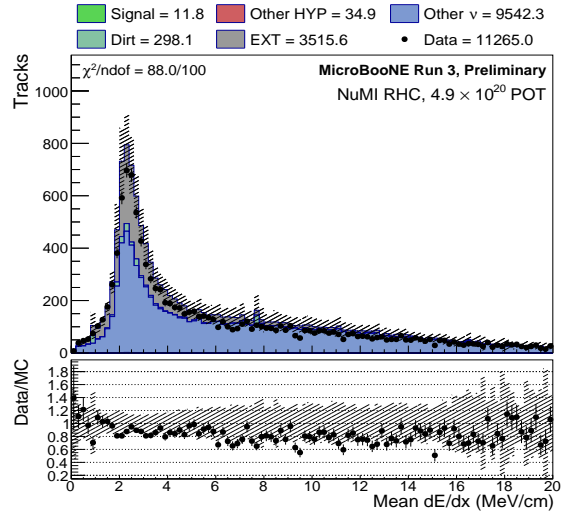
(a) LLR PID score in run 1 data.



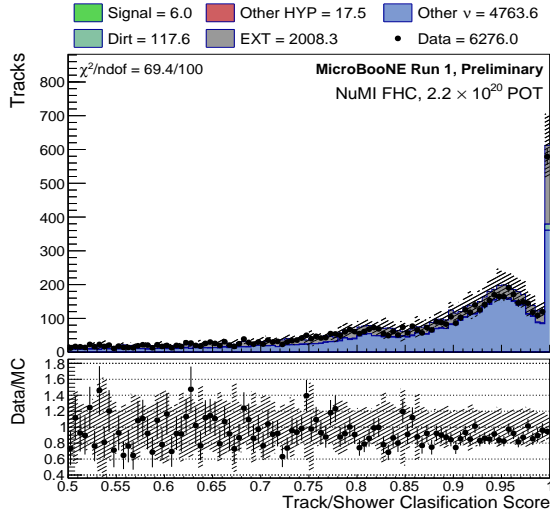
(b) LLR PID score in run 3 data.



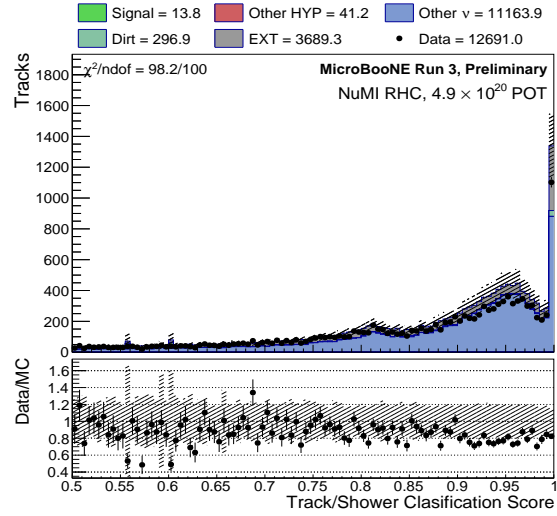
(c) Three plane mean dE/dx in run 1 data.



(d) Three plane mean dE/dx in run 3 data.



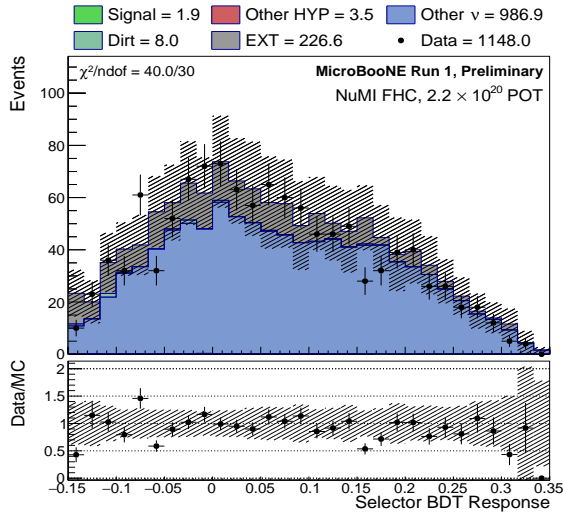
(e) Track/shower classification score.



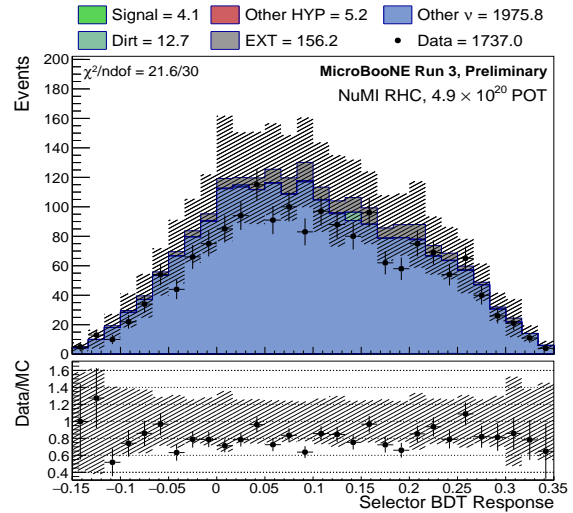
(f) Track/shower classification score.

Figure F.9: Three of the variables employed by the BDTs in the proton and pion track selection described in section 4.5. Calculated after applying the preselection and excluding the muon candidate.

F.10 BDT Response Score



(a) Run 1 data.



(b) Run 3 data.

Figure F.10: The response score generated by the BDTs employed to select the proton and pion tracks, described in Section 4.5), prior to application of the kinematic cuts and island finding.

F.11 Kinematic Variables

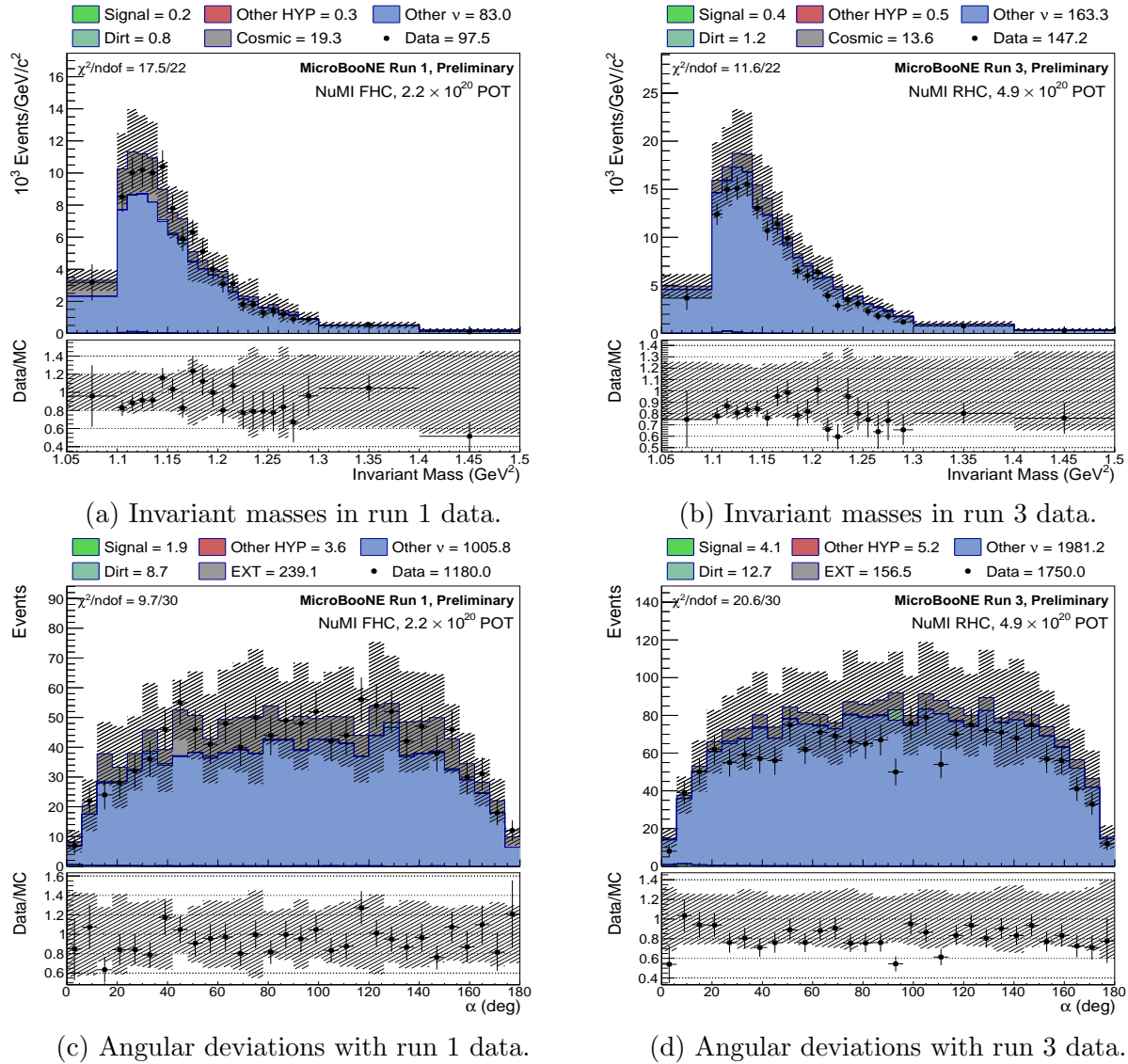


Figure F.11: Kinematic variables employed by the event selection, comparing MC simulation with data. Calculated using the Λ candidates identified in MC simulation and data without applying the island finding.

F.12 Sidebands

To sideband distributions are created by first applying the event selection minus one of the two kinematic variable cuts, before drawing the distribution of the other variable. The distributions were also produced using BNB data, though no systematic uncertainties are applied to these distributions.

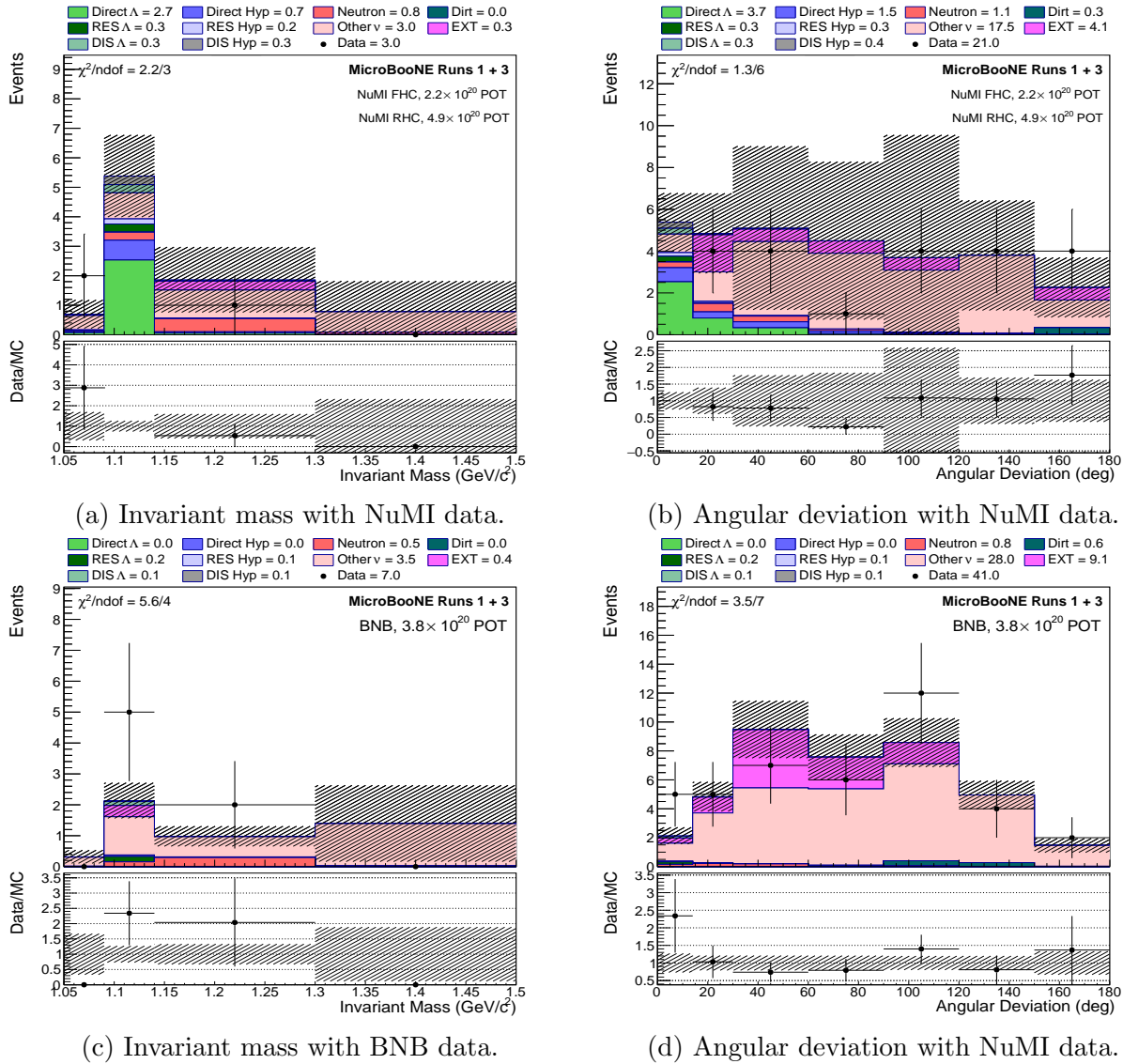


Figure F.12: Distributions of data in sidebands constructed using kinematic variables. In the case of the NuMI data, the signal bin has been kept blind. The plots containing BNB data do not include systematic uncertainties.

Appendix G

Flux

The data analysed in thesis belongs to periods in which the NuMI beam was operated in both of its neutrino and anti-neutrino modes, combined to maximise sensitivity. The flux required to calculate cross sections to be compared with this measurement is therefore unique. This flux is described as a probability mass distribution in Table G.1.

E (GeV)	Φ (GeV ⁻¹)						
0.02	4.5	1.26	0.069	2.50	0.01	3.74	0.01
0.06	4.663	1.30	0.071	2.54	0.009	3.78	0.009
0.10	1.756	1.34	0.07	2.58	0.009	3.82	0.009
0.14	1.934	1.38	0.063	2.62	0.009	3.86	0.009
0.18	2.04	1.42	0.063	2.66	0.009	3.90	0.009
0.22	1.73	1.46	0.059	2.70	0.008	3.94	0.008
0.26	1.223	1.5	0.058	2.74	0.008	3.98	0.008
0.30	0.899	1.54	0.054	2.78	0.008	4.02	0.008
0.34	0.689	1.58	0.05	2.82	0.008	4.06	0.008
0.38	0.562	1.62	0.047	2.86	0.008	4.10	0.008
0.42	0.47	1.66	0.044	2.90	0.007	4.14	0.007
0.46	0.394	1.70	0.039	2.94	0.007	4.18	0.007
0.50	0.324	1.74	0.038	2.98	0.006	4.22	0.006
0.54	0.268	1.78	0.036	3.02	0.006	4.26	0.006
0.58	0.238	1.82	0.033	3.06	0.006	4.30	0.006
0.62	0.209	1.86	0.03	3.10	0.006	4.34	0.006
0.66	0.185	1.90	0.029	3.14	0.006	4.38	0.006
0.70	0.17	1.94	0.028	3.18	0.005	4.42	0.005
0.74	0.152	1.98	0.025	3.22	0.005	4.46	0.005
0.78	0.142	2.02	0.025	3.26	0.005	4.50	0.005
0.82	0.127	2.06	0.024	3.30	0.005	4.54	0.005
0.86	0.12	2.10	0.023	3.34	0.005	4.58	0.005
0.90	0.108	2.14	0.021	3.38	0.005	4.62	0.005
0.94	0.107	2.18	0.019	3.42	0.004	4.66	0.004
0.98	0.097	2.22	0.017	3.46	0.004	4.70	0.004
1.02	0.09	2.26	0.017	3.50	0.004	4.74	0.004
1.06	0.089	2.30	0.015	3.54	0.004	4.78	0.004
1.10	0.081	2.34	0.015	3.58	0.004	4.82	0.004
1.14	0.077	2.38	0.014	3.62	0.003	4.86	0.003
1.18	0.076	2.42	0.012	3.66	0.004	4.90	0.004
1.22	0.077	2.46	0.011	3.70	0.003	4.94	0.003
1.26	0.069	2.50	0.01	3.74	0.003	4.98	0.003

Table G.1: The $\bar{\nu}_\mu$ flux used in Monte Carlo simulations normalised to 1, in bins of 40 MeV, corresponding to a weighted average of FHC and RHC fluxes to describe the two data taking periods analysed.